On the Dynamics of Plate Tectonics: Multiple Solutions, the Influence of Water, and Thermal Evolution

Dissertation Advisor: Professor Richard J. O'Connell John W. Crowley

On the Dynamics of Plate Tectonics: Multiple Solutions, the Influence of Water, and Thermal Evolution

Abstract

An analytic boundary layer model for thermal convection with a finite-strength plate and depth-dependent viscosity is developed. The model includes a specific energy balance for the lithosphere and accounts for coupling between the plate and underlying mantle. Multiple solutions are possible with three solution branches representing three distinct modes of thermal convection. One branch corresponds to the classic boundary layer solution for active lid plate tectonics while two new branches represent solutions for sluggish lid convection. The model is compared to numerical simulations with highly temperature dependent viscosity and is able to predict both the type of convection (active, sluggish, or stagnant lid) as well as the presence of single and multiple solution regimes. The existence of multiple solutions suggests that the mode of planetary convection may be history dependent.

The dependence of mantle viscosity on temperature and water concentration is found to introduce a strong dynamic feedback with plate tectonics. A dimensionless parameter is defined to quantitatively evaluate the relative strength of this feedback and demonstrates that water and heat transport may be equally important in controlling present-day plate-mantle dynamics for the Earth. A simple parameterized evolution model illustrates the feedback and agrees well with our analytic results. This suggests that a simple relationship may exist between the rate of change of water concentration and the rate of change of temperature in the mantle.

This study concludes by investigating the possibility of a magnetic field dynamo in early solar system planetesimals. The thermal evolution of planetesimals is modeled by considering melting, core formation, and the onset of mantle convection and then employing thermal boundary layer theory for stagnant lid convection (if possible) to determine the

cooling rate of the body. We assess the presence, strength and duration of a dynamo for a range of planetesimal sizes and other parameters. We find that a minimum radius of O(500) km is required for a thermally driven dynamo of duration O(10) My. The dependence of the results on model parameters is made explicit through the derivation of an analytic solution.

Contents

List of Figures

List of Tables

Acknowledgements

I have many people to thank for the great six years that I have had in Boston while working on my PhD at Harvard. I'll begin by thanking the members of my thesis committee: Jerry Mitrovica, Sujoy Mukhopadhyay, Jim Rice, Jeremy Bloxam, and Howard Stone. Funding for my PhD was provided by the US National Science Foundation (EAR-1015353), the Natural Sciences and Engineering Research Council of Canada (PGSD3-358659-2008), and by the Department of Earth and Planetary Sciences, Harvard University.

I would especially like to thank my advisor Rick O'Connell. He gave me complete freedom to work on problems that interested me and was always around to provide guidance and encouragement when I needed it. Without this, it's unlikely that I would have continued to struggle through the problem that is now the core of my thesis, having tried what seemed like hundreds of ideas in my first three years and having made, what seemed at the time, little progress. He allowed me to teach seven semesters and a total of ten sections, more than anyone else I know, and I feel that I have really learned a lot from this. Rick not only supported my research but also encouraged my travel to conferences and always introduced me to people he knew. In this way he helped me to start to build what is now a large network of friends and colleagues all over the world. His knowledge and experience in science as well as the politics of science was invaluable in helping me through some of the situations that I found myself in throughout the past few years. I feel very fortunate to have had such an excellent advisor.

I would like to thank my old undergraduate advisor Jerry Mitrovica for his continuous support and friendship over the years. Without his early guidance and encouragement I would have never applied to graduate school. He has continued to look out for me and I

think he even moved from Toronto to Boston just to try to keep me out of trouble. Thanks for everything Jerry.

I have had the pleasure of teaching with several faculty members throughout the years, including Brendan Meade, Jerry Mitrovica, Rick O'Connell, and Eli Tziperman. I would especially like to thank Eli who I have now taught three courses with. It's been a lot of fun and I have learnt a lot. I would also like to thank the fantastic staff in the department of Earth and Planetary Sciences, especially Sarah Colgan, Maryorie Grand, and Chenoweth Moffat for all their help throughout the years. Thank you John Shaw for providing us with several excellent espresso machines. My thesis would have certainly been a chapter shorter if I had not been awake for all those hours.

Several colleagues have gone out of their way over the years to look out for me, provide guidance, and help me further my scientific career. While there are too many to acknowledge everyone, I would like to thank John Hurnlund, Dave Bercovici, Adrian Lenardic, and Saswata Hier-Majumder for this. I have also had the pleasure to work with Tobias Hoink, Thorsten Becker, Marc Hirschmann, Andrew Schaeffer, and Peter Barry.

I want to thank all my amazing friends in the department that have kept things interesting and fun over the years. I don't think it would have been possible to work as hard as I did at times without balancing the work with short, sometimes uncontrolled, bursts of intense partying and adventure. Thanks Kate Dennis, Victor Tsai, Jon Gero, Allie Gale, Rick Kraus, Helen Amos, Justin Parella, Hilary Close, Ben Lee, Patrick Kim, Kristian Bergen, Meredith Langstaff, Chris Holmes, Carling Hay, Tom Benson and everyone else. I have a lot of great memories with you guys, such as struggling through the first two years and quals, the impromptu barbecues, the keg tour around Harvard yard, the time we almost died in death valley, the time we ate $250 of hipster tacos and then attempted to run hurdles, the road trips, the field trips, and new years in Europe. And if you think, Kate, that you have had the last laugh with that shot of Jagermeister, you are mistaken. Thanks also to my friends Sam Drake and Dustin Stokes for rescuing me from my thesis writing and instigating many great times over the past year.

One of the benefits of being a graduate student at Harvard, having plenty of funding, and having an advisor that gave me freedom to work on any projects that interested me, is that I was able to work on projects with some of my friends. I would especially like to thank Glenn Sterenborg, my office mate for five years, for his friendship, support, collaboration, and dutchness. Thanks for all the help, for reading my papers more times than hearing my stories, and for knowing me well enough to call me on things that no one else would. We had a lot of great times and I'm sure there will be many more. Another friend that I have had the pleasure of working with in Santa Barbara, San Francisco, Los Angeles, New York, and Boston is Mélanie Gérault. I look forward to finding more excuses to travel and work together and thank you for your support and friendship.

Thanks to all my great housemates that I have lived with over the years: Rick, Helen, Nathan, Cassie and Nick, and especially Andy and Clarissa. I consider myself very lucky to have met you all and living together has made the past few years of grad school so much more enjoyable.

Last but not least, I would like to thank my family and friends back home in Canada. Thanks mom and dad for always being so supportive. Thanks Joe, Mary, and Sarah for always making an effort to meet up whenever I was home. Thanks to all my friends back home, especially Steve, Dustin, Tyler, Krista, Dan, Hailey, Rob, and Anna. You guys have been awesome and even though I only see you a few times a year it always feels like I never left.

Chapter 1

Introduction

The classic boundary layer model for plate tectonics was proposed 45 years ago and provided a reasonable theoretical framework for understanding the motion of the Earth's tectonic plates (Turcotte, 1967; Turcotte and Oxburgh, 1967). The theory suggested that buoyant forces in the Earth's mantle would be sufficient to deform mantle rock and produce thermal convection over large distances and geological timescales. Tectonic plates were considered the surface manifestation of the convective flow in the mantle and the sinking of cold thick plates at subduction zones and upwelling of warm mantle material at ridges provided an efficient means for cooling the Earth's mantle. The boundary layer theory is based on the physics of thermal convection in a fluid layer with homogeneous material properties. The dynamics predicted by this theory are governed by the material properties and thermal state of the mantle and the model contains no information regarding the properties of the plate itself. The theory predicted values for tectonic plate speeds and surface heat flow that were in reasonable agreement with those observed for the Earth.

Other ideas were put forth regarding a dynamical theory for plate tectonics. Elsasser (1969) proposed that plates would be cold and, as a result of the strong temperature dependence of viscosity, would have sufficient mechanical strength to transmit stresses over hundreds to thousands of kilometers. He suggested that tectonic plates moved faster than the underlying mantle and that drag on the base of the plate was balanced by forces transmitted through the plate from the sinking of the cold (negatively buoyant) plate at the

subduction zone. This started a debate that remains alive to this day on whether plates drive mantle convection or mantle convection drives plates. Neither of the theories could address the nature of the coupling between the plate and mantle as the boundary layer theory did not explicitly contain any strong plate and the idea of Elsasser (1969) remained only a conceptual one (no dynamical theory was ever developed).

The classic boundary layer theory provides a simple means of estimating the tectonic plate speed and surface heat flow for a planet with a convecting mantle. If the Earth's mantle temperature and properties are approximately known (or specified) at some time in the past then the boundary layer theory can be used to estimate the surface heat flow at that time. The latter can then be used to determine the rate of cooling of the mantle from that time onwards. Boundary layer theory thus allows for the calculation of simple thermal histories for the Earth (e.g., Davies, 1980; Sharpe and Peltier, 1979; Spohn and Schubert, 1982). The historical temperatures predicted by these models were found to be very sensitive to the amount of internal heating in the mantle and the models were unable to achieve reasonable thermal histories consistent with present day mantle temperature, heat flow, and the geochemically inferred concentration of radiogenic elements in the mantle (see, for example the recent review by Korenaga, 2008). These thermal history calculations emphasized the importance of the temperature dependence of mantle viscosity and identified it as a key controlling factor in planetary thermal histories. If the Earth began hot, the mantle would have a low viscosity and boundary layer theory predicted a heat flow that was much greater than the heating supplied by radionuclides. The mantle would rapidly cool until the surface heat flow closely balanced the rate of internal heating. Conversely, if the Earth began cool, the mantle would have a high viscosity and boundary layer theory predicted a heat flow that was less than that supplied by internal heating. In this case the mantle warmed with time until the surface heat flow was close to the rate of internal heating in the mantle. This self-regulating feedback or 'mantle thermostat' is the result of the strong temperature dependence of viscosity and was first pointed out by Tozer (1970). Calculations using the classic thermal boundary layer theory for plate tectonics always

resulted in a mantle that cooled too quickly, requiring a higher rate of internal heating to account for the present day heat flow than is consistent with cosmochemical constraints. The key results of the early thermal history calculations are summarized in Christensen (1984). A great deal of work has been devoted to developing variations of these boundary layer models and thermal history calculations in the hopes of circumventing this discrepancy.

Early studies of mantle convection with strongly temperature dependent viscosity (see for example Booker, 1976; Christensen, 1984; Morris and Canright, 1984) demonstrated that mantle convection could still occur beneath a strong immobile cold boundary layer (so-called 'stagnant-lid' convection) and that plates were not required for mantle convection. However, this demonstrated only that mantle convection need not *always* be driven by plate tectonics. The question of whether convective flow in the mantle drives or resists plate motions has thus far remained unanswered.

Given the limited observations available at the time, the classic boundary layer theory of Turcotte and Oxburgh (1967) was a significant and important step in understanding plate tectonics and mantle convection. Moreover, it was likely that the simplicity of the dynamical theory contributed to its widespread acceptance and ultimately ended the long standing geological debate over whether plate tectonics was physically possible (most geodynamics texts, such as Davies, 1999, contain a discussion of this). However, this theory, while applied widely and often, is not appropriate for addressing problems involving strong tectonic plates and plate-mantle coupling. There is no plate in the classic boundary layer theory; the model assumes a free surface that offers no resistance to motion. This thesis will demonstrate that the presence of a strong surface boundary layer fundamentally changes the dynamics of the problem. Only under specific circumstances will the classic boundary layer model of Turcotte and Oxburgh (1967) still provide a viable solution when mechanically strong plates are present.

The need for a dynamical model that incorporates strong plates in a self consistent way was first realized by Conrad and Hager (1999) who developed a global energy balance model that included the energy required to deform and subduct strong plates. However,

they found that for reasonable (Wu et al., 2008) plate strengths the energy required to deform the plates had little effect on the global energy balance. Moreover, they pointed out that this effect would have been further diminished earlier in the Earth's evolution when the mantle was warmer and plates presumably moved faster (Conrad and Hager, 1999). Faster moving plates have less time to diffusively cool at the surface and are therefore thinner when they subduct. Thinner plates require less energy to bend and thus contribute less to the global energy balance. Thus, it seemed unlikely that the presence of strong plates would affect plate speeds or heat flow during the Earth's early evolution and this model offered no resolution to the issues regarding the Earth's thermal history discussed above. A variation of this global energy balance model suggested that the mechanical thickness of a plate might sometimes be controlled by dehydration rather than the thermal profile of the plate (Hirth and Kohlstedt, 1996; Korenaga, 2003). Partial melting in the mantle releases volatiles and results in a dehydrated lithosphere. Due to the sensitivity of rheology to water content, this may lead to an increase in mechanical plate strength that is more significant than the increase in strength due to temperature. In this model the effect of plate bending would be larger during Earth's early evolution if the mantle was warmer and melting occurred deeper. Korenaga (2003) presented thermal history calculations that implemented this idea and demonstrated the effect of lithospheric dehydration on limiting plate speeds, slowing the cooling of the Earth's mantle, and possibly satisfying the present day constraints on mantle temperature, heat flow, and internal heating. Davies (2009), however, pointed out that the model of Korenaga (2003) was extremely sensitive to the parameter values used. As such, this model, and in general the thermal history calculations for the Earth produced thus far, remain unsatisfactory. In Chapter 3, we will see that the energy required to bend plates, while very small in the global energy balance, plays an important role in the local energy balance of the plate.

The primary goal of this thesis is to develop a dynamical theory for plate tectonics and mantle convection in the presence of strong plates. Chapter 2 will re-derive the classic boundary layer solution for thermal convection in an isoviscous fluid layer and further extend

it to develop a new and more general solution that allows for mixed heating.

In Chapter 3 we will derive the energy balance equations for a new analytic model for plate-mantle dynamics. The model will be used to show that plate dissipation, while a small term in the global energy balance, can be a dominant term in the local lithospheric energy balance and control the plate speed and energy available for mantle convection. We will demonstrate that multiple solutions may occur for the same planetary properties and thermal state, with each solution corresponding to a distinct mode of thermal convection. The new modes will be shown to represent sluggish-lid convection in which plates move slowly over a more rapidly convecting mantle. These boundary layer solutions, or mantle convection modes, can be simply captured in analytical equations, which further demonstrate that mantle convection may *drive* or *resist* plate motions depending on the specific mode of convection. The existence of multiple solutions adds a new dimension of complexity to thermal history calculations for the Earth and other planets. Our model suggests that planets may transition between different states throughout their evolution, as first conceptually suggested by Sleep (2000) and that the state of a planet, when multiple states are possible, will depend on its earlier evolution. This raises questions regarding what defines a tectonic state of a planet and suggests that, if multiple solutions are possible, the presence of plate tectonics on a planet such as a super-Earth (O'Neill and Lenardic, 2007; Valencia et al., 2007), may depend more on the evolution of the planet than it does on its thermal state and material properties. Chapter 3 will conclude by comparing our new analytic model to numerical simulations of thermal convection that provide further evidence of the existence of sluggish-lid convection, multiple solutions and history dependence.

The secondary goal of this thesis is to explore interesting feedbacks associated with plate tectonics and mantle convection. Chapter 4 will examine a feedback that manifests itself through the dependence of mantle viscosity on water concentration in the mantle and consider how the transport of water to and from the mantle, via plate tectonics, may modify the evolution of a planetary body such as the Earth. The results suggest that a simple relationship may exist between the rate of change of water concentration and the rate

of change of temperature in the mantle. Chapter 5 will discuss the classic thermal feedback between temperature and viscosity in determining the cooling rate of planetesimals and the ability of these small bodies to support strong magnetic field dynamos over millions of years. We will demonstrate that the duration of a dynamo depends foremost on the planetesimal's radius and that bodies smaller than ~ 500 km are likely unable to maintain strong dynamos for millions of years.

In an early paper on numerical convection simulations (McKenzie et al., 1974), the authors made the comment that "although the equations and boundary conditions are highly simplified [...] the computations already display a wealth of complicated behavior. The simplification is deliberate: it is more profitable to begin with a carefully planned study of idealized models than to program every detail and generate results that are neither comprehensible nor accurate." Sophisticated numerical methods and readily available computational power have markedly improved the 'accuracy' of many numerical models. Nevertheless, many of the physically 'realistic' numerical convection models used today remain difficult to understand and obscure a full understanding of any results they produce. Our approach is to pursue simplicity and to solve problems analytically when feasible. If done carefully, we hope the gain in physical insight will outweigh the cost of having to settle for results that are considered 'approximate'.

Chapter 2

Simple convection scalings

"Chance favors the prepared mind."
–Louis Pasteur

I present here solutions to a few simple convection problems. These will provide insight and prepare us for the more involved problems to be discussed in the following chapters.

Before considering the complex dynamics of thermal convection in planetary systems with temperature dependent rheology, phase transitions, and other such complications, we will first consider the basic physics of 2D thermal convection in simple fluids. We will start by working out the dynamics of thermal convection in a fluid layer with homogeneous material properties. We will then consider the case when viscosity is temperature dependent and a strong cool thermal boundary layer is present at the surface. Finally, we will discuss thermal convection in an 'open' layer which may be useful for modeling the Earth's lower mantle.

Throughout this thesis we will repeatedly refer to various 'modes' of thermal convection and will rely on the following definitions to distinguish them from each other. A planet/system will be said to be in the *mobile-lid* convective mode when the surface (plate) velocity is comparable to or exceeds the maximum laterally averaged horizontal velocity in the convective flow beneath it. In other words, the plate moves at a rate comparable to the convective flow beneath it. The *active-lid* mode is the same as the mobile-lid mode and these two terms will be used interchangeably. A planet/system is in the *sluggish-lid*

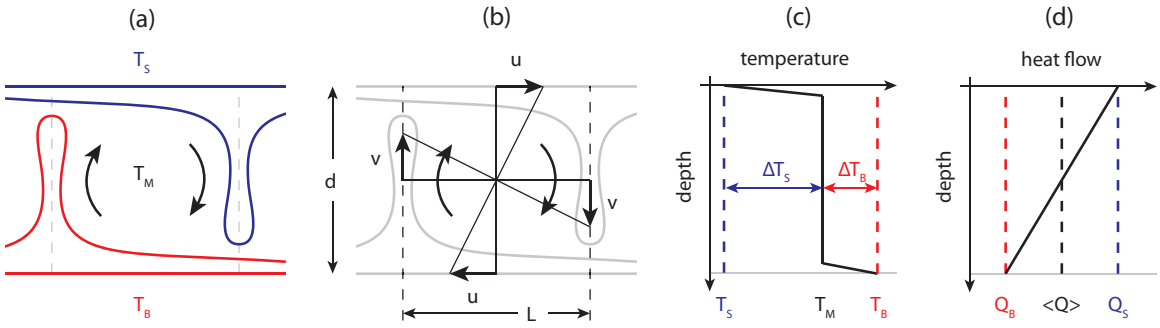

Figure 2.1: Diagram for thermal convection in a fluid layer. (a) Illustration of thermal boundary layers. (b) Simplified flow structure with horizontal surface velocity u. (c) Average temperature structure in the convective cell. (d) Heat flow as a function of depth in the convective cell. The heat flow increases from the base of the layer to the surface owing to internal heating.

convective mode when the surface (plate) velocity is non-zero and is moving slower than the laterally averaged horizontal flow in the convective flow beneath it. If the surface thermal boundary layer (plate) is strong (the notion of 'strong' will be discussed and defined in Chapter 3) and moving slowly enough, thermal convection beneath it may erode the base of the plate. The thickness of the plate will no longer be determined by the plate velocity and diffusive cooling from the surface (half-space cooling model), but rather by the growth and detachment of small scale thermal instabilities at its base (see for example Korenaga, 2009). In this case the system is said to be in the *stagnant-lid* regime. It should be noted that the plate velocity is not necessarily zero in the stagnant lid regime and this terminology can be misleading.

2.1 THERMAL CONVECTION IN A FLUID LAYER WITH MIXED HEATING

In this section we will solve the convective heat transport problem for an isoviscous fluid layer with mixed heating using an energy balance approach. This problem is generally worked out assuming either boundary or internal heating and this is the first time, to our knowledge, that the problem has been solved with both boundary and internal heating (i.e. mixed heating). We will find that this general solution can be used to obtain both the

boundary and internally heated end member cases and provides further insight into the behavior of the system when both forms of heating are present. We consider a convecting fluid layer, shown in Figure 2.1, with average convective cell width L and depth d. The fluid layer is homogenous and has density ρ, specific heat C_p, thermal conductivity k, thermal diffusivity $\kappa = k/(\rho C_p)$, and viscosity μ.

A small Reynolds number and large Prandtl number are assumed and the flow is considered to be incompressible. As such, the rate of change of potential energy is required to exactly balance the total dissipation in the fluid. The basic approach is addressed in most geodynamics texts, such as Turcotte and Schubert (2002), and the equations and other details can be found therein. Both the rate of change of potential energy and the viscous dissipation in the convecting fluid will be related to the convective velocity u. An energy balance will then be used to solve for u. We assume that the system is evolving slowly enough that changes in temperature, viscosity, etc., are small over the time scale of convective overturn. All energy terms are calculated per unit distance along the axis of the convective roll.

All external boundaries are considered to be free slip. The temperatures at the base and surface of the layer are T_B and T_S, respectively, and give a temperature drop of $\Delta T = T_B - T_S$ across the fluid layer. The fluid layer may also have internal heating at a rate of H and in units of W/m^3 (from, for example, the radiogenic decay of the elements ^{238}U, ^{235}U, ^{232}Th, and ^{40}K). The interior of the convective cell is assumed to be well mixed and of temperature T_M. The temperature drop across the cold thermal boundary at the surface is $\Delta T_S = T_M - T_S$. The temperature drop across the hot thermal boundary layer at the base is $\Delta T_B = T_B - T_M$. The sum of the temperature drop across the two thermal boundary layers is equal to the temperature drop across the fluid layer

$$\Delta T = \Delta T_B + \Delta T_S \tag{2.1}$$

The surface heat flow Q_S can be calculated using thermal boundary layer theory (Tur-

cotte and Schubert, 2002) and is given by

$$Q_S = 2k\Delta T_S \left(\frac{uL}{\pi\kappa}\right)^{\frac{1}{2}} \tag{2.2}$$

Similarly, the heat flow through the base of the layer is

$$Q_B = 2k\Delta T_B \left(\frac{uL}{\pi\kappa}\right)^{\frac{1}{2}} \tag{2.3}$$

It is important to keep in mind that the relationships given by equations (2.2) and (2.3) are kinematic relationships between the boundary velocity, temperature drop across the thermal boundary layer, and heat flow through the boundary layer. A useful relationship between the two heat flows and the temperature drop across the thermal boundary layers is obtained by taking the ratio of equations (2.2) and (2.3)

$$\frac{Q_S}{Q_B} = \frac{\Delta T_S}{\Delta T_B} \tag{2.4}$$

The rate of change of potential energy for a single convecting cell Φ_P is given by

$$\Phi_P = \frac{\alpha g d}{C_p} \langle Q \rangle = D_i \langle Q \rangle \tag{2.5}$$

where $\langle Q \rangle = \frac{1}{d}\int_0^d Q(z)dz$ is the depth averaged vertical heat flow through the convective cell and D_i is the dissipation number (note that advection within the convective cell is the dominant mode of heat transport and we have assumed $Q = Q_{adv} + Q_{cond} \approx Q_{adv}$ in equation (2.5)). Equation (2.5) is derived in full and discussed in section 3.2.1. In cartesian geometry and with uniformly distributed internal heating the depth averaged heat flow is simply

$$\langle Q \rangle = \frac{Q_S + Q_B}{2} = \frac{1}{2}\left(Q_S + \frac{\Delta T_B}{\Delta T_S} Q_S\right) = \frac{Q_S}{2}\frac{\Delta T}{\Delta T_S} \tag{2.6}$$

where we have used the relations in equations (2.1) and (2.4). If the convective cell is entirely internally heated then $\Delta T = \Delta T_S$ and $\langle Q \rangle = Q_S/2$ (zero heat flow at the base of

the layer with a linear increase up to Q_S at the surface). If the convective cell is entirely boundary heated than the thermal boundary layers at the base and surface will be equal in thickness (symmetry of the problem), $\Delta T = 2\Delta T_S$, and $\langle Q \rangle = Q_S$ (constant vertical heat flow through the layer).

Using equations (2.2), (2.5), and (2.6) the total rate of change of potential energy for the convective cell is then

$$\Phi_P = \frac{\alpha g d}{C_p} k \Delta T \left(\frac{uL}{\pi \kappa} \right)^{\frac{1}{2}} \tag{2.7}$$

The rate of change of potential energy will be balanced by viscous dissipation in the fluid. For a Newtonian fluid, the viscous dissipation in the convective cell can be calculated as

$$\Phi_V = 2 \int_0^L \int_0^d \mu \dot{\epsilon}_{ij}^2 dz dx \tag{2.8}$$

where $\dot{\epsilon}_{ij}$ is the deviatoric strain rate tensor

$$\dot{\epsilon}_{ij} = \frac{1}{2} \left(\frac{\partial u}{\partial z} + \frac{\partial v}{\partial x} \right) \tag{2.9}$$

Equations (2.8) and (2.9) are discussed in more detail in section 3.2.1. The strain rate tensor may be approximated by assuming that $\partial u / \partial z \approx 2u/d$ and $\partial v / \partial x \approx 2v/L$ (see Figure 2.1). Conservation of mass requires $ud = vL$. Then the strain rate tensor for the convective cell may be approximated as

$$\dot{\epsilon}_{ij} \approx \frac{1}{2} \left(\frac{2u}{d} + \frac{2v}{L} \right) = \left(\frac{u}{d} + \frac{(ud/L)}{L} \right) = \frac{u}{d} \left(1 + \left(\frac{d}{L} \right)^2 \right) \tag{2.10}$$

Substituting equation (2.10) into equation (2.8) and integrating then yields

$$\Phi_V = 2\mu \frac{L}{d} u^2 \left(1 + \left(\frac{d}{L} \right)^2 \right)^2 \tag{2.11}$$

Using equations (2.7) and (2.11) and $\Phi_P = \Phi_V$ (conservation of mechanical energy) the plate velocity can be solved for to provide the relationship

$$u = \frac{\kappa}{d} \frac{(L/d)^{7/3}}{(1+(L/d)^2)^{4/3}} \left(\frac{Ra_T}{2\sqrt{\pi}} \right)^{2/3} \tag{2.12}$$

where we define the Rayleigh number Ra_T as

$$Ra_T = \frac{\alpha \rho g \Delta T d^3}{\mu \kappa} \tag{2.13}$$

Turcotte and Schubert (2002) derived the following for the boundary heated case ($\Delta T_S = \Delta T/2$)

$$u_{T\&S} = \frac{\kappa}{d} \frac{(L/d)^{7/3}}{(1+(L/d)^4)^{2/3}} \left(\frac{Ra_T}{\sqrt{\pi}} \right)^{2/3} \tag{2.14}$$

Note that the solutions differ by a factor of $2^{2/3}$. This difference arises from the fact that Turcotte and Schubert (2002) overestimate (double) the contribution from buoyancy. The derivation is made more sound by use of equation (2.5) which removes the need (and confusion) of assessing the internal density structure of the convective cell and relates the total energy available to the heat flow. Also note that the convective velocity in equation (2.12) depends only on the temperature drop across the layer and is independent of the rate of internal heating.

A second small difference between equations (2.12) and (2.14) is the dependence on aspect ratio (note the powers in the denominators). This is due to small variations in our approach for calculating the viscous dissipation (see Turcotte and Schubert, 2002, for details). Both approaches make different approximations and this difference in equations is much smaller than the error introduced by the approximations themselves. Thus, this minor difference in equations should not concern us. We will use equation (2.12) in most of the discussions that will follow. We can use equations (2.2) and (2.12) to calculate the heat flow out of the convective cell

$$Q_{conv} = Q_S = k \Delta T_S \left(\frac{2}{\pi} \right)^{2/3} \frac{(L/d)^{5/3}}{(1+(L/d)^2)^{2/3}} Ra_T^{1/3} \tag{2.15}$$

It will sometimes be simpler to use the average heat flux (W/m^2) instead of the heat flow given by equation (2.15). We can obtain an average heat flux q_{conv} by dividing by the length of the convective cell L

$$q_{conv} = q_S = \frac{k\Delta T_S}{d}\left(\frac{2}{\pi}\,\frac{L/d}{1+(L/d)^2}\right)^{2/3} Ra_T^{1/3} \tag{2.16}$$

Both the heat flow and the heat flux depend on the temperature drop across the upper thermal boundary layer ΔT_S. If the system is at steady state then the heat flow out of the surface must balance the heat flow in through the base plus any contribution due to internal heating. We then require

$$q_S = q_B + Hd = \frac{\Delta T_B}{\Delta T_S} q_S + Hd \tag{2.17}$$

where we have again used equation (2.4) to relate the surface and basal heat flow (in this case heat flux). Rearranging equation (2.17), assuming that there is some internal heating ($H \neq 0$), and solving for the surface heat flux q_S gives

$$q_S = \left(\frac{\Delta T_S}{2\Delta T_S - \Delta T}\right) Hd \tag{2.18}$$

where equation (2.1) has again been used to relate ΔT_B to ΔT_S and ΔT. We now equate the surface heat flux in equations (2.16) and (2.18) and solve for ΔT_S

$$\Delta T_S = \frac{\Delta T}{2} + \frac{1}{2}\,\frac{Hd^2}{k}\left(\frac{\pi}{2}\frac{1+(L/d)^2}{L/d}\right)^{\frac{2}{3}} Ra_T^{-\frac{1}{3}} \tag{2.19}$$

Equation (2.19) demonstrates that $\Delta T_S \to \Delta T/2$ as $H \to 0$, as the symmetry of the problem requires. Equation (2.19) holds as long as

$$H \leq H_{crit} = \frac{k\Delta T}{d^2}\left(\frac{2}{\pi}\,\frac{L/d}{1+(L/d)^2}\right)^{2/3} Ra_T^{1/3} \tag{2.20}$$

For $H > H_{crit}$ the internal temperature T_M is larger than the basal temperature, a stable cool thermal boundary layer would form at the base of the fluid layer and the relationship

for the basal heat flow would change. Substituting ΔT_S from equation (2.19) back into equation (2.16) gives

$$q_{conv} = \frac{1}{2}\frac{k\Delta T}{d}\left(\frac{2}{\pi}\,\frac{L/d}{1+(L/d)^2}\right)^{2/3} Ra_T^{1/3} + \frac{1}{2}Hd \tag{2.21}$$

At this point we can also ask what the temperature drop ΔT would be if the system were entirely internally heated. In this case there would be no lower thermal boundary layer, i.e. $\Delta T = \Delta T_S$, $q_{conv} = Hd$, and equation (2.21) can be used to solve for ΔT_{int}

$$\Delta T_{int} = \frac{Hd^2}{k}\left(\frac{2}{\pi}\,\frac{L/d}{1+(L/d)^2}\right)^{1/2} Ra_H^{-\frac{1}{4}} \tag{2.22}$$

where the subscript on ΔT_{int} is a reminder that this is the temperature difference for the case with internal heating only and Ra_H is defined as

$$Ra_H = \frac{\alpha\rho g H d^5}{\eta k \kappa} \tag{2.23}$$

Equation (2.22) is consistent with the classic boundary layer solution for a purely internally heated layer (see for example O'Connell and Hager, 1980). The dimensionless convective heat flux (and flow) for the system, also known as the *Nusselt* number Nu, is given by dividing the convective heat flux given by equation (2.21) by the conductive heat flux $k\Delta T/d$ that would occur in the absence of convection for the boundary heated case

$$Nu = \frac{1}{2}\left(\frac{2}{\pi}\,\frac{L/d}{1+(L/d)^2}\right)^{2/3} Ra_T^{1/3} + \frac{1}{2}\frac{Ra_H}{Ra_T} \tag{2.24}$$

The dimensionless plate velocity $\tilde{u} = u/(\kappa/d)$ is, from equation (2.12)

$$\tilde{u} = \frac{(L/d)^{7/3}}{(1+(L/d)^2)^{4/3}}\left(\frac{Ra_T}{2\sqrt{\pi}}\right)^{2/3} \tag{2.25}$$

Again, note that the velocity is independent of the internal heating H and depends only on the temperature drop ΔT across the layer. The dimensionless temperature drop $\Delta\tilde{T}_S$ across the cold thermal boundary layer at the surface is obtained by dividing equation (2.19) by

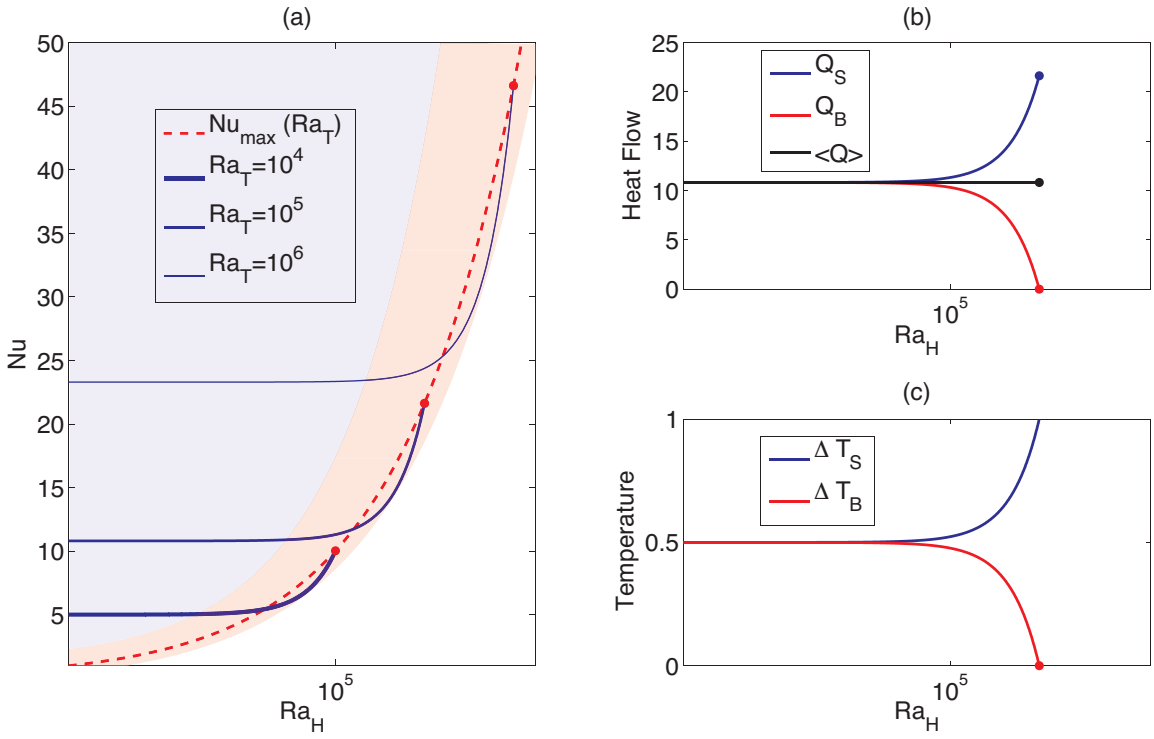

Figure 2.2: Nonlinear relation between Nu, Ra_T, and Ra_H for thermal convection with mixed heating. (a) Nu as a function of Ra_H for various fixed Ra_T. Results are plotted up to the Ra_H in which equation (2.27) is violated. (b) Dimensionless heat flow as a function of Ra_H for $Ra_T = 10^5$. (c) Dimensionless temperature drop across the upper and lower thermal boundary layers as a function of Ra_H for $Ra_T = 10^5$. Note that as Ra_H increases and $Ra_H \approx O\left(Ra_T^{4/3}\right)$ both the basal heat flow and the temperature drop across the lower thermal boundary layer approach zero.

ΔT and gives

$$\Delta \tilde{T}_S = \frac{\Delta T_S}{\Delta T} = \frac{1}{2} + \frac{1}{2}\frac{Ra_H}{Ra_T^{4/3}}\left(\frac{\pi}{2}\,\frac{1+(L/d)^2}{L/d}\right)^{\frac{2}{3}} \tag{2.26}$$

This is valid as long as (equation (2.20) rearranged and using the definitions of Ra_T and Ra_H)

$$Ra_H \leq Ra_T^{\frac{4}{3}}\left(\frac{2}{\pi}\,\frac{L/d}{1+(L/d)^2}\right)^{2/3} \tag{2.27}$$

Figure 2.2 demonstrates several important properties of the system. Figure 2.2 (a) shows

the calculated Nusselt number as a function of Ra_H for various fixed Ra_T and an aspect ratio of $L/d = 1$. Within the blue shaded region $Ra_H << O\left(Ra_T^{4/3}\right)$, there is little internal heating compared to heat entering the base of the layer, and the Nusselt number scales as $Nu \propto Ra_T^{1/3}$ and is independent of Ra_H. Physically, this is what we would expect and is predicted by equation (2.24) for small Ra_H. For $Ra_H \approx O\left(Ra_T^{4/3}\right)$ the contribution to the surface heat flow from internal heating is no longer negligable and the Nusselt number is increased up to a maximum of

$$Nu_{max} = \left(\frac{2}{\pi}\,\frac{L/d}{1+(L/d)^2}\right)^{2/3} Ra_T^{1/3} \tag{2.28}$$

The red shaded region of Figure 2.2 shows the region where $Ra_H \approx O\left(Ra_T^{4/3}\right)$ and the Nusselt number is a function of both Ra_T and Ra_H. In this region equation (2.24) needs to be used to calculate the Nusselt number as it *does not follow* a simple scaling relation with either Ra_T or Ra_H.

The maximum Nusselt number (surface heat flow) occurs when the left and right hand sides of equation (2.27) are equal. At this point the temperature of the interior of the convective cell T_M is equal to the temperature at the base of the fluid layer T_B. For this maximum heat flow there is no thermal boundary layer at the base of the convecting layer ($\Delta T_B = 0$), internal heating accounts for the entire surface heat flow, and the basal heat flow is equal to zero.

Figure 2.2 (b) and (c) show the dimensionless heat flow and dimensionless temperature drop across the surface and basal thermal boundary layers for the case of $Ra_T = 10^5$ from Figure 2.2 (a). As Ra_H approaches $O\left(Ra_T^{4/3}\right)$ the heat flow and temperature drop across the upper thermal boundary layer grow while the heat flow and temperature drop across the lower thermal boundary layer decrease. The depth averaged vertical heat flow $< Q >$ remains constant throughout the change in Ra_H. As the energy available to drive the system depends only on $< Q >$ (see equation (2.7)) the change in Q_B and ΔT_B as Ra_H increases has no effect on the available energy or the convective velocity u. This explains

Simulation #	Ra_T	Ra_H/Ra_T (H_s)	T_{mean} (dimensionless)	Q_t (dimensionless)
1	10^5	0	0.500	10.42 (2)
2	10^5	10	0.885 (10)	13.60 (15)
3	2×10^5	0	0.500	12.86 (19)
4	5×10^5	0	0.500	17.15 (11)
5	5×10^5	6	0.668 (6)	17.86 (18)
6	5×10^5	10	0.766 (2)	19.03 (31)
7	5×10^5	20	0.932 (4)	25.03 (38)
8	5×10^5	30	1.084 (5)	31.38 (18)
9	10^6	0	0.500	21.24 (19)
10	10^6	10	0.721 (5)	22.57 (23)
11	10^6	20	0.866 (3)	27.93 (59)
12	10^6	30	0.995 (3)	34.41 (26)
13	10^6	40	1.117 (3)	40.86 (41)
14	2×10^6	35	0.967 (4)	40.22 (74)
15	3×10^6	0	0.500	28.59 (37)
16	3×10^6	15	0.726 (7)	31.36 (59)
17	3×10^6	20	0.793 (3)	33.67 (36)
18	3×10^6	50	1.064 (3)	52.87 (59)
19	5×10^6	40	0.920 (3)	49.24 (63)
20	10^7	0	0.500	39.46 (65)
21	10^7	10	0.630 (4)	38.71 (65)
22	10^7	20	0.718 (4)	43.14 (90)

Table 2.1: Numerical results for convection with mixed heating from Sotin and Labrosse (1999).

why the convective velocity is independent of the amount of internal heating. The depth averaged vertical heat flow for the mixed heating case depends only on Ra_T (and some geometrical terms).

Equations (2.24) and (2.26) may be compared to the results of Sotin and Labrosse (1999). They performed numerical convection simulations with mixed heating and found that the dimensionless mean temperature θ and surface heat flow Nu were reasonably fit by the equations

$$Nu = 0.3446\, Ra_T^{\frac{1}{3}}\, \theta^{\frac{4}{3}} \tag{2.29}$$

$$\theta = \frac{1}{2} + 1.236\,\frac{Ra_H^{3/4}}{Ra_T} \tag{2.30}$$

The results of their numerical simulations are summarized in Table 2.1 which is reproduced from their paper. Both the powers and coefficients in equations (2.29) and (2.30) were found by fitting power law scalings to the results from the numerical simulations. The red markers in Figure 2.3 show the predicted values for θ and Nu, using equations (2.29) and (2.30), compared to the values from the numerical simulations. The fit is very good with the exception of points 1, 3, 4, 9, 15, and 20, which correspond to cases with no internal heating. For these points their scaling considerably underestimates the surface heat flow.

Without any loss of generality, equations (2.24) and (2.26) of this study may also be written as

$$Nu = \frac{A(L/d)}{2} Ra_T^{1/3} + \frac{1}{2}\frac{Ra_H}{Ra_T} \tag{2.31}$$

$$\Delta\tilde{T}_S = \frac{1}{2} + \frac{A^{-1}(L/d)}{2}\frac{Ra_H}{Ra_T^{4/3}} \tag{2.32}$$

where $A(L/d)$ is some undetermined function of the aspect ratio. Sotin and Labrosse (1999) do not mention any significant change in aspect ratio as the form of heating is varied. Let us assume that $A(L/d)$ is approximately constant and equal to some value A for all of the cases considered by Sotin and Labrosse (1999). Then we may calculate A using equation (2.31) and a least squares fit to the numerical simulation heat flow data in Table 2.1. This gives $A \approx 0.35$. The theory developed in this chapter (see equation (2.24)) suggests that

$$A(L/d) \approx \left(\frac{2}{\pi}\frac{L/d}{1+(L/d)^2}\right)^{\frac{2}{3}} \tag{2.33}$$

If we assume that $L/d \approx \sqrt{2}$ (marginal stability for a thermally convecting isoviscous fluid layer) then equation (2.33) predicts $A \approx 0.45$. Thus, the value predicted from theory and equation (2.33) is in surprisingly good agreement with the value obtained using the least

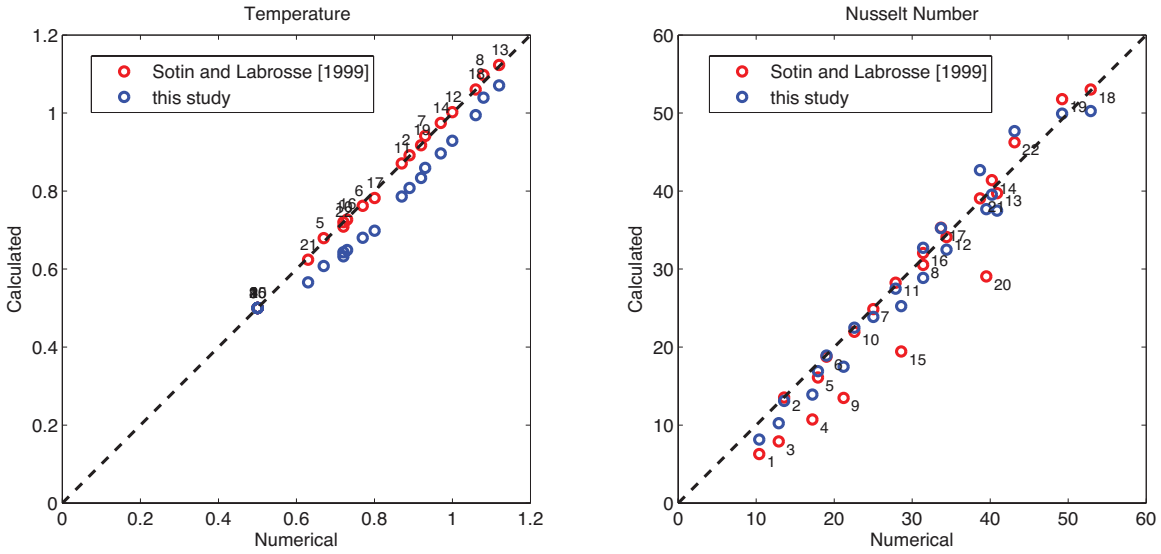

Figure 2.3: Comparison of mixed heating equation with the numerical simulations and scaling of Sotin and Labrosse (1999).

squares fit to the numerical simulation data.

The blue markers in Figure 2.3 compare the predicted values for $\Delta\tilde{T}_S$ and Nu, using equations (2.31) and (2.32) and $A = 0.35$, to the values obtained from the numerical simulations.

We expect the mean temperature of the convective cell θ to be approximately equal to the temperature drop across the upper thermal boundary layer $\Delta\tilde{T}_S$. Sotin and Labrosse (1999) note that there is sometimes a small temperature overshoot at the inner side of the boundary layers. The observed overshoot in temperature is attributed to the accumulation at each boundary of material coming from the other boundary. In this case we do not expect θ and $\Delta\tilde{T}_S$ to be exactly equal. This may partially explain some of the discrepancy between the theoretically predicted values of $\Delta\tilde{T}_S$ and the mean temperature θ. It is also possible that the function $A(L/d)$ is not constant and depends weakly on the form of heating. Nonetheless, the trend in predicted temperatures is reasonably good. The agreement between the predicted and numerical heat flow is improved over the scaling of Sotin and Labrosse (1999) as it works for both cases with and without internal heating.

The scaling laws of Sotin and Labrosse (1999) result from a best fit with 5 degrees of freedom (two coefficients and three exponents) for 22 data points. They fit the temperature well but fail to properly fit the heat flow for cases with no internal heating. The exponents and functional form in our equations arise from conservation laws rather than from a best fit. We are able to obtain a reasonably good fit for temperature and an improved fit for heat flow with only one free parameter. Furthermore, the value obtained for this parameter using a least squares fit to the numerical data agrees well with the theoretically predicted value. Based on this, we are confident that equations (2.24) and (2.26) properly describe Nu and $\Delta\tilde{T}_S$ for the mixed heating case. A more detailed statistical comparison with additional data will be the subject of future work.

Let us summarize the key results for the mixed heating case. The convective velocity was found to be independent of the amount of internal heating and depends only on Ra_T, as well as a geometrical factor. The heat flow (Nusselt number) depends on both Ra_T and Ra_H and for $Ra_H \approx O\left(Ra_T^{4/3}\right)$ the heat flow *cannot* be captured through a simple power law scaling with either Ra_T or Ra_H. The heat flow for the mixed heating case is given by equation (2.24). In addition, we found that a large internal heating can suppress or altogether prevent a basal heat flow regardless of the size of Ra_T. A final point to make has to do with comparing the energetics of basal and internal heating. In order to produce the same convective velocity as an entirely boundary heated case with a Rayleigh number of Ra_T, an entirely internally heated system must have a Rayleigh number of $Ra_H \propto Ra_T^{4/3}$. As an example, a purely internally heated system would require a Rayleigh number of $Ra_H \approx 10^8$ to achieve the same convective velocity as a purely boundary heated case with a Rayleigh number of $Ra_T \approx 10^6$. Thus, Ra_T and Ra_H are not comparable measures of the energetics of a convecting system.

2.2 STAGNANT LID CONVECTION

Most materials in the real world have physical properties that depend on temperature and pressure. For the Earth, the temperature dependence of mantle viscosity leads to many

orders of magnitude change in viscosity throughout the mantle and lithosphere. We will discuss this dependence in more detail in following chapters.

In some cases, the cold upper thermal boundary layer of a convecting system may be too strong to allow for surface recycling. In these cases a 'stagnant' lid forms at the surface of the fluid layer. Heat flows through the lid by conduction and can still provide enough energy to drive thermal convection beneath the stagnant lid. This type of convection occurs often in cases with highly temperature dependent viscosity and large viscosity variations. We will review the basic physics and scaling for stagnant lid convection, mainly following Solomatov (1995), as it will be used in Chapter 5 when we consider the cooling of small planetary bodies.

Let the thickness of the upper thermal boundary layer be δ. For simplicity we will assume that there is no basal heat flow and that the temperature drop across the upper thermal boundary layer ΔT_S is equal to the temperature drop across the entire fluid layer ΔT. We consider a fluid layer with a temperature dependent viscosity of the form

$$\eta = \eta_0 e^{-\gamma \Delta T} \tag{2.34}$$

where η_0 is a reference viscosity, $\Delta T = T - T_S$, and T_S is the surface temperature. The fluid beneath the surface boundary layer is well mixed with a temperature of T_M and viscosity of μ_m. The warm and weak lower portion of the thermal boundary layer participates in and drives thermal convection beneath the boundary layer. The temperature drop across the actively convecting lower portion of the thermal boundary layer may be approximated as

$$\Delta T_{rh} \approx 1/\gamma \tag{2.35}$$

ΔT_{rh} is the temperature drop over which viscosity increases (and strain rate decreases) by a factor of e. The colder upper portion of the thermal boundary layer will be too strong to actively participate in convection. Convective heat transport through the well mixed isoviscous layer beneath the lid is then calculated using equation (2.16) with ΔT_S replaced

with ΔT_{rh}

$$q_S \approx \frac{k\Delta T_{rh}}{d}\left(\frac{2}{\pi}\,\frac{L/d}{1+(L/d)^2}\right)^{2/3}\left(\frac{\alpha\rho g\Delta T_{rh}d^3}{\mu_m\kappa}\right)^{1/3} \tag{2.36}$$

At steady state the convective heat flux supplied to the base of the thermal boundary layer must be equal to the conductive heat flux of $k\Delta T/\delta$ through the boundary layer. This implies

$$k\frac{\Delta T}{\delta} \approx \frac{k\Delta T_{rh}}{d}\left(\frac{2}{\pi}\,\frac{L/d}{1+(L/d)^2}\right)^{2/3}\left(\frac{\alpha\rho g\Delta T_{rh}d^3}{\mu_m\kappa}\right)^{1/3} \tag{2.37}$$

Solving for δ in equation (2.37) gives

$$\delta \approx d\; p^{\frac{4}{3}}\left(\frac{\pi}{2}\frac{1+(L/d)^2}{L/d}\right)^{\frac{2}{3}} Ra_T^{-\frac{1}{3}} \tag{2.38}$$

where Ra_T is the mantle Rayleigh number defined in equation (2.13) using the total temperature drop across the thermal boundary layer of ΔT and the viscosity of the mantle μ_m. The parameter p is defined as $p = \gamma\Delta T$ and is useful for quantifying the total viscosity contrast across the thermal boundary layer as

$$log\left(\frac{max(\mu)}{min(\mu)}\right) = log\left(\frac{\mu(T_S)}{\mu(T_M)}\right) = log\left(exp\left(\gamma\Delta T\right)\right) = log\left(exp\left(p\right)\right) = p \tag{2.39}$$

Thus, the parameter p is equal to the natural logarithm of the total viscosity contrast (ratio) across the cold thermal boundary layer. Using equation (2.38) for the thermal boundary layer thickness the heat flux through the boundary layer is then given by

$$q_S = k\frac{\Delta T}{\delta} = \frac{1}{p^{4/3}}k\frac{\Delta T}{d}\left(\frac{2}{\pi}\,\frac{L/d}{1+(L/d)^2}\right)^{2/3} Ra_T^{1/3} \tag{2.40}$$

It is worth also pointing out the relationship between the stagnant lid heat flux in equation (2.40) and the isoviscous convective heat flux given by equation (2.16)

$$q_{S_{stg}} = p^{-4/3}\, q_{S_{mbl}} \tag{2.41}$$

where we have used the subscripts "stg" and "mbl" to distinguish the heat fluxes for stagnant lid and mobile lid convection respectively. Equation (2.41) reveals a simple scaling between the two forms of heat flow.

In Chapter 3 we will see that there are other solutions for the convective flow when a strong surface layer is present in which the surface (plate) velocity is much smaller than the mantle velocity. These sluggish lid solutions have thicker plates and reduced heat flow compared to the mobile lid solutions. If the plate moves too slowly then we expect the erosional process that we have been discussing, and thus stagnant lid convection, to control the heat flow rather than the slow diffusive cooling of the plate as it moves away from the ridge. It is therefore useful to calculate the critical plate velocity, u_c, at which the diffusive half-space cooling model gives a comparable heat flow to that predicted by the stagnant lid scaling. Should any of our models predict plate speeds less than u_c then we will know that the average plate thickness and heat flow are likely controlled by stagnant lid convection and should be treated independent of the plate velocity. Thermal boundary layer theory and equation (2.2) gives the kinematic relation between the plate velocity u, the temperature drop across the thermal boundary layer ΔT, and the heat flow Q_S. Setting Q_S from equation (2.40) (multiplied by L to get the heat flow) equal to the heat flow given by equation (2.2) and solving for the plate velocity gives

$$u_c \approx p^{-\frac{8}{3}} u_{mbl} \tag{2.42}$$

where u_{mbl} is the plate velocity for the isoviscous case given by equation (2.25). For a viscosity contrast 10^3 across the thermal boundary layer, equation (2.42) suggests that the plate velocity of the system would have to be approximately 200 times less than that predicted by the isoviscous scaling in order for stagnant lid convection to control the plate thickness and heat flow.

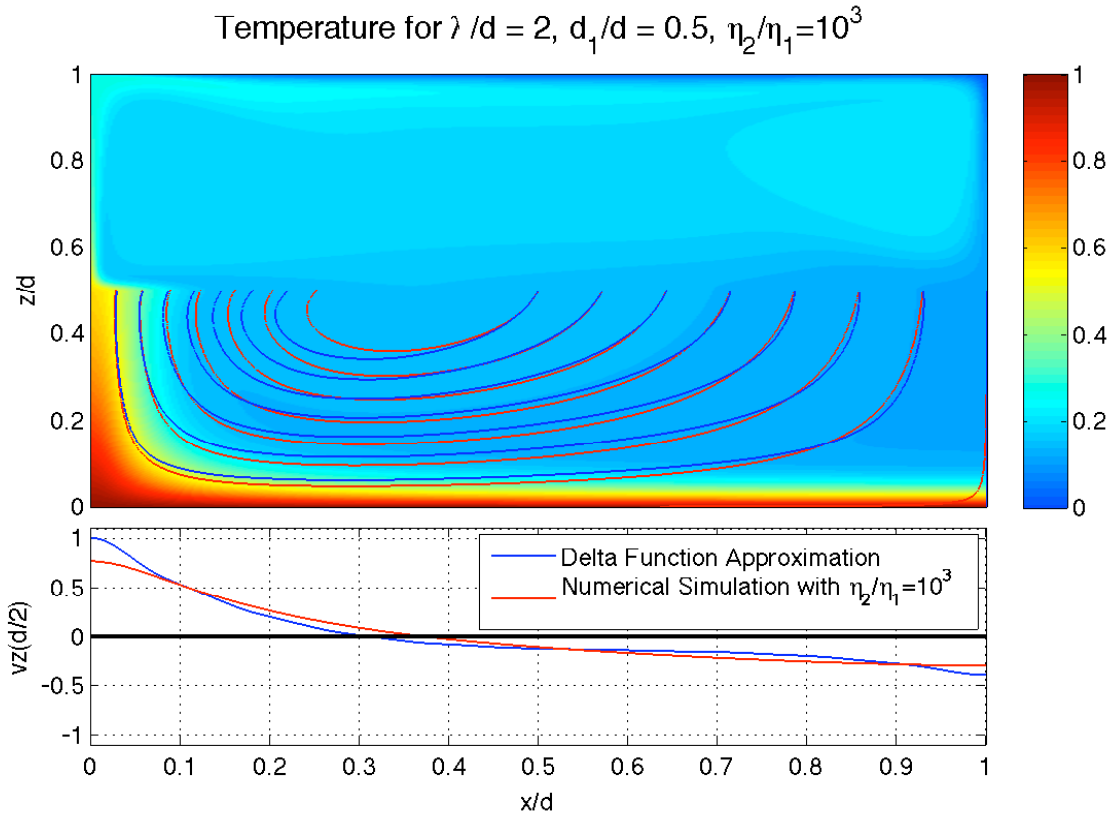

Figure 2.4: (A) Temperature field and velocity streamlines for a numerical simulation of thermal convection using a low viscosity upper mantle and run with a modified version of the thermal convection code MC3D (Gable, 1989; Gable et al., 1991). Streamlines calculated using the 'open' layer delta function solution (blue) are also included in the high viscosity lower mantle for comparison. (B) Vertical velocity calculated at mid depth (where the viscosity changes) from the numerical simulation (red) and using the delta function solution (blue). See Appendix A for details regarding the delta function solution.

2.3 CONVECTION IN AN 'OPEN' LAYER

Figure 2.4 shows the temperature field from a numerical simulation of boundary heated thermal convection in a cell of aspect ratio $L/d = 2$ and with a viscosity increase of a factor of 10^3 in the lower half of the fluid layer. Velocities are highest in the upper half of the layer where the viscosity is lower. Despite the large increase in viscosity with depth, the plot of the temperature field, as well as the streamlines for the flow, demonstrate that

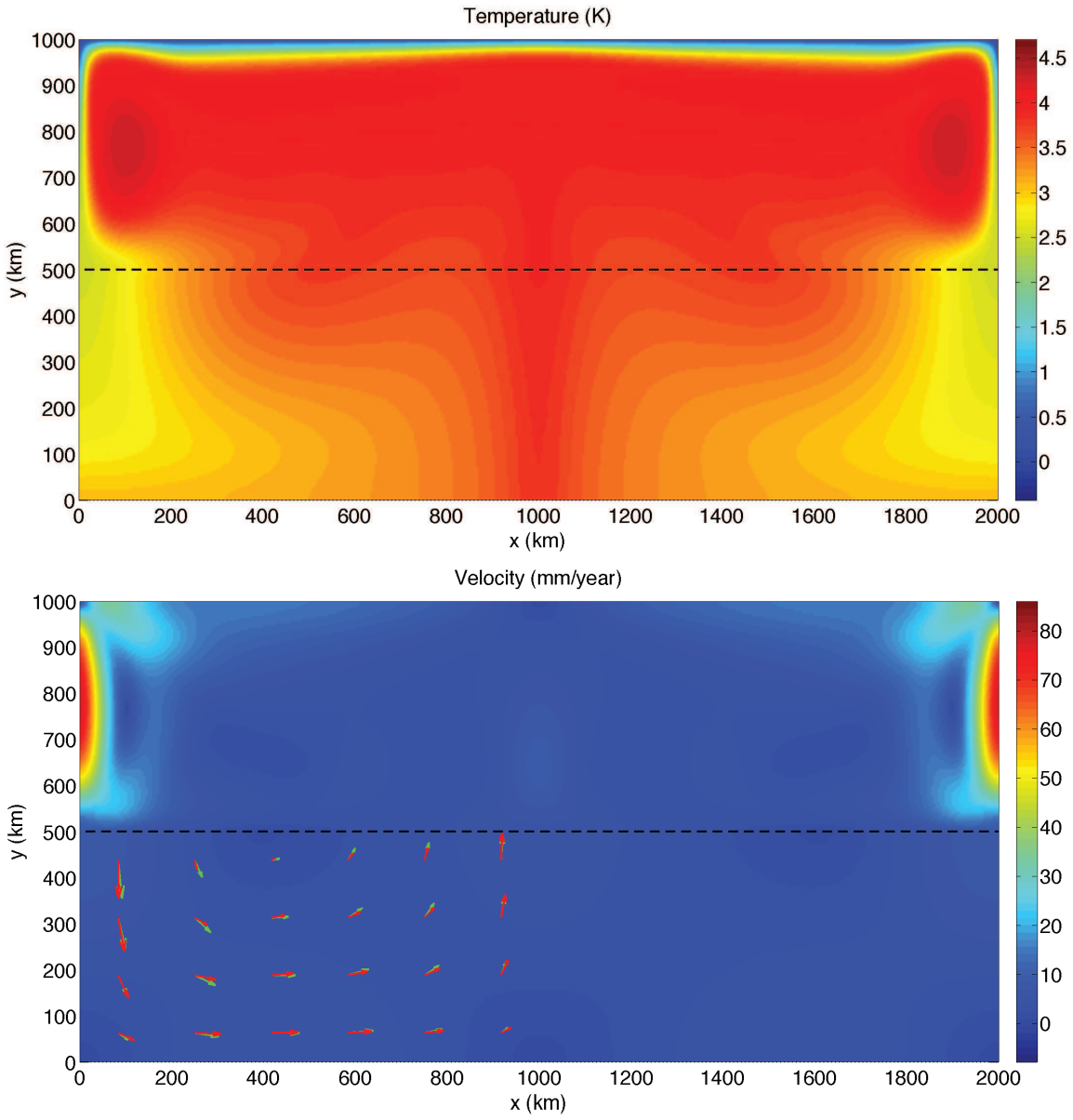

Figure 2.5: Numerical simulation run with a modified version of MC3D (Gable, 1989; Gable et al., 1991) that demonstrates the 'open' layer convective flow. (A) Temperature field. (B) Magnitude of Velocity. Vectors indicate magnitude and direction of velocity for the numerical simulation (green) and calculated using the delta function approximation (red). See Appendix A for details regarding the delta function solution.

some material still circulates into the lower half of the convective cell where it warms and eventually rises back up into the upper half. Figure 2.5 shows a similar situation with only internal heating. If the viscosity increase at mid depth is large enough then stresses at the surface of the high viscosity layer will be negligible compared to stresses within the layer and the boundary condition at the surface of the high viscosity region will be essentially stress free. This kind of flow may be relevant for the Earth where a significant increase in viscosity is observed to occur with depth (see for example Mitrovica and Forte, 2004). We would like to estimate the flow rates in the high viscosity lower region. This motivates the idea of a case which has not yet been considered - the 'open layer' case in which we consider the flow in the lower (high viscosity) portion of the convection cell in Figure 2.4.

The fluid layer we consider has a uniform viscosity and material is free to flow into and out of the upper boundary of the layer. Figure 2.6 shows streamlines for fluid layers with 'open' upper boundaries calculated using the analytic delta function solution (see Appendix A for details regarding this solution). This idea was first discussed by Crowley and O'Connell (2008).

The solution is fundamentally different from the closed layer solution worked out in section 2.1. The difference is in the thermal boundary condition at the surface. For the closed layer heat flow out of the layer is accomplished via conduction across a thermal boundary layer and scales with the square root of the convective velocity (see equation (2.2)). For the open layer, heat flow out of the system is accomplished via advection and scales linearly with the convective velocity.

We again consider a fluid layer of depth d and length L. The fluid layer has density ρ, specific heat capacity C_p, thermal conductivity k, thermal diffusivity $\kappa = k/\rho C_p$, and viscosity μ. The upper surface of the fluid layer is open and the viscous stresses on this boundary are considered to be equal to zero. Material flows in at a temperature of T_{in} and leaves at a temperature of T. The temperature difference is $\Delta T = T - T_{in}$.

Let the convective velocity again be u. The strain rate may be approximated as $\dot{\epsilon} \approx u/d$ and the local viscous dissipation as $2\mu\dot{\epsilon}^2 \approx 2\mu(u/d)^2$. Dissipation in the flow will occur

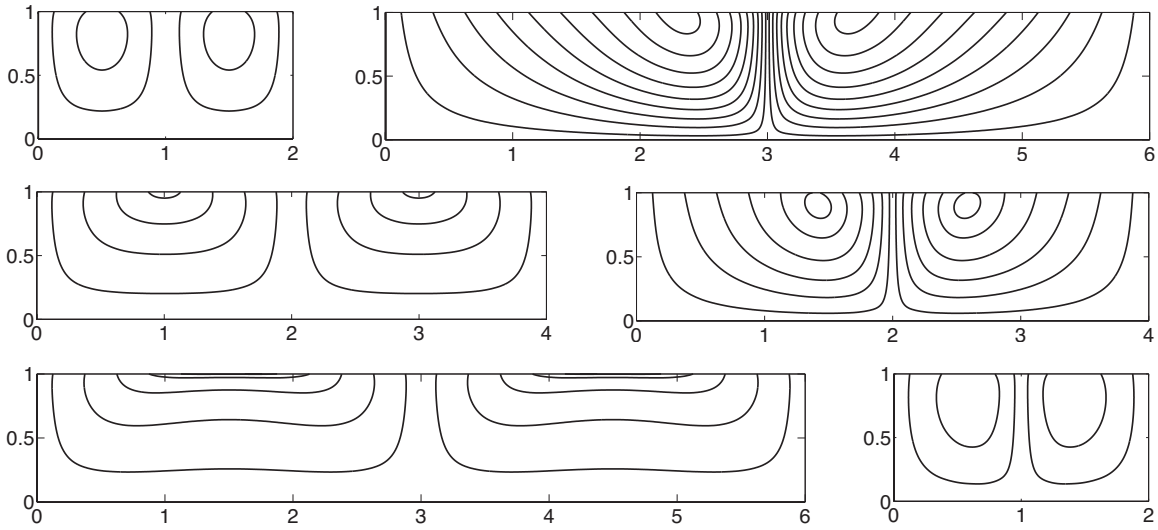

Figure 2.6: Streamlines for flow in a convecting open layer for various aspect ratios using the delta function solution. Symmetric cases on the left are for open cells driven by equivalent magnitude upwelling and downwelling density anomalies. Non symmetric cases on the right are driven entirely by an upwelling or downwelling at the center of the cell. See Appendix A for details regarding the delta function solution.

mainly in the ends of the cell (within $\approx d$ of the ends of the cell) where the fluid changes direction (Morris, 2008). Dissipation will then be mainly distributed over an area of $2d^2$ (the two ends of the cell). The total viscous dissipation in the convective cell may then be approximated as (see equation (2.8))

$$\Phi_V \approx 2\mu \left(\frac{u}{d}\right)^2 \cdot 2d^2 = 4\mu u^2 \tag{2.43}$$

Again, we are calculating all energetic quantities per unit distance in the third dimension and along the axis of the convective roll. The mass flow rate into (and out of) the convection cell is approximately

$$\dot{M} \approx \frac{1}{2} ud \tag{2.44}$$

The average advective heat flow through the surface may then be approximated as

$$Q_S \approx \rho C_p \Delta T \dot{M} = \frac{\rho C_p \Delta T u d}{2} \tag{2.45}$$

The total rate of change of potential energy in the cell is again given by equation (2.5) and is

$$\Phi_P = \frac{\alpha g d}{C_p} \langle Q_{adv} \rangle = \frac{\alpha g d}{C_p} \frac{B Q_S}{2} \tag{2.46}$$

where B is equal to 1 if entirely internally heated and 2 if entirely boundary heated. Requiring that the total rate of change of potential energy be equal to the total viscous dissipation, i.e. $\Phi_P = \Phi_V$, using equations (2.43) through (2.46), and solving for the convective velocity yields

$$u \approx \frac{B}{2^4} \frac{\kappa}{d} Ra_T \tag{2.47}$$

where the Rayleigh number Ra_T is once again defined as

$$Ra_T = \frac{\alpha \rho g \Delta T d^3}{\mu \kappa} \tag{2.48}$$

Substituting equation (2.47) into equation (2.45) gives a surface heat flow of

$$Q_S \approx \frac{B}{2^5} k \Delta T Ra_T \tag{2.49}$$

or an average surface heat flux of

$$q_S \approx \frac{B}{2^5} \left(\frac{d}{L} \right) \frac{k \Delta T}{d} Ra_T \tag{2.50}$$

Both the convective velocity and the heat flow scale linearly with the Rayleigh number. This makes the heat flow and convective velocity much more sensitive to the Rayleigh number than was the case for convective heat transport out of a closed layer (and through a thermal boundary layer). To get a sense of how significant this is, we can compare the Rayleigh

number required to achieve the same heat flow for both the closed (section 2.1) and open convecting layers.

We will assume that the temperature difference ΔT, layer thickness d, and thermal diffusivity κ are the same for each. The closed convecting layer has a Rayleigh number of Ra_{closed} while the open layer has a Rayleigh number of Ra_{open}. We can calculate Ra_{open} as a function of Ra_{closed} by using equations (2.15) and (2.49) and requiring that the heat flow out of each layer be equal. This gives

$$Ra_{open} = 2^5 \left(\frac{2}{\pi B}\right)^{2/3} \frac{(L/d)^{5/3}}{\left(1+(L/d)^2\right)^{2/3}} Ra_{closed}^{\frac{1}{3}} \tag{2.51}$$

Using $B = 2$ (all boundary heating) and $L = 2d$ gives $Ra_{open} \approx Ra_{closed}/10^2$ for the case where $Ra_{closed} = 10^6$ or $Ra_{open} \approx Ra_{closed}/10^4$ for the case where $Ra_{closed} = 10^9$. Thus, the Rayleigh number of the open layer may be many orders of magnitude less than the Rayleigh number of the closed layer and still achieve the same heat flow. This has important implications for the Earth as it may allow the lower mantle to have a much higher viscosity (lower Rayleigh number) and still efficiently transport heat to the upper mantle.

Let us now consider the difference in convective velocities that would occur when the heat flow in both cases is identical (i.e. the above relationship holds). To do this, we can use equation (2.12) to calculate the convective velocity of the closed layer, u_{closed}, as a function of Ra_{closed}. Equations (2.47) and (2.51) may then be used to calculate the convective velocity of the open layer, u_{open}, also as a function of Ra_{closed}. These relationships lead to

$$u_{open} \approx 2 \left(\frac{4\left(1+(L/d)^2\right)}{L/d}\right)^{\frac{2}{3}} \left(B\pi Ra_{closed}\right)^{-\frac{1}{3}} u_{closed} \tag{2.52}$$

Again using $B = 2$ and $L = 2d$ gives $u_{open} \approx 0.06\, u_{closed}$ for the case where $Ra_{closed} = 10^6$ or $u_{open} \approx 0.006\, u_{closed}$ for the case where $Ra_{closed} = 10^9$. Thus, to achieve the same heat flow, the convective velocity in the open layer may be orders of magnitude less than

the convective velocity in the closed layer. This could have important implications for the chemical evolution of the mantle as it may permit the lower mantle to efficiently cool without requiring a significant degree of mixing between the upper and lower mantle (small mass flux). This effect, however, will be considered in separate future studies.

Chapter 3

Thermal convection with strong plates

"Everything should be made as simple as possible, but no simpler."
–Albert Einstein

In this chapter an analytic boundary layer model for thermal convection with a finite-strength plate and depth-dependent viscosity will be developed. The model will allow for solutions in which convective flow rates in the mantle exceed the plate velocity by incorporating a separate energy balance for the lithosphere and solving for the coupling between the plate and underlying mantle. The model will predict the plate velocity, plate thickness and heat flow, as well as the laterally averaged horizontal flow profile for a convective cell.

3.1 Introduction

The Earth's thermal and chemical evolution is largely regulated by plate tectonics. Although plate tectonics is a surface manifestation of mantle convection, convection can also occur in a planet with a stationary lid and in the absence of plate tectonics. The development of simple models for understanding how mantle convection and plate tectonics interact is critical for understanding planetary dynamics and evolution.

An amended version of this Chapter was published with Richard J. O'Connell in Geophysical Journal International, vol. 188, p. 61-78, 2012.

The development of a boundary layer model to relate plate tectonics to thermal convection (Turcotte and Oxburgh, 1967) was a major advance, in that it provided a mechanism that quantitatively related plate tectonics, mantle convection, and the thermal evolution of the Earth and set the stage for further developments (as well as the wider acceptance of plate tectonics). The first model was a classic boundary layer model with a conductive thermal boundary layer at the surface overlying a deeper convective layer that was essentially isothermal. The horizontal speed of the boundary layer matched the horizontal speed of the top of the convecting layer. The boundary layer cooled by conduction as it moved from ridge to trench on the surface, and the sinking boundary layer provided the energy to balance viscous dissipation in the convecting region. The average surface heat flow, per unit length in the third dimension, for a plate of length L with constant (uniform) speed $U_{_P}$ is

$$Q_{conv} = 2k_c \Delta T \left(\frac{U_{_P} L}{\pi \kappa} \right)^{1/2}, \tag{3.1}$$

where k_c is the thermal conductivity, ΔT is the temperature difference across the boundary layer, and κ is the thermal diffusivity. The maximum thickness of the boundary layer is given by

$$d_L = C_o \left(\frac{\kappa L}{U_{_P}} \right)^{1/2}, \tag{3.2}$$

where C_o is a constant ≈ 2.32 (Turcotte and Schubert, 2002).

The boundary layer model gives a dimensionless heat flow (the Nusselt number) and dimensionless plate velocity of (for fixed aspect ratio)

$$Nu = \frac{Q_{conv}}{Q_{cond}} \sim Ra^{1/3} \tag{3.3}$$

and

$$\tilde{U}_{P} = \frac{U_{P}}{\kappa/d} \sim Ra^{2/3} \tag{3.4}$$

where d is the thickness of the fluid layer, $Q_{cond} = k_c \Delta T L/d$ is the conductive heat flow in the absence of convection, and Ra is the mantle Rayleigh number,

$$Ra = \frac{\alpha \rho g \Delta T d^3}{\kappa \mu_{M}}. \tag{3.5}$$

Here α is the coefficient of thermal expansion, ρ is the density, g is the gravitational acceleration, and μ_{M} is the mantle viscosity.

This model has only two dimensionless parameters: the Rayleigh number Ra and the aspect ratio (width/depth) $\lambda = L/d$ of the rectangular convection cell. Dimensional analysis requires that the (dimensionless) characteristics of convection in the model must be functions of only these two dimensionless parameters. Relationships for Nu, U_{P}, and d_{L}/d have been derived for convection in a fluid layer using a variety of thermal boundary conditions (O'Connell and Hager, 1980).

McKenzie et al. (1974) performed numerical calculations of convection and confirmed that steady convection results agreed with the results of boundary layer models. They also addressed cases of constant heat flux boundary conditions and internal heating, and made careful comparisons with geophysical observations. They found that numerical solutions for large aspect ratios tended to be unstable, and noted that a strong layer (lithosphere) on the surface might be needed to stabilize large aspect ratio cells similar to those observed.

It is interesting to note that Howard (1966), in considering the growth of thermal instabilities in the atmosphere from heating of the Earth's surface, obtained the same scaling given in equation (3.3). This model was based on the growth of a static conductive boundary layer on the heated surface that became unstable to convection when its thickness δ grew to the critical value for convection to occur, *i.e.*

$$Ra_{\delta} = \frac{\alpha \rho g \Delta T \delta^3}{\kappa \mu} \approx Ra_{c} \tag{3.6}$$

where Ra_c is the critical Rayleigh number $\sim 10^3$. Applying the same condition to the mantle convection situation gives the same $Nu \sim Ra^{1/3}$ scaling as before, as was proposed by Elder (1976). In both cases the boundary layer thickness δ would be limited by its convective stability, and its (dimensional) thickness would be independent of the total layer thickness d used to define the Rayleigh number. (In fact, in Howard's case, the region is a half space and there is no larger layer). The fact that the heat transport of the system can be derived from the local conditions and material properties of the boundary layer raises questions about how to apply the scaling relations to more complicated systems arising in mantle convection.

Concerns were raised regarding the fact that rigid plates, and thus plate tectonics, was not present in a model that only included a single fluid layer with a uniform free surface. Nevertheless, the surface velocity profiles of the boundary layer models were reasonably uniform (McKenzie et al., 1974) and the heat flow could be well represented by the model for lithospheric heat flow (McKenzie, 1967). However, a separate lithospheric layer with different mechanical properties, or viscosity layering in the mantle were not included in such models. In fact, there was a substantially different conceptual model of plate tectonics that had been proposed by Elsasser (1969), who suggested that the lithosphere was a "stress guide" sliding over the asthenosphere from ridge to subduction zone. Thus, unlike the boundary layer model where the surface is the top part of a uniformly convecting layer, the lithosphere in Elsasser's model moved faster than the mantle, which tended to impede its motion. The mechanics of this model were not worked out, although it remained in the vocabulary of discussions of plate tectonics.

In spite of these concerns, the boundary layer model was generally accepted as a first order approximation of plate tectonic rates and heat flow and was the basis for a number of thermal evolution models for the Earth (e.g. Davies, 1980; McKenzie and Weiss, 1975; Schubert et al., 1980; Sharpe and Peltier, 1979). However, these thermal evolution models predicted extremely high temperatures for the Earth's early mantle, clearly suggesting that something was lacking in the model (for discussion see Korenaga, 2008). Experimental (e.g.

Booker, 1976) and numerical (e.g. Torrance and Turcotte, 1971) convection experiments with temperature dependent viscosities also demonstrated that the classic scalings given in equations (3.3) and (3.4) did not apply for large viscosity variations when a strong boundary layer was present. It was soon recognized that the strength of the plates could play a role in limiting plate velocities.

Conrad and Hager (1999) added a term in the energy balance for lithospheric dissipation and several studies focused on plate bending dissipation followed (e.g. Buffett, 2006; Capitanio et al., 2009; Davies, 2009; Korenaga, 2003; Wu et al., 2008). These studies have focused on the idea that the work needed to bend plates during subduction may be large and could considerably reduce plate velocities. The analytic models, however, all assumed that the plate velocity was representative of the mantle flow velocity. We will demonstrate that this assumption is only valid if the plate is very weak and the mantle isoviscous, i.e. no asthenosphere.

The existence of a low viscosity zone beneath the lithosphere adds additional complexity to the system. In an effort to study the dynamical effects of an asthenosphere, Busse et al. (2006) and Lenardic et al. (2006) used a modification of established boundary layer theory to include symmetric low viscosity channels at the top and bottom of a convection cell. Their models assumed a Couette–type flow in the low viscosity channels and that velocities would be highest at the surface. Similarly, Morris (2008) looked at flow in a semi–infinite length viscosity–stratified layer driven by shear stresses at the ends of the cell in order to study wavelength dependence and the effect of a low viscosity channel. These studies, however, lacked a strong lithosphere and surface velocities in the bounding channels were predicted to be high. Numerical convection simulations have demonstrated that a near-surface plate analog can move slower than the peak velocity in the asthenosphere and that flow in the asthenosphere, although still channelized, was not necessarily of Couette-type (Höink and Lenardic, 2010). This seemed to indicate that the plate analog was providing a resistance to motion that was not accounted for in the analysis of Busse et al. (2006), Lenardic et al. (2006), or Morris (2008).

The existence of an asthenosphere, or in general any low viscosity layer, requires a change in viscosity with depth. Studies of mantle viscosity (e.g. Mitrovica and Forte, 2004) also indicate a viscosity increase in the deep mantle well beneath the base of the asthenosphere. The role of viscosity gradients on the thermal evolution of a deeply convecting mantle with mechanically strong plates has also not been addressed by current analytic models.

While many of the recent parameterized models mentioned above have focused on the addition of either a strong lithosphere or a weak asthenosphere, none have accounted for the effects of both simultaneously. The model we describe here will address this issue and demonstrate that both are important in determining the behavior of the system. The utility of our analytic model is to provide physical insight into the behavior of the system and to provide as simple as possible a relation between the model behavior and the parameters that describe it.

Our model includes a finite-strength lithosphere, defined by either an effective viscosity and/or a yield stress, and a low viscosity layer (LVL) above a mantle of constant viscosity. The low viscosity layer can represent either a low viscosity upper mantle or an asthenosphere depending on its thickness. Plate-mantle coupling occurs by means of viscous stresses between the plate and the mantle which depend on the vigor and pattern of flow there, as well as its viscosity. The average shear stress on the base of the plate can be calculated using a laterally averaged velocity profile and viscosity structure. A depth-dependent lateral pressure gradient allows for convective flow beneath the plate without requiring the plate to be in motion. This will be further explained in section 3.2. Two energy balances are constructed: a global energy balance for the entire convective cell and a local lithospheric energy balance. All energy terms in the system are expressed as functions of the model variables: the plate velocity U_P, and the stress on the base of the plate τ_P. The global and lithospheric energy balances are then solved together to yield U_P and τ_P. The model provides the depth-dependent horizontal velocity profile for the convective cell, and allows for the evaluation of the heat flow, internal temperature, interior mass flux, and dissipation rates. Results will be presented in section 3.3 followed by a discussion in section 3.4.

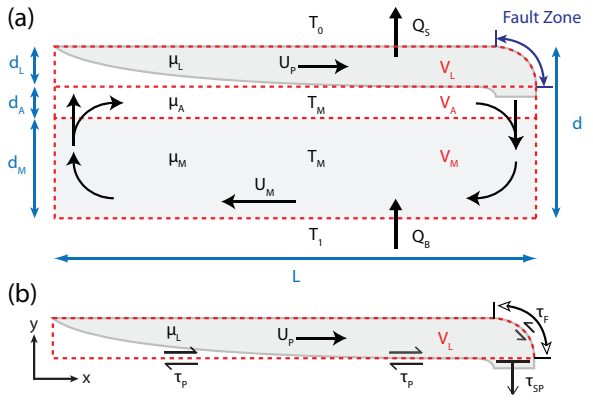

Figure 3.1: Geometry and model variables. (a) The system is divided into three layers of thickness d_L, d_A, and d_M that represent the lithosphere, low viscosity layer (LVL), and lower mantle, respectively. The total thickness and width of the convective system is d and L. The three layers have effective viscosities of μ_L, μ_A, and μ_M. The lithosphere moves at a horizontal velocity of U_P and bends with a bending radius of R. The base of the mantle moves at a velocity of U_M. The mantle is assumed to be well-mixed with a temperature of T_M. The temperatures on the upper and lower boundaries are T_0 and T_1, respectively. The system has a basal heat flow of Q_B, surface heat flow of Q_S, and internal heating rate of H. The volumes of the lithosphere, LVL, and lower mantle are V_L, V_A, and V_M. (b) The lithosphere and its boundaries. The shear stress on the base of the plate is τ_P, the shear stress on the fault is τ_F, and the deviatoric normal stress due to slab pull is τ_{SP}.

3.2 MODEL

We consider a single closed thermally convecting cell at steady state. Figure 3.1 (a) illustrates the geometry, viscosities, and flow patterns in the model. The plate moves over the surface as a rigid body and deformation occurs only at the subducting end of the cell. The model allows for a strong convective flow in the LVL (if present) and mantle flow rates that may exceed the plate velocity. All external boundaries are free-slip except for the fault zone. Figure 3.1 (b) shows the volume enclosing the lithosphere that will be used to construct a local lithospheric energy balance.

3.2.1 MECHANICAL ENERGY

The linear momentum balance for a system with a small Reynolds number ($R_e = \rho v l/\mu << 1$) is given by

$$0 = f_i + \frac{\partial \sigma_{ij}}{\partial x_j}. \tag{3.7}$$

where σ_{ij} is the stress tensor and f_i is the body force. Multiplying equation (3.7) by the velocity and integrating over the volume (Conrad and Hager, 1999) yields the integral formulation of the mechanical energy equation

$$0 = \int_S u_i \sigma_{ij} dS_j - \int_V \sigma_{ij} \frac{\partial u_i}{\partial x_j} dV + \int_V u_i f_i dV, \tag{3.8}$$

where u_i is the velocity. The first term represents work done on the boundaries of the system by stresses. The second term represents work done in the system from deformation. The third term accounts for work done by body forces and is responsible for driving convection. Using

$$\sigma_{ij} = -P\,\delta_{ij} + \tau_{ij}, \tag{3.9}$$

where P is the pressure, δ_{ij} is the Kronecker delta function, and τ_{ij} is the deviatoric stress, the second term in equation (3.8) may be written as

$$\int_V \sigma_{ij} \frac{\partial u_i}{\partial x_j} dV = \int_V \left(-P\,\dot{\epsilon}_{ii} + \tau_{ij}\,\dot{\epsilon}_{ij}\right) dV, \tag{3.10}$$

where the deviatoric strain rate tensor is

$$\dot{\epsilon}_{ij} = \frac{1}{2}\left(\frac{\partial u_i}{\partial x_j} + \frac{\partial u_j}{\partial x_i}\right). \tag{3.11}$$

The first term on the right-hand side of equation (3.10) is zero for an incompressible flow. We also assume that the material is a fluid with an effective Newtonian viscosity of μ, and

$$\tau_{ij} = 2\mu\dot{\epsilon}_{ij}. \tag{3.12}$$

We can separate dissipation in the lithosphere from dissipation in the asthenosphere and

mantle. Then

$$\int_V \sigma_{ij} \frac{\partial u_i}{\partial x_j} dV = \Phi_{_L} + \Phi_{_M}, \tag{3.13}$$

where Φ_L is the total volumetrically integrated dissipation in the lithosphere and

$$\Phi_{_M} = 2 \int_{V_M} \mu \dot{\epsilon}_{ij}^2 dV \tag{3.14}$$

is the total dissipation in the underlying mantle. Equation (3.13) allows for the insertion of a simple parameterized representation of the lithospheric dissipation and will be further addressed in section 3.2.2.

The third term in equation (3.8) is the rate of change of potential energy, $\Phi_{_P}$, and represents work done on the system by body forces. The body force f_i is the force of gravity acting on density anomalies and is given by $f = \Delta\rho g$, where g is the gravitational acceleration and $\Delta\rho$ is the density anomaly. The body force will be directed vertically, and with the vertical velocity component v, the rate of change of potential energy in the system is then given by

$$\Phi_{_P} = \int_V \Delta\rho g v dV. \tag{3.15}$$

We consider only the thermal density variation, with $\Delta\rho = \alpha\rho\delta T$, where α is the thermal expansion coefficient and δT is the temperature anomaly relative to the average mantle temperature, T_M. We can rewrite equation (3.15) as

$$\Phi_{_P} = \frac{\alpha g d}{C_p} \left[\frac{1}{d} \int_0^d \left[\int \int \rho C_p \delta T v \, dx dz \right] dy \right]. \tag{3.16}$$

The quantity enclosed within the inner square brackets is the vertically advected heat flow, $Q_{adv}(y)$. The quantity enclosed within the outer square brackets is the depth-averaged vertically advected heat flow and can be defined as

$$\langle Q \rangle_{adv} = \frac{1}{d} \int_0^d Q_{adv}(y) dy. \tag{3.17}$$

The rate of change of potential energy in the system is then

$$\Phi_{_P} = \frac{\alpha g d}{C_p} \langle Q \rangle_{adv} = D_i \langle Q \rangle_{adv}, \tag{3.18}$$

where $D_i = \alpha g d / C_p$ is the dimensionless dissipation number. Equation (3.18) is exact and applies for any incompressible flow. Advective heat transport dominates at high Rayleigh numbers and in the limit $Ra >> Ra_c \approx 10^3$ the depth-averaged advective heat flow $\langle Q \rangle_{adv}$ can be considered equal to the depth-averaged total heat flow $\langle Q \rangle$ (Golitsyn, 1979).

Equation (3.18) provides a simple way of relating the heat flow through the system to the rate of change of potential energy that drives convection. Only the heat flow is required and for several simple cases the calculation of $\langle Q \rangle_{adv}$ is straightforward. For a high Rayleigh number system at steady state and with uniform internal heating, equation (3.17) can be used to show that $\langle Q \rangle_{adv}$ is

$$\langle Q \rangle_{adv} \approx \langle Q \rangle = \left(q_b + \frac{1}{2} H d \right) L = \left(q_s - \frac{1}{2} H d \right) L, \tag{3.19}$$

where H is the internal heating per unit volume, q_b is the basal heat flux, q_s is the surface heat flux, and all quantities are per unit length in the third dimension. Equation (3.17) can of course also be used to calculate $\langle Q \rangle_{adv}$ for more complicated systems with non-uniform internal heating and time dependence. However, for most simple thermal convection models, equation (3.19) is adequate.

Using equations (3.9), (3.13), and (3.18), the integral form of the mechanical energy equation for the convective cell, given by equation (3.8), may now be expressed as

$$D_i \langle Q \rangle_{adv} = - \int_S \left(u_i P \delta_{ij} - u_i \tau_{ij} \right) dS_j + \Phi_L + \Phi_{_M} \tag{3.20}$$

The form of Φ_L will be considered in the following section. $\Phi_{_M}$ will be calculated using

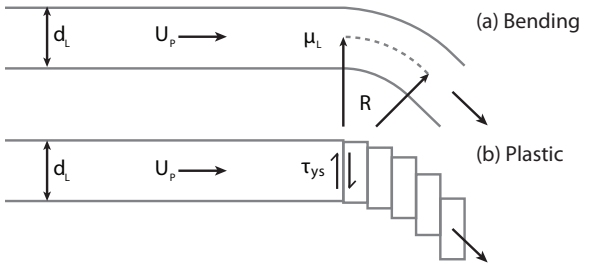

Figure 3.2: Models for plate bending. (a) Geometry and variables for the bending model parameterization for lithospheric dissipation. (b) Geometry and variables for the shearing model parameterization for lithospheric dissipation.

equation (3.14) and a simplified flow structure that will be developed in sections 3.2.4 and 3.2.5. The first term on the RHS of equation (3.20) represents work done on the external boundaries of the system and will be addressed in section 3.2.6.

It is worth noting that equation (3.20) does not require any information about the density or temperature field for calculating the amount of energy available to drive the system. Only the depth averaged advective heat flow is necessary.

3.2.2 Dissipation in the plate

Conrad and Hager (1999) parameterized dissipation in the plate by treating the plate as a bending beam with an effective lithospheric viscosity of μ_L, a thickness of d_L, and a radius of curvature R. The dissipation is

$$\Phi_L = \mu_L \left(\frac{d_L}{R} \right)^3 U_P^2 \tag{3.21}$$

where U_P is the plate velocity. Numerical simulations (Capitanio et al., 2009) have suggested that the radius of curvature of the plate adjusts to minimize plate bending dissipation during subduction. The exact functional form of R is still debated and is not considered in this study.

Dissipation in the lithosphere can also be approximated using a model suggested by Valencia and O'Connell (2009), in which the subducting plate is continuously sheared into

the mantle, as illustrated in Figure 3.2. At subduction zones, an infinitesimally small block is sheared from the plate into the mantle. For a yield stress of τ_y, a plate thickness of d_L, and a plate velocity of U_P, the dissipation for such a deformation mechanism is given by

$$\Phi_L = \tau_y d_L U_P. \tag{3.22}$$

The two dissipation models for the lithosphere represent end member models for how the plate would behave if it deformed either entirely viscously (equation (3.21)) or entirely plastically (equation (3.22)). The behavior of a real plate is expected to lie somewhere between these two end members. If the thickness of the plate is defined by its thermal thickness (equation (3.2)) then the dissipation for the viscously deforming plate scales as $d_L^3 U_P^2 \propto U_P^{-3/2} U_P^2 \propto U_P^{1/2}$. The dissipation for the plastically deforming plate scales as $d_L U_P \propto U_P^{1/2}$ and the models scale the same way with the plate velocity. In general, both models give the same result (for a fixed aspect ratio) when $d_L \propto U_P^{-1/2}$. Thus, either deformation model captures the physics of both deformation mechanisms. Furthermore, the models give the same result when the radius of curvature is related to τ_y, μ_L, L, and κ by

$$R = \left(C_o^2 \frac{\kappa L \mu_L}{\tau_y} \right)^{\frac{1}{3}}. \tag{3.23}$$

We can define an effective stress for the plate τ_Y equal to

$$\tau_Y = \mu_L \frac{d_L^2}{R^3} U_P \tag{3.24}$$

for the bending model and

$$\tau_Y = \tau_y \tag{3.25}$$

for the plastic model. Note that the effective stress is not a function of the plate velocity or thickness when the lithospheric thickness is determined by the thermal thickness since

$d_L \propto U_P^{-1/2}$ and τ_Y will be a constant model parameter. With τ_Y defined by equation (3.24) or (3.25) the dissipation in the lithosphere for either parameterization is given by

$$\Phi_L = \tau_Y d_L U_P. \tag{3.26}$$

3.2.3 Dissipation in the fault zone

Dissipation occurs at the interface between the subducting and overriding plates. This dissipation may be parameterized using an effective shear stress on the fault zone, τ_F. We assume that the surface area of the interface will be proportional to the thickness of the overriding plate (other criteria could be used). As in Conrad and Hager (1999) we can parameterize the dissipation in the fault zone, per unit length along strike, as

$$\Phi_F = \tau_F d_L U_P. \tag{3.27}$$

3.2.4 Interior cell flow and lateral dissipation

Flow beneath the plate will produce viscous dissipation and will be coupled to the plate by stresses on the lithosphere-mantle boundary. The plate in the convecting system simplifies the flow by driving a cell wide circulation and stabilizing the upper thermal boundary layer. Subduction of the plate at one end of the cell is balanced by an upwelling at the opposite end. We model the flow as a vertical flow that is restricted to the ends of the cell, and a horizontal flow across the entire length of the cell. Figure 3.3 illustrates the flow in the convective cell.

We consider first the interior horizontal flow. Flow in the interior of the cell is driven by the motion of the plate on the surface and by pressure gradients across the cell that arise from density gradients. The equation to be solved is the momentum equation given by equation (3.7) with the strain rate and stress defined by equations (3.11) and (3.12) and the vertical velocity set to zero (vertical flow between layers occurs only at the end of the cell). The horizontal velocity is then governed by

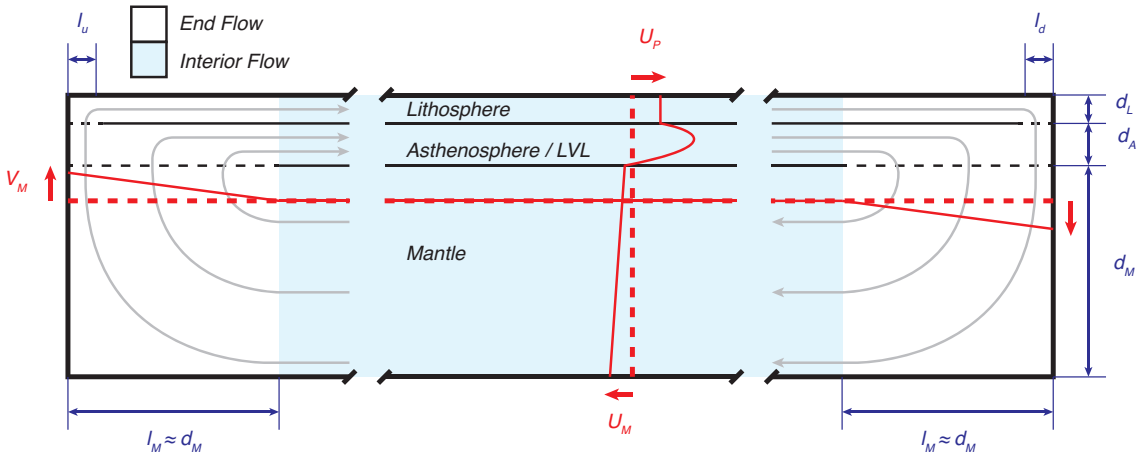

Figure 3.3: Flow structure of the model convection cell. The convective cell can have a low viscosity layer (LVL) or any number of layers of unique viscosity beneath the plate. Results in this paper will deal with a system with three layers. Velocity gradients and flow structure for the vertical flow and corner flow (white regions) are specified. The horizontal flow in the interior of the cell (blue region) is calculated as part of the solution and depends on the viscosity structure, model parameters, and energetics. Flow enters and leaves the lithosphere over length scales of l_u and l_d. The vertical velocity in the mantle changes over a length scale of d_M and corner flow occurs over an area of d_M^2. Flow is assumed to be entirely horizontal at distances greater than d_M from the ends of the cell.

$$0 = -P_x(y) + \mu(y)\frac{\partial^2}{\partial y^2}U(y) \tag{3.28}$$

where $P_x = dP/dx$. The plate moves at a velocity of $U_{_P}$ (for $d - d_{_L} \leq y \leq d$) and exerts a shear stress of $\tau_{_P}$ on the fluid below. The lower boundary of the mantle is free-slip and the shear stress and velocity are continuous at all interfaces. The boundary conditions for solving for $U(y)$ are

$$U(d - d_{_L}) = U_{_P}. \tag{3.29}$$

$$\mu_{_A}\frac{\partial U}{\partial y}\Big|_{y=d-d_{_L}} = \tau_{_P}. \tag{3.30}$$

$$\mu_{_M}\frac{\partial U}{\partial y}\Big|_{y=0} = 0. \tag{3.31}$$

The integrated horizontal mass flow rate must vanish for a closed system:

$$\int_0^d U(y)dy = 0. \tag{3.32}$$

We approximate the pressure gradient in the mantle with a simple linear dependence on the depth. Thus

$$P_x = \frac{\partial P}{\partial x} = Ay + b, \tag{3.33}$$

with constants A and b. This allows a pressure driven flow to exist beneath the plate regardless of whether the plate is moving or not. This assumption is equivalent to assuming a density anomaly field in the mantle of (see vertical component of equation (3.7))

$$\Delta\rho = -\frac{A}{g}x + f(y), \tag{3.34}$$

where A is the same constant from equation (3.33), g is the gravitational acceleration,

and $f(y)$ is an arbitrary function depending on the depth y but independent of the lateral position in the cell x. The functional form of equation (3.34) is a reasonable first order approximation for the density anomaly field in the convecting cell. The linear increase in density anomaly with lateral position captures, to first order, the increase in density anomaly that occurs through the cell moving from the warm buoyant upwelling to the cold dense downwelling (essentially we are keeping the first term in a polynomial expansion for the laterally varying density field). The linear depth-dependence of the pressure gradient also satisfies the condition that the pressure gradient should be anti-symmetric about $y = d/2$ for the boundary heated isoviscous case when no plate is present (all properties symmetric about $y = d/2$).

The viscosity and layer thicknesses control the shape of the flow profiles. The pressure gradient drives the flow and other simple depth-dependent pressure gradients could be used without significantly changing the results. We will demonstrate, in section 3.3.6, that the above assumption produces flow profiles that are in excellent agreement with numerical convection simulations.

Substituting equation (3.33) into equation (3.28) and integrating for the depth-dependent horizontal velocity yields an equation with the two unknown constants A and b from equation (3.33) and two unknown constants of integration. Using constraints (3.29) - (3.32) provides the depth-dependent horizontal velocity in the convective cell as a function of the viscosity structure, plate velocity U_P, and the basal shear stress τ_P. As such, A and b are completely determined by the boundary conditions and the mass conservation constraint. They are not free parameters in the model. The analytic solution for $U(y)$ is a third order polynomial in depth y. The coefficients of $U(y)$ are a complicated function of the layer thicknesses and viscosities and do not provide any physical insight (see Appendix B for details). Thus, we will continue to express the horizontal velocity field as $U(y)$ to avoid unnecessarily large equations. Then $U = U(y, U_P, \tau_P)$ and the dissipation from lateral flow in the asthenosphere and mantle, using equation (3.14), is given by

$$\Phi_{MH} = \frac{L}{2} \int_0^{d_M + d_A} \mu(y) \left(\frac{\partial U(y, U_P, \tau_P)}{\partial y} \right)^2 dy. \tag{3.35}$$

Equation (3.35) provides the dissipation rate for the horizontal flow in the mantle, Φ_{MH}, as a function of the viscosity structure $\mu(y)$, the plate velocity U_P, and the shear stress on the base of the plate τ_P.

3.2.5 Corner flow dissipation

Dissipation in the corner flow of the cell is difficult to calculate without a more complex flow model that accounts for the vertical flow in the ends of the cell. Morris (2008) found that dissipation in the corners was often larger than dissipation in the lateral flow. However, his model did not include a plate and lateral flow in his cells was localized near the ends of the cell. Including a plate forces a cell-wide flow and increases lateral flow dissipation. Nonetheless, corner flow will likely be a dominant term when the cell aspect ratio is small. Vertical flow is contained within $\sim d/2$ of the ends of the cell (e.g. Busse et al., 2006; Grigné et al., 2005; Lenardic et al., 2006). We estimate the velocity gradient in the corner flow by assuming that the vertical velocity decreases linearly away from the ends of the cell and over a length scale of $l_M \approx d_M$ (see Figure 3.3). The vertical flow at the ends must balance the horizontal flow in the middle. If the maximum vertical velocity at the ends of the cell is V_M then the vertical flow rate is $V_M l_M/2$. We can then estimate V_M by calculating the total horizontal flow rate in the cell from $U(y)$ and equating it to the total vertical flow rate. Then

$$V_M = \frac{2}{l_M} \int_0^{d_r} |U(y)| dy, \tag{3.36}$$

where d_r denotes the distance from the base at which the mantle return flow begins (i.e. $U(y) < 0$ in the mantle). The strain rate in the corners is then $\partial v/\partial y \approx V_M/l_M$ over an area of $\sim l_M^2$ and we can use equation (3.14) to calculate the mantle dissipation in the corners of the cell, Φ_{MC}, as

$$\Phi_{MC} \approx 2\mu_M V_M^2, \tag{3.37}$$

The total dissipation in the asthenosphere and lower mantle is then given by the sum of Φ_{MH} and Φ_{MC}, from equations (3.35) and (3.37) respectively

$$\Phi_M = \Phi_{MH} + \Phi_{MC}. \tag{3.38}$$

For simplicity, Φ_{MH} is evaluated over the entire length of the cell L even though this flow is only expected to be present over a length of $L - 2\,l_M$ (see Figure 3.3). This simplification is reasonable as the corner flow dissipation dominates for small aspect ratios ($\Phi_M \approx \Phi_{MC}$ for $L \approx d$, (see Morris, 2008)) and $L \approx L - 2\,l_M$ for larger aspect ratios ($L >> l_M$).

Φ_M is completely determined by specifying the viscosity structure $\mu(y)$, the plate velocity U_P, and the basal stress for the lithosphere τ_P.

3.2.6 ENERGY BALANCE EQUATIONS

All dissipation terms have now been expressed as a function of the viscosity structure $\mu(y)$, the plate velocity U_P, and the plate basal shear stress τ_P. We now return to the mechanical energy equation from section 3.2.1 and construct two energy balance equations, one for the lithosphere alone and one for the entire convective cell (lithosphere and mantle), which will be solved together to obtain U_P and τ_P.

We begin with the local energy balance for the lithosphere. Using equation (3.20) without Φ_M (since we are considering only the lithosphere), the energy balance for the lithosphere may be written as

$$D_{i_L} \langle Q \rangle_L = -\int_{S_L} (u_i p \delta_{ij} - u_i \tau_{ij})\, dS_j + \Phi_L, \tag{3.39}$$

where Φ_L is the dissipation in the lithosphere, $\langle Q \rangle_L$ is the depth averaged vertical advective heat flow through the lithosphere, $D_{i_L} = \alpha g d_L / C_p$ is the dissipation number defined using the thickness of the lithosphere, and all energy terms, unless otherwise stated, are

per unit length in the third dimension. The boundary term for the lithosphere will have contributions from stresses on the base of the lithosphere and from stresses on the fault zone. The contribution from the fault zone is given by equation (3.27) in section 3.2.3. The contribution from the base of the lithosphere can be further divided into contributions from the pressure gradient across the cell, the basal shear stress on the plate, and the deviatoric normal stress from an attached slab. Evaluating the boundary term yields (see Appendix B for details)

$$\int_{S_L} -\left(u_i P\delta_{ij} - u_i\tau_{ij}\right) dS_j \tag{3.40}$$

$$= \int_{S_{L-LVL}} -\left(u_i P\delta_{ij} - u_i\tau_{ij}\right) dS_j + \tau_{_F} d_{_L} U_{_P} \tag{3.41}$$

$$\approx d_{_L} U_{_P} P_{x_P} L - d_{_L} U_{_P}\tau_{SP} + d_{_L} U_{_P}\tau_{_F} + L U_{_P}\tau_{_P},$$

where S_{L-LVL} is the surface defining the lithosphere-LVL interface. The lithospheric energy balance then becomes

$$D_{i_L}\left\langle Q\right\rangle_{_L} = \left[LP_{x_p} + \frac{L}{d_{_L}}\tau_{_P} - \tau_{SP} + \tau_{_Y} + \tau_{_F}\right] d_{_L} U_{_P},$$

where P_{x_p} is the lateral pressure gradient evaluated at the base of the plate ($y = d - d_{_L}$), τ_{SP} is the magnitude of the deviatoric normal stress on the lithosphere from the slab, and $\tau_{_Y}$ and $\tau_{_F}$ are the magnitude of the effective yield stress for the plate and the shear stress on the fault, as discussed in sections 3.2.2 and 3.2.3. Equation (3.42) deals only with the magnitude of the stresses (see Figure 3.1 (b) for their orientations).

Work done on the plate by buoyancy may be separated into internal and external sources. The contribution from the density variation internal to the lithospheric volume is expressed as a local rate of change of potential energy and results from lateral variations in density within the lithospheric volume. Note that the volume used for the lithospheric energy balance extends to a constant depth equal to the maximum thickness of the plate (see Figure

3.1). Thus, lateral variations in plate thickness, from cooling or other causes, will result in an internal buoyancy source and will contribute to the local rate of change of potential energy for the lithosphere. The LHS of equation (3.42) is the local rate of change of potential energy in the lithosphere. This term is always positive and provides energy to drive the motion of the lithosphere. The *rate of change of potential energy in the lithosphere* can be shown to be equivalent to work done by the apparent force that was considered by Hager (1978) to arise from the thickening of the lithosphere and is also sometimes referred to as *ridge push* or *gravitational sliding* (although, for simplicity, we omit the small contribution that arises from surface topography).

'Slab-pull' is somewhat loosely defined (Forsyth and Uyeda, 1975) as the negative buoyancy force of the slab acting on the lithosphere. For our purposes, we define *slab* as the portion of the lithosphere that has been subducted and is deeper than the maximum thickness of the lithosphere d_L. The density anomaly external to the lithospheric volume, i.e. the attached slab, does work on the lithosphere through the normal stress that it exerts on the base of the lithosphere (τ_{SP} in Figure 3.1). We define *slab-pull* as the energetic contribution to the motion of the plate from the normal deviatoric stress of the attached slab (third term on the RHS of equation (3.42)).

The first term on the RHS accounts for work done on the lithosphere as material flows into the lithospheric volume at a high pressure and leaves the lithospheric volume at a lower pressure. LP_{x_p} gives the horizontal pressure difference across the cell at the base of the lithosphere and $d_L U_P$ is the flow rate. The second term on the RHS represents work done on the lithosphere by basal stresses. This term may be either positive, if the plate leads the flow beneath it, or negative if the plate lags behind it. The third term accounts for work done on the system by the slab-pull normal stress. The fourth and fifth terms on the RHS represent rates of dissipation for deforming the lithosphere and overcoming stress on the subduction zone fault.

The energetic contribution due to stresses on the base of the plate from flow driven by detached slabs is commonly referred to as 'slab-suction' (see for example Conrad and

Lithgow-Bertelloni, 2002). In our model the $L\tau_P U_P$ term in the lithospheric energy balance accounts for the work done by shear stresses on the base of the plate. τ_P is the laterally averaged basal shear stress and represents the net stress resulting from drag on the base of the plate, from the plate-driven component of the flow, and driving stresses from the density-driven component of the flow.

As the slab-pull, plate deformation, and fault-zone terms all scale in the same way, equation (3.42) may be further simplified by combining them and defining an effective net resistive stress for the plate, τ_R, as

$$\tau_R = \tau_Y + \tau_F - \tau_{SP}. \tag{3.42}$$

τ_R then represents a net stress that must be overcome to move the plate. This demonstrates that the individual values for slab-pull, plate yield stress, and fault zone stress are not important. Rather, it is the difference in these terms that matters. This effectively groups many of the large uncertainties in the model parameters τ_{SP}, τ_F, τ_y, μ_L, and R into a single model parameter τ_R which may be varied to explore the behavior of the system. If the thickness of the lithosphere is determined by its thermal thickness (equation (3.2)), then τ_Y, as discussed in section 3.2.2, will be independent of the plate velocity and τ_R will be a constant model parameter. The lithospheric energy balance can thus be written as

$$D_{i_L} \langle Q \rangle_L = LP_{x_p} d_L U_P + L\tau_P U_P + \tau_R d_L U_P. \tag{3.43}$$

If $\tau_Y + \tau_F > \tau_{SP}$ then $\tau_R > 0$ and the $\tau_R d_L U_P$ term may be thought of as a net dissipation in the lithosphere. On the other hand, if $\tau_Y + \tau_F < \tau_{SP}$ then $\tau_R < 0$ and the $\tau_R d_L U_P$ term may be thought of as a negative dissipation or energy source term for driving the motion of the lithosphere.

The global energy balance is much simpler. The only contribution to the boundary term in equation (3.20) is the fault zone dissipation term discussed in section 3.2.3. Substituting equations (3.26) and (3.27) into equation (3.20), the global energy balance is given by

$$D_i \langle Q \rangle = \tau_{_F} d_{_L} U_{_P} + \tau_{_Y} d_{_L} U_{_P} + \Phi_{_M} \tag{3.44}$$

The analytic form of $\Phi_{_M}$, from evaluating the integral in equation (3.35), is lengthy and does not provide any real insight. Thus, we simply leave it as $\Phi_{_M}$ in equation (3.44). The solution for $\Phi_{_M}$ is given in Appendix B.

At this point it is useful to non-dimensionalize the energy balances. The velocity and stresses can be non-dimensionalized using a characteristic velocity and stress of κ/d and $\mu_{_M}\kappa/d^2$, respectively. There are two choices for the dimensionless heat flow. The first uses a given temperature difference in the system, such as the temperature difference ΔT between the upper and lower boundaries of the cell, and is $\tilde{Q}_T = Q/(k_c \Delta T d)$, where the '$\sim$' denotes a dimensionless quantity. The second uses the internal heating rate H and is given as $\tilde{Q}_H = Q/(Hd^3)$. For a system with both boundary and internal heating, ΔT and H can be independent and the choice of non-dimensionalization has an effect on the magnitude of the dimensionless heat flow. The lithospheric and global energy balances are then

$$R_a \langle \tilde{Q} \rangle_{_L} = \left(\frac{d^2 L P_{x_p}}{\mu_{_M} \kappa} + \frac{L}{d_{_L}} \tilde{\tau}_{_P} + \tilde{\tau}_{_R} \right) \tilde{U}_{_P}, \tag{3.45}$$

and

$$R_a \langle \tilde{Q} \rangle = \frac{d_{_L}}{d} \tilde{\tau}_{_F} \tilde{U}_{_P} + \frac{d_{_L}}{d} \tilde{\tau}_{_Y} \tilde{U}_{_P} + \frac{\Phi_{_M}}{\mu_{_M}} \left(\frac{d}{\kappa} \right)^2. \tag{3.46}$$

R_a is either

$$Ra_{_T} = \frac{\alpha \rho g \Delta T d^3}{\kappa \mu_{_M}} \tag{3.47}$$

if the heat flow is non-dimensionalized using the temperature scale ΔT or

$$Ra_{_H} = \frac{\alpha \rho g H d^5}{k_c \kappa \mu_{_M}} \tag{3.48}$$

if the heat flow is non-dimensionalized using the internal heating rate H. The form of the

Rayleigh number that enters the energy balance is specifically linked with the form of the non-dimensionalization used for the heat flow. Either Rayleigh number may be used as long as the heat flow is non-dimensionalized in a consistent way. Generally, the choice of Ra is based on parameters in the model that are prescribed (for example, as boundary conditions) and other formulations of Ra exist (for details, see O'Connell and Hager, 1980). Note that the two Rayleigh numbers Ra_T and Ra_H are not energetically equivalent, as discussed in section 2.1. Thus, the larger of Ra_T and $Ra_H^{4/3}$ should be used to give the Rayleigh number that is most appropriate (from an energetic view).

Equations (3.45) and (3.46) can now be solved together to yield solutions for the plate velocity U_P and the basal stress τ_P.

3.3 RESULTS

We begin by demonstrating that the model reproduces the classic scaling law given by equation (3.4) for a boundary-heated isoviscous fluid layer with a weak plate. The behavior of the system with a strong plate is then investigated. This demonstrates how the model differs from classic parameterizations and allows for new solutions in the sluggish-lid convective regime. The existence of multiple solutions and their behavior is addressed. We then demonstrate how a low viscosity layer beneath the plate can have a significant impact on the dynamics of the system. Finally, we end with a comparison of our analytic model with some numerical convection simulations.

3.3.1 MULTIPLE SOLUTIONS

Combined, equations (3.45) and (3.46) offer multiple roots for the plate velocity U_P. The exact number of roots depends on the functional form of the lithospheric thickness and the heat flow and whether they depend on the plate velocity. Unphysical complex or negative roots are discarded. The remaining roots may however, and in many cases do, represent multiple solutions for the state of the system. Each unique solution for the plate velocity has a corresponding unique basal stress, flow profile, heat flow, etc. The multiple solutions are

For both two and three layer models			
ρ	3500	kg/m^3	Density
k_c	3.2	W/m·K	Thermal conductivity
C_p	1200	J/kg·K	Specific heat
κ	7.6×10^{-7}	m^2/s	Thermal diffusivity
α	2.5×10^{-5}	1/K	Thermal expansion
g	10	m/s^2	Gravitational acceleration
E	200	kJ/mol	Activation Energy
R_g	8.31	J/mol·K	Ideal gas constant
$\mu_{_M}$	eq. (3.49)	Pa·s	Mantle viscosity
T_o	1300	K	Reference temperature
d	3000	km	Total layer thickness
$d_{_L}$	eq. (3.2)	km	Plate thickness
L	6000	km	Convective cell length
R	300	km	Radius of curvature
$\tau_{_F}$	0	MPa	Fault zone stress
C_0	2.32		Plate thickness parameter
Two layer model (lithosphere and mantle)			
μ_o	10^{21}	Pa·s	Reference viscosity
τ_{SP}	0	MPa	Slab-pull normal stress
$d_{_M}$	$d - d_{_L}$	km	Lower mantle thickness
$d_{_A}$	0	km	LVL thickness
Three layer model (lithosphere, LVL and lower mantle)			
μ_o	10^{23}	Pa·s	Reference viscosity
τ_{SP}	200	MPa	Slab-pull normal stress
$d_{_M}$	2400	km	Lower mantle thickness
$d_{_A}$	$d - d_{_L} - d_{_M}$	km	LVL thickness

Table 3.1: Fixed parameters for model calculations in sections 3.3.3 through 3.3.5.

all energetically equivalent and each of them satisfy the energy balance and flow equations. Physically, the multiple solutions emerge as distinct balances between different terms in the lithospheric energy balance. This will be shown in the following examples.

3.3.2 THERMAL BOUNDARY CONDITIONS

We assume that the surface heat flux and lithospheric thickness can be determined by thermal boundary layer theory (equations (3.1) and (3.2)) and implicit in this is the assumption that the plate is moving. This excludes the zero plate velocity solution from our results. Other scalings for stagnant-lid or dehydration thickening could also be used for the heat flux and lithospheric thickness but a full exploration of these is beyond the scope of this study.

This study will consider a fluid layer with a surface temperature of $T_S = 0$ and an internal potential mantle temperature of $\Delta T = T_M - T_S$. The surface heat flow Q_S is determined by equation (3.1) and the basal heat flow Q_B is assumed to be zero. This is appropriate for a system that is internally heated or is cooling over time. We consider a high Rayleigh number convective cell and as such the advective heat flow $\langle Q \rangle_{adv}$ is assumed to be equal to the total heat flow $\langle Q \rangle$ (conductive heat flow is small within the layer). With zero basal heating the depth-averaged heat flow will be equal to half the surface heat flow and $\langle Q \rangle_{adv} = Q_S/2$. The heat flow at the base of the lithosphere (bottom red dashed line in Figure 3.1 (b)) will be entirely advective. The heat flow at the top surface of the lithosphere (upper red dashed line in Figure 3.1 (b)) will be entirely conductive. We therefore assume the depth-averaged advective heat flow through the lithosphere will be $\langle Q \rangle_L = Q_S/2$ as conduction accounts for approximately half of the heat flow. Our model can be applied just as easily to the boundary heated case. For a boundary heated system at steady state $\langle Q \rangle_{adv} = Q_S = Q_B$ and again $\langle Q \rangle_L = Q_S/2$. However, a complete treatment of the lower thermal boundary layer (present for boundary heated cases) leads to more complicated energy balance equations and would provide no further insight beyond that which the internally heated or cooling cases offer.

Table 3.1 provides a list of model parameters that are fixed at a constant value for all calculations in this paper. Table 3.2 lists parameters that are varied for several different cases that we consider.

Both the bending and shearing models for plate dissipation scale as $U_P^{-1/2}$ when the

Two layer model (lithosphere and mantle)

Case	ΔT (K)	μ_L 10^{21} (Pa·s)	τ_Y (MPa)	Ra_M
VaryRa1		33	30	
VaryRa2	$1100 - 1800$	100	90	$10^6 - 10^{10}$
VaryRa3		300	270	
LithStr1	1100			10^6
LithStr2	1360	$10 - 1000$	$9 - 900$	10^8
LithStr3	1800			10^{10}

Three layer model (lithosphere, LVL, and lower mantle)

Case	ΔT (K)	μ_L 10^{21} (Pa·s)	τ_Y (MPa)	Ra_M
WkPlate	1360	100	90	10^6
StPlate	1360	300	270	10^6

Table 3.2: Variable parameter values for model calculations in sections 3.3.3 through 3.3.5. The bending and plastic models for plate deformation scale in the same way and the strength of the plate may be equivalently described by specifying either an effective lithospheric viscosity or a yield stress. Both μ_L and τ_Y are given for reference.

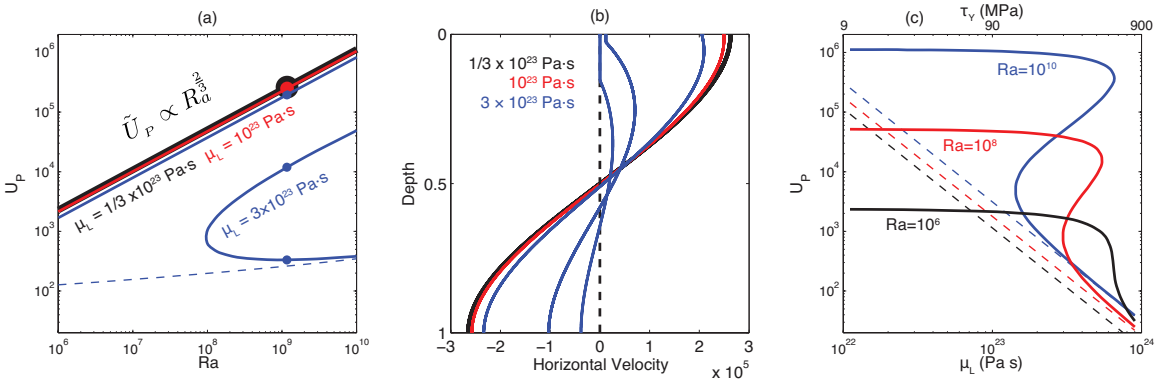

Figure 3.4: Model results for an isoviscous mantle with a finite strength plate. (a) Predicted plate velocity, U_P, as a function of the mantle Rayleigh number for cases $VaryRa1$ (black), $VaryRa2$ (red), and $VaryRa3$ (blue). (b) Horizontal velocity profiles for solutions marked with points in (a). (c) Predicted plate velocity, U_P, as a function of the effective lithospheric viscosity for cases $LithStr1$ (black), $LithStr2$ (red), and $LithStr3$ (blue). The plate velocity for the lower branch of solutions, predicted by equation (3.51), is plotted as a thin dashed line.

plate thickness is determined by its thermal thickness. As such, both models behave in the same way and the strength of the plate can be equivalently described by referring to either the effective lithospheric viscosity or the effective yield stress of the plate. The effective lithospheric viscosity will be varied in the results that follow and the effective yield stress for the plate, calculated using equation (3.23), will be given for reference. Table 3.2 shows that the effective yield stress considered ranges from $\sim 10\,MPa$ for weak plates to $\sim 10^3\,MPa$ for very strong plates.

3.3.3 Behavior with a weak plate

If the plate is made sufficiently weak and the mantle is isoviscous (either by setting $d_A = 0$ or $\mu_A = \mu_M$), then the model should behave in the same way as the classic boundary layer model (Turcotte and Oxburgh, 1967) that is based on a simple isoviscous fluid layer.

Plot (a) of Figure 3.4 shows results for a convective cell with a fixed aspect ratio of $L/d = 2$ and where the temperature difference between the surface and the mantle, ΔT, is varied. The (uniform) mantle viscosity is determined by

$$\mu_{_M} = \mu_o e^{\frac{E}{R_g}\left(\frac{1}{\Delta T} - \frac{1}{T_o}\right)} \tag{3.49}$$

and will be consistent with the temperature of the mantle. The model results are then plotted as a function of the mantle Rayleigh number (defined by equation (3.47)) for three different lithospheric viscosities. The variation of parameters for these three runs is given in Table 3.2 as cases $VaryRa1 - VaryRa3$.

The predicted plate velocities for the cases with the lower lithospheric viscosities ($VaryRa1$ and $VaryRa2$) are almost identical and follow the classic parameterized scaling of $\tilde{U}_{_P} \propto R_a^{2/3}$, as given in equation (3.4). These cases are independent of the lithospheric viscosity. The lithosphere is weak and dissipation in the plate ($< 10\%$) does not significantly affect the energy balances. Thus, the model recovers the classic parameterized scaling in the absence of an asthenosphere and strong plate.

The model produces flow profiles, shown as black and red lines in Figure 3.4 (b), that are identical to those of a simple isoviscous convection cell and have $U_{_P} \approx U_{_M}$ (see for example the many solutions in Schubert et al., 2001). The velocity gradient at the surface is near zero and the presence of the weak plate has little effect on the mantle flow.

3.3.4 Behavior with a strong plate

As the lithospheric viscosity increases further its effect on the predicted plate velocity becomes apparent. The results in Figure 3.4 (a) for the case with the high lithospheric viscosity (case $VaryRa3$) show a reduced plate velocity as well as multiple solutions at high Rayleigh numbers. Dissipation in the plate is now a significant term (up to 25%) in the global energy balance. Three branches of solutions exist at high Rayleigh numbers and all three branches satisfy the flow and energy balance equations. The three solutions differ in their plate velocity, and thus also in the thickness of the plate and the surface heat flow.

Plot (b) of Figure 3.4 shows the horizontal flow profiles for the solutions indicated by dots in (a). These profiles are part of the analytic model and represent the laterally averaged horizontal flow profiles that would be expected in a convecting cell. As the lithospheric

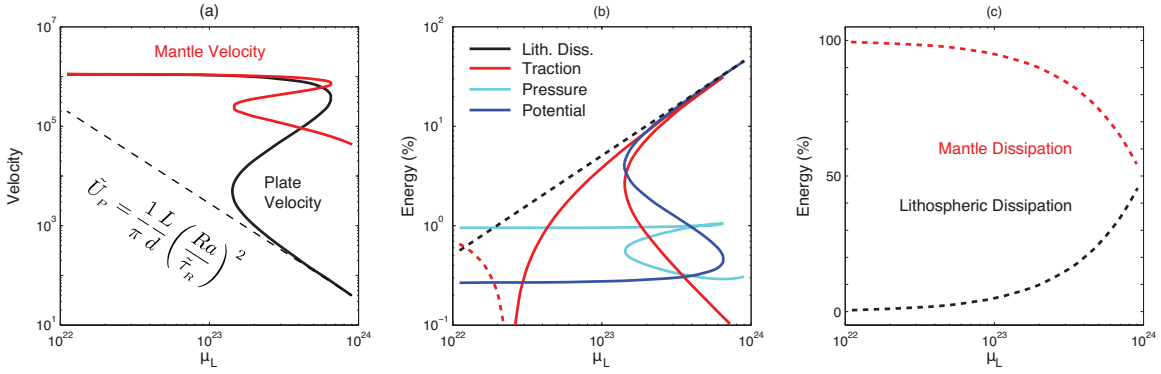

Figure 3.5: Results for an isoviscous mantle with a finite strength plate. (a) Dimensionless plate velocity (black) and mantle velocity (red) for case *LithStr*3. The plate velocity for the lower branch, predicted by equation (3.51), is plotted as the dashed black line. (b) Lithospheric dissipation (black), work done by basal tractions (red), work done by the pressure gradient (light blue), and the rate of change of potential energy in the lithosphere (dark blue), all from the lithospheric energy balance and normalized by the total rate of change of potential energy in the system. (c) Lithospheric (black) and mantle (red) dissipation from the global energy balance and normalized by the total rate of change of potential energy in the system. Dashed lines indicate negative values (work done by the lithosphere) while solid lines indicate positive values (work done on the lithosphere).

viscosity increases the plate begins to resist and the plate velocity is decreased relative to the lower lithospheric viscocity cases. Three possible solutions are present for the high lithospheric viscosity case (blue) and their plate velocities range over almost three orders of magnitude. Of the three, the fast solution (upper branch) has a thin plate that moves at a similar velocity to the flow beneath it. The other two solutions (intermediate and lower branches) have mantle flow rates that exceed the slower plate velocities and therefore represent sluggish-lid solutions.

Figure 3.4 (c) shows predicted plate velocities as a function of the effective lithospheric viscosity (or yield stress) for a range of Rayleigh numbers from 10^6 to 10^{10}. The variation of parameters for these three runs is given in Table 3.2 as cases $LithStr1 - LithStr3$. The low Rayleigh number case (black) is single-valued for the entire range of lithospheric viscosities considered. The higher Rayleigh number cases (red and blue) are multi-valued for large lithospheric viscosities. The range of lithospheric viscosity that leads to multiple

solutions increases for increasing Rayleigh number. Larger Rayleigh numbers allow for multiple solutions at lower lithospheric strengths.

Figure 3.5 looks at case *LithStr*3 in more detail. Plot (a) shows both the plate (black) and mantle (red) velocities as a function of the effective lithospheric viscosity. The mantle velocity varies much less than the plate velocity. Figure 3.5 (c) plots the relative dissipation in the plate (black) and mantle (red) as a percentage of the total rate of change of potential energy in the system (total available energy). The global dissipation curves have only a single branch when divided by the total energy. This demonstrates that the multiple solutions have the same ratio of plate dissipation to mantle dissipation, regardless of which solution branch they are on. Only for very large effective lithospheric viscosities does the plate dissipation approach the mantle dissipation. Multiple solutions for the system can occur for reasonable lithospheric viscosities when the lithospheric dissipation is still a small term in the global energy balance ($\approx 10\%$).

Figure 3.5 (b) shows the various terms from the lithospheric energy balance for case *LithStr*3 and demonstrates the different dominant energy balances that give rise to the multiple solutions. For low lithospheric viscosities dissipation in the plate is small, the plate is fast and thin, and thus the local rate of change of potential energy in the lithosphere is also small. The boundary energy terms dominate for weak plates and the plate is driven by the mantle pressure gradient and resisted by drag from the mantle. As the lithospheric viscosity is increased the plate begins to lag, the basal shear stress becomes negative, and tractions from the flow beneath provide the additional work to overcome the increase in lithospheric dissipation. The upper branch represents a branch of solutions in which the plate is driven by the mantle coupling terms. The mantle flow rate determines the speed of the plate, and as a result, this branch of solutions depends entirely on the material properties of the mantle.

The upper branch of plate velocity solutions resembles a simple cellular flow with $U_{_P} \approx U_{_M}$. This branch cannot continue indefinitely as the lithospheric viscosity is increased. The lithospheric dissipation scales linearly with the effective lithospheric viscosity. Thus, as

lithospheric viscosity increases dissipation in the plate becomes significant and slows the system down. A slower plate becomes thicker and a thicker plate has more dissipation. This positive feedback leads to a rapid increase in plate thickness that quickly slows the system as lithospheric viscosity is increased and no solutions of the form $U_P \approx U_M$ exist for large lithospheric viscosities. Termination of the upper branch for large lithospheric viscosity is clearly seen in Figure 3.5 (a). Conrad and Hager (1999, 2001) also found that solutions with $U_P \approx U_M$ were not possible for very large lithospheric viscosities and their model provided no solution. Our model predicts a transition from the cellular flow with $U_P \approx U_M$ to a sluggish-lid flow and provides a feasible mode of convection for plates with large lithospheric viscosities.

The intermediate branch of plate velocity solutions exists as a dominant energy balance between lithospheric dissipation and work done by basal tractions. Solutions on the intermediate branch represent a sluggish-lid convective state (as shown in Figure 3.4 (b)).

Solutions on the lower branch represent a convective state in which the dynamics of the system are entirely controlled by the lithosphere and not affected by the flow beneath it. The contribution from the plates' local buoyancy is large for thick plates and the lower branch exists due to a dominant energy balance between the rate of change of potential energy in the plate (from buoyancy) and work done against the net resisting stress τ_R (recall that $\tau_R = \tau_Y + \tau_F - \tau_{SP}$ and includes the contribution from the deformation of the plate, the stress on the fault, and the normal deviatoric stress on the base of the lithosphere). The pressure and traction boundary terms are negligible for this branch of solutions. The lithospheric energy balance controls the motion of the plate and the surface heat flow. As the energy available for convection in the mantle is proportional to the heat flow, mantle flow rates are also regulated by the lithospheric energy balance. Thus, while plate-mantle coupling through boundary stresses is negligible, the lithosphere-mantle system remains energetically coupled. Setting the pressure gradient and basal traction terms to zero in the lithospheric energy balance (equation (3.43)) gives

$$D_{i_L} \langle Q \rangle_L = \tau_R d_L U_P. \tag{3.50}$$

Using $\langle Q \rangle_L = Q_S/2$, equation (3.1) for Q_S, and solving for the plate velocity yields the simple relationship

$$\tilde{U}_P = \frac{1}{\pi} \frac{L}{d} \left(\frac{Ra}{\tilde{\tau}_R} \right)^2. \tag{3.51}$$

The plate velocity predicted by equation (3.51) is shown as dashed lines in Figures 3.4 (a) and (c) as well as Figure 3.5 (a) and accurately captures the behavior of the lower branch. While equation (3.51) scales with Ra^2 it is important to recall that the stresses, including the effective resistive stress τ_R, are nondimensionalized by dividing by the characteristic mantle stress of $\mu_M \kappa / d^2$. Thus the ratio $Ra/\tilde{\tau}_R$ and equation (3.51) are independent of the mantle viscosity. The small increase in predicted plate velocity for the lower branch in Figure 3.4 (a) is due to the change in temperature. The dynamics of the lower branch depend only on the lithospheric material properties and the heat flow through the lithosphere.

3.3.5 Behavior with a low viscosity layer

We now consider the behavior of the system when a low viscosity layer (LVL) is present beneath the plate. The LVL could represent either a low viscosity upper mantle or an asthenosphere, depending on its thickness. The thickness of the plate, LVL, and lower mantle are given by d_L, $d_A = d - d_L - d_M$, and d_M, respectively, with d_L again defined by equation (3.2).

One of the fundamental parameters required to determine the behavior of the plate is the effective net resistive stress $\tau_R = \tau_Y + \tau_F - \tau_{SP}$ (equation (3.42)), and more specifically, the sign of τ_R. We consider two cases: one with $\tau_R < 0$ in which the slab-pull stress is larger than the combined fault-zone and bending stresses, and one with $\tau_R > 0$ in which the fault-zone and bending stresses exceed the stress provided by slab-pull.

Figure 3.6 shows the results for the first case with $\tau_R < 0$ and plotted as a function

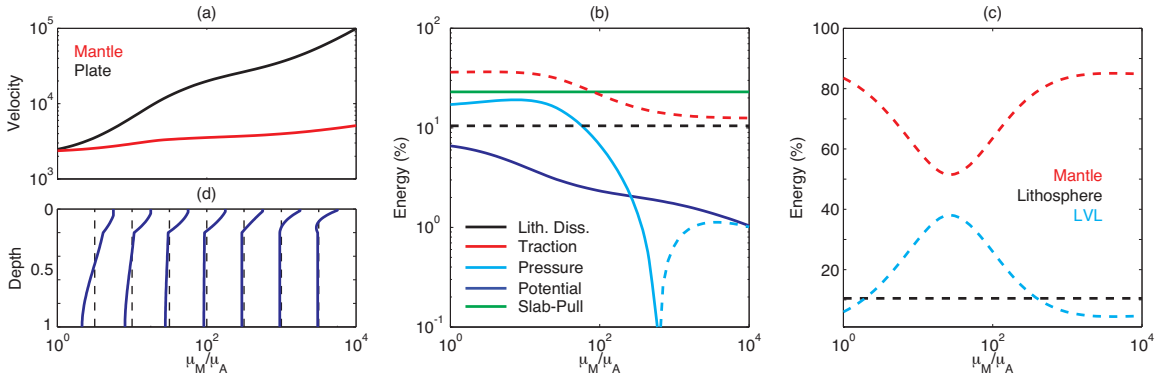

Figure 3.6: Results for case $WkPlate$. (a) Dimensionless plate (black) and mantle (red) velocities. Flow profiles, normalized by the maximum velocity in each profile, are shown below. (b) Lithospheric dissipation (black), work done by basal tractions (red), work done by the pressure gradient (light blue), work done by slab-pull (green), and the rate of change of potential energy in the lithosphere (dark blue), all from the lithospheric energy balance and normalized by the total rate of change of potential energy in the system. (c) Lithospheric (black), LVL (light blue), and mantle (red) dissipation from the global energy balance and normalized by the total rate of change of potential energy in the system. Dashed lines indicate negative values in the energy balances (work done by the lithosphere) while solid lines indicate positive values (work done on the lithosphere).

of the viscosity contrast between the lower mantle and the LVL. For this case a slab-pull normal stress of $200\,MPa$ is used and roughly corresponds to the expected weight of an attached slab of $400\,km$ length. The effective viscosity of the lithosphere is $10^{23}\,Pa \cdot s$. All parameters are held fixed with the exception of the LVL viscosity μ_A which is varied between the viscosity of the lower mantle μ_M and $\mu_M/10^4$. A decrease in the viscosity of the LVL lubricates the base of the plate, reducing drag from basal tractions, and allowing the plate velocity to increase relative to the lower mantle peak velocity. For very large viscosity contrasts a counter flow develops in the LVL and the pressure gradient driving flow beneath the plate switches sign.

Figure 3.6 (b) plots the individual energy terms in the lithospheric energy balance, all normalized by the total dissipation in the system. The slab-pull and the lithospheric dissipation terms do not depend on the viscosity in the mantle and, when normalized by the total dissipation in the system, are also independent of the plate velocity. Thus, they remain

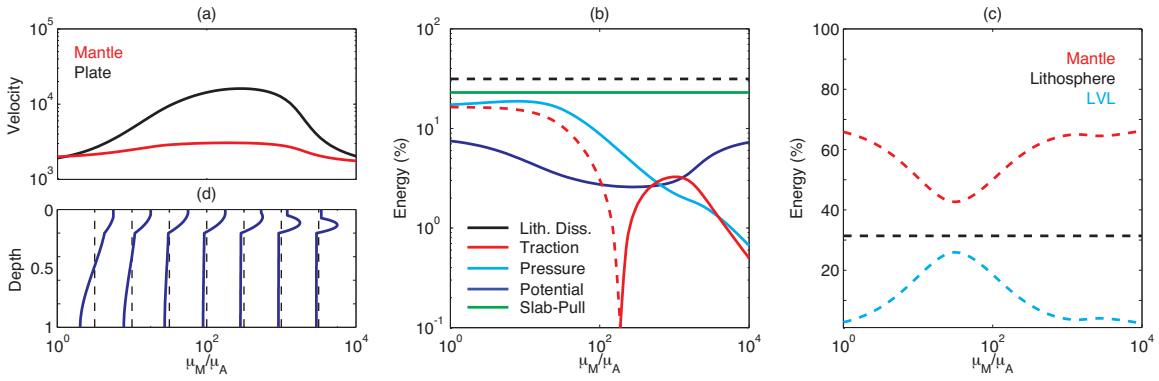

Figure 3.7: Results for case *StPlate*. (a) Dimensionless plate (black) and mantle (red) velocities. Flow profiles, normalized by the maximum velocity in each profile, are shown below. (b) Lithospheric dissipation (black), work done by basal tractions (red), work done by the pressure gradient (light blue), work done by slab-pull (green), and the rate of change of potential energy in the lithosphere (dark blue), all from the lithospheric energy balance and normalized by the total rate of change of potential energy in the system. (c) Lithospheric (black), LVL (light blue), and mantle (red) dissipation from the global energy balance and normalized by the total rate of change of potential energy in the system. Dashed lines indicate negative values in the energy balances (work done by the lithosphere) while solid lines indicate positive values (work done on the lithosphere).

constant as a function of μ_M/μ_A. As $\tau_R < 0$, the energy provided by slab-pull is larger than the energy lost to dissipation in the lithosphere (τ_R acts as a net driving stress) and both the net resisting stress and the rate of change of potential energy drive the plate (see equation (3.42)). This energy must be transferred through the lithosphere back to the mantle via (positive) basal tractions and, for very small μ_A, by generating a negative pressure gradient that drives a return flow in the LVL. In order to generate a positive average basal traction and mantle pressure gradient, the plate must be moving faster than the mantle beneath it. Therefore, solutions with $\tau_R < 0$ are always of the mobile-lid type. Furthermore, the lower the LVL viscosity, the larger the plate velocity that is required to produce the necessary stresses and pressure gradient to balance the driving terms.

We now consider the results when $\tau_R > 0$ and dissipation in the plate exceeds the energy supplied by slab-pull. Figure 3.7 shows the results for this case. The slab-pull normal stress remains at $\tau_{SP} = 200\,MPa$ and the effective lithospheric viscosity is now

$\mu_L = 3 \times 10^{23}\, Pa \cdot s$, a factor of 3 higher than the results of Figure 3.6. Initially, for low viscosity contrasts, the results appear similar. Decreasing the viscosity of the LVL provides lubrication for the lithosphere and the plate velocity increases relative to the peak lower mantle velocity. However, for a very low LVL viscosity the plate moves slower than the flow in the LVL, leading to a channelized flow beneath the plate. For the calculation shown in Figure 3.7, with a mantle Rayleigh number of $Ra = 10^6$, the maximum plate velocity occurs at a critical viscosity contrast of $\mu_M/\mu_A \approx 200$. At higher mantle Rayleigh numbers, such as $Ra = 10^{10}$ (not shown), the critical viscosity contrast can be as low as $\mu_M/\mu_A \approx 20$. For viscosity contrasts less than this critical value the LVL acts as a lubricating layer and decreasing the LVL viscosity increases the plate velocity. For viscosity contrasts greater than the critical value a sluggish-lid solution exists and decreasing the LVL viscosity decreases the plate velocity.

With $\tau_R > 0$, energy needs to be supplied to overcome the net dissipation in the plate. This energy can be provided in three different ways, each corresponding to one of the three boundary layer solutions. For low viscosity contrasts, the mantle pressure gradient provides the additional energy. However, for a very low LVL viscosity, the LVL cannot support a large pressure gradient and the contribution from the pressure term becomes too small. Basal tractions can provide the required energy to drive the plate. But in order to generate a negative shear stress the plate must be moving slower than flow in the mantle and a sluggish-lid solution is obtained. Finally, the plate can be driven by the local rate of change of potential energy in the lithosphere. This term is small and again results in a slow moving sluggish-lid solution.

For very low LVL viscosities, the traction and pressure terms are too small and plates are driven by the local rate of change of potential energy, leading to slow moving sluggish lid solutions. This example demonstrates that while a LVL can promote plate tectonics, it can also inhibit plate motions by reducing the available energy from mantle coupling. Figure 3.7 also demonstrates that, when a LVL is present, the plate velocity of a sluggish-lid solution can be of the same order of magnitude or larger than the isoviscous mobile-lid solutions.

Thus, a sluggish-lid solution does not necessarily imply a slow moving and thick plate, as was the case for the isoviscous solutions considered in section 3.3.4.

For very large viscosity contrasts, and thus very low μ_A, the model predicts either a return flow in the LVL with fast moving plates when $\tau_R < 0$ or a channelized flow in the LVL with slow moving plates when $\tau_R > 0$. Thus, the sign of τ_R is critical in determining the behavior of the system. $\tau_R < 0$ could result from a large amount of slab-pull or a weak plate. $\tau_R > 0$ can occur for either a strong plate or a plate that has little slab-pull. The results of Figures 3.6 and 3.7 demonstrate that the difference in dynamics may only be noticeable for large viscosity contrasts.

It is also worth noting that most of the terms in the lithospheric energy balance are of comparable size. The behavior is complex and is best captured by solving the full energy balance equations. Simplified scalings that balance only two or three terms will not capture these solutions and transitions.

3.3.6 Sluggish-lid solutions in numerical simulations

While the intermediate and lower branches of solutions are theoretically and conceptually viable steady-state solutions (they satisfy the energy and fluid flow equations), the stability of solutions on these branches has not yet been determined. As such, it is reasonable to ask whether there is any evidence of these forms of solutions in nature or in the large body of literature on numerical mantle convection simulations. We now compare our model to the 2D and 3D numerical convection results of Höink and Lenardic (2010).

Höink and Lenardic (2010) solved the Boussinesq equations governing thermal convection in an incompressible, infinite-Prandtl number fluid with CitcomCU (Moresi and Gurnis, 1996; Zhong, 2006), and used a finite element full multigrid solver for 3-D simulations and the conjugate gradient solver for 2-D simulations. All outer boundaries were free slip. Their model had a simple depth-dependent viscosity structure with a high viscosity lithosphere (upper 10%), a low viscosity channel for the asthenosphere (10%), and an intermediate viscosity lower mantle (lower 80%). Their numerical simulations focussed on the effects of

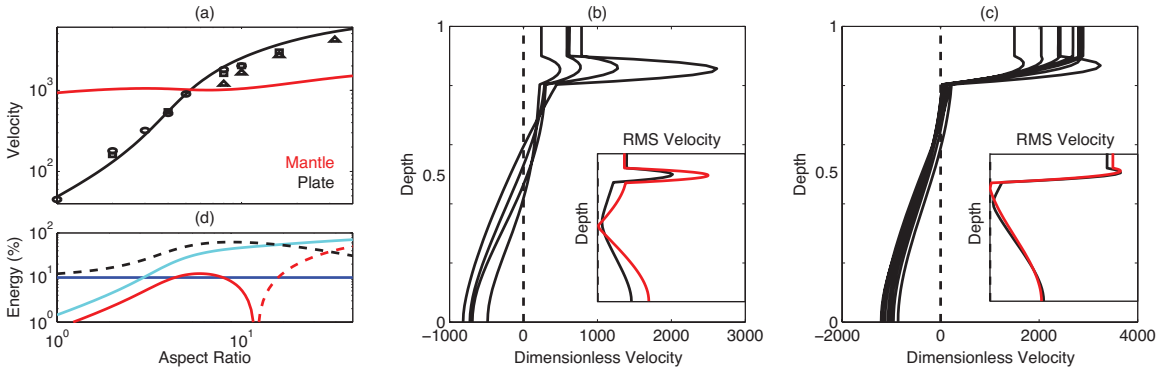

Figure 3.8: Comparison of model with finite strength plates to numerical simulations. (a) Plate velocities from the numerical simulations of Höink and Lenardic (2010) (black markers) and plate (black line) and mantle (red line) velocities from our analytic model. (b) and (c) Flow profiles from the numerical simulations (black) and analytic model (red) for aspect ratios of 4 and 10 respectively. Inset figures show the RMS average of the horizontal velocity profiles through the convective cell. (d) Lithospheric dissipation (black), work done by basal tractions (red), work done by the pressure gradient (light blue), and the rate of change of potential energy in the lithosphere (dark blue), all from the lithospheric energy balance and normalized by the total rate of change of potential energy in the system. Dashed lines indicate negative values in the energy balances (work done by the lithosphere) while solid lines indicate positive values (work done on the lithosphere).

changing aspect ratio. See Höink and Lenardic (2010) for further details.

Their results demonstrated a channelization of flow in the asthenosphere at low aspect ratios and a rapid increase in plate velocity with increasing aspect ratio. Their calculated plate velocities from their paper (Höink and Lenardic, 2010) are shown as the black symbols in Figure 3.8 (a). They noted that two scaling regimes exist, one at low wavelength and one at larger wavelengths. They proposed that the negative buoyancy increases with cell wavelength and at the regime transition it overcomes the bending resistance.

As in their study, we use dimensionless parameters $\tilde{\mu}_L = 10$, $\tilde{\mu}_A = 0.01$, $\tilde{\mu}_M = 1$, $Ra_T = 10^6$, $Ra_H = 10^7$, $\tilde{d} = 1$, $\tilde{d}_L = 0.1$, $\tilde{d}_A = 0.1$, $\tilde{d}_M = 0.8$. The simulations of Höink and Lenardic (2010) were primarily internally heated ($> 85\%$ of heating). For simplicity we assume that internal heating is the main mode of heating and we use a dimensionless heat flux of 10. Thus, the dimensionless heat flow is given by $Q_S = 10\,L/d$, with L/d being the aspect ratio for the convective cell. Again, the depth averaged advective heat flow through

both the convective cell and the lithosphere are assumed to be $\langle Q \rangle = Q_S/2$.

In all previous calculations the thermal and mechanical thickness of the lithosphere was assumed to be the same. For this case they are independent and we define the thickness of the lithosphere, $d_{_L}$, using the (fixed) mechanical thickness. Their simulations did not include lateral viscosity variations. As such, the slab has little strength in the asthenosphere and we set the slab-pull normal stress, $\tilde{\tau}_{_{SP}}$, to zero. A consequence of the absence of slab-pull is that deformation in the lithosphere is not focused at the ends of the cell and can be diffuse (see surface velocity in Figure 5 of Höink and Lenardic (2010)). As a result, the plate does not deform like a bending viscous beam and we treat dissipation in the lithosphere by using the constant stress model given in equation (3.22), with τ_y representing a characteristic stress in the lithosphere. The characteristic stress for the lithosphere is $\tau_y \approx \mu_{_L} U_{_M}/d_{_L}$, where $U_{_M}$ is the mantle velocity (a characteristic velocity for the problem), $\mu_{_L}$ is the effective viscosity of the lithosphere, and $d_{_L}$ is the thickness of the lithosphere. From their simulations, we use $\tilde{U}_{_M} = 1200$ for the characteristic mantle velocity.

Figure 3.8 (a) shows the calculated plate (black line) and mantle (red line) velocities from our analytic model as a function of the aspect ratio and agrees well with the numerical simulation results (black markers). Figure 3.8 (b) and (c) show flow profiles from their numerical simulations (black lines) for convective cells with aspect ratios of 4 and 10, respectively (these are the same flow profiles shown in Figure 1 of Höink and Lenardic (2010)). A channelized flow occurs in the asthenosphere for small wavelengths. For larger wavelengths the asthenosphere acts as a lubricating layer for the plate and the flow in the asthenosphere is Couette-like. The inset plots in (b) and (c) show the RMS horizontal velocity averaged over the convective cell for the numerical simulations (black line) and calculated from our model (red line). Given the simplicity of the our analytic model, the agreement is quite good. The analytic model slightly overestimates mantle flow rates for the small aspect ratio cell. Nonetheless, the model does a reasonable job at getting the plate velocity and characteristic flow profiles correct.

Figure 3.8 (d) plots the various terms in the lithospheric energy balance, again normal-

ized by the total dissipation in the system ($D_i \langle Q \rangle$). For small aspect ratios, the short and low viscosity asthenosphere cannot support a large pressure drop and work done by the mantle pressure gradient is small. Both the magnitude of the shear stress on the base of the plate and the surface area over which the stresses can be applied are small for a low viscosity asthenosphere and a small aspect ratio convective cell. Thus, energy provided by basal tractions is also very small. All that remains to drive the motion of the plate at small aspect ratios is the local rate of change of potential energy in the lithosphere. This term is small and results in a solution that is a slow moving self-driven plate. This is another example of how the presence of an asthenosphere can inhibit plate motions by effectively decoupling the plate and mantle.

As the aspect ratio of the convective cell increases, so does the length of the asthenosphere. A longer channel can, for similar flow rates, support a larger pressure drop across the mantle and work done by the mantle pressure gradient is larger for large aspect ratio cells. Similarly, a longer channel provides more surface area for tractions to act on the lithosphere and the contribution of tractions to the lithospheric energy balance is larger for large aspect ratios. The boundary terms drive the plate at large aspect ratios and result in a solution that is a fast moving mantle-driven plate.

Our analytic model predicts that tractions help to drive the plate at low aspect ratios but can provide drag that inhibits the motion of the plate at larger aspect ratios. The sign of the average basal stress changes at an aspect ratio of $L/d \approx 10$. At this aspect ratio the flow in the asthenosphere changes from mainly Poiseuille flow to mainly Couette flow. This explains the transition in flow style observed in the numerical simulations of Höink and Lenardic (2010). Furthermore, our energy balance results suggest that the transition between the two different scaling regimes noted by Höink and Lenardic (2010) is not the result of an increase in plate buoyancy relative to plate resistance (which actually decreases), but is instead due to the dominant plate driving force changing from the local rate of change of potential energy (gravitational sliding) at small aspect ratios to work done by the mantle pressure gradient (mantle coupling) at large aspect ratios. This transition in dominant plate

driving force is responsible for the transition from the sluggish lid mode of convection to the active lid mode.

3.3.7 Multiple states and hysteresis in numerical simulations

We now consider a series of thermal convection simulations that exhibit multiple solutions and demonstrate a path dependence, and thus hysteresis, of the convective state. The convection simulations and results that we will discuss here were both carried out and supplied by Adrian Lenardic (personal communication, 2012). The methods and equations are those of Moresi and Solomatov (1998).

The fluid domain is a box of aspect ratio $L/d = 1$ and the layer is entirely boundary heated. The temperatures of the lower and upper boundaries are T_B and T_S, respectively, and the total temperature difference across the layer is fixed at $\Delta T = T_B - T_S$. For stresses below the yield stress, τ_Y, the viscosity in the fluid is temperature dependent and is given by

$$\mu(T) = \mu_S e^{-\theta(T-T_S)} \tag{3.52}$$

At the yield stress the flow law switches to a plastic branch with a viscosity given by

$$\mu_{plastic} = \frac{\tau_Y}{\dot{\epsilon}} \tag{3.53}$$

where $\dot{\epsilon}$ is the strain rate. This allows localized zones of failure to form and allows for weak zones and plate-like behavior in a self-consistent manner. The yield stress is a function of depth and is given by

$$\tau_Y = \tau_0 + \tau_1 z \tag{3.54}$$

where τ_0 is the yield stress at the surface, τ_1 is a depth dependent component, and z is the depth below the surface.

In the simulation results shown in Figure 3.9, the surface Rayleigh number, defined using

the total temperature difference ΔT and the fixed surface viscosity μ_S, is fixed at $Ra_S = 10$. The dimensionless surface yield stress is fixed at $\tilde{\tau}_0 = 0.1$. Figure 3.9 (a) indicates the mode of thermal convection, either active-lid (blue), episodic (green), or stagnant-lid (red), that the convective cell evolves to at steady state (statistical steady state for time dependent cases) for different values of the total viscosity variation $\mu(T_S)/\mu(T_B)$ and dimensionless depth dependent yield stress $\tilde{\tau}_1$.

Results from numerical simulations are shown for total viscosity contrasts of 10^5, 3×10^5, 6×10^5, 10^6, 2×10^6, and 3×10^6, with each viscosity variation having two branches of solutions slightly offset from each other. The simulation suites on the lower branches begin with a simulation with zero depth dependent yield stress and produce the active lid mode of convection. The depth dependent yield stress is slowly increased and the steady state solution of the previous run (smaller yield stress) is used as the initial condition for the next. This generates the suite of convection simulations that occupy the lower branches for each viscosity contrast. The upper branches of results are generated in a similar way, but by beginning with a very high yield stress and a stagnant lid solution and slowly decreasing the depth dependent yield stress, each time using the previous case (higher yield stress) as the initial condition. The light blue shaded regions indicate where multiple convective modes are found for the same model parameters. Within this range, active lid convection occurs only if the system began in the active lid mode and the plate strength was increased. Similarly, within this range stagnant lid convection occurs if the system began in the stagnant lid regime. Specifying the model parameters is not sufficient to determine the state of the system. The history of the system is also required. The numerical results also demonstrate that the region of multiple solutions grows with increasing viscosity contrast, allowing for episodic convection at lower yield stresses and active lid convection at higher yield stresses.

Let us compare our analytic model to these numerical results to see if we can capture any of the complex behavior exhibited. The situation we now consider is quite different from the cases we explored earlier in this study, where the viscosity was, at its most complicated, a simple function of depth. We now have a convecting system with a fully temperature

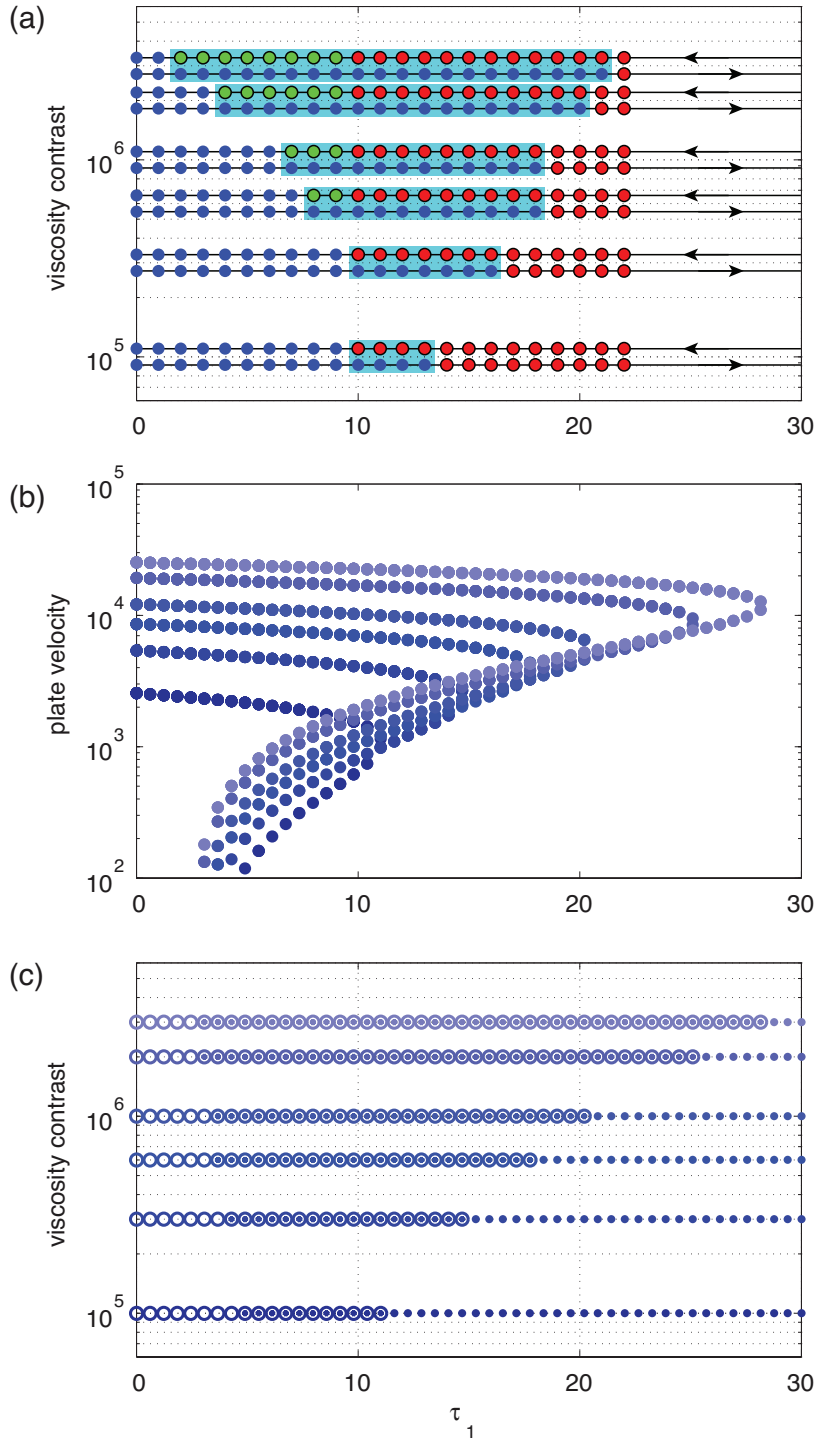

Figure 3.9: Convective mode as a function of plate strength and viscosity contrast. (a) Results from numerical simulations supplied by Adrian Lenardic. (b) Solutions predicted using the analytic model. (c) Convective mode predicted by the analytic model. An open marker represents the active lid mode, a small closed marker indicates stagnant lid mode, and an open marker around a closed marker corresponds to multiple solutions.

dependent viscosity and a depth dependent yield stress.

Let us model this case as a strong plate above a well mixed isoviscous layer. Both the strength of the plate as well as the viscosity of the well mixed interior will be related to the yield stress and temperature dependence of the viscosity below. In order to better compare with the numerical simulations shown in Figure 3.9 (a) and ensure that we are using the correct values for all dimensionless parameters, we non-dimensionalize the energy balance equations (3.43) and (3.44) of section 3.2.6 with the surface viscosity μ_S instead of the mantle viscosity μ_M. The lithosphere and global energy balances are then

$$\tilde{d}_L \tilde{L} Ra_S \langle \tilde{Q}_L \rangle = \tilde{d}_L \Delta \tilde{P}_P \tilde{U}_P + \tilde{L} \tilde{\tau}_P \tilde{U}_P + \tilde{d}_L \tilde{\tau}_Y \tilde{U}_P \tag{3.55}$$

and

$$\tilde{L} Ra_S \langle \tilde{Q} \rangle = \tilde{d}_L \tilde{\tau}_F \tilde{U}_P + \tilde{d}_L \tilde{\tau}_Y \tilde{U}_P + \tilde{\Phi}_m \tag{3.56}$$

where all terms in the energy balances are expressed in dimensionless form using the characteristic length d, velocity κ/d, and stress $\mu_S \kappa/d^2$. For simplicity we have assumed that the net resistive stress in equation (3.55) is $\tau_R \sim \tau_Y$. $\tilde{\Phi}_m$ is the total dissipation in the mantle flow, divided by $\mu_S/(\kappa/d)^2$ (to make it dimensionless) and the surface Rayleigh number Ra_S is defined in this section as

$$Ra_S = \frac{\alpha \rho g \Delta T d^3}{\kappa \mu_S} \tag{3.57}$$

Due to the large viscosity contrast, we expect solutions with a plate velocity that is smaller than the velocity at the base of the mantle. The temperature drop across the upper thermal boundary layer will therefore be larger than the temperature drop across the lower thermal boundary layer. As a first guess, let us assume that the temperature of the well mixed interior of the convective cell is close to the base temperature T_B. The viscosity of the well mixed interior of the convective cell will then be $\mu_M \sim \mu(T_B) = \mu_S/(viscosity\, contrast)$.

Let us again use thermal boundary layer theory and equations (3.1) and (3.2) for calculating the average heat flow $\langle Q \rangle$ and thermal thickness $d_{_L}$ for the cold surface thermal boundary layer. Again, as a first guess, let us assume that the maximum yield stress in the plate is approximately equal to the depth dependent yield stress evaluated at a depth equal to the thickness of the plate $d_{_L}$. Then we have $\tau_{_Y} = \tau_0 + d_{_L}\tau_1$.

Figure 3.9 (b) shows the calculated plate velocity as a function of the depth dependent yield stress and for various viscosity contrasts, using all the same parameters as the numerical simulations in plot (a) and the approximations discussed above for our analytic energy balance equations. The analytic model predicts regions with active lid solutions for small yield stresses and multiple solutions for intermediate yield stresses. Plot (c) of Figure 3.9 shows the convective mode as a function of the dimensionless depth dependent yield stress and viscosity contrast. An open marker indicates that the only solution predicted by the model was on the upper branch of solutions and is thus the active lid mode of convection. A solid round marker indicates that the analytic model did not yield a result and that the system must therefore be in the stagnant lid mode (recall that the physics of stagnant lid convection is not incorporated into the energy balance equations in this study). An open marker around a smaller solid marker indicates that the model found multiple solutions for the given parameter values and that both the active lid and sluggish lid modes of convection are predicted.

The analytic model predicts active lid solutions for small yield stresses, stagnant lid solutions for large yield stresses, and a region with both active and sluggish lid solutions for intermediate yield stresses. The analytic results show an increasing range of yield stresses for which multiple solutions are possible as the viscosity contrast is increased. This is consistent with the results of the numerical simulations. Furthermore, the yield stresses for which transitions from single to multiple and multiple to single solution regimes occur agree remarkably well with the numerical simulations. As an example, consider the case where the viscosity contrast is 10^6. The numerical simulations demonstrate that only active lid convection occurs for $\tilde{\tau}_1 < 6$. Episodic convection occurs, and thus multiple solutions, for

$\tilde{\tau}_1 > 6$. The analytic model suggests that multiple solutions are possible for $\tilde{\tau}_1 > 4$. The numerical simulations exhibit only stagnant lid convection for $\tilde{\tau}_1 > 18$. The analytic model suggests that solutions with moving plates (active or sluggish) are not possible for $\tilde{\tau}_1 > 21$.

The qualitative and to some extent quantitative agreement between the numerical simulations and the analytic model is remarkably good given the number of simplifications that were made. This result is encouraging and suggests that the simple analytic model may be correctly capturing the behavior of the different convective modes.

The representative stress $\tau_{_Y}$ used in the analytic model to calculate the dissipation in the plate will not be exactly equal to the yield stress at the base of the plate. The base of the plate will be warm and will have a lower viscosity than the shallow part of the plate. It is therefore unlikely that stresses at the base of the plate would reach the yield stress and the maximum stress likely occurs in the interior of the plate. The mean temperature and interior of the convecting cell will not be exactly equal to the base temperature $T_{_B}$ or there would be no thermal gradient at the base of the fluid layer and no heat flow through the base. Thus the interior temperature must be slightly less than the base temperature and the mean viscosity of the interior will be larger than we have estimated above. These potential (over)simplifications may explain some of the differences between the numerical convection simulations and analytic model predictions. It should also be pointed out that solutions in plot (a) of figure 3.9 are classified as either active or stagnant lid convection. The possibility of sluggish lid convection was not considered there. The analytic model suggests that there should be sluggish lid modes for intermediate yield stresses for which the plates are thick and move slowly. It is possible that the numerical simulations with sluggish lid convection been classified as stagnant lid convection due to their thick lids. A more detailed study that considers the velocity and thermal structure of the numerical convection simulations and focuses on the difference between sluggish and stagnant lid convection is beyond the scope of this study and will be the subject of future work.

3.4 DISCUSSION

3.4.1 IMPLICATIONS FOR THE EARTH AND PLANETS

The Earth is a complex fluid dynamical system that has many plates, three dimensional geometry, and time dependence. Neighboring plates interact and transfer energy to each other through boundary forces. By comparison, our analytic model represents a much simpler system that has a single plate and only two dimensions. As such, it would be tenuous at best to use our model to try to predict plate velocities for specific plates on the Earth. Nonetheless, if the first order physics is correct, then our model can be expected to predict average values for plate velocity, heat flow, plate thickness, etc., for various times in the Earth's history and for planets with different properties.

The mantle Rayleigh number for present day Earth ranges from $10^6 - 10^8$, the effective lithospheric viscosity is likely between $3 \times 10^{22} - 3 \times 10^{23}\, Pa \cdot s$ (Wu et al., 2008), and the upper and lower mantle viscosities are $10^{21}\, Pa \cdot s$ and between $10^{21} - 10^{23}\, Pa \cdot s$, respectively (Mitrovica and Forte, 2004). Our results suggest that solutions for this parameter range, with an aspect ratio of $L/d = 2$ (plate length of $\sim$ 6000 km), and with attached slabs of several hundred kilometers (see Figure 3.7) should be in the mobile-lid regime and have plate velocities of order $O(1 - 10)$ cm/year. Increasing the effective lithospheric viscosity decreases the plate velocity. Increasing the amount of slab-pull increases the plate velocity. This is all consistent with observations and our current understanding of present day plate tectonics on the Earth.

The situation may have been very different when the Earth's mantle was warmer and less viscous. Figure 3.4 demonstrated that sluggish lid solutions can exist when the mantle Rayleigh number is high and the contrast between the viscosity of the lithosphere and the mantle is large. The added presence of a low viscosity upper mantle and/or asthenosphere would further promote sluggish or even stagnant-lid behavior. During the Earth's early evolution the mantle viscosity may have been too low to allow for efficient coupling between the mantle and the plates, thereby resulting in sluggish-lid plate tectonics and a reduced

heat flow. The magnitude of the plate velocity in this sluggish lid regime would likely have been similar to the magnitude of present day plate tectonics. This would have slowed the cooling of the Earth and regulated plate tectonic rates through time. Eventually, due to a slow cooling of the mantle and gradual increase in viscosity, the mantle viscosity would become large enough that mantle flow could more efficiently couple to the plates. This would cause plate tectonics to change from the sluggish-lid regime to the mobile-lid regime, increasing heat flow. This has significant implications for the thermal evolution of the Earth and for the present day Urey ratio (ratio of internal heating to heat loss from the mantle). It also has significant implications for the geochemical evolution of the Earth, as chemical differentiation of the mantle at ridges and the creation of large scale heterogeneity as plates are subducted at trenches are both modulated by plate tectonic rates. A detailed study of the thermal evolution of the Earth, with a heat flow scaling that allows for the full stagnant-lid convective regime, will be the focus of a separate study.

The sluggish-lid solutions presented in section 3.3.4, with an isoviscous mantle, have plate velocities that are orders of magnitude less than the mobile-lid solutions. The thickness of these plates, through the $d_L \propto U_P^{-1/2}$ dependence in equation (3.2), would then be significantly larger. In fact, solutions on the lower branch plotted in Figure 3.4 have plate thicknesses that are on the order of 500 km. For plates this thick, it is likely that other physical processes, such as small scale convection (Korenaga, 2009), would take over and might limit the thickness of the plate. However, section 3.3.5 demonstrated that plate velocities for the sluggish-lid solutions can be of the same order of magnitude as the mobile-lid solutions when a low viscosity layer is present beneath the plate (compare mobile-lid and sluggish-lid solutions at viscosity contrasts of $\mu_M/\mu_A = 1$ and $\mu_M/\mu_A = 10^4$). Moreover, it would be premature to dismiss these solutions, regardless of their plate thickness, as thick plate solutions might be possible under different situations, such as early Earth or on other planets.

While our analytic model makes no claims with regard to the episodicity (or any time dependence) of convection, it does predict that a region of multiple solutions can exist

(see for example Figure 4), separating the mobile-lid and sluggish-lid regimes. Episodic convection could occur in this region as the system transitions between the different branches of solutions due to either perturbations in the system (irregular) or a natural hysteresis (periodic). Silver and Behn (2008) suggested that the Earth may have had intermittent plate tectonics in the past. Such behavior might be explained by jumps between the various solution branches. Transitions between branches could be smooth, such as the transitions in Figures 6 and 7, or could be abrupt, as suggested in Figures 4 and 5. This behavior will largely depend on the stability of the different solution branches and this will be the subject of future work. It is worth noting again, however, that the sluggish-lid solutions shown in Figure 8 correspond to stable sluggish-lid solutions in the numerical simulations of Höink and Lenardic (2010). This suggests that at least some of the sluggish-lid solutions predicted by our model are stable. Furthermore, the numerical convection simulations discussed in section 3.3.7 exhibited both regions of single and multiple solutions, as well as regions in which episodic convection was occurring. When applied to the same problem, our analytic model predicted regions of multiple solutions that compared well to those of the numerical simulations. Such a numerical counterpart to our analytic solution provides some vicarious verification.

Multiple solutions also allow for the possibility that two planets with similar properties, such as the Earth and Venus, could be on different solution branches and therefore exhibit very different convective states. The particular state of the system, in a region of parameter space with multiple solutions, could depend on the evolution of the system leading to that region of parameter space. Different initial conditions or perturbations throughout two similar planets' evolutions could result in the two planets ending up in different convective states. Such path dependency may be fundamental to our understanding of planetary evolution.

It is important to note that the upper branch of solutions, and thus the classic boundary layer solution (Turcotte and Oxburgh, 1967), does not exist throughout the entire parameter space. This is demonstrated in Figure 5 where the mobile-lid solution terminates for large

lithospheric viscosities and in Figures 7 and 8 where the solution transitions from a mobile-lid solution to a sluggish-lid solution. Furthermore, there are regions of parameter space where only the sluggish-lid boundary layer solution exists. Thus, while the classic boundary layer scaling may capture the dynamics of present day plate tectonics on the Earth, it should not be blithely applied to the early Earth, where conditions may have been very different, or to other terrestrial planets with different properties, sizes (e.g. super-earths), etc, without first verifying that such a particular boundary layer solution exists. Our analytic model provides a tool that may be used to explore and map out the parameter space for the different solution branches.

3.4.2 Limitations and extensions of the model

We have kept the model as simple as possible in order to keep the physics clear and we recognize that it can be improved and made more accurate. Our aim has been to determine the nature of the forces driving plates and to be able to extract simple analytic expressions that capture the model behavior and reveal the effects of various parameters and features of the model.

We have explored solutions where the lithospheric thickness is controlled by the thermal thickness. Other models for predicting lithospheric thickness have been proposed. One such model determines the lithospheric thickness based on dehydration of the lithosphere (Hirth and Kohlstedt, 1996; Korenaga, 2003). Our model allows for the simple substitution of other parameterizations for plate thickening and dissipation and provides a general framework for studying a simple convection cell with a finite-strength plate.

We have used simple representations of the flow in the model. This could be made more accurate by using eigenfunctions of solutions of the Navier Stokes equations, as in Busse et al. (2006) or Hager and O'Connell (1981), although it would most likely not change the basic scaling of the various parameters. We have also limited our analysis to a conductively defined lithosphere with a thickness that can increase until it subducts. Hence we have not limited the thickness of the plate, as Conrad and Hager (1999) did, even though this may

be more realistic for the Earth.

Our model is steady state, and does not address the formation of subduction zones and ridges that are necessary for plate tectonics, which is an important problem in its own right. The plate resistance from bending and/or faulting in our model is that related to the continued motion of plates. The depth of the frictional resistance at a subduction zone is taken as the plate thickness, although other choices could be made from considerations of the mechanics and state of material subducted. These may change the results somewhat, but as our analysis shows (equation (3.42)), the resisting stresses combine in a single term, so that the effect would not fundamentally change the results.

The results presented here have not included any effects of a boundary layer at the bottom of the mantle. Nevertheless, the driving force for convection is related to the convected heat flow through the mantle (equation (3.18)), and the nature of bottom heating does not matter. The problem can be formulated for either constant temperature or heat flux lower boundary conditions. For either boundary condition and the appropriate definition of the Rayleigh number as $\rho\alpha\Delta T d^3/\mu\kappa$ or $\rho\alpha(Q_b/k_c)d^4/\mu\kappa$, the temperature drop ΔT_b and heat flow at the boundary Q_b are related by (O'Connell and Hager, 1980)

$$\Delta T_b^4 \approx \frac{\mu(Q_b/k_c)^3\kappa}{16\rho g\alpha} Ra \tag{3.58}$$

This essentially gives the thermal impedance of the boundary layer.

Little attention was given to the effect of slab-pull in this study. Slab-pull is an important driving force for plates (Wu et al., 2008). However, we demonstrated in section 3.2.6 that both the effects of slab-pull and fault zone dissipation can be incorporated into the effective strength of the plate. The presence of slab-pull simply reduces the effective yield stress (or bending stress) of the plate. Thus, explicitly including slab-pull in the model will not change the behavior of the system.

3.5 CONCLUSIONS

Including the lithospheric energy balance is important for properly predicting the plate velocity. The plate velocity modulates the heat flow out of the system (equation (3.1)). As the rate of change of potential energy scales with the heat flow (equation (3.18)), the plate velocity directly controls the total energy available to drive the system. Thus, even though the magnitude of the lithospheric dissipation term may be small in the global energy balance, the total energy available for driving mantle convection is determined by the plate velocity and thus by the lithospheric energy balance.

We have demonstrated that the model reduces to the classic parameterization (Turcotte and Oxburgh, 1967) and predicts a simple cellular convective flow when a weak plate and isoviscous mantle are present. As the strength of the plate is increased the model deviates from the classic parameterization and convective solutions in the sluggish-lid regime become possible.

The strength of the lithosphere is determined by the effective lithospheric viscosity and radius of curvature in the plate bending model, or the plate yield stress in the shearing model. The two different models for calculating lithospheric dissipation are equivalent and independent of the plate velocity when the thickness of the lithosphere is determined by its thermal boundary layer thickness (for fixed aspect ratio). Thus, all of the results presented are independent of the choice of model for calculating lithospheric dissipation. The contrast between the strength of the lithosphere and the strength of the mantle determines the convective regime of the solutions. Solutions in the mobile-lid convective regime ($U_P \approx U_M$) occur when either the plate is weak or the mantle viscosity is high and the contrast in strength is low. Solutions in the sluggish-lid convective regime ($U_P < U_M$) occur when the contrast in strength is high and either the plate is strong or the mantle viscosity is low. Multiple solutions for the plate velocity are present for intermediate contrasts in strength between the lithosphere and the mantle.

The upper branch of plate velocity solutions corresponds to the classic form of convective

cell in which a simple cellular flow carries a weak plate on the surface. The plate and mantle velocities for the upper branch ($U_P \approx U_M$) are well described by the classic boundary layer model of Turcotte and Oxburgh (1967) and the dynamics of the system are characterized by the mantle Rayleigh number and the aspect ratio of the convective cell. This mode of convection is controlled by the material properties of the mantle.

The intermediate branch of plate velocity solutions represents a convective cell in the sluggish-lid regime with a plate velocity that is less than the mantle velocity. The plate-mantle coupling terms (pressure and tractions) are the dominant driving forces on the plate while deformation of the lithosphere is the dominant resistance. The dynamics for this branch depend on both the mantle and lithosphere material properties.

The lower branch of plate velocity solutions represents a mode of convection in which the lithosphere controls the dynamics of the system. The local negative buoyancy of a thick and strong lithosphere drives the motion of the plate. Work done by basal tractions and any mantle pressure gradient are negligible compared to the rate of change of potential energy and local dissipation in the lithosphere. This mode of convection occurs for strong plates and can exist with little slab-pull. Furthermore, it is controlled by the strength of the lithosphere and is independent of the mantle properties. Although this is the only possible mode of convection available to systems with very strong plates, it can also occur for reasonably small amounts of lithospheric dissipation ($< 10\%$ of total dissipation in system). The lithosphere modulates the heat flow out of the convective cell, regulating the amount of energy available to drive mantle convection, and thus also controlling flow rates in the mantle.

The lower branch of plate velocity solutions exists only for plates with a positive net resisting stress τ_R and when the contrast in strength between the lithosphere and mantle is high. The required net resisting stress for the lower branch of plate velocity solutions is possible for plates on the Earth, especially earlier in the Earth's history when the mantle was likely warmer and less viscous.

The introduction of a low viscosity layer (LVL) can significantly change the dynamics by

altering the plate-mantle coupling. Lowering the LVL viscosity, relative to the lower mantle, can promote plate motion by providing a lubricating layer. However, a very low viscosity LVL beneath a strong plate can inhibit plate motion and produce a slow moving plate with a channelized flow in the LVL. Our model is able to capture and explain the transition in plate driving forces responsible for this behavior. Thus, a LVL or asthenosphere does not always promote plate tectonics.

The distinct multiple solutions that occur are all energetically equivalent. Thus, the state of the system may depend on its history (this idea of transitioning between different modes of convection is discussed by Sleep (2000)). It is also possible that the system may transition between the various states due to natural perturbations in the velocity and density fields that occur in high Rayleigh number thermal convection flows. Examining the stability of the various solution branches will be the subject of future work.

Chapter 4

On the relative influence of heat and water transport on planetary dynamics

The dynamics of a planet and its evolution are controlled to a large extent by its viscosity. In this Chapter, we demonstrate that the dependence of mantle viscosity on temperature and water concentration introduces strong dynamic feedbacks. We derive a dimensionless parameter to quantitatively evaluate the relative strength of those feedbacks, and show that water and heat transport are equally important in controlling present-day dynamics for the Earth. A simple parameterized evolution model illustrates the strong feedbacks and behavior of the system and agrees well with our analytic results. The analysis identifies characteristic times for changes of viscosity, temperature, and water concentration and demonstrates, for time scales greater than a few hundred million years, that the system should either be degassing while warming or regassing while cooling. This yields a characteristic evolution in which, after an initial period of rapid adjustment, the mantle warms while degassing, and subsequently cools rapidly while regassing. As the planet continues to cool, the entire surface ocean may eventually return to the mantle. Our results suggest that a simple relationship may exist between the rate of change of water concentration and the rate of change of temperature in the mantle. This connection is extended by deriving an explicit equation for the Urey ratio that depends on both heat and water transport.

4.1 INTRODUCTION

The importance of the deep water cycle for the Earth's dynamics has been emphasized by several studies, both experimental and numerical (e.g. Iwamori, 2007; Li et al., 2008; McGovern and Schubert, 1989; Sandu et al., 2011). The presence of water has a significant impact on the viscosity of the mantle (e.g. Mei and Kohlstedt, 2000a), which controls to a large extent the Earth's dynamics, its thermal evolution, and plate tectonics. Current estimates of mantle temperatures and water concentrations suggest that both properties can control mantle viscosity to a similar extent.

Iwamori (2007) suggested that regassing, the transport of water into the mantle, might become more effective with time as the Earth cools down. This could provide a means of sustaining mantle convection despite the diminution of internal heat sources. The purpose of this study is to identify and quantify the interplay between the deep water cycle of a planet and the heat transport that drives convection and plate tectonics. This study is not intended to provide a detailed treatment of the Earth's evolution in particular, but rather to understand how water affects the evolution of a planet with active plate tectonics and Earth-like material properties.

4.2 A MODEL PLANET

The planet that we consider has a surface area S and mantle volume V. For simplicity, we assume that the mantle is a single layer that is 'well mixed' by convection. By 'well mixed', we mean that the scale of heterogeneity is small enough and evolving fast enough that the large scale mechanical, thermal, and compositional properties of the mantle are reasonably characterized by an average viscosity μ, potential temperature T, internal heating rate H, and water concentration χ_m.

The mantle is heated internally and cools through a loss of heat from its surface. For simplicity, we do not consider heat flow into the base of the mantle from the core. The

An amended version of this Chapter was published with Mélanie Gérault and Richard J. O'Connell in Earth and Planetary Science Letters, vol. 310, p. 380-388, 2011.

thermal state of the mantle is then determined by the balance (or imbalance) between the rate of internal heating and the surface heat flow. Conservation of energy requires

$$C_p \rho V \dot{T} = -Q_s + H \tag{4.1}$$

where $\dot{T}$ is the rate of change of temperature with respect to time, ρ is the average mantle density, C_p is the specific heat capacity, Q_s is the total surface heat flow, and H is the total heat production for the mantle. The system is in thermal equilibrium when the rate of internal heating is exactly balanced by the surface heat flow i.e. $Q_s = H$. The planet has an ocean on its surface, and water is transported from the mantle to the surface by degassing at ridges and returned to the mantle by regassing at subduction zones. The concentration of water within the mantle is governed by the balance (or imbalance) in the rate of regassing R and degassing D. Conservation of mass requires that

$$\rho V \dot{\chi}_m = R - D \tag{4.2}$$

where $\dot{\chi}_m$ is the rate of change of the mass fraction of water in the mantle with respect to time. The water cycle is in equilibrium when the rate of degassing is exactly balanced by the rate of regassing and $R = D$. We assume that plate tectonics is mainly responsible for driving the transport of both heat and water between the mantle and surface of the planet. The mechanisms of transport are discussed in section 4.6.

Deriving the relative strength of the thermal and water feedbacks does not require a dynamical theory for plate motion. We do however, rely on a few basic assumptions when discussing the feedbacks present in the system. The first assumption is that the viscosity is dependent on both temperature and water concentration, and decreases in response to an increase of either. We assume that the plate speed increases with a decrease in mantle viscosity. While several authors have pointed out that this may not always be the case (Crowley and O'Connell, 2012; Korenaga, 2003; Sleep, 2000), it is a reasonable assumption for a simple model. We assume that an increase in plate speed or mantle temperature leads

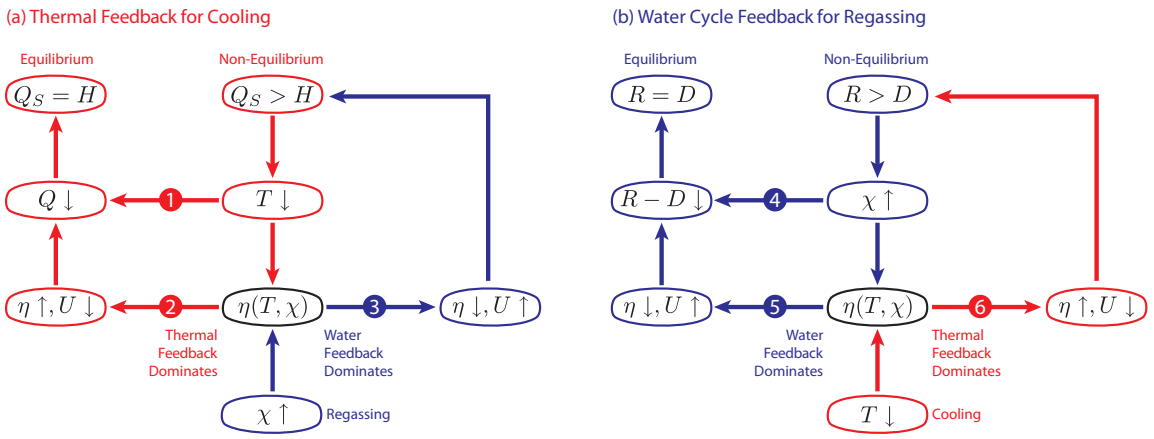

Figure 4.1: Interaction of the thermal and water feedbacks during cooling and regassing. Red arrows indicate changes resulting from the thermal feedback. Blue arrows indicate changes resulting from the water cycle feedback. (a) Thermal feedback structure during cooling. In the absence of the water cycle, feedback paths (1) and (2) both decrease the surface heat flow and move the system towards thermal equilibrium. With the water cycle, a decrease in viscosity (3) may result in an increase in surface heat flow that keeps the system out of thermal equilibrium. (b) Feedback structure for the water cycle during regassing.

to an increase in surface heat flow. This is easily justified using kinematic thermal boundary layer theory (e.g. Turcotte, 1967; Turcotte and Schubert, 1982). Finally, we assume that an increase in mantle water concentration or plate velocity will lead to an increase in the net rate of degassing, which is discussed in section 6.

4.3 RELATIVE STRENGTH OF THE THERMAL AND WATER FEEDBACKS

We first consider the case where the viscosity depends only on temperature. In this case, the relationship between temperature, viscosity, plate velocity, and heat flow, induces a strong negative feedback. This is illustrated by the red feedback paths in Figure 4.1a. An increase in surface heat flow, relative to the equilibrium state ($Q_s = H$), results in cooling and decreases the temperature of the system. This increases the mantle viscosity and decreases the plate velocity. The surface heat flow then decreases in response to both the decreasing temperature and the decreasing plate velocity. Thus, the feedback may be divided into two separate feedbacks. The first is the direct feedback between heat flow and temperature and

is illustrated in Figure 4.1a as feedback (1). The second is the feedback between heat flow and plate velocity that arises through the temperature dependence of the viscosity and is illustrated in Figure 4.1a as feedback path (2). In this case, both feedbacks are negative and therefore return the system to equilibrium. This 'thermostat' effect was first proposed by Tozer (1970).

We now consider the case where the viscosity only depends on the water concentration of the mantle. An increase in the net regassing rate $R_{net} = R - D$ increases the concentration of water in the mantle which decreases the viscosity. The increase in water concentration increases the degassing rate D and helps to reduce R_{net}. The decrease in viscosity leads to an increase in plate velocity which decreases R_{net} (this will be demonstrated in section 4.6). Thus, the water cycle feedback structure (Figure 4.1b) is conceptually the same as the thermal feedback structure and consists of two parts: the direct feedback between the net regassing rate and the water concentration of the mantle (feedback path (4)) and the feedback between the regassing rate and the plate velocity that arises through the dependence of viscosity on water (feedback path (5)). In this case, both feedbacks are negative and decrease the net regassing. This returns the water cycle to equilibrium.

The blue feedback path in Figure 4.1a illustrates a possible behavior when both temperature and water content affect viscosity. If the decrease in viscosity from regassing exceeds the increase in viscosity from cooling, the effect of the increase in plate speed (feedback path (3)) may outweigh the effect of the decrease in temperature and keep the surface heat flow from decreasing. In this case, the thermal feedback is not able to reduce the surface heat flow and approach equilibrium. If, however, the rate of change of viscosity from regassing is less than the rate of change of viscosity from cooling, the viscosity increases as the system cools and the feedback structure, while slightly weakened, operates as described above (red feedback paths). Many of these aspects are described in the recent numerical work of Sandu et al. (2011).

We now quantify the relative strength of the two feedbacks on viscosity. The coupling between temperature and water concentration is controlled by changes in viscosity. The

speed with which either heat or water transport is able to change the viscosity can be used as a measure of the strength of the feedback. Thus, we consider the time rate of change of viscosity:

$$\dot{\eta} = \frac{\partial \eta}{\partial T}\frac{dT}{dt} + \frac{\partial \eta}{\partial \chi_m}\frac{d\chi_m}{dt} = \eta_T \dot{T} + \eta_\chi \dot{\chi}_m$$

where $\dot{x}$ denotes the derivative of the variable x with respect to time. Solving for $\dot{T}$ and $\dot{\chi}_m$ in equations (4.1) and (4.2) and substituting them into equation (4.3) yields

$$\dot{\eta} = \eta_T \frac{1}{\rho C_p V}\left(H - Q_s\right) + \eta_\chi \frac{1}{\rho V}\left(R - D\right) \tag{4.3}$$

The first term on the right-hand side of equation (4.3) is responsible for producing the strong thermal-viscosity feedback present in classic thermal evolution models (e.g. Davies, 1980). The second term represents the contribution of water to the viscosity feedback.

We now define the relative strength number S_{WT}, a dimensionless parameter, as the absolute value of the ratio of the water feedback term to the thermal feedback term in equation (4.3):

$$S_{WT} = \left|\frac{\eta_\chi \dot{\chi}_m}{\eta_T \dot{T}}\right| = \left|\frac{\eta_\chi \left(R - D\right)}{\eta_T \left(H - Q_s\right)/C_p}\right| \tag{4.4}$$

The viscosity feedback is dominated by the thermal feedback when $S_{WT} < 1$. Reciprocally, the viscosity feedback is dominated by the water cycle feedback when $S_{WT} > 1$. Thus, the parameter S_{WT} allows us to quantitatively evaluate the relative importance of heat and water transport.

4.4 Relative strength of the feedbacks for present day Earth

While there are uncertainties associated with the rheology and present-day thermal and volatile state of the Earth, S_{WT} can still be estimated. This allows us to determine whether or not the water cycle need be considered in thermal evolution models or if its influence is

$R-D$ $\left(10^{11}\,\frac{kg}{yr}\right)$	U_r	E $\left(\frac{kJ}{mol}\right)$	r	χ_m (ppm)	S_{WT}
± 9	0.5	300	0.68	300	1.3
± 9	0.5	300	0.68	600	0.57
± 9	0.5	300	0.68	900	0.34
± 9	0.5	500	0.68	300	0.80
± 9	0.5	300	1	300	2.0
± 9	0.5	500	1	300	1.2
± 9	0.25	300	0.68	300	0.89
± 9	0.75	300	0.68	300	2.7
± 6	0.5	300	0.68	300	0.89
± 3	0.5	300	0.68	300	0.44

Table 4.1: Calculation of S_{WT} for a range of parameters.

negligible.

The viscosity for either diffusion or dislocation creep may be written in the form (Mei and Kohlstedt, 2000a,b)

$$\eta = \eta_o f_{H_2O}^{-\frac{r}{n}} \exp\left(\frac{E}{R_g T n}\right) \tag{4.5}$$

where η_o is a reference viscosity, f_{H_2O} is the water fugacity, r is an experimentally determined power law coefficient that ranges from 0.68 to 1.25 (depending on the assumed activation volume), E is the activation energy, $n \approx 1$ for diffusion creep or $n \approx 3$ for dislocation creep, and R_g is the ideal gas constant. The water fugacity is related to the water concentration through the experimentally determined relation (equation 3 of Li et al. (2008))

$$f_{H_2O}(\chi_m) = e^{C_0 + C_1 ln(C_{OH}) + C_2 ln^2(C_{OH}) + C_3 ln^3(C_{OH})} \tag{4.6}$$

where $C_0 = -8.0$, $C_1 = 4.4$, $C_2 = -0.57$, and $C_3 = 0.033$ are experimentally determined constants, $C_{OH} = 6.3 \cdot \chi_m$, and χ_m is the mass fraction of water. Equations (4.5) and (4.6) yield

$$\eta_T = -\frac{E}{R_g T^2 n}\eta \tag{4.7}$$

and

$$\eta_\chi = \frac{-r\,\eta}{n\,\chi_m}\left(C_1 + 2C_2 ln\left(C_{OH}\right) + 3C_3 ln^2\left(C_{OH}\right)\right) \tag{4.8}$$

Considering the large uncertainties in many of these parameters for the Earth, we calculate S_{WT} (see Table 4.1) using several reasonable values for the net regassing rate $R-D$, the Urey ratio $U_r = H/Q_s$, the activation energy E, the power law exponent r, and the mantle water concentration χ_m. We assume $T = 1300\,K$, $C_p = 1200\,J/kg\,K$, and $Q_s = 36\,TW$ (total heat flow from the mantle only, see Davies, 1999). The ratio η_χ/η_T, and therefore S_{WT}, are independent of the exponent n and the reference viscosity η_0.

The results of Table 4.1 indicate that S_{WT} is of order $O(1)$ for a large range of parameter values. This suggests that the water feedback may be just as important in controlling present day dynamics for the Earth as the thermal feedback. In the following sections, we demonstrate that $S_{WT} \approx 1$ may be a robust result for the evolution of an 'Earth-like' planet.

4.5 TIME SCALES AND RELATIVE RATES OF CHANGE

The evolution of the system is determined by the relative rates at which the temperature, water concentration, and viscosity change. If the water cycle is near equilibrium ($\dot{\chi}_m \approx 0$) then equations (4.3) and (4.5) yield

$$\frac{d\eta}{dt} = \frac{\partial\eta}{\partial T}\frac{dT}{dt} = \left(\frac{-E}{R_g T^2}\eta\right)\frac{dT}{dt} \tag{4.9}$$

Rearranging equation (4.9) and non-dimensionalizing time using a characteristic time τ, we find

$$\left(-\frac{1}{\eta}\frac{d\eta}{d(t/\tau)}\right)\left(\frac{1}{T}\frac{dT}{d(t/\tau)}\right)^{-1} = \frac{\tau_T}{\tau_\eta} = \frac{E}{R_g T} \tag{4.10}$$

The quantity $x^{-1}\,dx/d(t/\tau)$ is the dimensionless rate of change of the variable x. Therefore, the left-hand side of equation (4.10) provides the ratio of the dimensionless rate of change of viscosity to the dimensionless rate of change of temperature, which is equal to the ratio of their time constants τ_T and τ_η. For an Earth-like planet, we expect the parameters E and T to be of the order $E \approx 300\,kJ/mol$ and $T \approx 10^3\,K$, respectively. Then, using $R_g = 8.314$, we find that $\tau_T/\tau_\eta \approx 36$. A similar calculation can be performed to determine τ_χ/τ_η. Using $0.68 < r < 1$ in equation (4.5), and $300\,ppm < \chi_m < 600\,ppm$ for the mantle water concentration, one obtains $9 < \tau_\chi/\tau_\eta < 15$. Therefore, the time constant for the rate of change of viscosity is an order of magnitude smaller than the time constants for the rate of change of the temperature and water concentration. Thus, the viscosity of the system can evolve much faster than either temperature or water concentration.

We now estimate the time scale for the evolution of the viscosity in response to cooling/heating. Using equation (4.9) and substituting in $\dot{T}$ from equation (4.1) yields

$$\frac{1}{\eta}\frac{d\eta}{dt} = \frac{E}{R_g T^2}\frac{Q_s - H}{\rho C_p V} \tag{4.11}$$

In estimating the instantaneous time constant for the viscosity, we can treat the terms on the right hand side of equation (4.11) as constant, based on the above time scale analysis. Integrating with respect to time yields

$$\eta = \eta_0 \cdot exp\left((t - t_0)/\tau_\eta\right) \tag{4.12}$$

where the instantaneous time constant for the viscosity is equal to

$$\tau_\eta = \frac{R_g C_p \rho V T^2}{E(Q_s - H)} \tag{4.13}$$

Using, for example, $C_p \approx 1200\,J/kg\,K$, $\rho \cdot V \approx 3 \times 10^{24}\,kg$, $T = 1300\,K$, $E \approx 300\,kJ/mol$,

and $(Q_s - H) \approx 10 \times 10^{12}\, W$ (cooling), the time constant is then $\tau_\eta \approx 400\, My$.

The radiogenic sources (^{238}U, ^{235}U, ^{232}Th, and ^{40}K) provide heat to drive mantle convection. The time constants for their decay range from billions to tens of billions of years and may be considered a natural time scale for planetary thermal evolution. With this in mind, the viscous time scale τ_η estimated above is relatively short compared to planetary evolution time scales.

The previous arguments provide two important pieces of information: the viscosity of the system evolves faster than the temperature or water concentration and the time scale for changes in viscosity is short on planetary evolution time scales. Thus, if the sum of the terms in equation (4.3) is not close to zero, then the viscosity will change rapidly until the positive (negative) rate of change of viscosity from heat transport balances the negative (positive) rate of change of viscosity from the water cycle and $\dot{\eta} \approx 0$. For a water dependent rheology, if either the thermal state or the water cycle is out of equilibrium, i.e. either $Q_s \neq H$ or $R \neq D$, the change in viscosity will force the other out of equilibrium in order to balance the feedback terms and achieve $\dot{\eta} \approx 0$. As a consequence, non-equilibrium behavior of the water cycle can force the thermal state to be out of equilibrium as well, producing a fundamentally different evolution than the case of a water independent rheology.

This basic time scale analysis suggests that the thermal and water feedback terms should always approximately balance each other, and that $S_{WT} \approx 1$ may be a robust feature of the evolution of Earth-like planets. The result of the previous section, suggesting that $S_{WT} \approx 1$ for the present-day Earth, supports this theory.

4.6 HEAT AND WATER TRANSPORT FOR AN EARTH-LIKE PLANET

The surface heat flow Q_s and thermal plate thickness d_l are well described by kinematic thermal boundary layer theory (e.g. McKenzie and Weiss, 1975; Turcotte, 1967; Turcotte and Schubert, 1982) and are given by

$$Q_s = 2Sk_cT\left(\frac{U}{\pi L\kappa}\right)^{\frac{1}{2}} \tag{4.14}$$

$$d_l = 2\left(\frac{\kappa L}{U}\right)^{\frac{1}{2}} \tag{4.15}$$

where L is the length of the plate from ridge to subduction zone (L may be treated as an effective or average length when considering a spherical surface in 3D), S is the surface area of the planet, k_c is the thermal conductivity, κ is the thermal diffusivity, and U is the plate velocity.

Water is transported out of the mantle by degassing and is returned to the mantle by regassing. Degassing occurs primarily at ridges as melting releases water. The depth of melting depends on the mantle temperature and water concentration (e.g. Dixon et al., 2002; Hirose and Kawamoto, 1995; Hirschmann et al., 2009). If the depth of melting is given by z_m and the plate velocity by U, then the mass flow rate into the melt zone, per unit length along the ridge, is given by $\rho(U \cdot z_m)$. If a fraction F_d of water leaves the melt, then the mass flux of water, in units of $kg/s\,m^2$, due to degassing is given by

$$D = F_d\frac{z_m}{L}U\rho\chi_m \tag{4.16}$$

where χ_m is the mass fraction of water in the mantle. F_d is the degassing efficiency parameter; it is equal to unity if all water in the melt is released and is less than one otherwise. In general, F_d will be very close to 1.

Regassing of the mantle occurs via subduction of a partially hydrated slab. Water is transported to the deeper mantle mainly by hydrated basalt and serpentine layers. If the plate has a thickness of d_l, a density of ρ, and an average water concentration of χ_p, then the average mass flux of water into the mantle, per unit length along the subduction zone, is simply $\rho(U \cdot d_l)\chi_p$. However, only a fraction F_r of this water is transported to depths greater than a few hundred kilometers (Hacker, 2008; Hirschmann et al., 2005; Iwamori,

2007; Rüpke et al., 2004). The remaining fraction of water $1 - F_r$ is released at shallow depths in the mantle wedge and returns to the surface via volcanism. Thus, the mass flux of water back into the mantle, in units of $kg/s\,m^2$, is given by

$$R = F_r \frac{d_l}{L} U \rho \chi_p \tag{4.17}$$

Degassing and regassing occur simultaneously but rarely balance each other. This results in a state of net regassing or net degassing. The ratio of regassing to degassing R/D is

$$\frac{R}{D} = 2 \left(\frac{L}{d} \cdot \frac{\kappa/d}{U} \right)^{\frac{1}{2}} \frac{d}{z_m} \frac{F_r}{F_d} \frac{\chi_p}{\chi_m} \tag{4.18}$$

where we have used equation (4.15) for the plate thickness d_l. When $R/D > 1$, the mantle is gaining water, otherwise it is losing water.

Equation (4.18) indicates a negative feedback in the water system. R/D depends inversely on χ_m. Thus, as the concentration of water in the mantle decreases (during degassing), R/D increases and the system moves towards a state of net regassing. Conversely, as the concentration of water in the mantle increases (during regassing), R/D decreases and the system moves towards a state of net degassing.

The dependence of the regassing and degassing rates on the plate velocity also creates a feedback. Taking the derivative of the net regassing rate $R_{net} = R - D$ with respect to plate velocity yields

$$\frac{d}{dU} R_{net} = F_r \frac{\sqrt{\kappa L}}{L} \frac{1}{\sqrt{U}} \rho \chi_p - F_d \frac{z_m}{L} \rho \chi_m \tag{4.19}$$

In evaluating equation (4.19), we have assumed that χ_p does not depend on the plate velocity. This need not be the case, and other parameterizations of χ_p could be used. The right-hand side of equation (4.19) is negative for

$$\frac{d}{dU} R_{net} < 0 \; for \; U > U_c = \left(\frac{F_r}{F_d} \right)^2 \frac{\kappa L}{z_m^2} \left(\frac{\chi_p}{\chi_m} \right)^2 \tag{4.20}$$

where U_c is the critical plate velocity for which the sign of the feedback switches. For $U > U_c$, the sign of the derivative is negative and the net regassing of the system increases with a decreasing plate velocity. Using $F_r = 0.15$, $F_d = 1$, $\kappa = 10^{-6}\, m^2/s$, $L = 6000\, km$, $z_m = 150\, km$, $\chi_p = 2000\, ppm$, and $\chi_m = 400 ppm$, we find that $U_c \approx 0.5\, cm/year$. The sign of the derivative is therefore likely to be negative for the majority of the planet's evolution until plate speeds become very low. This feedback, along with the water concentration feedback discussed above, tends to move a system from a state of net degassing towards a state of net regassing as both the water concentration and plate speed decrease (as shown in Figure 4.1).

4.7 EVOLUTION OF AN EARTH-LIKE PLANET

In this section, we illustrate the behavior described above by means of a simple numerical model based on parameterized convection. The thermal evolution presented is only meant to illustrate the behavior that our theory predicts and is not intended to represent the specific thermal evolution of the Earth, which would involve significantly more model detail and complexity.

The arguments made in the preceding sections do not depend on the model/parameterization used for calculating the plate velocity as a function of the state of the mantle, or for calculating the amount of water transported to depth by the plate. We therefore choose to use as simple a formulation as possible to illustrate the system's behavior.

We numerically solve equations (4.1) and (4.2) for the evolution of the temperature and water concentration. Equation (4.5) couples the thermal state and water cycle through the temperature and water dependence of the viscosity. The surface heat flow and plate velocity are calculated as a function of the viscosity and mantle temperature using classic boundary layer theory. Degassing and regassing fluxes are calculated using equations (4.16) and (4.17), respectively. The depth of melting z_m is estimated using a simple linearized fit of melting depth as a function of temperature and water concentration from Hirschmann et al. (2009). Finally, we calculate the average water concentration in the plate by assuming

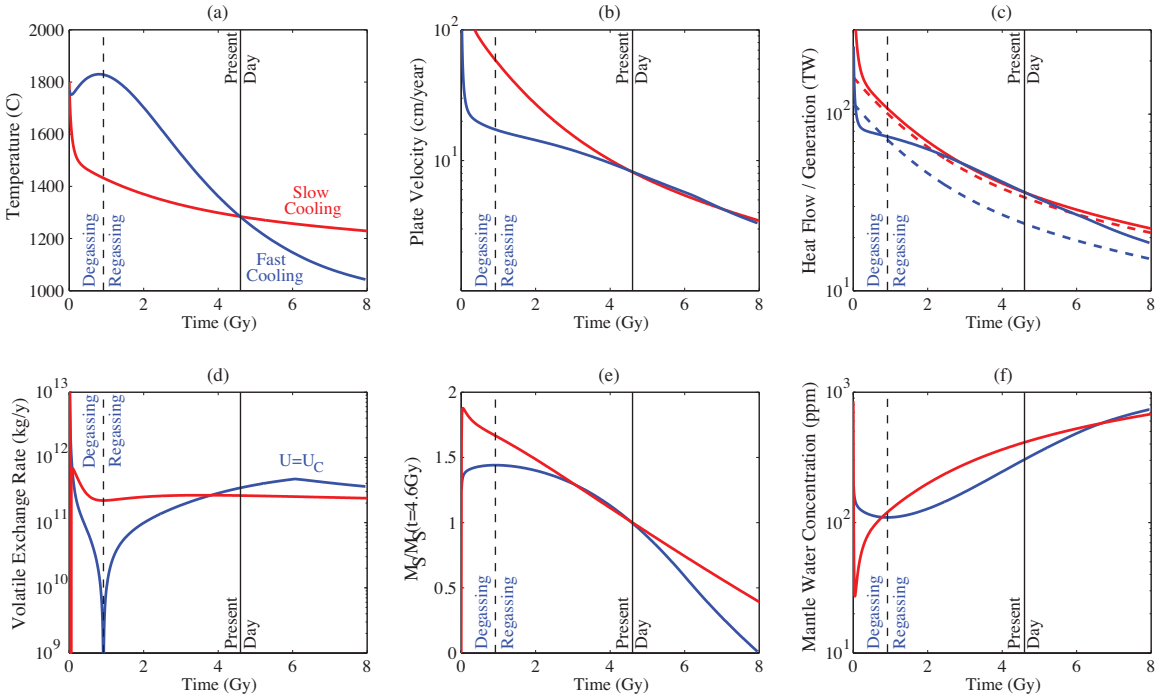

Figure 4.2: Characteristic evolution for cases W-D (blue lines) and W-I (red lines): (a) Temperature. (b) Plate velocity. (c) Surface heat flow (solid lines) and rate of internal heating (dashed lines). (d) Absolute value of the volatile exchange rate $|R-D|$. Degassing occurs during the first stage of the evolution and regassing during the later. A kink occurs in $|R-D|$ around $t \approx 6\,Gy$ as U becomes smaller than U_c (as defined in equation 4.20) and the sign of dR_{net}/dU changes. (e) Mass of surface water reservoir normalized by the present day mass of the ocean. At $t \approx 8\,Gy$, all of the water has been returned to the mantle, and no water remains on the surface. (f) Water concentration in the mantle.

that the depth of the hydrated layer increases with increasing plate age and is proportional to the thermal thickness of the plate. This is a reasonable approximation for the purpose of this example as the mineral stability of serpentine is temperature dependent and the depth of an isotherm scales with the thermal thickness of the plate. For simplicity, we assume that the exponent $n \approx 1$ as we are considering a single mantle reservoir, and it is likely that dislocation creep is restricted to the uppermost mantle (e.g. Becker et al., 2008; McNamara et al., 2001). The reader is referred to the appendix for full model details.

Figure 4.2 presents the results from two distinct model runs. The first has a viscosity that depends only on temperature (red lines) and we will refer to this case throughout as case W-I (water independent). The second case has a viscosity that depends on both temperature and water concentration (blue lines) and we will refer to this case throughout as W-D (water dependent). Water is present in the mantle for both simulations, but in the W-I case, it does not affect the viscosity. All parameter values are the same for both simulations except for the amount of internal heating and the initial amount of water. These two parameters are tuned in each case such that the surface heat flow and surface mass of the ocean at a time of $t = 4.6Gy$ are equal to $36\,TW$ and $1\,OM$ (one present day ocean mass), respectively. Both simulations begin with potential mantle temperatures of 1800^oC.

The initial phase of the evolution is qualitatively similar for both cases. At the beginning, the viscosity is low (shown in Figure 4.3a), due to the high temperature and water concentration of the mantle, and the plate velocity and heat flow are large. The large heat flow results in rapid cooling, increasing viscosity and reducing the heat flow towards the rate of internal heating. As the surface heat flow approaches the rate of internal heating, the thermal state nears equilibrium and the temperature-viscosity feedback becomes small. At this point, the W-I case switches from a state of rapid cooling to a state of slow cooling, in which $Q_s \approx H$, and the surface heat flow closely tracks the rate of internal heating for the remainder of the simulation. This behavior has been noted in classic thermal evolution calculations (for example, Davies, 1980) and results from $\dot{\eta} \approx 0$ requiring $Q_s \approx H$ when $\eta_\chi = 0$. For the W-D case, however, the surface heat flow does not stabilize as it approaches

the rate of internal heating. This is due to the influence of the water cycle on the viscosity.

As the plate velocity and water concentration are initially very large, R/D begins small and the system is in a state of net degassing (see Figure 4.2d). As the system continues to lose water the viscosity increases further since $\dot{\eta} \approx \eta_\chi \dot{\chi} > 0$ (when $Q_s \approx H$), which causes the plate velocity to continue to decrease. This drives the surface heat flow below the internal heating rate and forces the thermal state away from equilibrium, resulting in a net warming of the system. The rate of warming increases until $\dot{\eta} \approx \eta_T \dot{T} + \eta_\chi \dot{\chi} \approx 0$ and the thermal state and water cycle both evolve out of equilibrium. Note that while $\dot{\eta} \approx 0$, it is not exactly equal to zero and the viscosity does still slowly evolve.

Degassing continues to decrease the mantle water concentration χ_m, increasing R/D towards unity, and decreasing the net degassing. As R/D approaches unity, the net degassing rate approaches zero and the strength of the water feedback term $\eta_\chi \dot{\chi}_m$ becomes negligible. At this point the system operates as if the viscosity were only temperature dependent and the thermal feedback forces $Q_s \approx H$. Thus, both temperature and water concentration approach their equilibrium states at the same time. This point in time is marked with a dashed black line in Figure 4.2. However, as the rate of internal heating decreases with time, the system cools, causing a gradual increase in viscosity and a corresponding decreases in the plate velocity. The decrease in plate velocity drives R/D above unity and the system switches from a state of net degassing to a state of net regassing.

Regassing increases the water concentration of the mantle, resulting in a drop in viscosity that counteracts the increase from cooling. Again, both the thermal state and the water cycle are out of equilibrium and evolving such that $\dot{\eta} \approx \eta_T \dot{T} + \eta_\chi \dot{\chi} \approx 0$. For the W-D case, the coupling of the thermal and water feedbacks results in a much more rapid release of heat than in the W-I case, and the temperature of the mantle is not as strongly buffered by the thermal feedback. The W-D case has less internal heating than the W-I case and this difference cannot be used to explain either the warmer evolution or the more rapid cooling of the W-D case.

A kink occurs in the W-D case late in the evolution as the plate velocity falls beneath

the critical velocity calculated in section 4.6 and the feedback between plate velocity and net regassing changes sign. At this point the water cycle feedback becomes less efficient and the thermal feedback begins to dominate. This leads to a positive water cycle feedback that reduces both the regassing rate and the plate velocity.

The system begins in a state of degassing and moves to a state of regassing. Regassing decreases the mass of water in the surface reservoir, returning water to the mantle, and eventually removing the surface ocean. This occurs in Figure 4.2e at $t \approx 8\,Gy$ for the W-D case. Thus, the W-D evolution results in a cool planet with a dry surface. We do not calculate the future evolution of such a system.

These sample model runs are presented to illustrate the significant differences that arise from the addition of the water cycle. The results shown in Figure 4.2 are representative of the behavior of a large number of numerical simulations that we performed (not shown). The calculations begin with a period of rapid adjustment in which $\dot{\eta}$ approaches zero. Afterwards, if the mantle is sufficiently hydrated, a period of degassing and warming occurs followed by a period of regassing and cooling. If the mantle begins with little water content, the initial phase of rapid adjustment is followed directly by an evolution in which the mantle regasses and cools. Clearly, the timing of events and magnitude of variables in the evolution will depend on the parameter values used and the details of both the dynamical model and the degassing/regassing parameterizations. However, the basic feedbacks described here are likely to govern. A large number of thermal history calculations for the Earth that include water cycling are presented by Sandu et al. (2011) and, while differing slightly in their parameterizations and specific model results, agree well with our theory.

4.8 DISCUSSION

Figure 4.3c shows the calculated value of the relative strength number S_{WT} using the output from the W-D case illustrated in Figure 4.2. After a brief period of adjustment, the dimensionless parameter S_{WT} is close to unity and the rate of change of viscosity due to the thermal feedback is closely balanced by the rate of change of viscosity from the water

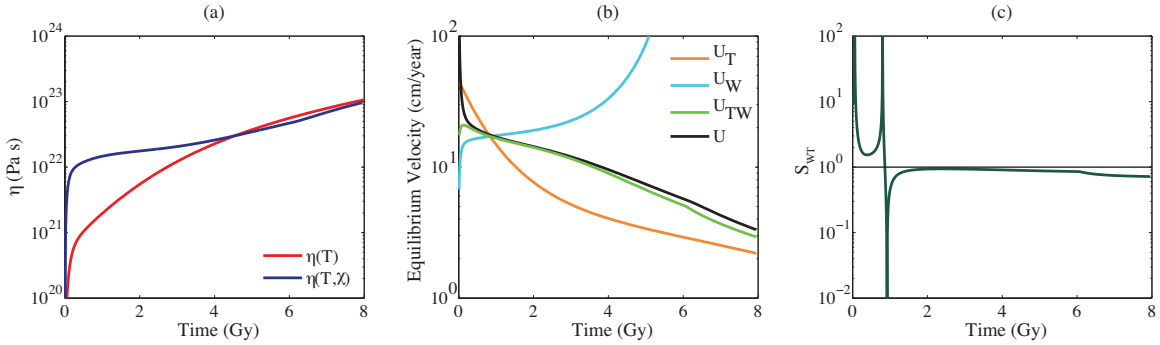

Figure 4.3: (a) Mantle viscosity for the W-D (blue) and W-I (red) cases. (b) Simulation plate velocity U (black) and theoretically determined plate velocities U_T (orange), U_W (light blue), and U_{TW} (green). As expected, $U \approx U_{TW}$ for all times after an initial period of rapid adjustment. (c) Relative strength number S_{WT} evaluated using the output from the sample evolution calculation shown in Figure 4.2. Note that S_{WT} is almost identically unity. Singularities occur, by definition, when $Q_S = H$.

cycle feedback (note that singularities in S_{WT} occur, by definition, when $Q_s = H$).

The fact that $S_{WT} \approx 1$ and $\dot{\eta} \approx 0$ can be used to calculate a kinematic relation for the plate velocity. This only requires that the assumptions stated in section 4.2 are reasonable. We can define a plate velocity U_T for a system with a viscosity that only has a temperature dependence and a plate velocity U_{TW} for a system with both temperature and water dependence. U_T is then found by solving for the plate velocity for which $\dot{\eta} = 0$ in equation (4.3) with $\eta_\chi = 0$. This plate velocity corresponds to the plate velocity for which $Q_s = H$ and thermal equilibrium is achieved. We also define an equilibrium velocity U_W for a system with a viscosity that only has a dependence on water concentration. This will be useful in understanding how the two feedbacks affect plate velocity. U_W is found by solving for the plate velocity for which $\dot{\eta} = 0$ in equation (4.3) with $\eta_T = 0$. U_W represents the plate velocity for which $R = D$ and the water cycle is in equilibrium. U_{TW} corresponds to a plate velocity for which $\dot{\eta} = 0$ but with neither the thermal state or water cycle in equilibrium. See Appendix C.2 for details.

Figure 4.3b plots U_W (light blue), U_T (orange), and U_{TW} (green) using the output for T, χ_m, H, Q_s, R, and D from the W-D case. The simulation plate velocity U is also plotted

(black line) and, after an initial period of rapid adjustment, it agrees very well with the predicted plate velocity U_{TW}. Note that while the plate velocity U depends on a specific dynamic parameterization for plate speed (used in the simulation), U_{TW} does not and is predicted by solving for the plate velocity that gives $\dot{\eta} = 0$.

U_{TW} is forced to lie between U_T and U_W such that the signs of the two feedback terms in equation (4.3) are opposite. U_{TW} is initially lower than U_T and higher than U_W. $U_{TW} < U_T$ corresponds to $Q_s < H$ and the system warms. $U_{TW} > U_W$ corresponds to $D > R$ and there is a net degassing of the mantle. U_{TW} provides the expected plate velocity for the system and the magnitude of U_{TW}, relative to U_T and U_W, provides information on the state of heat and water transport. The predicted curves for U_T and U_W cross at a time t_c when both the thermal state and the water cycle are in equilibrium. The system then evolves to a state of cooling and regassing.

Using $\dot{\eta} \approx 0$ in equation (4.3) allows us to write

$$\eta_\chi \dot{\chi}_m \approx -\eta_T \dot{T} \tag{4.21}$$

Equation (4.21) simply relates, through the temperature and water dependence of the viscosity, the rate of change of temperature and water concentration in the mantle and shows the strong coupling that exists. Furthermore, the signs of the terms on the right and left hand sides of equation (4.21) only match if the system is degassing while warming or regassing while cooling. Thus, our theory predicts that degassing while cooling or regassing while warming are not consistent with evolutions that are longer than the time scale for the rate of change of the viscosity. The mantle may only cool once regassing begins, which suggests that as an Earth-like planet cools, its surface ocean is emptied and water eventually returns to the mantle. This is consistent with some estimates of the water fluxes for the present-day Earth (Hacker, 2008; Iwamori, 2007; Parai and Mukhopadhyay, 2012).

The viscosity cannot respond instantaneously to changes in the rate of, for instance, internal heating, temperature, or water concentration, but instead takes a finite amount

of time that is of the order of the viscosity time constant τ_η (equation 4.13). Thus, we expect a temporal lag in the dynamics of the system that can be reasonably approximated by $\Delta t \approx \tau_\eta$. Figure 4.3b shows that the simulation plate velocity U begins to depart from the theoretically predicted plate velocity U_{TW} and that the lag in time is approximately $400\,Ma$ at a time $t = 4.6\,Gy$, in agreement with the estimate made in section 4.5.

Setting $\dot{\eta} \approx 0$ in equation 4.3 and solving for the Urey ratio, $U_r = H/Q_s$, yields

$$U_r \approx 1 - \frac{\eta_\chi}{\eta_T}\frac{C_p}{Q_s}(R - D) \tag{4.22}$$

If the mantle viscosity were to only depend on temperature, $\eta_\chi = 0$ and equation (4.22) would reduce to $U_r \approx 1$. U_r would not be exactly one as the surface heat flow lags behind (and remains higher than) the decreasing rate of internal heating by a time that is governed by the viscosity time constant. The lag in time between the surface heat flow and the internal heating rate results in a Urey ratio that is smaller than expected from equation (4.22). Models that do not include the dependence of viscosity on water content will therefore approach a Urey ratio that is close to, but less than one. If the viscosity does depend on water content, equation (4.22) clearly demonstrates that the water cycle can further decrease the Urey ratio when the system is regassing ($R - D > 0$).

For the Earth, equation (4.22) may offer a partial solution to the apparent discrepancy in Urey ratio estimates that arise from geochemical ($U_r \sim 0.2 - 0.3$) and most reasonable geophysical models ($U_r > 0.6$) (see for example Korenaga, 2008). There is a limited amount of heat that can be released over the evolution of the Earth. Admitting both a low present day Urey ratio and an acceptable thermal evolution requires: (1) a high present day heat flow with a small amount of internal heating and (2) a reduced or regulated heat flow in the past. (1) provides the low Urey ratio and (2) ensures that heat is retained early in the evolution and is available to supply the elevated (non-equilibrium) present day heat flow.

Using a present day net regassing rate of $R - D = 4 \times 10^{11}\,kg/yr$ (within current bounds estimated by Parai and Mukhopadhyay (2012)) and $E = 300\,kJ/mol$, $r = 0.68$,

$\chi_m = 300\,ppm$, $C_p = 1200\,J/kg \cdot K$, $Q_s = 36\,TW$, and $T = 1300\,K$, equation (4.22) gives $U_r = H/Q_s = 0.31$. Thus, regassing of the mantle provides a natural mechanism to drive the thermal state out of equilibrium, allowing for elevated cooling rates and a low Urey ratio, and satisfying (1) above. The analytic results of section (4.6) suggest a transition from an early state of degassing and warming to a subsequent state of regassing and cooling (this is also seen in the simple evolution of Figure 4.2) and may help to satisfy (2) by retaining heat early in the evolution and allowing it to be released later.

We have used a simple parameterization for the regassing flux that assumes that the depth of hydration is proportional to the thickness of the plate. The feedback would be less effective if hydration were controlled by mid-ocean ridge processes and if the total amount of water in the plate were independent of the plate age and thickness. However, it has also been suggested that the total amount of water retained by the mantle, and thus the regassing efficiency F_r, is likely to depend on and increase with the age of the plate (Rüpke et al., 2004). This would act to amplify the feedback of the water cycle by increasing F_r as U decreases (see equation (4.18)).

Other important features that characterize the Earth and its evolution, such as a depth dependent viscosity, strong plates, mantle plumes, heat flow from the core, treatment of different convective regimes (plate tectonics, stagnant-lid, magma ocean) and transitions between them, mixing, and multiple reservoirs were not considered. Changes in mantle viscosity will alter the contrast in strength between the plate and the mantle and may result in complex behavior through plate-mantle coupling (Crowley and O'Connell, 2012). Furthermore, differential partitioning of water between multiple reservoirs (upper mantle, transition-zone, lower mantle) or inefficient mixing may modify the time constants associated with water transport, and therefore also the strength and timing of the feedbacks. To provide meaningful values, a thermal evolution calculation for the Earth should incorporate all of the above features, which is beyond the scope of this study. While including such complexities would certainly add to the richness of the dynamics, the basic feedbacks presented here are still expected to govern.

4.9 CONCLUSIONS

In this study, we have considered a simple planet with plate tectonics and a mantle viscosity that is dependent on both temperature and water concentration. A dimensionless parameter S_{WT} was derived, defined as the ratio of the rate of change of viscosity due to the water feedback to the rate of change of viscosity from the thermal feedback, and provides a quantitative measure of the relative importance of the two cycles on the dynamics of the system.

We then demonstrated, through an analysis of time scales, that the mantle viscosity for an Earth-like planet changes faster than either temperature or water concentration. This implies that $S_{WT} \approx 1$ should be a robust result, for times greater than the viscosity time constant, and that water transport is then just as important in regulating the dynamics as heat transport. We have showed that $S_{WT} \approx 1$ for the present-day Earth, assuming a plausible range of values for all parameters.

One of the most general results of the study is that $\eta_\chi \dot{\chi}_m \approx -\eta_T \dot{T}$, which relates the rate of change of temperature to the rate of change of water concentration in the mantle. This connection was further extended to demonstrate that the water cycle feedback leads to the lowering of the Urey ratio while the mantle is in a state of net regassing. The theory suggests that, over long time scales, the system should warm while degassing or cool while regassing. The other combinations, warming while regassing or cooling while degasssing are therefore not compatible states. This characteristic behavior was illustrated through the evolution of a simplified parameterized convection model. The exact evolution of the mantle temperature and water concentration will depend on the specific parameterizations for heat flow, degassing, and regassing. Given the large uncertainties associated with these processes, we do not attempt here to construct specific models of the evolution of the Earth. Nevertheless, the general results described here should provide guidance for such models, as well as for models of other planets whose evolution may depend on convection and recycling of volatiles that affect rheology.

The purpose of this study was to address, through the use of an analytic model, how feedbacks induced by the temperature and water dependance of the viscosity play a role in planetary dynamics and evolution. The theory provided in this paper has demonstrated that the water cycle can have a significant effect on the dynamics of such a system. Conversely, heat flow also has a strong effect on the dynamics of the water cycle. Addressing either heat or water transport therefore requires the simultaneous treatment of both the thermal evolution and the water cycle.

Chapter 5

Thermal evolution of early solar system planetesimals and the possibility of sustained dynamos

In this Chapter we consider the possible presence and longevity of a stable dynamo powered by thermal convection in early solar system planetesimals. We model the thermal evolution of planetesimals starting from an initially cool state. After melting, core formation, and onset of mantle convection have occurred we employ thermal boundary layer theory for stagnant lid convection to determine a cooling rate and thermal boundary layer thickness that are dynamically self consistent. We assess the presence, strength and duration of a dynamo for a range of planetesimal sizes and other parameters. We will demonstrate that the duration of a dynamo depends foremost on the planetesimal's radius and that bodies smaller than ~ 500 km will be unable to maintain a sufficiently strong dynamo for a duration of the order of ten million years. We will also show that dynamo duration, to a lesser extent, also depends on the effective temperature dependence of the mantle viscosity and on the rotation rate of the body. These dependencies will be made explicit through the derivation of an analytical approximation for the dynamo duration.

This work is part of a collaborative effort with Glenn Sterenborg. An amended version of this Chapter will be submitted to the journal Physics of the Earth and Planetary Interiors.

5.1 INTRODUCTION

Our solar system began when the first solids condensed in the Sun's protoplanetary disk and the subsequent dust grains collected to form the first small bodies orbiting the Sun. Either by means of gravitational instability (Cuzzi et al., 1993; Youdin and Shu, 2002) or through gradual aggregation (Weidenschilling and Cuzzi, 1993) solid bodies several kilometers in size, planetesimals, were generated (Chambers, 2004). In a process called runaway growth, gravitational focusing and dynamic friction then served to accrete these planetesimals together, dwindling their numbers to a handful of oligarchic planetary embryos with masses between 0.01 to 0.1 Earth masses (Chambers, 2004; Thommes et al., 2003). Gravitational interactions between the oligarchs led to massive collisions, ultimately forming the final terrestrial planets.

Of the eight planets, five dwarf planets, hundreds of moons and countless small solar system bodies, thus far only a handful have been observed to possess a dynamo generated magnetic field at one time (Stevenson, 2003). The understanding of the timing, origin as well as the processes governing these dynamos, remains incomplete. However, in recent literature an avenue of research has emerged which may yield new insights as paleomagnetic arguments have been presented in support of early dynamos in meteorite parent bodies (Weiss et al., 2008; Weiss et al., 2010). Uniformly magnetized angrites, i.e. achondritic meteorites, revealed the potential for an angrite parent body with an internally generated magnetic field present during their formation with an intensity up to a few tens of microtesla (Weiss et al., 2008; Weiss et al., 2010). Building on this work, and relying on continuous accretion of new chondritic material, a further argument was made in favor of a differentiated planetesimal sustaining a dynamo whilst maintaining an undifferentiated outer crust in accordance with observations of magnetized CV chondrites (Elkins-Tanton et al., 2011). Such early solar system planetesimals may thus represent novel realizations of planetary dynamos which may add to our understanding of them.

Several conditions must be met for a planet(esimal) to have a dynamo. The body

must contain a sufficiently electrically conducting fluid layer. This fluid must experience convective motions with enough vigour to render the magnetic Reynolds number $Re_m = u_c l/\lambda > O(10 - 10^2)$, where u_c and l are the characteristic fluid speed and length scale, respectively. l is typically chosen as the depth of the fluid layer, however, an appropriate choice of u_c depends on the dominant force balance in the fluid layer (Christensen, 2010). $\lambda = 1/\mu_0\sigma$ is the magnetic diffusivity, μ_0 is the vacuum magnetic permeability and σ is the electrical conductivity. A source of energy must be present to maintain these convective motions against ohmic dissipation in the fluid (Buffett, 2002; Gaidos et al., 2010; Monteux et al., 2011). This can take the form of a heat flow out of the layer that exceeds the amount of heat that can be transported conductively (for a thermally driven dynamo), or a release of latent heat and the expulsion of light, buoyant elements during iron solidification (for a compositionally driven dynamo).

It is thus clear that any investigation into the presence and duration of a planetary dynamo ultimately reduces to several key questions. Did the body experience enough heating to segregate the metal and silicate and form a liquid core? Is the body cooling sufficiently fast to provide a source of energy for convective motions in the core? An understanding of a body's thermal history is therefore paramount to any dynamo investigation.

The thermal evolution of an early solar system planetesimal is governed by several factors. The start time (relative to the formation time of CAIs) and rate of accretion of a planetesimal determines the amount of short-lived radionuclides, ^{26}Al and ^{60}Fe (Urey, 1955), that are present and contribute to internal heating, possible melting and differentiation of the body. Furthermore, the accretion rate, and how it is treated in models, impacts the peak central temperatures in the body, i.e., the maximum temperature the planetesimal cools down from (Merk et al., 2002). To what extent, and how fast the planetesimal experiences melting (Ghosh and McSween, 1998; Hevey and Sanders, 2006; Sahijpal et al., 2007) sets the stage for planetesimal differentiation and core formation (Ghosh and McSween, 1998; Gupta and Sahijpal, 2010; Sahijpal et al., 2007; Senshu et al., 2002). In practice, this sequence of events may have occurred, to some degree, simultaneously (Merk et al., 2002). The dynamics

and time scales of metal-silicate separation and core formation has been the subject of much debate (Golabek et al., 2008; Monteux et al., 2009; Ricard et al., 2009; Samuel et al., 2010; Stevenson, 1990) and will not be treated here. Models of planetesimal thermal evolution tend to solve the 1D heat transport equation in some form (Elkins-Tanton et al., 2011; Ghosh and McSween, 1998; Hevey and Sanders, 2006; Merk et al., 2002; Sahijpal et al., 2007; Weiss et al., 2008; Weiss et al., 2010), and convection in the post-differentiated mantle, if treated at all, is approximated by increasing the thermal diffusivity in the mantle by several orders of magnitude at a certain melt or temperature threshold (Gupta and Sahijpal, 2010; Hevey and Sanders, 2006). Furthermore, these models either fix the thickness of the outer conducting thermal boundary layer (often referred to as the 'lid') or assume a steady state process in order to determine its thickness. Neither of these approaches should be used when addressing the transient (warming/cooling) state of the planetesimal.

The present work has several objectives. By explicitly accounting for mantle convection we determine the thickness of the outer thermally conducting boundary layer that is dynamically self-consistent with the convective heat flow from the interior of the planet(esimal). We construct a thermal evolution model and address the requirements for the presence of a thermally driven dynamo and the key model parameters involved in determining its longevity for a range of planetesimal sizes. We then evaluate specific scenarios suggested in the literature in support of the hypothesis that carbonaceous chondrites are the remains of the crust of a partially differentiated magnetized body (Elkins-Tanton et al., 2011; Sahijpal and Gupta, 2011).

Before discussing our model we present a simple energy balance calculation that places lower bounds on the size of a planetesimal that is able to support a dynamo of a specified minimum magnetic field strength and duration. Given a specified accretion age for a planetesimal we can *a priori* calculate the maximum temperature change $\Delta T_{max} = T_c - T_i$, above the initial temperature of the core T_i, if we assume that all available heating went into warming the core and neglect any latent heat effects. Clearly this is an upper bound for ΔT_{max} as some heat would have been lost due to cooling and heat would be also be re-

quired to warm the mantle and overcome any latent heat requirements. A simplified energy balance then yields

$$\rho_c V_c C_{p_c} \Delta T_{max} = M_p \frac{H_0 C_0}{\lambda_{Al}} e^{-\lambda_{Al} t_a} \tag{5.1}$$

where ρ_c, V_c, and C_{p_c} are the core density, volume and specific heat, respectively, M_p is the mass of the planetesimal, H_0 is the internal heating rate of ^{26}Al, and C_0 is the concentration of ^{26}Al in units of kg per unit kg of planetesimal. t_a is the time after CAI at which accretion occurs (assumed instantaneously) and λ_{Al} is the decay constant of ^{26}Al. The right hand side represents the energy provided by radiogenic heating. This can be simplified to

$$\Delta T_{max} = \left[1 + \frac{\rho_m V_m}{\rho_c V_c}\right] \frac{H_0 C_0 e^{-\lambda_{Al} t_a}}{C_{p_c} \lambda_{Al}} \tag{5.2}$$

where we have used $M_p = \rho_m V_m + \rho_c V_c$ for the mass of the planetesimal. Equation (5.2) gives an upper bound on the temperature that the core could reach with the available energy from internal heating. Figure 5.1 plots ΔT_{max} (black lines) for accretion times of $t_a = 0$ Myr, $t_a = 1$ Myr, and $t_a = 2$ Myr.

We now consider the minimum core temperature change ΔT_{min} required to maintain a minimum heat flux of $F_{c_{min}}$ from the core for a duration of time Δt. This is simply

$$\Delta T_{min} = \frac{A_c F_{c_{min}}}{\rho_c V_c C_{p_c}} \Delta t \tag{5.3}$$

where A_c is the core surface area.

Different scaling laws may be deemed appropriate to estimate the core convective speed u_c depending on the leading order force balance in the core (Christensen, 2010). In all cases (see Appendix D.5 for scaling laws) the core convective speed is related to the core convective heat flux F_c. We can relate the magnetic Reynolds number Re_m to F_c through their dependence on u_c and obtain a minimum core temperature change for a given minimum (critical) magnetic Reynolds number. For example, using a scaling law based on the

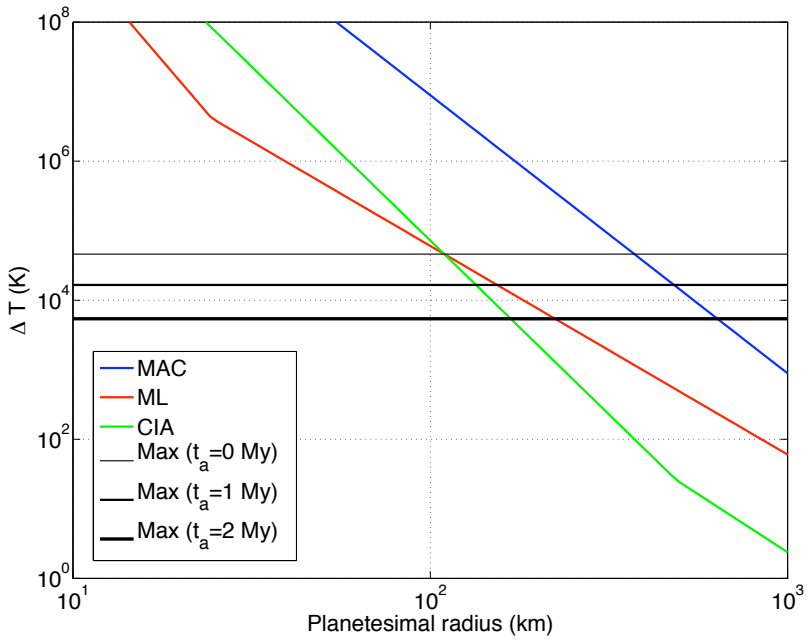

Figure 5.1: Calculation of the maximum dynamo time using a simple energy balance argument. The horizontal black lines represent the maximum achievable temperature in the core above its melting temperature for different accretion times. The minimum required core temperature for a dynamo of magnetic field strength 20 μT that persists for 10 Myr is indicated by the colored lines. The blue line is based on a scaling law which derives from a balance between magnetic, buoyancy and Coriolis forces in the core. Similarly, the red and green lines are based on mixing length theory (ML) and a force balance between Coriolis, inertial and buoyancy forces (CIA). The rotation period is 10 hours and the critical magnetic Reynolds number required for a dynamo is 10.

balance between the magnetic, buoyancy and Coriolis forces (MAC) we can express the core convective speed as (Christensen, 2010)

$$u_c = \left(\frac{4\pi G \alpha_c r_c F_c}{3\Omega c_{p,c}} \right)^{1/2} \tag{5.4}$$

which, using the definition of the magnetic Reynolds number $Re_m = u_c r_c / \lambda$, can be recast as

$$F_{c_{min}} = (Re_m \lambda)^2 \frac{3 c_{p,c} \Omega}{4\pi G \alpha_c r_c^3} \tag{5.5}$$

$F_{c_{min}}$ is the minimum heat flux required to achieve a magnetic Reynolds number of Re_m. We can substitute this into equation (5.3) to obtain

$$\Delta T_{min} = \frac{9\Omega}{4\pi G \alpha_c \rho_c} \frac{(Re_m \lambda)^2}{r_c^4} \Delta t \tag{5.6}$$

ΔT_{min} in equation (5.6) is the minimum core temperature drop required to maintain a magnetic Reynolds number of Re_m for a duration of Δt. Note the strong r_c^{-4} dependence on the core radius. Thus, a factor of 3 decrease in core radius would require an initial core temperature approximately 100 times larger to maintain the same magnetic Reynolds number for the same duration.

By assuming that the thermodynamically available power per unit volume is completely converted to magnetic energy we can write (Christensen, 2010)

$$\frac{B^2}{2\mu_0} \sim \frac{r_c}{u_c} \frac{\alpha_c g_c F_c}{c_{p,c}} \tag{5.7}$$

where we have used the core radius for the length scale l. We can now solve for the heat flux in terms of a minimum magnetic field strength B_{min} and use equation (5.3) to relate the minimum core temperature change to B_{min} and the duration Δt

$$\Delta T_{min} = \frac{9 B_{min}^4}{16 \mu_0^2 \pi \alpha_c G \Omega \rho_c^3 r_c^4} \Delta t \tag{5.8}$$

ΔT_{min} in equation (5.8) is the minimum core temperature drop required to maintain a magnetic field strength of B_{min} for a duration of Δt.

In Figure 5.1 we also plot (colored lines) ΔT_{min} required to obtain a core dynamo ($Re_m \geq Re_{m,cr}$) with a magnetic field strength of $B_{min} \sim 20$ μT and for a duration of $\Delta t \sim$10 Myr (Weiss et al., 2008; Weiss et al., 2010), where we choose the ΔT_{min} that is the larger of equations (5.6) and (5.8) such that both magnetic Reynolds number and magnetic field strength conditions are satisfied. Similarly, we plot the results for the two other scaling laws that are often used in the literature (Christensen, 2010). For a particular accretion time and choice of scaling law the permissible area in this plot is below the black line (maximum core temperature that could be reached) and above a colored line (minimum temperature required to release enough heat). Hence, the very simplified energy balance represented in this plot indicates that the minimum required radius is approximately 100 km if it is to have a dynamo of sufficient strength and duration for an accretion time of 0 Myr. A more restrictive scenario is for an accretion time of 2 Myr and the MAC scaling law, for which the minimum planetesimal radius becomes approximately 650 km. Furthermore, any energy consumed by warming the mantle, overcoming latent heat, and cooling at the surface of the planetesimal will subtract from the energy available to warm the core and for a realistic case we expect ΔT_{max} to be less than indicated in Figure 5.1. The extent to which ΔT_{max} is reduced will depend on the amount of cooling that occurs and properly accounting for this is one of the primary goals of this study. Overall, this exercise suggests that we need not look for meteorite parent bodies smaller than 100 km with an internally generated magnetic field that can last for millions of years. Nonetheless, in the more sophisticated approach below we will seek to confirm this tentative envelope by investigating the range of possible sizes from 25 to 1000 km radius.

Our approach is to start with an initially cool chondritic body that has accreted all of its mass. Its accretion age will determine how much of the short-lived radionuclides remain, the decay energy of which will heat up the planetesimal until a critical temperature is reached and differentiation, along with core formation, is thought to occur. The body will continue

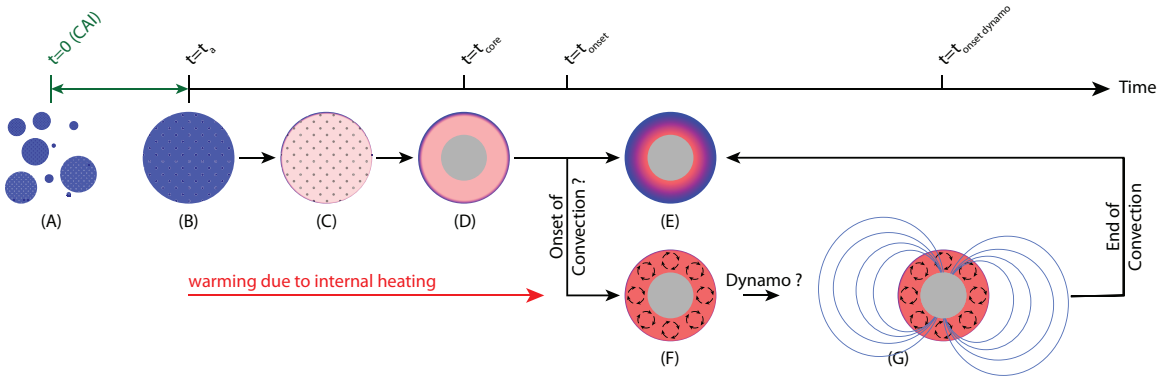

Figure 5.2: Stages of Planetesimal evolution.

to warm until thermal convection sets in. The thermal state of the planetesimal at this time is considered the initial state with which we start our thermal evolution models. We carry out such thermal evolutions for a range of parameters: planetesimal radius, core radius, mantle reference viscosity, accretion age, critical melt fraction and temperature dependence of viscosity. For each case we assess if a dynamo is present, its mean and peak magnetic field strength, and its duration. We compile these results and compare them with analytical predictions for dynamo duration and discuss the relevant parameters.

5.2 MODEL

5.2.1 THE INITIAL STATE

In this study we are primarily interested in whether a planetesimal can develop and maintain a thermally driven dynamo. A thermally driven dynamo requires the transport of heat out of the core and therefore core cooling. As such, any phase during the thermal evolution of a planetesimal prior to secular cooling is only of interest to us insofar as it provides information regarding the planetesimal's initial state just before cooling. We define the start of secular cooling as the time at which the total surface heat flow out of the planetesimal exceeds radiogenic heating integrated over the volume of the planetesimal. We first consider the evolution during the warming phase that leads to the initial state for secular cooling.

Figure 5.2 shows the various stages of development a planetesimal is thought to go

through from rapid accretion to ultimately conductively cooling down. The manner in which a planetesimal undergoes accretion determines its thermal state to a great extent (Kaula, 1979). There exists a trade-off between heating of the planetesimal by short-lived nuclides and surface cooling, mediated by the rate of accretion. A rate that is high relative to surface cooling will allow the body to heat up and may lead to a certain degree of melting (Kleine et al., 2002; Yoshino et al., 2003), whereas a relatively low rate may leave the body undifferentiated. In the latter case a core never forms and a dynamo is not possible. We do not consider other sources of energy to heat the planetesimal such as impact heating, which have been treated elsewhere (Monteux et al., 2011), or accretional heating which yields enough energy to only marginally increase the temperature in the planetesimal (Elkins-Tanton et al., 2011). In the present work we assume instantaneous accretion. By 'instantaneous' we simply mean that the time scale involved is very small compared to the time scales of millions to tens of millions of years that we are interested in. The error we incur by making this assumption is to slightly overestimate the peak central temperature in the planetesimal during accretion (Merk et al., 2002). This will not extend or shorten the duration of any dynamo, instead it will simply delay its development. In the following section we will explain why it is unlikely that continuous accretion will permit any thick outer layer of undifferentiated material to persist for a planetesimal that also maintains a dynamo, as suggested by Elkins-Tanton et al. (2011); Gupta and Sahijpal (2010).

We assume a planetesimal with a chondritic composition (see Table 5.1 for material properties and glossary) at an initial temperature equal to the ambient nebular temperature of approximately 250 K (Woolum and Cassen, 1999). For heating by short-lived nuclides we only consider that by uniformly distributed ^{26}Al, which has a half-life of $\sim$0.73 Myr, a decay energy of 3.12 MeV (Castillo-Rogez et al., 2009) and an initial ^{26}Al/^{27}Al ratio of 5×10^{-5} (MacPherson et al., 1995) . We neglect ^{60}Fe as its energetic contribution is relatively small. As the core radius is a free parameter in our model the metal-to-silicate ratio is assumed to support this.

As the system radiogenically heats up, the interior temperature uniformly increases as a cold thermal boundary layer of thickness D grows diffusively inward. The thickness of this boundary layer can be estimated with the simple diffusion relation $D \sim \sqrt{\kappa t}$ where κ is the thermal diffusivity and t is time after accretion. At a temperature of approximately 700 K sintering occurs at which time the initially porous body loses its porosity and decreases in volume (Hevey and Sanders, 2006; Sahijpal et al., 2007). As this plays no role in the consideration of dynamo presence and duration we do not consider the details of sintering. If the planetesimal's accretion time is sufficiently small, there will likely be enough ^{26}Al to guarantee partial to complete differentiation and the formation of an iron core, see (D) in Figure 5.2. At around the eutectic temperature of the Fe-FeS system, 1213 K (Ghosh and McSween, 1998; Larimer, 1995), but depending on the sulfur content (Neumann et al., 2012), the metal fraction of the chondritic body will start to melt. We assume core formation to occur instantaneously and any remaining ^{26}Al will segregate into the differentiated silicate mantle leaving the core without radiogenic heating. Naturally, we are only interested in planetesimals in which a core forms. Following the formation of a core there are two possible warming phases that could occur based on the development or absence of thermal convection in the silicate mantle.

The conductive case

To gain insight into the conductive cooling rate of a planetesimal we can consider the simple cooling of a sphere of radius a, uniform initial temperature T_i, surface temperature $T_s = 0$, and thermal properties equivalent to our planetesimal. The solution, as a function of time and radial position is given by (Carslaw and Jaeger, 1986)

$$T(r,t) = \frac{2aT_i}{\pi r} \sum_{n=1}^{\infty} \frac{(-1)^{n+1}}{n} \sin\left(\frac{n\pi r}{a}\right) e^{-\kappa n^2 \pi^2 t/a^2} \tag{5.9}$$

Parameter	symbol	value	dimensions	source
Radius of planetesimal	r		km	-
Radius of core	r_c		km	-
Time of accretion after CAI	t_a			
Gravity	g	$4\pi Gr\rho$	m s^{-2}	-
Aluminium-26 percentage by mass	ψ_{26}	0.9	%	(Hevey and Sanders, 2006)
$^{26}Al/^{27}Al$ ratio	$c_{26/27}$	5×10^{-5}	-	(Sahijpal et al., 2007)
Decay energy ^{26}Al	d_{Al26}	6.4×10^{-13}	J $atom^{-1}$	(Hevey and Sanders, 2006)
Half life ^{26}Al	τ_{Al}	0.73	Ma	ibid.
Activation energy	E	300	kJ $mole^{-1}$	ibid.
Density of core	ρ_c	9000	kg m^{-3}	(Nimmo and Stevenson, 2000)
Specific heat capacity of core	$c_{p,c}$	800	J kg^{-1} K^{-1}	ibid.
Temperature of core	T_c		K	-
Thermal expansivity of core	α_c	2×10^{-5}	K^{-1}	ibid.
Thermal diffusivity of core	κ_c	8×10^{-6}	m^2 s^{-1}	ibid.
Thermal conductivity of core	k_c	43-88	W m^{-1} K^{-1}	ibid.
Magnetic diffusivity of core	λ	1.3	m^2 s^{-1}	-
Magnetic permeability of core	μ	$4\pi \times 10^{-7}$	N A^{-2}	-
Electrical conductivity of core	σ	5×10^{-4}	S m^{-1}	(Weiss et al., 2008)
Viscosity of core	η_c	0.001	Pa s	-
Latent heat of core	L_c	4×10^5	J kg^{-1}	(Ghosh and McSween, 1998)
Density of mantle	ρ_m	3400	kg m^{-3}	(Nimmo and Stevenson, 2000)
Specific heat capacity of mantle	c_p	1200	J kg^{-1} K^{-1}	ibid.
Temperature of mantle	T_m		K	-
Thermal expansivity of mantle	α	4×10^{-5}	K^{-1}	ibid.
Thermal diffusivity of mantle	κ	8×10^{-7}	m^2 s^{-1}	ibid.
Thermal conductivity of mantle	k	4	W m^{-1} K^{-1}	(Reese and Solomatov, 2006)
Latent heat of mantle	L_m	4×10^5	J kg^{-1}	(Ghosh and McSween, 1998)
Silicate solidus temperature	$T_{m,s}$	1425	K	(Hevey and Sanders, 2006)
Silicate liquidus temperature	$T_{m,l}$	1850	K	ibid.
Melt fraction in mantle	ϕ			
Critical melt fraction in mantle	ϕ_{crit}	0.3 - 0.5		
Reference viscosity of mantle	$\hat{\eta}_o$	10^{21}	Pa s	(Reese and Solomatov, 2006)

Table 5.1: Parameter values for thermal evolutions of planetesimals.

The heat flux for the cooling sphere at depth r can be derived from the above equation and is

$$\begin{aligned} q(r,t) &= 2\frac{kT_i}{a}\sum_{n=1}^{\infty}\left(\frac{a}{r}\right)^2\left[\frac{(-1)^{n+1}}{\pi n}\sin\left(\frac{n\pi r}{a}\right)\right. \\ &+ \left.\frac{r}{a}(-1)^n\cos\left(\frac{n\pi r}{a}\right)\right]e^{-\kappa n^2\pi^2 t/a^2} \end{aligned} \tag{5.10}$$

The heat flux at the surface ($r = a$) is

$$q_s(t) = 2\frac{kT_i}{a}\sum_{n=1}^{\infty}e^{-\kappa n^2\pi^2 t/a^2} \tag{5.11}$$

This series converges for all times $t > 0$. The dominant time constant (for $n = 1$) for cooling in equations (5.9) through (5.11) is $\tau = \kappa^{-1}(a/\pi)^2$. The time constant for a planetesimal with a radius of 100 km, conductivity $k = 4$ W/m/K, and thermal diffusivity $\kappa = 10^{-6}$ m^2/s is $\tau = 32$ Myr. For an initial temperature of $T_i = 1800$ K the maximum heat flux occurs at the surface and is equal to 0.6 W/m^2 at a time of $t = 1$ Myr after the start of cooling.

With the above heat flux (an overestimate since the heat flux at depth will be less), a core radius of $r_c = a/2$, a rotation period of 10 hours, and typical values for core density, specific heat and magnetic diffusivity, see Table 5.1, we obtain with the MAC scaling a core convective speed of $u_c = 2.8 \times 10^{-5}$ m/s and a magnetic Reynolds number of $Re_m \approx 1$, which is insufficient for a dynamo (Christensen et al., 1999; Stevenson, 2003).

The surface heat flux q_s is inversely proportional to the planetesimal radius. As gravity scales linearly with radius, the core convective speed depends on the ratio between core and planetesimal radii. As a result Re_m scales approximately linearly with the radius. A magnetic Reynolds number of the order 10 could be obtained with a planet of radius of 1000 km that is cooling conductively and would support a dynamo for a duration of order $\tau = \kappa^{-1}(a/\pi)^2 \approx 3$ Gyr.

As the surface heat flux scales inversely with radius, the total surface heat flow $Q_s =$

$4\pi a^2 q_s$ will be proportional to the radius. The total thermal energy available will scale with the volume of the planetesimal, a^3. The rate of change of temperature in the planetesimal will then scale as a^{-2}. A planetesimal with a radius of 100 km would thus cool approximately 100 times faster than a 1000 km radius planet. For the purely conductive case, the smaller the planetesimal, the faster the cooling rate. Given the short half life of ^{26}Al, ~ 0.7 Myr, a small planetesimal must heat up enough within the first few million years for thermal convection to occur. If convection has not set in within that time it likely never will, as conductive cooling will efficiently cool the planetesimal over longer time scales.

Onset of thermal convection

A fluid layer of thickness D and with uniform material properties will experience thermal convection if the Rayleigh number across that layer is supercritical. The Rayleigh number for the fluid layer is defined as

$$Ra_m = \frac{\alpha \rho g \Delta T D^3}{\kappa \eta} \tag{5.12}$$

where α is the thermal expansivity, ρ is the density, g is the gravitational acceleration, ΔT is the temperature difference across the layer, κ is the thermal diffusivity, and η is the viscosity of the fluid. The Rayleigh number represents a dimensionless ratio between buoyant and viscous forces. For an isoviscous fluid the critical Rayleigh number is of order $Ra_c \sim 10^3$ (Schubert et al., 2001).

The *onset* of convection in a fluid with a highly temperature dependent viscosity requires a slightly modified criterion (Stengel et al., 1982). If the temperature dependence of viscosity is strong enough, the upper cool portion of the thermal boundary layer will be too viscous to deform and only the warm, less viscous base of the thermal boundary layer will participate in convection. The criterion for the onset of thermal convection is then given by

$$\frac{\alpha \rho g \Delta T D^3}{\eta_m \kappa} > p^4 \frac{Ra_c}{24} \tag{5.13}$$

where D is again the thickness of the fluid layer, $p = \beta\Delta T = \ln(\Delta\eta)$ with $\Delta\eta$ the viscosity contrast across the surface thermal boundary layer, β is a constant and $\eta_m = \eta\ (T_m)$ is the viscosity evaluated at the warm base of the layer. The above is based on a temperature dependent viscosity relation

$$\eta(T) = \hat{\eta}_o e^{-\beta T} \tag{5.14}$$

where $\hat{\eta}_o$ is the mantle reference viscosity. In equation (5.13) $\Delta T = T_m - T_s$ where T_s is the surface temperature. Equation (5.13) is derived in Appendix D.1 and is in agreement with the results of Stengel et al. (1982) for the onset of convection in a variable viscosity fluid.

The onset of convection requires a thermal gradient. It will therefore occur at the base of the cold thermal boundary layer that is diffusively growing from the surface of the planetesimal and into its warm interior. Once the 'local' Rayleigh number in the thermal boundary layer exceeds the effective critical Rayleigh number given in equation (5.13) the lower part of the thermal boundary layer becomes unstable, detaches, and drives thermal convection in the mantle. Once the onset of convection has occurred, thermal gradients will exist throughout the full depth of the planetesimal mantle and thermal convection will extend to the base of the mantle. The average thickness of the thermal boundary layer will then be δ_o and is given by the stagnant lid scaling. This will be further discussed in the following section.

If the interior of the planetesimal is sufficiently warm it may have a significant degree of melt and a corresponding viscosity that is very small. One may wonder whether the application of a solid state convection theory might be inappropriate for such a case. However, the thermal gradient through the cold thermal boundary layer and strong temperature dependence of viscosity ensures that viscosity increases rapidly from the base of the thermal boundary layer to the cold (sub solidus temperature) surface and there will always exist a layer in which solid state convection can occur. Thus, a low viscosity planetesimal mantle does not negate the use of such a scaling to determine the surface thermal boundary layer

thickness.

It is important to point out that stagnant lid convection implies that heat transported to the base of the cold thermal boundary layer by convection is balanced by the conductive heat flow through the boundary layer. The thickness of the thermal boundary layer and the convective heat transport are determined by the thermal expansivity, density, gravitational acceleration, temperature, layer thickness, thermal diffusivity, and viscosity of the fluid, all encapsulated in the Rayleigh number, as well as the temperature dependence of the viscosity (Solomatov, 1995). The convective heat transport does not depend on and is not required to balance the rate of internal heating.

Part of the thermal boundary layer may contain partial melt and as such would have a different effective diffusivity than regions without any melting. This effective diffusivity can be calculated as the sum of the regular diffusivity κ plus a contribution due to the latent heat and is at most a factor of two larger than κ (see Appendix D.4). Thus, melting could change the local Rayleigh number of the thermal boundary layer by a small factor, however this will have little effect on the timing of the onset of convection since that is mainly determined by changes in the viscosity which range over orders of magnitude.

We argued in the previous section that the onset of convection must occur within the first few million years, when there is still a significant contribution to internal heating from ^{26}Al, if it is to occur at all. The thickness of the thermal boundary will be of the order of $D \sim \sqrt{\kappa t} \sim 5$ km where we have used $\kappa = 10^{-6}$ m^2/s and $t = 1$ Myr. Note that the thickness D is independent of the radius of the planetesimal and depends only on the diffusivity. Using this thickness for the thermal boundary layer D, a temperature difference of $\Delta T = O(10^3)$ K, equation (5.13) and the properties listed in Table 5.1, one finds that the viscosity at the base of the cold thermal boundary layer, and thus the interior of the planetesimal, must be $\eta_m \sim 10^{14}$ Pa s. Planetesimals of this size and smaller will therefore require high temperatures and partial melt if convection is to occur within their mantles.

In the presence of partial melt the mantle viscosity may undergo a rheologial transition at a critical melt fraction ϕ_{crit}, decreasing over many orders of magnitude as the temperature

reaches a critical value T_{crit}. As a result, the onset of convection occurs at $T_{onset} \sim T_{crit}$ as the sudden decrease in viscosity leads to satisfaction of equation (5.13) and this result is largely independent of the radius of the planetesimal. The temperature is then the controlling factor in determining the onset time of convection. Even in the absence of such a rheological transition, the thickness of the cold surface boundary layer, D, prior to the onset of convection, is independent of the radius of the planetesimal. Thus, the Rayleigh number for the cold thermal boundary layer in equation (5.13) depends only weakly on the radius of the planetesimal, through the linear dependence in the gravitational acceleration. Decreasing the radius of a planetesimal by an order of magnitude will require only a small temperature increase of $\sim$ 50 K to obtain a low enough viscosity to achieve the same Rayleigh number and the onset of convection.

For a range of accretion times there will be enough radiogenic heat available to form a core, but not enough to continue heating until the critical melt fraction is reached. In practice, we expect this range to be quite small. Beyond this range, accretion will occur too late to generate sufficient metal-silicate separation to form a core, rendering it not relevant for consideration in this work.

In summary, we start the convective regime of the thermal evolution of a planetesimal at a temperature $T_{onset} \sim T_{crit}$. For the consideration of the presence and duration of a dynamo the thermal state of the planetesimal prior to this regime is irrelevant. Either a planetesimal will have had enough radiogenic heating to reach T_{onset}, or not.

In the next section we discuss the thermal boundary model in more detail as well as the viscosity law we use throughout the thermal evolution.

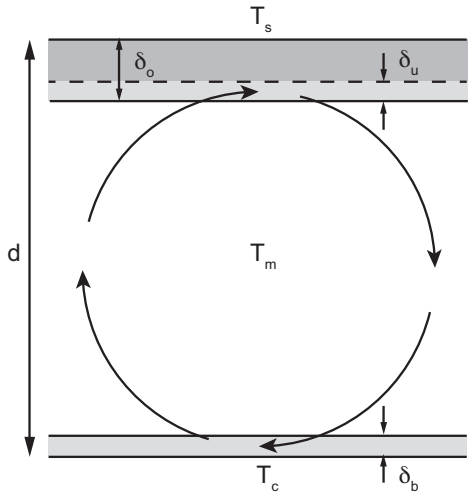

Figure 5.3: Schematic representation of mantle convection defining various lengths used in the thermal evolution model.

5.2.2 THERMAL BOUNDARY LAYER MODEL

Governing equations

Our thermal evolution model is based on two coupled first order differential equations we solve for the core temperature T_c and mantle temperature T_m

$$\begin{aligned} \frac{dT_c}{dt} &= -\frac{A_c F_c}{c_{p,c} m_c} \\ \frac{dT_m}{dt} &= -\frac{A_m F_{surf}}{c_p m_m} + \frac{A_c F_c}{c_p m_m} + \frac{Q_r}{c_p} \end{aligned} \tag{5.15}$$

where A_c and A_m are the core and mantle surface areas, F_c and F_{surf} the core and surface heat fluxes, m_c and m_m are the core and mantle masses, Q_r is the amount of internal radiogenic heating per unit mass, $c_{p,c}$ and c_p are the core and mantle specific heat capacities. We do not include mantle latent heat as it is equivalent to changing the mantle specific heat, see Appendix D.4, which has a negligible effect on the duration of any present dynamo as we will show in section 5.3.

We calculate the contribution of radiogenic heating to the planetesimal's heat budget

with

$$Q_r(t) = H_0 C_0 e^{-(t+t_a)\log(2)/\tau} \tag{5.16}$$

where H_0 is the rate of heat release in W/kg, C_0 is the initial concentration of ^{26}Al (kg radiogenic element/kg mantle), τ is its half-life, t_a is the time after CAI at which instantaneous accretion occurs and t is the time since accretion. See Table 5.1 for their respective values.

The core heat flux is calculated using

$$F_c = \frac{k_c(T_c - T_m)}{\delta_b} \tag{5.17}$$

where k_c is the core thermal conductivity and δ_b is the thermal boundary layer thickness at the core-mantle interface, see Figure 5.3 for a schematic of stagnant lid convection in which we define various lengths. During stagnant lid convection a high viscosity thermal boundary of thickness δ_0 exists on the surface with a thin sub-layer of thickness δ_u actively participating in a near isoviscous convection beneath the lid. The thickness of the actively convecting upper and lower thermal boundary layers will be of the same order and we thus set δ_b equal to the upper thermal boundary layer δ_u. δ_o and δ_u are given by (Solomatov, 1995)

$$\delta_o = d\left(\frac{\gamma\Delta T}{c_1}\right)^{4/3}\left(\frac{Ra_m}{Ra_{cr}}\right)^{-1/3} \tag{5.18}$$

$$\delta_u = c_1\frac{\delta_o}{\gamma\Delta T} \tag{5.19}$$

with the mantle Rayleigh number Ra_m given as

$$Ra_m = \frac{\alpha\rho_m g\Delta T d^3}{\kappa\eta_m}, \tag{5.20}$$

and where $c_1 \sim 8$, $\Delta T = T_m - T_s$ and T_s is the surface temperature. $\gamma = E/RT_o^2$, where T_o

is a reference temperature for which the mantle viscosity is equal to a reference value, see 5.2.2. The layer thickness d is equal to the depth of the mantle, i.e., $d = r - r_c$. E is the activation energy and R is the gas constant. We use a Dirichlet boundary condition and set the temperature at the surface T_s equal to that of the ambient environment. The effect of a radiation boundary condition, albeit physically more appropriate, is negligible (Hevey and Sanders, 2006).

The surface heat flux is given by

$$F_{surf} = \frac{k\Delta T}{\delta_o} \tag{5.21}$$

which gives, using equation (5.18),

$$F_{surf} = k \left(\frac{c_1}{\gamma} \right)^{4/3} \left(\frac{\rho_m \alpha g}{\kappa \eta Ra_{cr}} \right)^{1/3} \tag{5.22}$$

Viscosity

Our thermal evolution model may track the thermal state of a planetesimal from partially molten magma ocean to solid mantle, which, given the temperature dependence of viscosity, implies a change in the mantle viscosity over a very large range from as low as $\sim$1 Pa s for supercritical silicate melt fractions, to $\sim 10^{21}$ Pa s for the solid mantle. As such, it is clear from equation (5.22) that the temperature dependence of viscosity will play an important role in the thermal evolution.

Crystal formation and their subsequent distribution in the mantle as it cools is not well understood (Reese and Solomatov, 2006). After crystallization, crystals may sink to form a (possibly stable) layer above the core, or remain distributed in the mantle due to convective flow. Sinking of crystals formed near the upper thermal boundary layer would effectively decrease the thickness of the boundary layer and result in a higher surface conductive heat flux. By neglecting crystal formation and sinking we pursue a lower bound on the heat flux, yielding a slower cooling of the planetesimal, providing a conservative estimate of dynamo

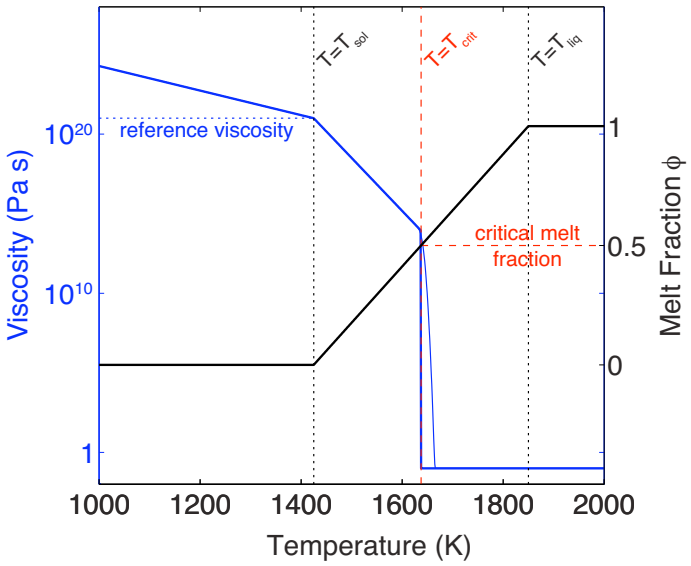

Figure 5.4: Left ordinate: Variation of mantle viscosity with mantle temperature including a rheological transition at a critical temperature T_{crit} for which a critical melt fraction ϕ_{crit} is obtained. To make the problem computationally more tractable the rheological transition at T_{crit} is approximated with an error function (thin blue line). Right ordinate: Melt fraction ϕ which varies linearly between the silicate solidus and liquidus.

duration.

We assume a linear melt gradient from mantle liquidus, $T_{m,l}$, to solidus, $T_{m,s}$, and a well-mixed mantle that is cooling uniformly. We can write for the mantle melt fraction (Reese and Solomatov, 2006)

$$\phi_m = \frac{T_m - T_{m,s}}{T_{m,l} - T_{m,s}} \tag{5.23}$$

which we use to vary the mantle viscosity η with changing temperature

$$\begin{aligned} \eta &= \hat{\eta}_o \exp\left(-\gamma \Delta T_\eta\right) \exp\left(-\alpha_n \phi_m\right), \qquad T_m \;\; &\leq T_{crit} \\ \eta &= \eta_{crit}, \qquad T_m \;\; &> T_{crit} \end{aligned} \tag{5.24}$$

where $\Delta T_\eta = T_m - T_o$ and the melt constant is either $\alpha_n \sim 25$ or 30 in the case of diffusion or dislocation creep respectively (Reese and Solomatov, 2006). Strictly speaking, this law is only valid for $0.05 < \phi_m < 0.25$ (Reese and Solomatov, 2006). This means we underestimate

the viscosity by up to 70% for melt fractions $\phi_m < 5\%$ where this is not strictly applicable. However, that is still within the same order of magnitude, and given the range over which the viscosity varies, the error incurred will have a very small effect on the whole evolution.

We choose a reference viscosity $\hat{\eta}_o = 10^{21}$ Pa s at a reference temperature equal to the mantle solidus, $T_o = T_{m,s}$. Using equation (5.24) we let the viscosity vary between 1 Pa s above the critical temperature T_{crit}, rapidly changing over ~ 20 orders of magnitude as the mantle goes from partial melt to solid, and is 10^{21} Pa s for temperatures just below the solidus, see Figure 5.4. We refer the reader to Reese and Solomatov (2006) for a more complete description and background of our model of viscosity.

We have experimented with different melt constants between $15 < \alpha_n < 30$ and found that lower melt constants lead to higher mantle temperatures. This is expected as changing the melt constant α_n will have a similar effect (equation (5.24)) to changing the activation energy E (and γ). For example, during the initial stages of the evolution, when radiogenic heating is large, the mantle temperature adjusts until the viscosity is low and a thin enough thermal boundary layer forms such that the surface heat flow approximately (but not exactly) balances the radiogenic heating rate. Thus, for a weaker temperature dependence of the viscosity (i.e., lower $\gamma + \alpha_n$), the system must reach a higher temperature to arrive at the viscosity that approximately balances the heat flow. This is the same self-regulating feedback between temperature, viscosity, and internal heating, often referred to as the 'mantle thermostat', that was first noted by Tozer (1970) for the Earth. Changing the melt constant changes the temperature but has little effect on the evolution of the heat flow, which controls the duration of the dynamo.

We now proceed by considering several reference scenarios for which we investigate the behavior of the thermal evolution model in depth. This is followed by the exploration of a larger parameter space in which we vary parameters such as the accretion time, core radius, reference viscosity and critical melt fraction, and determine the dynamo duration as a function of planetesimal radius. We will then compare our results to an analytical determination of dynamo duration.

A reference scenario

Figure 5.5 (a-e) shows a typical planetesimal thermal evolution over 50 Myr, for a planetesimal with a radius of 400 km and a core radius of 200 km, starting from $T_m = T_c = T_{onset} \sim$ 1640 K and using parameters as specified in Table 5.1. For this case the planetesimal begins with all of its radiogenic heating intact, i.e. $t_a = 0$, so as to present an "end-member" scenario. In essence, the planetesimal thus accreted and differentiated instantaneously at $t_a = 0$ Myr, at no cost to the radiogenic heating budget. Figure 5.5a shows T_m and T_c as a function of time. The temperatures increase slightly beyond T_{onset} due to radiogenic heating. However, the temperature cannot increase very much due to the temperature dependence of the mantle viscosity, which is around the rheological transition as $T_{onset} \sim T_{crit}$. This strong dependence means that the mantle temperature is effectively buffered at the temperature where a critical melt fraction is reached. Any temperature increase beyond that is immediately met with a strongly decreasing viscosity and a large increase in surface heat flow, cooling the system. Once radiogenic heating has decayed enough, the mantle enters its secular cooling phase at which time T_m starts to decrease.

In Figure 5.5b we show the planetesimal's heat fluxes. It is clear that the dominant part of the surface heat flux comes from the radiogenic heating in the first few million years, with a small surplus for mantle cooling. After $\sim$6 Myr, the amount of radiogenic heating becomes small due to the short half life of ^{26}Al and the surface heat flux becomes mainly devoted to cooling the mantle. In practice, the radiogenic heating does not decay to zero, because of the presence of other radiogenic elements, not included in our model, which have a much longer half-life than ^{26}Al. The cooling phase is also reflected in the core heat flux which sees an increase at $\sim$6 Myr. After this time, throughout the evolution the core heat flux is consistently higher than the conductive core heat flux ($F_{cond,c} \approx 2$ mW/m^2, not shown), yielding an always positive convective core heat flux.

Figure 5.5c shows the variation of the magnetic Reynolds number over time, as determined using the MAC scaling law. The shape of the curve is a reflection of the shape of the core heat flux curve. In this scenario the magnetic Reynolds number does not exceed a

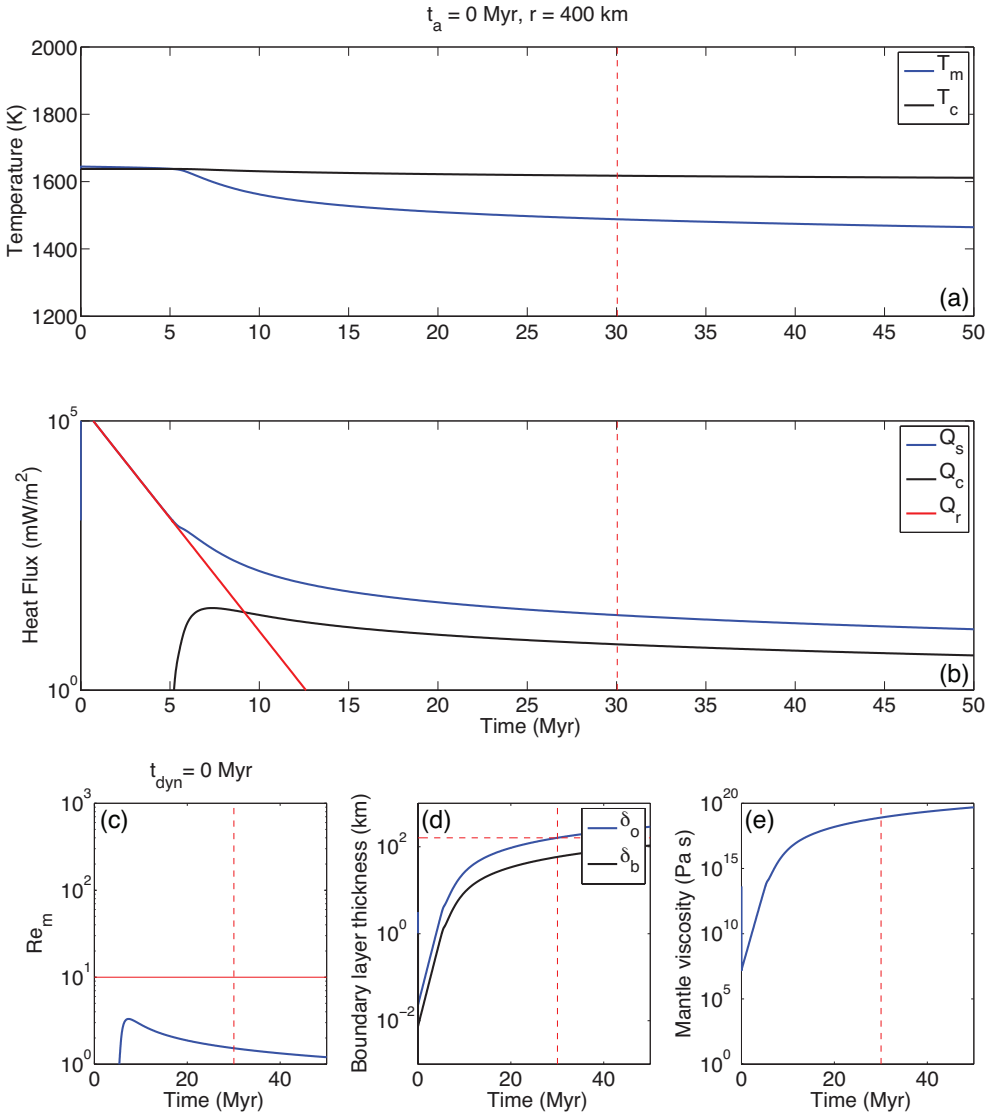

Figure 5.5: A reference scenario of a thermal evolution for a planetesimal with a radius of 400 km, a core radius of 200 km, a rotation period of 10 hours and all other parameters given in Table 5.1. The planetesimal accreted at 0 Ma. The initial core and mantle temperatures are the same and equal to $T_{onset} = 1638$ K. (a) Evolution of core (black) and mantle (blue) temperatures. (b) Evolution of core (black) and surface (blue) heat fluxes and radiogenic heating Q_r (red). (c) Evolution of magnetic Reynolds number. (d) Variation of thermal boundary layer thickness. The boundary layer grows until it reaches a critical thickness approximately equal to $r - r_c$. After that the model becomes unphysical and the simulation is stopped (red dashed line). (e) Evolution of mantle viscosity.

critical value of 10 and no dynamo is present.

Evolution of the boundary layer thickness is illustrated in Figure 5.5d. The simulations begin with thin thermal boundary layers as there is a substantial amount of heat in the system, the viscosity of the mantle is very low and convective vigour is great. As the system cools, the thermal boundary layers gradually thicken until thermal convection is no longer possible, i.e. when the Rayleigh number drops below the critical value. This point is indicated by the horizontal red dashed line in Figure 5.5.

Figure 5.5e shows the evolution of the mantle viscosity which starts at a value determined by T_{onset}. However, as the system continues to heat up beyond that temperature, the exponential dependence on temperature very rapidly decreases the viscosity several orders of magnitude within the first 2,000 years. This is followed by a much slower increase along with secular cooling of the planetesimal ending at a large value.

In Figure 5.6 we show the evolution of a planetesimal with a radius of 1000 km and a core radius of 500 km. Here the magnetic Reynolds number does become supercritical and a dynamo is present for $\sim$16 Myr. The vertical solid red lines in Figure 5.6c indicate the times for which the magnetic Reynolds number first becomes subcritical and when the dynamo shuts off.

In varying the mantle reference viscosity, which is typically set to 10^{21} Pa s, we found that for increasing reference viscosity, T_m and T_c increase. Conversely, decreasing the mantle reference viscosity resulted in a slight decrease in T_m and T_c. However, both cases predict similar cooling rates and the duration of the dynamo is only slightly altered. Again, this is the result of the self regulating thermal feedback between temperature and viscosity (Tozer, 1970).

Before further considering the dependence of the dynamo duration on various parameters, we discuss the conditions for a dynamo in more detail and derive an analytical solution for dynamo duration which we will compare to our results.

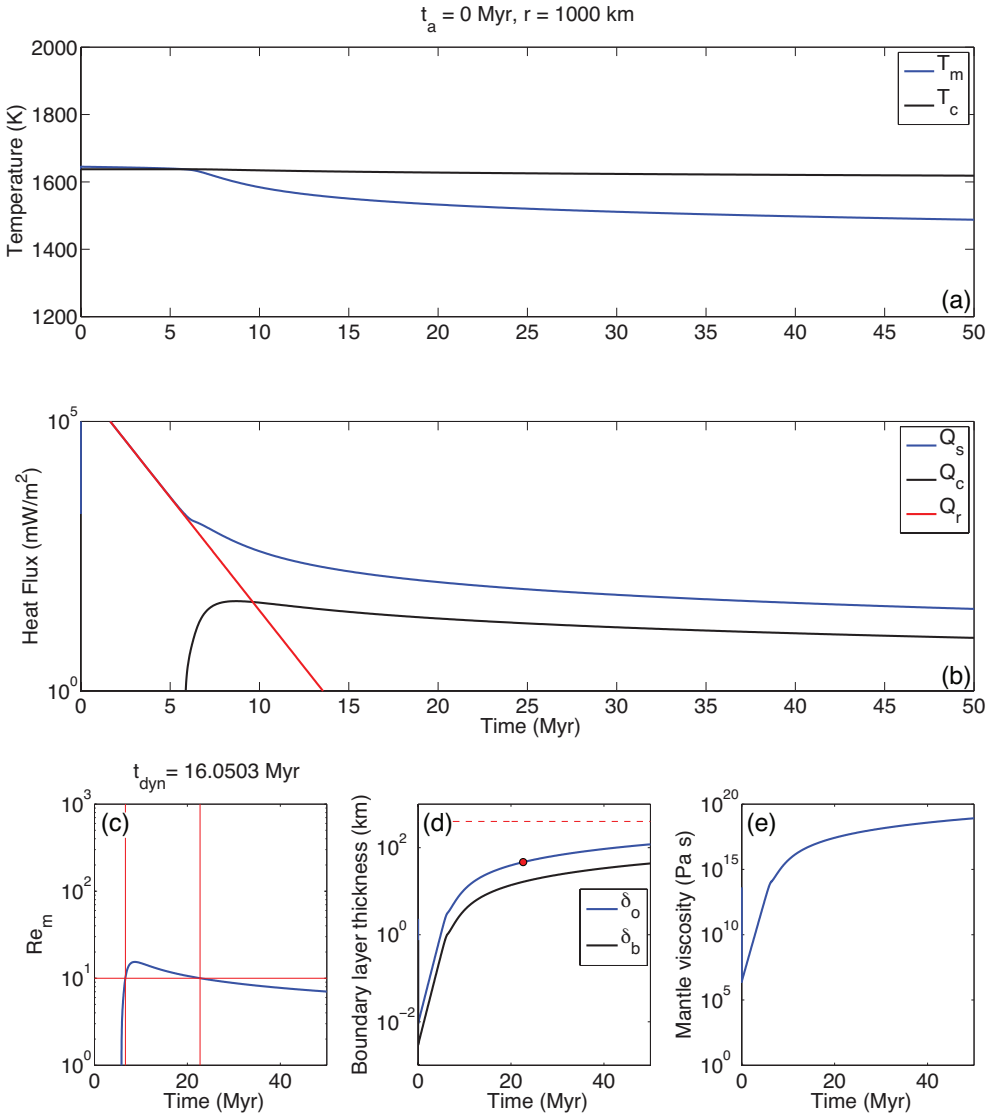

Figure 5.6: A reference scenario of a thermal evolution for a planetesimal with a radius of 1000 km, a core radius of 500 km, a rotation period of 10 hours and all other parameters given in Table 5.1. The planetesimal accreted at 0 Ma. The initial core and mantle temperatures are the same and equal to $T_{onset} = 1638$ K. (a) Evolution of core (black) and mantle (blue) temperatures. (b) Evolution of core (black) and surface (blue) heat fluxes and radiogenic heating Q_r (red). (c) Evolution of magnetic Reynolds number. Dynamo duration is $\sim$16.1 Myr based on a critical magnetic Reynolds number of 10. (d) Variation of thermal boundary layer thickness. The boundary layer grows until it reaches a critical thickness approximately equal to $r - r_c$. After that the model becomes unphysical and the simulation is stopped (red dashed line). (e) Evolution of mantle viscosity. The red dot in (d) illustrates what the lid thickness is when the magnetic Reynolds number becomes subcritical.

5.2.3 CONDITIONS FOR A DYNAMO

As discussed in the introduction, a planetesimal may have a dynamo if it contains a sufficiently electrically conducting fluid layer or core. A source of energy needs to be present to maintain convective motions in this layer against ohmic dissipation, and the convection must be sufficiently vigorous to ensure a supercritical magnetic Reynolds number (Gaidos et al., 2010). In the present work we investigate the likelihood of thermal convection dynamos in planetesimals. Compositional convection is considered to be energetically more efficient and has been studied elsewhere (Gubbins, 1977; Nimmo, 2009). However, it is difficult to place bounds on compositionally driven dynamos due to uncertainties associated with core compositions as well as the dynamics and thermodynamics of a freezing core.

The condition for convection is that the heat flux out of the core must exceed the heat flux along the adiabat, i.e., the conductive heat flux .

$$F_{cond,c} = k_c \alpha_c T_c / c_{p,c} \approx 2 \text{ mW/m}^2 \tag{5.25}$$

where k_c is the core thermal conductivity, α_c is the core thermal diffusivity and $c_{p,c}$ is the core specific heat capacity. We can thus calculate the core convective heat flux as $F_{conv,c} = F_c - F_{cond,c}$. If $F_{conv,c} > 0$ the core is convecting. Given how small $F_{cond,c}$ is, $F_{conv,c} \approx F_c$ which is easily satisfied in each of our thermal evolutions, see for example Figures 5.5b and 5.6b.

In order to maintain a magnetic field, the induction effect must be able to at least balance the diffusive losses, which, in practice, means that Re_m has to exceed a critical value $Re_{m,cr} = 10 - 100$ for a dynamo to operate (Christensen et al., 1999; Monteux et al., 2011; Stevenson, 2003). The magnetic Reynolds number is typically defined as

$$Re_m = u_c r_c / \lambda \tag{5.26}$$

where λ is the magnetic diffusivity. We assess Re_m by estimating the core convective speed

u_c. As discussed in the introduction, u_c may be estimated by using different scaling laws, each reflecting a different leading order force balance in the core (for a full discussion, see Christensen, 2010) . Appendix D.5 lists three scaling laws.

The scaling law based on mixing length theory, in which inertial terms are balanced against buoyancy terms, yields a velocity $u_c \propto r_c^{2/3} F_c^{1/3}$, where the core radius r_c was used as the mixing length. This scaling law may be appropriate for systems with highly turbulent convection and where rotation is not a dominant force in the core (Stevenson, 2003). The CIA scaling law represents a three-fold force balance between the Coriolis, inertial and buoyancy terms, and the velocity scales as $u_c \propto r_c^{3/5} F_c^{2/5}$. For the Boussinesq approximation, the characteristic length scale is again the core radius. This scaling law represents rapidly rotating convection well (Aubert et al., 2001), but it is not clear if it would represent magnetohydrodynamic flow equally well, where the Lorentz force would replace the inertial term in the force balance (Christensen, 2010). The MAC scaling law is based on the magnetostrophic balance between the Lorentz, buoyancy and Coriolis forces. The velocity scales as $u_c \propto (r_c F_c)^{1/2}$. As discussed in the previous section, we monitor the magnetic Reynolds number Re_m throughout each thermal evolution. We assess Re_m using the MAC scaling law with the planetesimal rotation rate as a free parameter. In the discussion we evaluate to what extent the mixing length and CIA scaling laws yield different results.

To evaluate the magnetic field strength of any dynamo we rely on a balance between the thermodynamically available power in the core and that which is lost by ohmic dissipation (Christensen, 2010).

$$\frac{B^2}{2\mu_0} \propto f_{ohm} \frac{L}{U} \frac{\alpha_c g_c F_c}{c_{p,c}} \tag{5.27}$$

where B is the magnetic field strength, μ_0 is the magnetic permeability, f_{ohm} is the fraction of the available power that is converted to magnetic energy, L is the characteristic length scale, U is the characteristic speed in the core, λ is the magnetic diffusivity, F_c is the core heat flux, α_c is thermal expansivity and g_c is the gravity in the core. Assuming $L \sim r_c$, we

can then use a scaling law for u_c and evaluate the magnetic field strength in the core, also see Appendix D.5.

We calculate the dipole magnetic field strength at the surface of the planetesimal by assuming that the dipole field at the core-mantle boundary is around 10% of the total field which gives

$$B_{surf} = 0.1 B_{core} \left(\frac{r_c}{r}\right)^3 \tag{5.28}$$

As the mantle cools, convection becomes less vigorous and the Rayleigh number decreases, the thermal boundary layers increase in thickness, and there is a corresponding decrease in the heat flow. We determine the duration of the dynamo in each thermal evolution based on positive core convective heat flux and exceedance of the critical magnetic Reynolds number. We also calculate both the mean and peak magnetic field strength.

5.3 An analytic solution for dynamo duration

An approximate analytic solution may be derived for the dynamo duration. Such a solution is useful in that it explicitly demonstrates the dependence of the dynamo duration on the various model parameters and initial conditions.

Let the mantle and core temperatures begin at a temperature $T = T^*$. Initially, the difference between the core and mantle temperatures is small and the core heat flow is also small and may be neglected in mantle energy balance of equation (5.15). Furthermore, after a short time, of order a few million years, internal heating from ^{26}Al has sufficiently decayed such that the surface heat flow is primarily due to cooling of the mantle. Then the rate of change of the mantle temperature may be approximated as

$$\rho_m c_p V_m \frac{dT_m}{dt} = -A_m F_{surf} \tag{5.29}$$

Using the definition of δ_o, equation (5.18), we can write

$$\frac{dT_m}{dt} = -\chi e^{\beta T_m/3} \tag{5.30}$$

where $\beta = \gamma + \alpha_n/(T_{m,l} - T_{m,s})$ and

$$\chi = \kappa \left(\frac{c_1}{\gamma}\right)^{\frac{4}{3}} \frac{A_m}{V_m} \left(\frac{\alpha \rho_m g}{\kappa \tilde{\eta}_o Ra_c}\right)^{\frac{1}{3}} \tag{5.31}$$

and we have used

$$\eta = \tilde{\eta}_o e^{-\beta T_m} \tag{5.32}$$

with

$$\tilde{\eta}_o = \hat{\eta}_o \exp\left[\gamma\, T_o + \alpha_n T_{m,s}/(T_{m,l} - T_{m,s})\right] \tag{5.33}$$

The solution to equation (5.30) with initial condition $T(t=0) = T^*$ is

$$T_m = -\frac{3}{\beta} \log\left(\frac{\beta\chi}{3} t + e^{-\beta T^*/3}\right) \tag{5.34}$$

The parameter β provides the effective dependence of viscosity on temperature and affects both the magnitude of the temperature (the β^{-1} prefactor in equation (5.34)) as well as the time scale of the evolution ($T_m(t)$ is a function of the product $\beta \cdot t$). Thus, a decrease in either the activation energy E or the melt constant α_n will decrease β and will yield a warmer and slower evolution. Equation (5.34) also demonstrates the weak dependence of the solution on the reference viscosity $\tilde{\eta}_o$ through the parameter $\chi \propto \tilde{\eta}_o^{-\frac{1}{3}}$.

Substituting equation (5.34) back into equation (5.30) gives

$$F_{surf} = \frac{-c_p m_m \chi}{\frac{\beta\chi}{3} t + e^{-\beta T^*/3}} \tag{5.35}$$

Let us now consider the relative surface and core heat flux. The ratio of the core to surface heat flux is equal to

$$\begin{aligned} \frac{F_c}{F_{surf}} &= \frac{k\frac{T_c - T_m}{\delta_b}}{k\frac{T_m - T_s}{\delta_o}} = \frac{T_c - T_m}{T_m - T_s}\frac{\delta_o}{\delta_b} \\ &= \frac{T_c - T_m}{T_m - T_o}\frac{\gamma(T_m - T_s)}{c_1} = \frac{\gamma}{c_1}(T_c - T_m) \end{aligned} \tag{5.36}$$

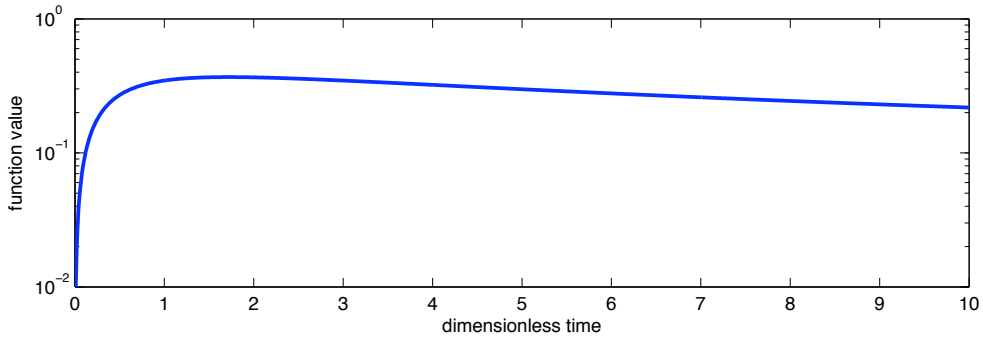

Figure 5.7: Normalized heat flux for the analytic solution as a function of dimensionless time $t' = t/\tau$.

where we have used equation (5.19). Then solving for the core heat flux gives

$$F_c = \frac{\gamma}{c_1}(T_c - T_m)F_{surf} \tag{5.37}$$

During the initial cooling T_m changes much faster than T_c as the latter cannot change until the former has changed enough that a sufficient thermal gradient exists to draw heat out of the core. We may then approximate the core temperature during this initial stage as approximately equal to the initial temperature $T_c \approx T^*$. Using equation (5.34) for the mantle temperature, substituting in the stagnant lid heat flow F_{surf} using equation (5.22) and using the definition of χ in equation (5.31) gives

$$F_c = \frac{\gamma}{c_1}\left(\frac{3}{\beta}\right)^2 \frac{V_m}{A_m}\frac{c_p\rho_m}{t+\tau}\log\left(\frac{t}{\tau}+1\right) \tag{5.38}$$

with the time constant

$$\tau = \frac{3}{\beta\chi}e^{-\beta T^*/3} \tag{5.39}$$

Figure 5.7 shows the shape of the heat flux predicted by equation (5.38), with the magnitude normalized and as a function of dimensionless time $t' = t/\tau$ (i.e., $(t'+1)^{-1}\log(t'+1)$ is plotted as a function of t'). The maximum heat flux occurs near $t' = 1$ or $t = \tau$. The shape of the core heat flux evolution compares very well with any of our simulations.

The parameters used in the present work, Table 5.1, give a time constant of $\tau = 0.4$ Myr for a planetesimal radius of $r = 1000$ km and $\tau \propto r^{2/3}$. This is small so we can consider the solution for large t. For $t >> \tau$, equation (5.38) can be simplified to

$$F_c = \frac{\gamma}{c_1}\left(\frac{3}{\beta}\right)^2 \frac{V_m}{A_m}\frac{c_p\rho_m}{t}\log\left(\frac{t}{\tau}\right) \tag{5.40}$$

Using the MAC scaling law, equation (5.4), we can relate F_c to u_c and to the magnetic Reynolds number with equation (5.26). We may thus calculate the time at which the magnetic Reynolds number is equal to the critical magnetic Reynolds number, $Re_{m,cr}$, required for a dynamo

$$t_{dyn} = \frac{\gamma}{c_1}\left(\frac{3r_c}{\beta Re_{mc}\lambda}\right)^2 \frac{V_m}{A_m}\frac{\rho_m c_p}{\rho_c c_{p,c}}\frac{\alpha_c g_c}{\Omega}\log\left(\frac{t}{\tau}\right) \tag{5.41}$$

This is equal to the dynamo duration. Eequation (5.41) is an implicit equation in terms of the time t. However, due to the weak $\log(t/\tau)$ sensitivity of the right hand side, this equation is easily solved iteratively. Given that $\tau \sim O(1)$ Myr, we expect that our approximation will deviate from our numerical thermal evolutions around $t_{dyn} \sim 1$ Myr.

Because $V_m \propto r^3$, $A_m \propto r^2$ and $g_c \propto r$, (as $r_c \propto r$ in our simulations), equation (5.41) is strongly dependent on the radius of the planetesimal, $t_{dyn} \propto r^4$, just as our simple estimate in the introduction suggested. The time scale for the dynamo depends inversely on β^2 (which contains both the activation energy and the melt constant for the viscosity). Furthermore, the time scale is inversely proportional to the rotation rate of the planet, or proportional to the rotation period.

In the next section we discuss the results of the numerical thermal evolutions in which we, among other parameters, calculate if and for how long the magnetic Reynolds number is supercritical and compare with the above analytical approximation given by equation (5.41).

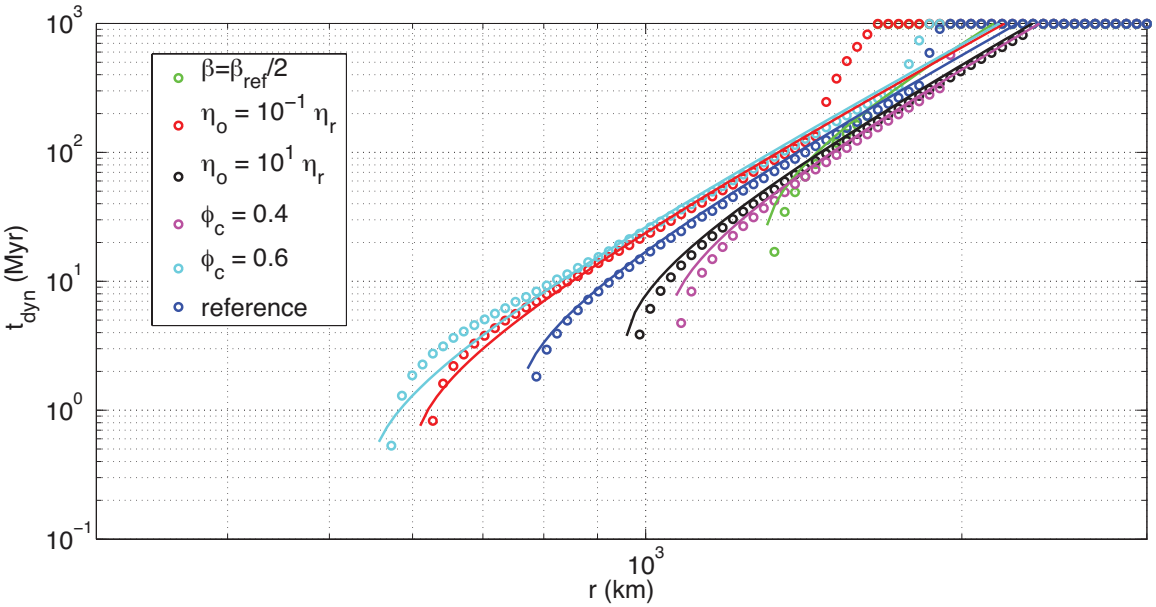

Figure 5.8: Dynamo duration as a function of planetesimal radius for a critical magnetic Reynolds number of, $Re_{m,cr} = 10$, rotating with a period of 10 hours. The reference scenario (blue) is for: $t_a = 0$ Myr; critical melt fraction $\phi_c = 0.5$; and core radius $r_c = 0.6r$. Compared are cases with different reference viscosities (red and black), different critical melt fractions (light blue and purple) and lower temperature-dependence of viscosity (green) as well as their analytical approximations from Eq. (5.41).

5.4 RESULTS

Figure 5.8 shows how dynamo duration varies with planetesimal radius for planetesimals with a rotation period of 10 hours. We investigate 6 different cases each consisting of 80 planetesimal radii between 25 to 3000 km and evaluate the presence of a dynamo with a critical magnetic Reynolds number of 10. The reference case (blue circles) represents planetesimals with a critical melt fraction $\phi_c = 0.5$ and a large core radius $r_c = 0.6r$. Each circle represents the dynamo duration measured throughout the thermal evolution of a single planetesimal. To illustrate an "end-member scenario" the planetesimals in this case are accreted and differentiated instantaneously ($t_a = 0$ Myr) and the mantle has retained all radiogenic heating. We present this case, as well as the other end-member scenario of no radiogenic heating from the onset of convection, in Figure 5.9, to demonstrate that the amount of radiogenic heating, i.e., the age of accretion of the planetesimal, is only relevant to the possible melting and differentiation of the body. It plays no role, however, in determining the duration of the dynamo.

The general behavior of the reference case is indicative of most cases. Although the range of planetesimal radii extends from 25 km to 3000 km, a dynamo is not obtained until $\sim$800 km. Planetesimals smaller than this do not achieve a high enough core heat flux to ever obtain a dynamo (compare Figures 5.5b and 5.6b). The curvature of the lines for smaller radii is due to the initial supercriticality of Re_m, or of the core heat flux just becoming large enough after the radiogenic heating has decayed ($\sim 6 - 7$ Myr in Figure 5.6b). For larger bodies this initial effect plays a relatively smaller role and the longer, slow decay of the core heat flux, and thus of Re_m, governs the dynamo duration. As the planetesimal radius is increased, the variation of dynamo duration with radius scales approximately as r^4, as predicted in the previous section. In fact, the predicted increase in dynamo time with radii is slightly larger than a r^4 power law scaling due to the logarithmic term in equation (5.41). Towards the high end of the range of planetesimal radii the dynamo duration appears to increase rapidly for some of the cases considered. The thermal evolutions of these

larger planetesimals reach sub-solidus mantle temperatures. The temperature dependence of viscosity for sub-solidus temperatures is reduced as the effect of partial melt no longer contributes (see Figure 5.4). As such, the parameter β in equation (5.41) is reduced from $\beta = \gamma + \alpha_n/(T_{m,l} - T_{m,s})$ to $\beta = \gamma$. This reduction in β results in an increase in dynamo time, as is predicted by equation (5.41) and as such the observed increase for larger radii is expected. This effect can only occur in planets that are larger than $r \approx 1000$ km. Smaller planets must have some degree of partial melt (super solidus temperatures) in order to achieve low enough viscosities to counter the r^3 dependency in the mantle Rayleigh number and remain in the convecting regime. The numerical thermal evolutions are continued up to 1 Gyr. The saturation of dynamo duration seen for large planetesimals is due to the fact that these bodies have a dynamo that is present for longer than 1 Gyr.

Increasing the reference mantle viscosity to 10^{22} Pa s (black circles), with respect to the reference case, results in higher core and mantle temperatures throughout the evolution. However, it does not strongly affect the core heat flux and thus has little effect on the dynamo duration. This is not unexpected given that the dynamo time in equation (5.41) depends only on the natural log of the cubed root of the reference viscosity (the time constant τ is proportional to the cubed root of the reference viscosity). For a larger reference viscosity τ becomes larger and t_{dyn} becomes slightly smaller. Conversely, for a smaller reference viscosity (red circles), the planetesimal temperatures are slightly reduced and the effect on dynamo duration is again small.

Changing the critical melt fraction has a more pronounced effect. For a larger ϕ_c (cyan circles) we not only observe a small increase in dynamo duration, but also the presence of a dynamo for smaller bodies. Planetesimals with a larger ϕ_c are able to reach higher temperatures before the critical transition in viscosity is able to effectively buffer temperature. As a result the surface and core heat fluxes are initially higher when the planetesimal begins to cool and a dynamo becomes possible for smaller bodies. For a smaller ϕ_c (purple circles) the initial temperature and core heat flux is smaller and dynamos are only possible in larger bodies.

We also consider a case with a reduced temperature dependence of viscosity, as expressed through the parameter β. For a value of β equal to half of that of the reference case we find that planetesimals have to be larger than 1000 km in order for a dynamo to be present. These cases have larger viscosities and must to be larger in size to allow for thermal convection (supercritical Rayleigh number) and the sufficiently fast rate of cooling required to drive a dynamo.

For each scenario we also plot the analytical approximation t_{dyn} (solid lines) according to equation (5.41) which matches the numerical results very well in terms of slope, $t_{dyn} \approx r^4$, curvature for small radii, and predicted termination of the curves at small radii. Note that we have not allowed β to vary according to presence of melt, which is why the analytical approximations do not follow the curvature for larger planetesimals that cool down to sub-solidus temperatures.

We should note that although we investigate a range of planetesimal radii up to 3000 km we cannot reasonably call these larger bodies planetesimals. Not only would it be highly unlikely that such large bodies could be formed on such short time scales (Merk et al., 2002), but pressure effects need to be taken into account as they affect such planetesimal properties as viscosity and solidus and liquidus temperatures with depth.

In Figure 5.9 we compare several more cases to the reference case (blue circles). The other aforementioned "end-member scenario" for internal heating represents thermal evolutions in which no radiogenic heating occurred (green circles). Effectively, these evolutions represent planetesimals that accreted late enough to just achieve the (partial) melting necessary to reach the onset of convection. Clearly, the presence of radiogenic heating during the start of the thermal evolution plays little to no role in the duration of a dynamo. This scenario is virtually identical to the reference scenario in which the convective thermal evolutions start with all the radiogenic heating. As the analytical approximation to the reference scenario assumes no radiogenic heating, it also applies to this case.

The effect of smaller cores in the planetesimals is investigated as well (red and black circles) and for increasingly smaller cores the duration of a dynamo strongly decreases. In

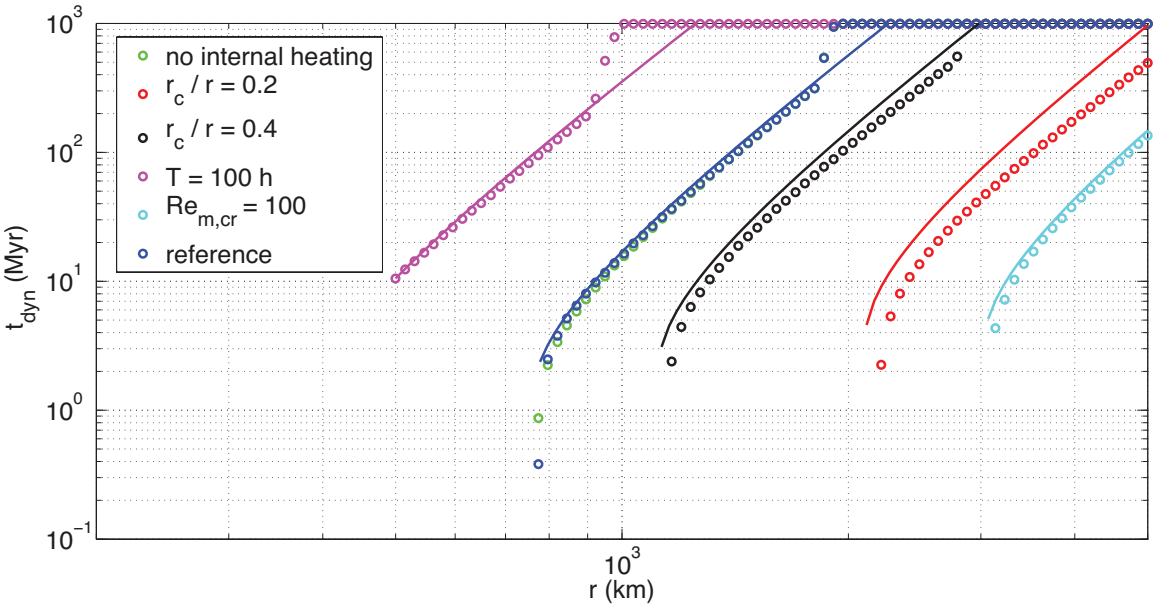

Figure 5.9: Dynamo duration as a function of planetesimal radius for a critical magnetic Reynolds number of, $Re_{m,cr} = 10$, rotating with a period of 10 hours. The reference scenario (blue) is for: $t_a = 0$ Myr; critical melt fraction $\phi_c = 0.5$; and core radius $r_c = 0.6r$. Other cases shown are for a smaller cores (black and red), larger $Re_{m,cr}$ (light blue), longer rotation period (purple) and no internal heating during the convection stage of the evolution (green). Solid lines depict the analytical approximations to each case as based on Eq. (5.41).

other terms, the smaller the core, the larger a planetesimal needs to be in order to have a dynamo. This is in complete agreement with equation (5.41). We can understand this physically as a small core can be cooled faster than a large core. This also explains why for smaller cores the analytical approximation starts to slightly overestimate the numerical results. In the derivation of the analytical approximation we assumed that the core temperature remains near the initial temperature during the initial cooling of the core (i.e. the core cools slowly). For smaller cores, however, this assumption breaks down more rapidly.

The MAC scaling law depends on the rotation rate Ω. As such, we also plot the case for a much longer planetesimal rotation period of 100 hours (purple circles). These results exhibit a longer dynamo for smaller planetesimal radii, as expected from equation (5.41) which shows that dynamo duration is proportional to rotation period. For these cases planetesimals with radii $\sim$500 km are able to sustain dynamos for a duration of $t_{dyn} \sim 10$ Ma.

Whether the magnetic Reynolds number becomes supercritical depends on what is *apriori* defined as the critical value. In all our thermal evolutions we have used $Re_{m,cr} = 10$, however this is considered to be low (Christensen et al., 1999; Monteux et al., 2011; Stevenson, 2003). For the higher, and arguably more realistic value of $Re_{m,cr} = 100$ (cyan circles) the condition on minimum planetesimal radius to obtain a dynamo becomes considerably more stringent.

To evaluate our use of the MAC scaling law we also plot the reference scenario for the mixing length (ML) and the CIA scaling laws in Figure 5.10. The top panel shows the calculated dynamo duration as a function of planetesimal radius and demonstrates that the two other scaling laws are less stringent than the MAC scaling law, with the ML scaling law allowing for dynamos to be present in planetesimals as small as 40 km. This relaxation of the radius constraints is due to the alternative scaling laws which generally give higher core convective speeds. This allows the magnetic Reynolds number, which is proportional to u_c, to remain supercritical for much longer. However, the magnetic field values obtained from these dynamos are substantially lower for these scaling laws. In the lower panel we

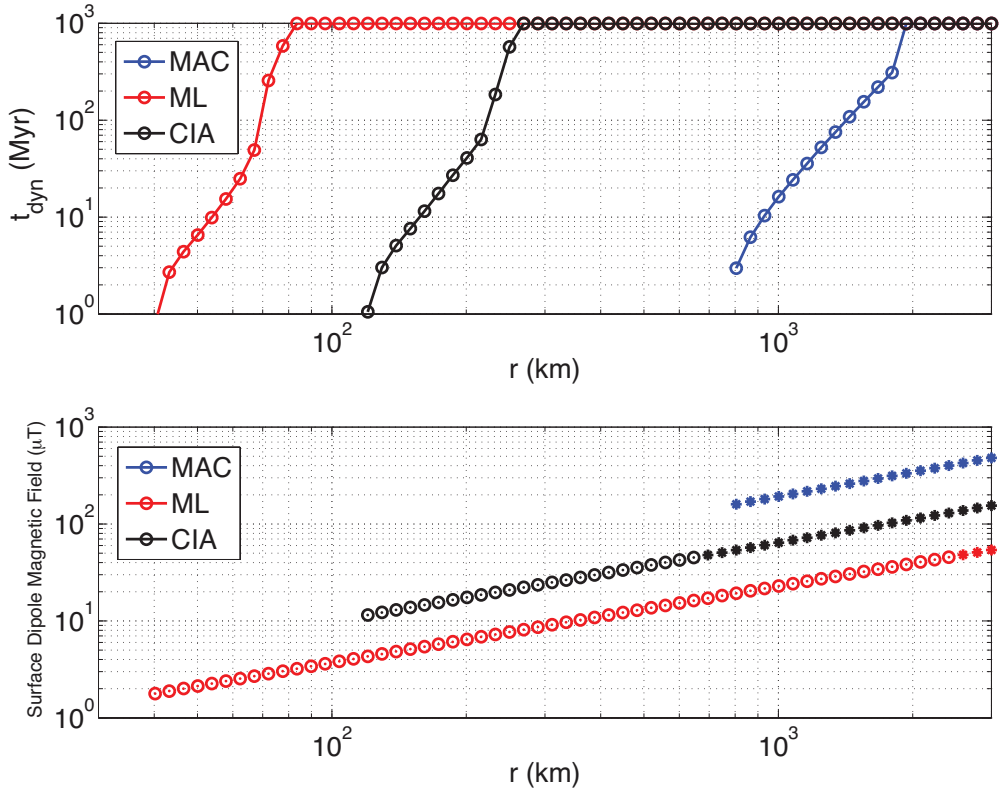

Figure 5.10: Top: Dynamo duration as a function of planetesimal radius for $Re_{m,cr} = 10$, rotating with a period of 10 hours. The reference scenario is for: $t_a = 0$ Myr; critical melt fraction $\phi_c = 0.5$; and core radius $r_c = 0.6r$. Compared are cases based on different scaling laws for the core convective speed u_c. Bottom: Magnetic field strength during thermal evolutions. The peak magnetic field strength during the evolution plotted. Open circles: Mean value during thermal evolution $< 20\ \mu T$. Closed circles: Mean value during thermal evolution $> 20\ \mu T$..

plot the peak surface dipole magnetic field strength as calculated by equation (5.28) with equations (D.34), (D.41) and (D.45) in Appendix D.5. The open circles represent mean magnetic field values during the thermal evolution < 20 μT and the closed circles represent mean values > 20 μT. The 20 μT threshold is approximately based on the magnetic field strength required by Weiss et al. (2008); Weiss et al. (2010) for the angrite parent body dynamo. This condition implies that a planetesimal with a dynamo of sufficient magnetic field strength must have a radius of no less than ~ 700 km for any of the scaling laws. This demonstrates that while the other scaling laws may allow for dynamos in smaller planetesimals, they also predict magnetic field strengths that are far weaker. As such, all of the scalings are approximately consistent in their prediction of the minimum radius that a planetesimal must have in order to meet *both* the magnetic field strength and dynamo duration requirements.

5.5 Discussion

These results indicate that a dynamo driven by thermal convection may not be present in planetesimals smaller than $\sim 500 - 1000$ km, providing an important constraint on the required size of a meteorite parent body as the source of uniformly magnetized meteorites. We have varied numerous parameters in our thermal evolution models such as core radius, accretion time, mantle reference viscosity, critical melt fraction, temperature-dependence of the mantle viscosity and planetesimal rotation period to investigate their effect on dynamo duration. Furthermore, we have derived an analytical approximation to dynamo duration that made both the dependencies and independencies of these parameters explicit, and which matches our numerical results very well.

5.5.1 Conductive versus convective modeling

Previous attempts to model the thermal evolution of planetesimals have typically relied on some implementation of the heat equation representing conductive heat transport from the interior of the planetesimal to the surface (e.g. Elkins-Tanton et al., 2011; Ghosh and

McSween, 1998; Gupta and Sahijpal, 2010; Hevey and Sanders, 2006; Sahijpal et al., 2007; Weiss et al., 2008; Weiss et al., 2010). In some cases convection in the mantle was not considered at all (Ghosh and McSween, 1998), was simulated by increasing the thermal conductivity by several orders of magnitude at a threshold temperature (Hevey and Sanders, 2006), or was invoked by assuming a homogeneous adiabatic mantle under a conductive unmelted crust (Elkins-Tanton et al., 2011). To investigate planetary accretion and the possibility of differentiation and core formation a conductive approach may well be justified. To study the possibility of magnetic field dynamos and their durations, however, accounting for convection in the mantle becomes very important as it increases heat transport and reduces the planetesimal's cooling time along with the duration of a dynamo.

Explicitly including convection in the mantle is critical as it controls the thickness of the outer thermal boundary layer. Models that estimate the boundary layer thickness using steady state assumptions (such as surface heat flow balancing internal heating) are in significant error and are unable to address the transient (warming/cooling) nature of the problem. Elkins-Tanton et al. (2011) assume a fixed thermal boundary layer thickness that is specifically chosen to allow for a large enough heat flow to produce a dynamo and a small enough heat flow to allow for a long duration. However, no physical explanation for the mechanism that maintains the thickness of the layer, preventing it from convectively eroding, melting, or thinning, is proposed. In that work, a fixed layer thickness is dynamically inconsistent with the assumption of a convecting mantle and the convective heat flow that is determined (see section 5.2.1). Even in the absence of convection the time scale to diffusively melt and thin the upper thermal boundary layer would be of the order of a million years or less (see the discussion regarding the Stefan problem for the propagation of a moving melt interface in Carslaw and Jaeger, 1986). Without a mechanism that would naturally allow for maintenance of a fixed thermal boundary layer an appeal must be made to an 'insulating' outer layer that has a low thermal conductivity. In theory, such a layer must always exist for stagnant-lid convection where at least part of the thermal boundary never experiences melting or even sintering and so a porous outer layer would maintain its

low thermal conductivity. However, such a layer has been shown to be very thin, on the order of meters in numerical simulations (Hevey and Sanders, 2006), in which case Appendix D.2 has shown this to be of little consequence. This leaves the external mechanism of continuous accretion as the remaining possibility where new cold porous material is delivered to the platenetesimal during the course of the thermal evolution at a rate or combination of rates (Sahijpal and Gupta, 2011) that would maintain such an insulating outer layer. We have derived an analytical solution for stagnant-lid convection with continuous accretion in Appendix D.3 and placed bounds on the accretion rates for which stagnant-lid convection can 'correct' for the addition of new material. For reasonable accretion rates, this is also unable to provide any form of 'insulation' and stagnant lid convection is able to quickly adjust the boundary layer thickness to compensate for any added material.

5.5.2 The role of temperature-dependent viscosity

The results in the present work can, for a large part, be reduced to a discussion about the temperature dependence of viscosity and the feedback that exists between the mantle's viscosity and temperature. The specific features of the viscosity law we rely in the present work do not control the resulting behavior we observed in the results. The absolute values over which the viscosity varies throughout the temperature range the planetesimal experiences are only important insofar as they allow the mantle to become sufficiently mobile to consider convection and its associated increased heat transport. The rheological transition the viscosity undergoes at $T = T_{crit}$ for a critical melt fraction is less important than the fact that viscosity has an exponential dependence on temperature. Any viscosity law that incorporates such a dependency will yield results similar to those found in this work. The degree to which the viscosity is dependent on temperature, as illustrated by β, does exert some control on the duration of a planetesimal dynamo. For a smaller dependence the viscosity will be larger and planetesimals must be larger to achieve a supercritical Rayleigh number for thermal convection along with the the sufficiently fast rate of cooling required

to drive a dynamo.

5.5.3 FUTURE WORK

Our consideration of convection in the thermal evolution of planetesimals is a necessary step beyond purely conductive modeling efforts towards a more complete understanding of the viability and duration of planetesimal dynamos. However, more work and questions remain to be addressed.

1. How will the constraints on planetesimal radius change if we allow for the development of a dynamo powered by compositional convection? This question was already addressed by Nimmo (2009) and it would be useful to revisit that work within the framework outlined in the present work.

2. Modeling the thermal evolutions of larger planetesimals should take pressure-dependent effects into account. For example, the slopes of the mantle solidus and liquidus with depth control how melting and solidification of the interior proceeds. As a result, rather than considering melting to occur simultaneously throughout the mantle, we must treat the outwardly propagating melt front as a Stefan problem with a convective boundary condition.

3. Evaluating specific planetesimal scenarios as they have been inferred from paleomagnetic and cosmochemical studies of meteorites (Weiss et al., 2008; Weiss et al., 2010).

5.6 CONCLUSIONS

In the present work we have attempted to place bounds on the space of possible parameters relevant to planetesimal dynamo occurrence and duration. As such, this work can be thought of as a broad strokes effort as there may be countless fortuitous combinations of parameters that would yield a early solar system planetesimal with a thermal convection dynamo. It is of course entirely possible that the realization of such a body resides in the tails of the probability distribution of any of the relevant parameters. However, although we

must keep the above in mind, any arguments made in this research endeavor are necessarily based on parameter values that are most likely.

Using a thermal boundary layer theory for stagnant lid mantle convection we have investigated to what extent an early solar system planetesimal could have generated and sustained a dynamo. Starting from an initially cool, undifferentiated body with a concentration of short-lived nuclides based on accretion age, we assess how the body heats up, differentiates and forms a core, and at what temperature the mantle begins to convect. This temperature T_{onset} is the starting temperature of our numerical thermal evolution model which we have evaluated for many parameter values. During each thermal evolution we determine if and for how long a dynamo is present, as well as the peak and mean magnetic field strengths. Our calculations allow us to place constraints on the minimum radius of a planetesimal for which it obtains a dynamo. The duration of a dynamo depends foremost on the planetesimal's radius. This strong dependence ($t_{dyn} \propto r^4$) makes our estimates of minimum radii robust against uncertainties in the various parameters involved. Our results suggest that planetesimals smaller than ~ 500 km will be unable to maintain a sufficiently strong dynamo for a duration of the order of ten million years. We found that dynamo duration, to a lesser extent, also depends on the effective temperature dependence of the mantle viscosity, β, and on the rotation rate of the planetesimal, Ω. These dependencies were made explicit by our derivation of an analytical approximation to the dynamo duration. Moreover, this approximation performed very well in capturing the behavior of dynamo duration in all of the thermal evolutions. The definition of the critical magnetic Reynolds number also plays a role, in a constitutive sense, as well as what scaling law we rely on to arrive at a magnetic Reynolds number.

Consideration of the changing thickness of the thermal boundary layer as the planetesimal thermally evolves is pivotal. Because this thickness varies dynamically, allowing for a strong feedback between heat flow and interior temperature, the model planetesimals can shed a relatively large amount of heat in the initial stages of the thermal evolution. This strongly affects the cooling time and dynamo duration with it. Models where the ther-

mal boundary layer thickness is held constant are able to retain heat for longer artificially extending the duration of any dynamo.

Chapter 6

Conclusions and future work

In addition to the conclusions given at the end of Chapters 3, 4, and 5, we will end with a few final remarks regarding future work and applications of the models developed in this study.

Much of the work done in Chapters 2 through 4 was motivated by the desire to be able to calculate a thermal history for the Earth. This requires a model for calculating the surface heat flow as a function of the material properties (plate and mantle) as well as the thermal state (temperature and internal heating rate) of the system. Such a model, that included strong surface plates, was developed in Chapter 3 and revealed a rich and complex solution space with multiple solutions and various modes of convection. Any calculation of a thermal history also requires the ability to properly assess how the state and properties of the system evolve as a function of time. In Chapter 4 we demonstrated that the transport of water to and from the mantle, via regassing at subduction zones and degassing at ridges, leads to a significant change in mantle viscosity. We demonstrated that this effect created a strong feedback that fundamentally changed the nature of the thermal evolution. The application of the theory developed in Chapters 3 and 4 will affect thermal history calculations for the Earth (and other planets) in a first order way. However, there are many new questions that need to be addressed before such thermal histories may be calculated.

The model derived in Chapter 3 demonstrated that multiple solutions are often possible when strong plates are present. Each solution found corresponded to a unique mode of

τ_R	Convective Mode	Dominant Driving Force	Dominant Resisting Force	Plate Velocity Depends On
< 0	plate driven ($\approx$ mobile lid)	net slab pull τ_R	tractions	mantle properties
< 0	asthenospheric counter flow	net slab pull τ_R	mantle pressure gradient	mantle properties
> 0	mobile lid	tractions or pressure gradient	pressure gradient or tractions	mantle properties
> 0	sluggish lid (intermediate)	tractions or pressure gradient	net resisting stress τ_R	mantle and lithosphere properties
> 0	sluggish lid (slow)	gravitational (local potential)	net resisting stress τ_R	lithosphere properties

Table 6.1: Summary of distinct convective modes. Names for each convective mode are only suggestions at this point. The type of convective mode depends on the sign of the net resisting stress τ_R. The dynamics of the plate can depend on the properties of the mantle, lithosphere, or both, depending on the branch of solutions. Each convective mode has a distinct pair of dominant plate driving and resisting forces.

convection with a distinct pair of dominant plate driving and resisting terms. While only three branches of solutions were found to occur at the same time, five distinct modes were noted. One of the key parameters in determining the type of solution was the net resisting stress, defined as $\tau_R = \tau_F + \tau_Y - \tau_{SP}$, where τ_F represents the magnitude of the stress on the subduction zone interface, τ_Y is the magnitude of the effective stress associated with the deformation of the plate (depends on the model used), and τ_{SP} is the normal deviatoric stress on the base of the plate due to slab pull. These three stresses were grouped together as they all scaled in the same way in the lithospheric energy balance. This grouping reduced the number of free model parameters and therefore also the difficulty of exploring the very large solution space that exists.

Table 6.1 summarizes the different convective modes that were found to occur. The second mode, asthenospheric counter flow, can only occur if a low viscosity asthenosphere (or upper mantle) is present. In addition, the two sluggish lid modes can have a channelized flow beneath the plate if a low viscosity layer is present there. The type of convective mode depends critically on the sign of the net resisting stress τ_R. τ_R may be thought of as a 'net'

slab pull stress when $\tau_R < 0$ or as a 'net' resisting stress when $\tau_R > 0$. Each convective mode has its own distinct pair of dominant plate driving and resisting forces.

Clearly, priority should be given to trying to determine the sign of τ_R for the Earth's plates. This is made difficult, however, as many of the models that predict the amount of slab pull and the effective strength of the plate are based on incomplete energy (or force) balances. As an example, Wu et al. (2008) have most recently attempted to estimate the strength of plates using a 3D model with realistic plate geometries for the present day surface of the Earth. Plates are implemented as boundary conditions and therefore have an effective thickness of zero (no plate material enters or leaves the mantle). Thus, any term in the energy balance that scales with the plate thickness, such as the plate bending term, gravitational sliding, and the work done by the mantle pressure gradient, will all be zero unless explicitly parameterized and added in. The plate bending and gravitational sliding terms have been parameterized and added. The pressure term, however, is absent from the model. As such, the model will underestimate the strength of the plate. The addition of the pressure term to a model such as this, that is otherwise an excellent model, is trivial. The problem of evaluating the present day force balance for the Earth's plates needs to be revisited and all terms properly accounted for. This will allow us to better estimate the material properties of the plate-mantle system, which will be necessary for properly determining the energy balance and dynamics in Earth's early evolution when the state of the system was likely very different.

Table 6.1 also indicates whether the plate velocity depends on the properties of only the mantle, only the lithosphere, or both the mantle and the lithosphere. Different solution branches are sensitive to different properties of the plate-mantle system and as such different solution branches are likely to have their own distinct dynamic feedbacks in an evolution calculation. For example, water is likely to generate very different feedbacks during a dynamic evolution for the mobile lid and sluggish lid solution branches. The mobile lid solutions are mainly sensitive to the mantle properties. As such, we expect water to lead to the dynamic feedback that arises from the affect of water on mantle viscosity, as discussed

in Chapter 4. The sluggish lid solutions are partially (intermediate branch of solutions) or almost entirely (lower branch of solutions) dependent on the properties of the plate. In this case the dominant role of water may be related to the dehydration and strengthening of the plate, as suggested by Hirth and Kohlstedt (1996) and the effect of water on the Earth's mantle viscosity may be negligible.

Chapter 3 noted that the number of solutions obtained from the model depends on the functional form of the mechanical plate thickness and surface heat flow. The calculations presented there, unless otherwise noted (section 3.3.6), assumed that the plate thickness and heat flow could be represented using thermal boundary layer theory and assuming the simple half space cooling model. Other parameterizations could be used, such as the model of Korenaga (2003) that assumes that the mechanical thickness of the plate is determined by the dehydration depth. This could lead to a different number of solutions with different solution branch behavior. The same global and lithospheric energy balances derived in section 3.2.6 will still govern and the solutions must still involve one of the previously mentioned dominant balances. The plate velocity determined for each solution branch may, however, be very different. The behavior of the system will be all the more complicated should the functional form of the plate thickness, and thus the behavior of the different solution branches, change throughout the thermal history of the Earth. This is in fact exactly what is suggested by Korenaga (2003). The model derived in Chapter 3 provides a theoretical and conceptual framework for addressing such issues.

The analytic model was compared to complex numerical convection simulations that exhibited transitions in convective mode, multiple solutions, path dependence, and episodic convection. The analytic model was able to reproduce the transition in convective mode that was discussed in section 3.3.6 and demonstrated that the transition occurred as the result of a change in dominant plate driving force. The regions of multiple solutions predicted by the analytic model are in agreement with those found in the numerical simulations. As the analytic model is a steady state model and has no time dependence we cannot say that we are able to 'reproduce' the results of the numerical simulations that demonstrate path

dependence or episodic convection. Nonetheless, the shape of the solution curve that the analytic model predicts is consistent with the path dependence observed and the analytic model predicts multiple solutions where episodic convection is present in the numerical simulations. Thus, all predictions of the analytic model regarding possible time dependence of the system are at least consistent with observations from the numerical simulations.

The existence of multiple solutions and path dependence is another complication that needs to be further studied and addressed prior to any thermal evolution calculation. Should multiple solutions be present, a theory for determining which convective mode will occur needs to be developed. This will likely involve a stability analysis of the different solution branches. Furthermore, the path dependence suggested by the analytic model and demonstrated in the numerical simulations implies that the initial condition or early evolution of the Earth may play a more important role in controlling the tectonic state and subsequent thermal evolution. Thus, the convenience provided by the self-regulating 'mantle thermostat' (Tozer, 1970) present in the Early thermal history calculations may be lost. This issue is important for any planet and suggests that, if multiple solutions are possible, the presence of plate tectonics on a planet such as a super-Earth (O'Neill and Lenardic, 2007; Valencia et al., 2007), may depend more on the evolution of the planet than it does on its thermal state and material properties.

Chapter 4 demonstrated that a strong feedback between heat and water transport exists when the volatile dependence of mantle viscosity is considered. Both theory and a simple evolution calculation were used to argue that the feedback with water would result in a fundamentally different evolution for a planet such as the Earth. Thermal history calculations that have not accounted for this effect (all but a couple simple ones) may be in significant error. One of the strengths of the theory developed in Chapter 4 is that it is a kinematic theory (see section 4.2). As such, it may be easily applied to any of the modes of convection found in Chapter 3.

Both strong plates and volatiles have been demonstrated to have a first order effect on the tectonic state and thermal evolution of a planet. Considered separately, each is likely to

provide a rich and diverse range of possible evolutions. Their effects, when combined, may very well lead to complex evolutions that are beyond the scope of simple analytic models. Numerical models may be needed to address such calculations. Nonetheless, the theory developed in this work will provide guidance for numerical models and a framework for interpreting their results.

Appendix A

The delta function solution

We consider here a new analytic solution for simple 2D thermal convection rolls in an isoviscous fluid layer. Figure 2.1 shows the assumed thermal structure and simple flow for thermal convection in an isoviscous layer with mixed heating. All material properties are assumed to be homogenous throughout the cell and the system is in steady state.

Flow in the convective cell is driven by lateral variations in density resulting from the warm upwelling and the cool downwelling. At high Rayleigh numbers the thermal boundary layers, upwellings, and downwellings all become extremely thin relative to the depth of the layer (d is the characteristic length scale of the problem). We will approximate the density field for the upwelling and downwelling using delta functions. This will allow us to work out a simple spectral solution to the velocity field which can then be combined with thermal boundary layer theory to calculate the amplitude of the convective flow.

We begin by parameterizing the heat flow as a function of the temperature drop across the thermal boundary layers, the material properties of the fluid, and the average boundary velocities. The heat flow is related to an approximate density field. An analytic solution for the full 2D velocity field is then calculated using the approximate density field. The average boundary velocities are then found and the amplitude of the flow is determined.

A.1 THE DENSITY FUNCTION

We first consider the simple case where the basal heat flux is zero (the boundary is insulated) and no thermal boundary layer exists at the base of the fluid layer. Cool material from the upper thermal boundary layer sinks at position $x = 0$ and creates the cool downwelling that drives the convective cell. We assume an infinitely long fluid layer with convection cells of wavelength of $\lambda = 2L$. We approximate the density anomaly field in the convective cell as

$$\Delta\rho(x) = \Delta\rho_{eff}\delta\left(\frac{x}{2L}\right) \tag{A.1}$$

where $\Delta\rho_{eff}$ is a normalization factor that will be determined through conservation of mechanical energy. Note that $\Delta\rho$ in equation (A.1) is independent of the vertical position in the fluid cell z (where $z = 0$ at the base of the convective cell and $z = d$ at the surface). This is also an approximation to allow a simple solution to be worked out. The total rate of change of potential energy in the cell, per unit distance along the axis of the convective roll (third dimension), is given by equation (2.7) and is again

$$\Phi_P = \frac{\alpha g d}{C_p} k\Delta T \left(\frac{\bar{U}L}{\pi\kappa}\right)^{\frac{1}{2}} \tag{A.2}$$

where α is the thermal expansion coefficient, g is the gravitational acceleration, d is the depth of the fluid layer, k is the thermal conductivity, ΔT is the temperature drop across the fluid layer (in this case also equal to the temperature drop across the cold thermal boundary layer), $\bar{U}$ is the average horizontal surface velocity, L is the length of a single convection cell, and κ is the thermal diffusivity. The rate of change of potential energy in the cell can also be calculated using equation (3.15) which gives, per unit distance along the axis of the convective roll,

$$\Phi_P = \frac{1}{2}\int_0^d \int_{-L}^{L} \Delta\rho(x,z) g v(x,z) dx dz \tag{A.3}$$

where we are integrating across two convective cells ($-L < x < L$) and taking half to obtain the energy for a single cell. Substituting equation (A.1) into equation (A.3) gives

$$\begin{aligned}
\Phi_P &= \frac{g}{2}\int_0^d \int_{-L}^{L} \Delta\rho_{eff}\delta\left(\frac{x}{2L}\right) v(x,z)dxdz \\
&\approx \frac{g\Delta\rho_{eff}}{2}\int_0^d \int_{-\infty}^{\infty} \delta\left(\frac{x}{2L}\right) v(x,z)dxdz \\
&= g\Delta\rho_{eff}L\int_0^d v(x=0,z)dz \\
&= g\Delta\rho_{eff}Ld\bar{V} \qquad \text{(A.4)}
\end{aligned}$$

where

$$\bar{V} = \frac{1}{d}\int_0^d v(x=0,z)dz \qquad \text{(A.5)}$$

is the depth averaged vertical velocity at $x = 0$. Equating the right hand sides of equations (A.2) and (A.4) and solving for $\Delta\rho_{eff}$ then gives

$$\Delta\rho_{eff} = \frac{\alpha\rho\Delta T}{\bar{V}}\left(\frac{\bar{U}\kappa}{\pi L}\right)^{\frac{1}{2}} \qquad \text{(A.6)}$$

where we have also used $\kappa = k/\rho C_p$. Equation (A.6) relates the magnitude of the effective density anomaly represented by the delta function approximation to the average horizontal velocity at the surface $\bar{U}$ and the average vertical velocity in the downwelling ($x = 0$) $\bar{V}$. Equation (A.6) ensures that energy is conserved in the system.

We will now briefly review the propagator solution in order to determine the average surface velocity $\bar{U}$ and average downwelling velocity $\bar{V}$ as a function of $\Delta\rho_{eff}$. $\bar{U}$ and $\bar{V}$ will then be substituted into equation (A.6) and $\Delta\rho_{eff}$ solved for. The size of $\Delta\rho_{eff}$ will determine the finite amplitude of the convective flow.

A.2 THE PROPAGATOR METHOD

The propagator approach of Hager and O'Connell (1981) is used to derive an analytic solution using the density anomaly defined in equation (A.1). As in Hager and O'Connell

(1981), the relevant equations for a high Prandtl number and low Reynolds number flow are the momentum equation

$$0 = \nabla \cdot \tau + \Delta\rho\mathbf{g} \tag{A.7}$$

and the constitutive equation for a Newtonian fluid

$$\tau = -p\mathbf{I} + \eta\left[\nabla\mathbf{u} + (\nabla\mathbf{u})^{\mathbf{T}}\right] \tag{A.8}$$

where τ is the deviatoric stress, p is the pressure, η is the viscosity, and $\mathbf{u}$ is the velocity. An incompressible flow is assumed. Thus

$$\nabla \cdot \mathbf{u} = 0 \tag{A.9}$$

The velocities, stresses, pressure, and density are represented using Fourier expansions in the x dimension as

$$u(x,z) = \sum_{n=1}^{\infty} u_n(z)\ sin(k_n x) \tag{A.10}$$

$$v(x,z) = \sum_{n=1}^{\infty} v_n(z)\ cos(k_n x) \tag{A.11}$$

$$\tau_{zz}(x,z) = \sum_{n=1}^{\infty} \tau_{zz_n}(z)\ cos(k_n x) \tag{A.12}$$

$$\tau_{xx}(x,z) = \sum_{n=1}^{\infty} \tau_{xx_n}(z)\ cos(k_n x) \tag{A.13}$$

$$\tau_{xz}(x,z) = \sum_{n=1}^{\infty} \tau_{xz_n}(z)\ sin(k_n x) \tag{A.14}$$

$$p(x,z) = \sum_{n=1}^{\infty} p_n(z)\ cos(k_n x) \tag{A.15}$$

and

$$\Delta\rho(x,z) = \sum_{n=1}^{\infty} \Delta\rho_n(z)\ cos(k_n x) \tag{A.16}$$

with the n^{th} Fourier coefficient being denoted by the subscript n. A solution using the propagator technique can be derived that relates the Fourier coefficients through the equation

$$\mathbf{U_n}(z) = \mathbf{P_n}(z, z_o) \cdot \mathbf{U_n}(z_o) + \int_{z_o}^{z} \mathbf{P_n}(\zeta, z_o) \cdot \mathbf{b_n}(\zeta) d\zeta \tag{A.17}$$

where the vector $\mathbf{U_n}$ is defined as

$$\mathbf{U}_n(z) = \begin{bmatrix} v_n(z) \\ u_n(z) \\ \frac{\tau_{zz_n}(z)}{2k_n\eta} \\ \frac{\tau_{xz_n}(z)}{2k_n\eta} \end{bmatrix} \tag{A.18}$$

with v_n, u_n, ${}_n\tau_{zz}$, and ${}_n\tau_{xz}$ being the n^{th} Fourier coefficient of the vertical velocity, horizontal velocity, vertical normal stress, and shear stress, respectively. The propagator matrix $\mathbf{P_n}(z, z_o)$ is defined as

$$\mathbf{P_n}(z, z_o) = e^{\mathbf{A_n}(z - z_o)} \tag{A.19}$$

with the matrix $\mathbf{A_n}$ given by

$$\mathbf{A}_n = \begin{bmatrix} 0 & -k_n & 0 & 0 \\ k_n & 0 & 0 & 2k_n \\ 0 & 0 & 0 & -k_n \\ 0 & 2k_n & k_n & 0 \end{bmatrix} \tag{A.20}$$

and the wavenumber $k_n = 2\pi n/\lambda$. The vector $\mathbf{b_n}$ in equation (A.17) is given by

$$\mathbf{b}_n(z) = \begin{bmatrix} 0 \\ 0 \\ \frac{\Delta\rho_n(z)g}{2k_n\eta} \\ 0 \end{bmatrix} \tag{A.21}$$

The Fourier coefficients for the density anomaly defined in equation (A.1) are independent of n and z and are simply

$$\Delta\rho_n = \Delta\rho_{eff} \tag{A.22}$$

The delta function is useful for approximating the density field as its Fourier representation is extremely simple. As there is no depth dependence in $\Delta\rho_n$, $\mathbf{b_n}$ will also have no depth dependence and the integral in equation (A.17) may be evaluated to give

$$\mathbf{U_n}(z) = \mathbf{P_n}(z, z_0) \cdot \mathbf{U_n}(z_0) + \mathbf{A_n^{-1}} \cdot (\mathbf{P_n}(z, z_0) - \mathbf{I}) \cdot \mathbf{b_n} \tag{A.23}$$

This equation may be used to relate solutions within the layer (vertical position z) to solutions at the base of the layer ($z_0 = 0$) through

$$\mathbf{U_n}(z) = \mathbf{P_n}(z, 0) \cdot \mathbf{U_n}(0) + \mathbf{A_n^{-1}} \cdot (\mathbf{P_n}(z, 0) - \mathbf{I}) \cdot \mathbf{b_n} \tag{A.24}$$

Equation (A.24) gives the solution for the velocity and stress fields as a function of depth and requires the solution at the base of the layer $\mathbf{U_n}(0)$ as well as the amplitude of the density anomaly $\Delta\rho_{eff}$.

A.3 SOLUTION FOR A LAYER WITH FREE-SLIP BOUNDARIES

For free-slip closed boundaries the vertical velocities and shear stresses will both be zero on the horizontal boundaries ($z = 0$ and $z = d$). We can solve for the horizontal velocity and normal stress on these boundaries by setting $z = d$ in equation (A.24)

$$\begin{bmatrix} 0 \\ u_n(d) \\ \frac{\tau_{zzn}(d)}{2k_n\eta} \\ 0 \end{bmatrix} = \mathbf{P_n}(d, 0) \cdot \begin{bmatrix} 0 \\ u_n(0) \\ \frac{\tau_{zzn}(0)}{2k_n\eta} \\ 0 \end{bmatrix} + \mathbf{A_n^{-1}} \cdot (\mathbf{P_n}(d, 0) - \mathbf{I}) \cdot \mathbf{b_n} \tag{A.25}$$

Equation (A.25) represents a system of four equations for each of the n Fourier coefficients with $u_n(0)$, $u_n(d)$, $\tau_{zz_n}(0)$, and $\tau_{zz_n}(d)$ being the four unknown boundary conditions. Equation (A.25) can be rearranged to solve for the unknown boundary conditions. This then provides a solution for the lower boundary condition

$$\mathbf{U_n}(0) = \frac{\Delta\rho_n g}{2k_n^2\eta} \begin{bmatrix} 0 \\ \frac{\sinh(k_n d)-k_n d}{1+\cosh(k_n d)} \\ \frac{-2\sinh(k_n d)+k_n d}{1+\cosh(k_n d)} \\ 0 \end{bmatrix} \tag{A.26}$$

$\mathbf{U_n}(0)$ from equation (A.26) can now be substituted back into equation (A.24) and yields the Fourier coefficients for the velocities as a function of depth

$$\begin{aligned} u_n(z) &= \frac{\Delta\rho_{eff} g}{2k_n^2\eta}\left[\frac{\sinh((d-z)k_n)-\sinh(zk_n)}{1+\cosh(dk_n)}\right. \\ &\left. +\frac{k_n(z\cosh((d-z)k_n)+(z-d)\cosh(zk_n))}{1+\cosh(dk_n)}\right] \end{aligned} \tag{A.27}$$

$$\begin{aligned} v_n(z) &= \frac{\Delta\rho_{eff} g}{2k_n^2\eta}\left[\frac{k_n(z\sinh((d-z)k_n)+(d-z)\sinh(zk_n))}{1+\cosh(dk_n)}\right. \\ &\left. +\frac{2(\cosh((d-z)k_n)-\cosh(dk_n)+\cosh(zk_n)-1)}{1+\cosh(dk_n)}\right] \end{aligned} \tag{A.28}$$

We can now calculate the average horizontal surface velocity and vertical velocity in the downwelling as

$$\bar{U} = \frac{1}{L}\int_0^L u(x, z=d)dx \tag{A.29}$$

and

$$\bar{V} = \frac{1}{d}\int_0^d v(x=0, z)dz \tag{A.30}$$

Using equations (A.10) and (A.11) along with equations (A.28) through (A.30) gives

$$\bar{U} = 2\frac{\Delta\rho_{eff}g}{\eta\lambda}\sum_{n=1,2,\ldots}^{\infty}\frac{1}{k_n^3}\frac{\sinh(dk_n)-dk_n}{1+\cosh(dk_n)} \tag{A.31}$$

and

$$\bar{V} = \frac{\Delta\rho_{eff}g}{\eta d}\sum_{n=1,2,\ldots}^{\infty}\frac{1}{k_n^3}\frac{3\sinh(dk_n)-dk_n(2+\cosh(dk_n))}{1+\cosh(dk_n)} \tag{A.32}$$

To keep things reasonably compact we define the functions f_1 and f_2 as

$$f_1(s) = \sum_{n=1,2,\ldots}^{\infty}\frac{1}{n^3}\frac{\sinh(\pi ns)-\pi ns}{1+\cosh(\pi ns)} \tag{A.33}$$

and

$$f_2(s) = \sum_{n=1,2,\ldots}^{\infty}\frac{1}{n^3}\frac{3\sinh(\pi ns)-\pi ns(2+\cosh(\pi ns))}{1+\cosh(\pi ns)} \tag{A.34}$$

Note that as $n \to \infty$ the terms in equations (A.33) and (A.34) scale as n^{-3} and n^{-2} and thus both series are sure to converge. Using equations (A.33) and (A.34) we can now rewrite equations (A.31) and (A.32) as

$$\bar{U} = \frac{\Delta\rho_{eff}gL^2}{\eta\pi^3}f_1\left(\frac{d}{L}\right) \tag{A.35}$$

and

$$\bar{V} = \frac{\Delta\rho_{eff}gL^3}{\eta d\pi^3}f_2\left(\frac{d}{L}\right) \tag{A.36}$$

where $\lambda = 2L$ has been used. We now substitute equations (A.35) and (A.36) into equation (A.6) and solve for $\Delta\rho_{eff}$

$$\Delta\rho_{eff} = \alpha\rho\Delta T\left(\frac{\pi^2}{Ra}\right)^{\frac{1}{3}}\left(\frac{d}{L}\right)^{\frac{5}{3}}\frac{f_1\left(\frac{d}{L}\right)^{\frac{1}{3}}}{f_2\left(\frac{d}{L}\right)^{\frac{2}{3}}} \tag{A.37}$$

with the Rayleigh number again defined as

$$Ra = \frac{\alpha \rho g \Delta T d^3}{\eta \kappa} \tag{A.38}$$

We can also consider the case where the system is driven by both a downwelling (again at $x = 0$) and an upwelling (at $x = \pm L = \pm\lambda/2$) of equal magnitude. The density field is now given by

$$\Delta\rho_b(x) = \Delta\rho_{eff_b}\left[\delta\left(\frac{x}{2L}\right) - \delta\left(\frac{1}{2} - \frac{x}{2L}\right)\right] \tag{A.39}$$

The b subscript on these solutions indicate that a bottom boundary layer and upwelling are present. The solution for the flow field is still given by equations (A.28) and (A.29) with $\Delta\rho_n$ given by

$$\Delta\rho_n = \Delta\rho_{eff_b}\left(1 + (-1)^{n+1}\right) \tag{A.40}$$

The second term accounts for the negative density anomaly (same magnitude) offset by half a wavelength. Note that odd terms will have $\Delta\rho_{n=odd} = 0$ and the solution will be symmetric about the center of the convective cell. For this case the average velocities are

$$\bar{U}_b = 4\frac{\Delta\rho_{eff} g}{\eta\lambda} \sum_{n=1,3,5,\ldots}^{\infty} \frac{1}{k_n^3} \frac{\sinh(dkn) - dk_n}{1 + \cosh(dk_n)} \tag{A.41}$$

and

$$\bar{V}_b = 2\frac{\Delta\rho_{eff} g}{\eta d} \sum_{n=1,3,5,\ldots}^{\infty} \frac{1}{k_n^3} \frac{3\sinh(dkn) - dk_n(2 + \cosh(dk_n))}{1 + \cosh(dk_n)} \tag{A.42}$$

Again we define functions f_{1b} and f_{2b} as

$$f_{1b}(s) = \sum_{n=1,3,5,\ldots}^{\infty} \frac{1}{n^3} \frac{\sinh(\pi ns) - \pi ns}{1 + \cosh(\pi ns)} \tag{A.43}$$

and

$$f_{2b}(s) = \sum_{n=1,3,5,\ldots}^{\infty} \frac{1}{n^3} \frac{3\sinh(\pi ns) - \pi ns(2 + \cosh(\pi ns))}{1 + \cosh(\pi ns)} \tag{A.44}$$

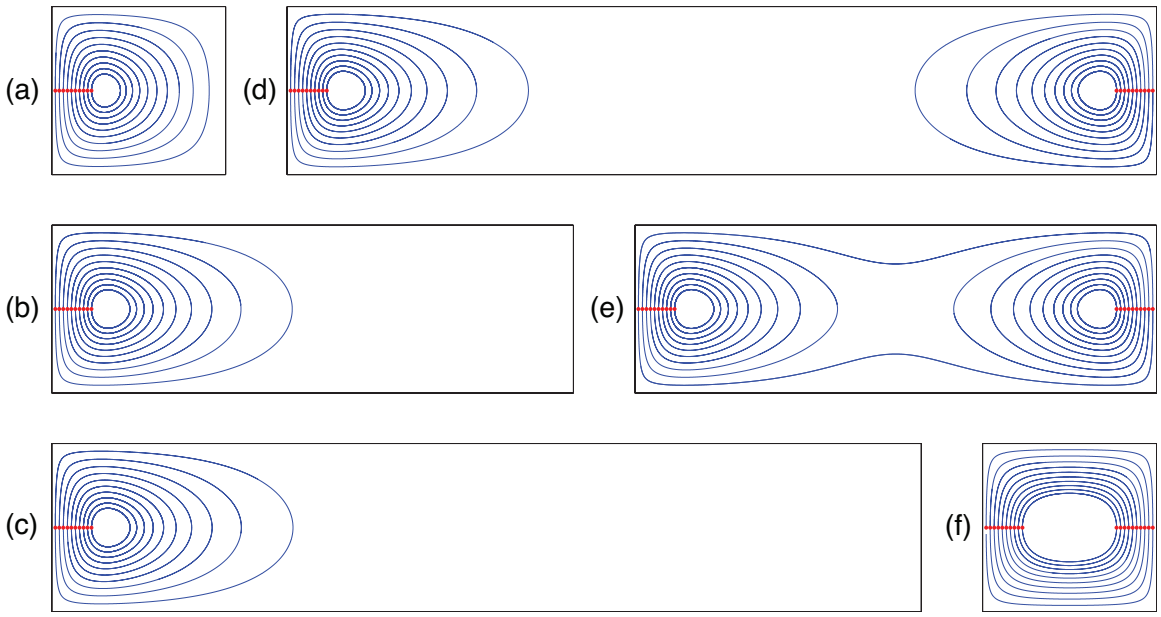

Figure A.1: Streamline plots for delta-function solution with closed cell.

Using equations (A.43) and (A.44) we can now rewrite equations (A.41) and (A.42) as

$$\bar{U}_b = 2\frac{\Delta\rho_{eff}gL^2}{\eta\pi^3}f_{1b}\left(\frac{d}{L}\right) \tag{A.45}$$

and

$$\bar{V}_b = 2\frac{\Delta\rho_{eff}gL^3}{\eta d\pi^3}f_{2b}\left(\frac{d}{L}\right) \tag{A.46}$$

For this case, $\Delta\rho_{eff_b}$ is given by

$$\Delta\rho_{eff_b} = \alpha\rho\Delta T\left(\frac{4\pi^2}{Ra}\right)^{\frac{1}{3}}\left(\frac{d}{L}\right)^{\frac{5}{3}}\frac{f_{1b}\left(\frac{d}{L}\right)^{\frac{1}{3}}}{f_{2b}\left(\frac{d}{L}\right)^{\frac{2}{3}}} \tag{A.47}$$

and only differs from that of the downwelling case by a factor of $2^{2/3}$.

These new solutions *do not* provide us with any new insight as far as scalings are concerned. The boundary velocities above scale as $Ra^{2/3}$ and the heat flow scales as $Ra^{1/3}$, as expected from the simple derivation in section 2.1. What these new solutions *do* provide us with is insight regarding the nature of the flow as a function of the wavelength. Plots (a)

through (c) of Figure A.1 show streamlines, calculated using equations (A.28) and (A.29) for cases with $L/d = 1$, 2, and 3, respectively, and when only a downwelling is present. We see that there is a natural horizontal length scale for the circulation of fluid in the layer that is of order d. Plots (d) through (f) of Figure A.1 show streamlines for cases with $L/d = 3$, 2, and 1, respectively, and when both downwelling and upwelling are present. Again, there is a natural horizontal length scale for flow driven by the downwelling and upwelling. At small aspect ratios the superposition of the flows driven by the downwelling and upwelling produces a single simple cellular flow. As the aspect ratio increases, however, the flows decouple and for very large aspect ratios two separate circulatory cells are present; one driven by the downwelling and one driven by the upwelling. Fluid away from the ends of cells with very large aspect ratios is then stationary and the use of thermal boundary layer theory for calculating the surface heat flow is then questionable. Nonetheless, this analysis is useful for demonstrating the natural horizontal length scale for a convecting isoviscous fluid layer.

A.4 Extended applications of the delta function solution

This type of solution easily lends itself to several other interesting problems with different boundary conditions.

In section A.3 we considered solutions where the upper and lower boundaries of the convective cell were closed and free-slip. These boundary conditions led to equation (A.24) which was then solved to obtain the solution for the fluid flow. We noted that Figure A.1 revealed a decoupling of the two flows driven by the upwelling and downwelling at large aspect ratio. This decoupling was possible due to the free-slip (zero shear stress) boundary condition at the base and surface of the fluid layer.

For the Earth, strong plates exist at the surface and the strong upper boundary layer would couple flows across the length of the convective cell. Another reasonable problem to consider is then one in which the horizontal velocity at the surface is constant for a single convection cell. This can be accomplished by representing the horizontal velocity at the

surface as a square wave with wavelength $\lambda = 2L$ and amplitude U. The surface velocity is then given by

$$u(x,d) = U\left(2\left[H\left(\frac{x}{L}\right) - H\left(\frac{x}{L} - 1\right)\right] - 1\right) \tag{A.48}$$

where H is the Heaviside function. Fortunately this also has a simple Fourier representation as

$$u(x,d) = U\sum_{n=1,3,5,\ldots}^{\infty} \frac{4}{n\pi} sin\left(k_n x\right) = U\sum_{n=1,2,3,\ldots}^{\infty} \tilde{u}_n \; sin\left(k_n x\right) \tag{A.49}$$

where $\tilde{u}_n = 4/n\pi$ for $n = odd$ and $\tilde{u}_n = 0$ for $n = even$. The vertical velocity at the surface is again zero (closed boundary) and the bottom boundary is again free-slip and closed. We can then use equation (A.24) with $z = d$ to relate the lower and upper boundaries through the equation

$$\begin{bmatrix} 0 \\ U\tilde{u}_n \\ \frac{\tau_{zz_n}(d)}{2k_n\eta} \\ \frac{\tau_{xz_n}(d)}{2k_n\eta} \end{bmatrix} = \mathbf{P_n}(d,0)\cdot\begin{bmatrix} 0 \\ u_n(0) \\ \frac{\tau_{zz_n}(0)}{2k_n\eta} \\ 0 \end{bmatrix} + \mathbf{A_n^{-1}}\cdot\left(\mathbf{P_n}(d,0) - \mathbf{I}\right)\cdot\mathbf{b_n} \tag{A.50}$$

Equation (A.50) provides a system of four equations for each of the n Fourier coefficients. The boundary conditions U, $\tau_{zz_n}(d)$, $\tau_{xz_n}(d)$, $u_n(o)$, and $\tau_{zz_n}(0)$ represent five unknown variables that need to be determined. We need one more equation in order to fully solve this problem. The final equation comes from requiring that the net force on the base of the surface (plate) be equal to zero. The net force on the base of the plate is required if the plate is not accelerating and thus we have as our fifth equation

$$\int_0^L \tau_{xz}(x)dx = 0 \tag{A.51}$$

Solving equations (A.50) and (A.51) together provide the unknown Fourier coefficients and the magnitude of plate velocity in terms of $\Delta\rho_{eff}$. The rest of the problem can then be worked out to determine $\Delta\rho_{eff}$ as in the previous section.

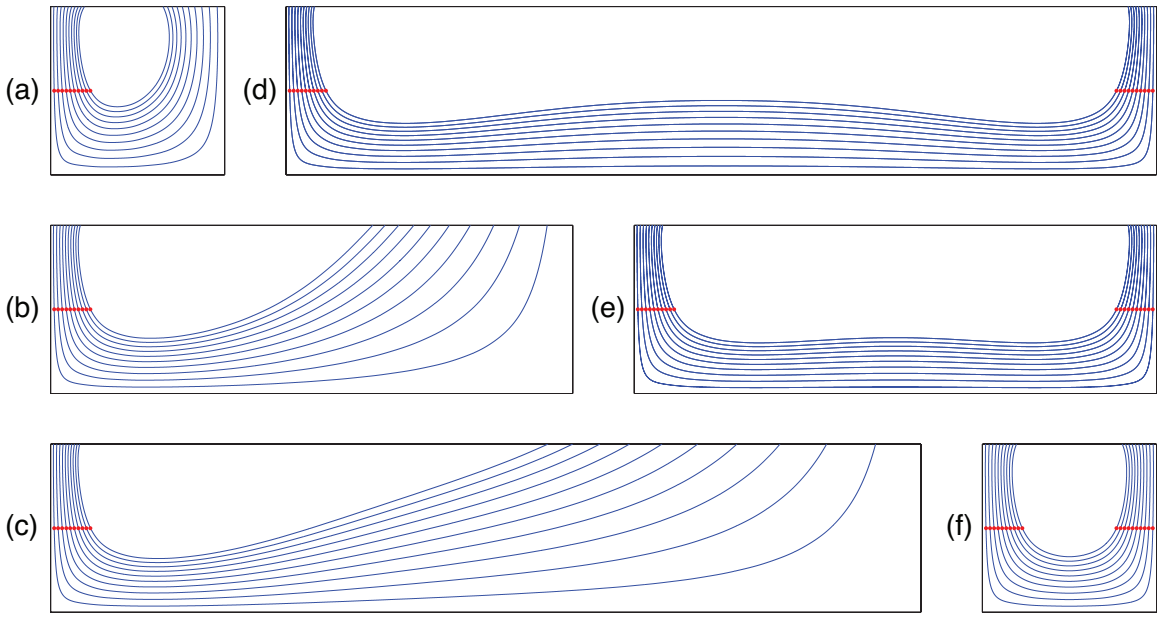

Figure A.2: Streamline plots for delta-function solution with open cell.

An additional interesting boundary condition is for the case when the upper boundary is not closed but instead open so that fluid may freely flow into and out of the surface of the convecting layer. We consider the case where the stresses on the upper boundary are very small. The viscosity contrast between the Earth's upper and lower mantle may provide a physical example of when such a case might be expected to occur. The Earth's upper mantle viscosity is thought to be between one and two orders of magnitude lower than the viscosity in the lower mantle. Stresses on the surface of lower mantle would then be very small compared to stresses within the lower mantle itself. If we then consider our fluid layer to represent the lower mantle then fluid is free to flow through the upper boundary (into the upper mantle) and stresses at the upper boundary (from upper mantle flow) are very small. We then look to solve for the velocities at the upper surface with the stresses on this boundary set to zero. The lower boundary is again free-slip (zero shear stress) and closed (zero vertical velcoity). Then, using equation (A.24) the lower and upper boundaries are related through the equation

$$\begin{bmatrix} v_n(d) \\ u_n(d) \\ 0 \\ 0 \end{bmatrix} = \mathbf{P_n}(d,0) \cdot \begin{bmatrix} 0 \\ u_n(0) \\ \frac{\tau_{zz_n}(0)}{2k_n\eta} \\ 0 \end{bmatrix} + \mathbf{A_n^{-1}} \cdot (\mathbf{P_n}(d,0) - \mathbf{I}) \cdot \mathbf{b_n} \tag{A.52}$$

Again, equation (A.52) provides a system of four equations for the four unknown Fourier coefficients $v_n(d)$, $u_n(d)$, $u_n(0)$, and $\tau_{zz_n}(0)$ for each n. This is easily solved by rearranging equation (A.52) and provides the coefficients in terms of the effective density anomaly $\Delta\rho_{eff}$ given by equation (A.1) for the downwelling or equation (A.39) with both the upwelling and downwelling. We could calculate the magnitude of the flow by relating $\Delta\rho_{eff}$ to the heat flow and boundary velocities as we did in section A.3. However, we will not do this here as a scaling for the open layer convective case is worked out in section 2.3.

We can plot the streamlines for the open layer case by normalizing the velocity by the density anomaly. The velocities are then independent of the magnitude of the density anomaly. Plots (a) through (c) of Figure A.2 show streamlines for the open layer case with aspect ratios of $L/d = 1$, 2, and 3, respectively, and when only a downwelling is present. Plots (d) through (f) of Figure A.2 show streamlines for aspect ratios of $L/d = 3$, 2, and 1, respectively, when both upwelling and downwelling are present. The results demonstrate that the flow extends over a much larger horizontal length scale for the open cell cases then the closed cell cases shown in Figure A.1.

Figure 2.4 shows a comparison between the streamlines calculated using the analytic solution discussed here and the streamlines from a numerical simulation of thermal convection with a viscosity increase of a factor of 10^3 in the lower half of the fluid layer. The streamlines agree reasonably well and the numerical simulation further corroborates the idea an 'open' convecting fluid layer.

Appendix B

Additional calculations for Chapter 3

B.1 Calculation of the boundary term for the lithosphere

The purpose of this section is to evaluate the boundary term in equation (3.42) for work done on the base of the lithosphere.

Material enters the lithosphere over a length scale of l_u at the upwelling end of the cell. Material leaves the lithosphere over a length scale of l_d at the downwelling end of the cell. Vertical velocities between the lithosphere and mantle are assumed to be zero in the interior of the cell (i.e. $u_y = 0$ for $l_u < x < l_d$). The total flow rate of material in the lithosphere is $d_{_L} U_{_P}$. Then the average vertical velocity of material entering the lithosphere near $x = 0$, by conservation of mass, is $\bar{u}_{y_0} = (d_{_L}/l_u) U_{_P}$. Similarly, the average vertical velocity of material leaving the lithosphere, near $x = L$, is $\bar{u}_{y_L} = -(d_{_L}/l_d) U_{_P}$. The boundary term for the base of the lithosphere ($dS_j = dS_y$ and $y = d_{_M} + d_{_A}$ for all terms) may now be evaluated, per unit length in the third direction, as

$$
\begin{aligned}
& \int_{S_{LA}} (u_i P\delta_{ij} - u_i\tau_{ij})\, dS_j \qquad \text{(B.1)} \\
= \;& \int_0^L (u_y P + u_y\tau_{yy} - u_x\tau_{xy})\, dx \\
= \;& \int_0^{l_u} u_y\,(P+\tau_{yy})\, dx + \int_{L-l_d}^{L} u_y\,(P+\tau_{yy})\, dx \\
& -U_{_P}\tau_{_P}L \\
\approx \;& \bar{u}_{y_0}\,(P(0)+\tau_{yy}(0))\, l_u + \bar{u}_{y_L}\,(P(L)+\tau_{yy}(L))\, l_d \\
& -U_{_P}\tau_{_P}L \\
= \;& \frac{d_{_L}}{l_u}U_{_P}\,(P(0)+\tau_{yy}(0))\, l_u \\
& +\frac{-d_{_L}}{l_d}U_{_P}\,(P(L)+\tau_{yy}(L))\, l_d - U_{_P}\tau_{_P}L \\
= \;& -d_{_L}U_{_P}\,(P(L)-P(0)) - d_{_L}U_{_P}\,(\tau_{yy}(L)-\tau_{yy}(0)) \\
& -LU_{_P}\tau_{_P} \\
= \;& -d_{_L}U_{_P}P_{x_P}L - d_{_L}U_{_P}\,(\tau_{yy}(L)-\tau_{yy}(0)) \\
& -LU_{_P}\tau_{_P}.
\end{aligned}
$$

where $P_{x_P} = \frac{\partial P}{\partial x}(y = d - d_{_L})$ and $\tau_{_P} = \tau_{xy}(y = d - d_{_L})$ are the lateral pressure gradient and shear stress evaluated on the base of the lithosphere. In evaluating equation (B.1) we have assumed that l_u and l_d are small enough that the pressure and deviatoric stress do not vary significantly over the area of integration and a single representative average can be used.

The second term on the right hand side of equation (B.1) includes the normal deviatoric stresses on the base of the ends of the plate. For the Earth, this would correspond to the deviatoric stress on the base of the plate at the ridge and at the subduction zone. A significant normal deviatoric stress may be expected at the subducting end of the plate due to slab pull. The normal stress due to slab pull should be much larger than any deviatoric normal stress exerted on the ridge end of the plate. We will simplify the second term on the right hand side of equation (B.1) by making two further assumptions. The first is that

$\tau_{yy}(L) - \tau_{yy}(0) \approx \tau_{yy}(L)$. This assumes that the contribution from the deviatoric normal stress at the subduction zone is much larger than the contribution from the ridge end of the plate. The energy term associated with $\tau_{yy}(L)$ represents part of what is commonly known as slab-pull. For this reason and for purposes of clarity we will rename it as $\tau_{SP} = \tau_{yy}(L)$. We can estimate the maximum normal stress that could by exerted by the weight of a slab by considering the average temperature difference in the slab and by assuming that all of the weight of the slab is supported by the plate above. If the average temperature difference in the slab is ΔT, then the stress exerted by a slab of length h would be $\sigma_{yy} = \alpha\rho\Delta T g h$. Conrad and Lithgow-Bertelloni [2002] estimated that the slab-pull component was about half the weight of the slab in the upper mantle. Using $h \approx 330\,km$ and $\Delta T \approx 500\,K$, this corresponds to a normal stress of $\tau_{SP} \approx \alpha\rho\Delta T g h \approx 150\,MPa$ and is of the order of the estimated yield stress of plates. With the above assumptions and notation, equation (B.1) then simplifies to

$$\begin{aligned} & \int_{S_{LA}} (u_i P \delta_{ij} - u_i \tau_{ij})\, dS_j \\ \approx \; & -\left(d_{_L} U_{_P} P_{x_P} L + d_{_L} U_{_P} \tau_{SP} + L U_{_P} \tau_{_P}\right). \end{aligned} \tag{B.2}$$

B.2 CALCULATING LATERAL FLOW AND DISSIPATION IN THE MANTLE

This section will describe how the energy balance equations are solved in practice.

Flow and dissipation in the mantle may be calculated for an arbitrary number of layers. To keep things simple we will solve the equations for a plate above a two layer system with an upper mantle (or an asthenosphere) and a lower mantle.

The horizontal component of the velocity, as a function of depth, is solved using the momentum equation with zero vertical velocity and is given by equation (3.28). A linear approximation for the pressure gradient is used and is given by equation (3.33). The parameters A and b in equation (3.33) depend on the viscosity structure, layer thicknesses, plate strength, heal flow, etc. Substituting equation (3.33) into equation (3.28) yields

$$\mu(y)\frac{\partial^2}{\partial y^2}U(y) = Ay + b. \tag{B.3}$$

Any continuously vertically varying viscosity structure $\mu(y)$ may be approximated by dividing it into n distinct layers with each layer having a constant viscosity. Our model has three layers that are meant to represent the lithosphere, upper mantle (or asthenosphere), and the lower mantle. Within a single layer ($y_0 < y_n < y_1$) equation (B.3) may be solved with a constant viscosity of μ_n to provide the velocity and stress in that layer. Continuity of velocity and stress between adjacent layers can then be used to calculate the full depth dependent horizontal velocity. Defining U_1 and τ_1 as the velocity and stress at the top of any given layer, the solution to equation (B.3) for the horizontal flow in an arbitrary layer is

$$U(y) = U_1 + \frac{y - y_1}{6\mu_n}\left(6\tau_1 + (y - y_1)(3b + Ay + 2Ay_1)\right). \tag{B.4}$$

From equation (B.4) the base velocity U_0 and stress τ_0 ($\mu_n \partial U/\partial y$) for the layer are

$$U_0 = U_1 + \frac{y_0 - y_1}{6\mu_n}\left(6\tau_1 + (y_0 - y_1)(3b + Ay_0 + 2Ay_1)\right) \tag{B.5}$$

and

$$\tau_0 = \tau_1 - \frac{1}{2}(y_1 - y_0)\left(2b + A(y_0 + y_1)\right). \tag{B.6}$$

Equations (B.5) and (B.6) relate the stress and velocity at the base of the layer to the stress and velocity at the surface of the layer through the thickness of the layer, the viscosity of the layer, and the parameters A and b in the pressure gradient. We now define U_P, U_A, and U_M as the velocity at the base of the plate, upper mantle (or asthenosphere), and lower mantle. Similarly, we define τ_P, τ_A, and τ_M as the stress at the base of the plate, upper mantle (or asthenosphere), and lower mantle. Then equations (B.5) and (B.6) can be used to couple the velocity and stresses between the layers. Continuity of velocity between adjacent layers

requires

$$U_A = U_P - \frac{d_A}{6\mu_A}\left(6\tau_P - d_A[3b + 3Ad_M + 2Ad_A]\right), \tag{B.7}$$

$$U_M = U_A - \frac{d_M}{6\mu_M}\left(6\tau_A - d_M[3b + 2Ad_M]\right). \tag{B.8}$$

Continuity of stress between adjacent layers requires

$$\tau_A = \tau_P - \frac{d_A}{2}\left[2b + A(2d_M + d_A)\right], \tag{B.9}$$

$$\tau_M = \tau_A - \frac{1}{2}d_M\left[2b + Ad_M\right]. \tag{B.10}$$

Conservation of mass requires that the total vertically integrated horizontal velocity in the layer vanish

$$\int_0^d U(y)dy = 0. \tag{B.11}$$

Using equation (B.4) to calculate the integral in equation (B.11) for all four layers yields

$$\begin{aligned} 0 &= (d_A + d_L)U_P + d_M U_A - \frac{d_A^2}{2\mu_A}\tau_P - \frac{d_M^2}{2\mu_M}\tau_A \\ &+ \left(\frac{d_A^4}{8\mu_A} + \frac{d_A^3 d_M}{6\mu_A} + \frac{d_M^4}{8\mu_M}\right)A \\ &+ \left(\frac{d_A^3}{\mu_A} + \frac{d_M^3}{\mu_M}\right)\frac{b}{6}. \end{aligned} \tag{B.12}$$

The base of the mantle is free-slip and thus

$$\tau_M = 0. \tag{B.13}$$

The stress on the base of the plate can be solved for by using the lithospheric energy balance (equation (3.43))

$$\tau_{_P} = \frac{D_{i_L} \langle Q \rangle_{_L}}{LU_{_P}} - d_{_L} P_{x_p} - \frac{d_{_L}}{L}\tau_{_R}. \tag{B.14}$$

Equations (B.7), (B.8), (B.9), (B.10), (B.12), (B.13), and (B.14) provide 7 equations to solve for the 7 unknown variables $U_{_A}$, $U_{_M}$, $\tau_{_P}$, $\tau_{_A}$, $\tau_{_M}$, A, and b in terms of the model parameters and the plate velocity $U_{_P}$. With $U_{_A}$, $U_{_M}$, $\tau_{_P}$, $\tau_{_A}$, A, and b now known, equation (B.4) may be used to calculate the velocity in any of the layers.

From equation (3.14), the dissipation from lateral flow for an arbitrary layer in the interior of the cell (where vertical velocity is negligible) is given by

$$\Phi_n = 2\int_V \mu_n \dot{\epsilon_{ij}}^2 dV = \frac{L}{2}\int_{y_0}^{y_1} \mu_n \left(\frac{\partial U}{\partial y}\right)^2 dy. \tag{B.15}$$

Using equation (B.4) for the velocity in an arbitrary layer yields

$$\begin{aligned}
\Phi_n &= \frac{y_1 - y_0}{\mu_n^2}\left(\tau_1^2 + \frac{\tau_1}{3}(y_0 - y_1)\left[3b + A(y_0 + 2y_1)\right]\right) \\
&+ \frac{1}{60}\frac{y_1 - y_0}{\mu_n^2}\left(20b^2 + 5Ab\left[3y_0 + 5y_1\right]\right) \\
&+ \frac{1}{60}\frac{y_1 - y_0}{\mu_n^2}A^2\left(3y_0^2 + 9y_0 y_1 + 8y_1^2\right).
\end{aligned} \tag{B.16}$$

Equation (B.16) allows for the calculation of dissipation in any of the fluid layers in the mantle as a function of the plate velocity $U_{_P}$. The total mantle dissipation for horizontal flow $\Phi_{_{MH}}$ is the sum of the dissipation in each of the mantle layers. This dissipation, along with equation (B.14) for the basal stress, can be substituted into the global energy balance (equation (3.44)) to solve for the single remaining variable, $U_{_P}$.

Appendix C

Additional calculations for Chapter 4

C.1 Model equations and parameters for numerical simulations

Equation 4.1 is solved using equation 4.14 and

$$H(t) = H_{sf} \cdot \sum_i \rho V C_i H_i e^{\frac{log(2)(t_{pd}-t)}{\tau_i}} \tag{C.1}$$

where C_i, H_i, and τ_i represent the radiogenic element concentration, the heat production rate, and the half-life of radiogenic element i respectively. Values for internal heating are taken from Schubert et al. (2001). The factor H_{sf} is a scale factor for the rate of internal heating that is tuned to adjust the surface heat flow. The plate velocity is calculated using the classic scaling that arises from boundary layer theory (e.g. Turcotte and Schubert, 1982)

$$U = \frac{\kappa}{d}\left(\frac{L}{\pi d}\right)^{\frac{1}{3}} R_a^{\frac{2}{3}} \tag{C.2}$$

with

$$R_a = \frac{\alpha \rho g T d^3}{\kappa \eta} \tag{C.3}$$

and where α is the thermal expansion coefficient, g is the gravitational acceleration, d is the depth of the mantle, and the viscosity η is calculated using equation 4.5. The viscosity of the W-I case is normalized in such a way that the viscosities in both cases are equal

when the potential temperature of the mantle is equal to $T = 1300^oC$ (this is equivalent to having a fixed water concentration of $\approx 300\,ppm$ for the calculation of the viscosity in the W-I case).

The water mass balance (equation 4.2) is solved using equations 4.16 and 4.17 for the degassing and regassing, respectively. The depth of melting, z_m, is based on a simple linearized fit of Figure 11 from Hirschmann et al. (2009) for the depth of melting as a function of the mantle temperature and water concentration

$$z_m(T, \chi_m) = z_1 T + z_2\,\chi_m + z_3 \tag{C.4}$$

where $z_1 = 286\,m/K$, $z_2 = 164\,m/ppm$, and $z_3 = -3.2 \times 10^5\,m$ are constants. We assume that the upper 20% of the plate is serpentinized and using $\chi_{serp} \approx 1.3\%$ then gives an average water concentration for the plate of $\chi_p = 0.26\%$ $(2600\,ppm)$. The initial concentration of water in the mantle was adjusted for both cases to give the present-day ocean mass of the Earth of $1.39 \times 10^{21}\,kg$. All other parameter values are the same for both simulations and can be found in Table C.1.

C.2 A KINEMATIC PLATE VELOCITY FOR THE THERMAL-WATER FEEDBACK

The rate of change of the viscosity is related to the plate velocity through the kinematic relations of equations 4.14-4.17. These derivations do not rely on any specific dynamic parameterizations for plate speed.

If the viscosity has no dependence on the water concentration then $\eta_\chi = 0$ and equation 4.21 simplifies to $\eta_T \dot{T} \approx 0$. This is satisfied when $\dot{T} = 0$ and $Q_s = H$. Using equation 4.14 for Q_s and solving for the plate velocity gives

$$U_T = \frac{\pi L \kappa}{\sqrt{\pi}} \left(\frac{H}{S k_c T} \right)^2 \tag{C.5}$$

If the viscosity has no dependence on temperature then $\eta_T = 0$ and equation 4.21 simplifies to $\eta_\chi \dot{\chi}_m \approx 0$ and is satisfied when $D = R$ and $\dot{\chi}_m = 0$. Setting $D = R$ and using

equations 4.16 and 4.17 gives $F_d z_m \chi_m = F_r d_l \chi_p$. Using equation 4.15 and solving for the plate velocity yields

$$U_W = 4\frac{\kappa}{z_m}\left(\frac{L}{z_m}\right)\left(\frac{F_r}{F_d}\frac{\chi_p}{\chi_m}\right)^2 \tag{C.6}$$

If the viscosity is dependent on both temperature and water concentration then equation 4.21 becomes

$$\eta_\chi \frac{R-D}{\rho V} = \eta_T \frac{Q_s - H}{\rho C_p V} \tag{C.7}$$

where we have used equations 4.1 and 4.2 for $\dot{T}$ and $\dot{\chi}_m$. Substituting the relations for Q_s, d_L, D, and R from equations 4.14, 4.15, 4.16, and 4.17 into equation C.7 and simplifying yields

$$\begin{aligned}\frac{\eta_\chi}{\eta_T}\left[2F_r\chi_p\sqrt{\frac{\kappa U_{TW}}{L}} - F_d\frac{z_m}{L}\chi_m U_{TW}\right] \quad = \\ 2ST\sqrt{\frac{\kappa U_{TW}}{\pi L}} - \frac{H}{\rho C_p}\end{aligned} \tag{C.8}$$

Equation C.8 can be solved for the plate velocity U_{TW} analytically using the quadratic method or numerically.

Parameter description		Value	Units
Density	ρ	3500	kg/m^3
Thermal conductivity	k_c	3.2	W/m·K
Specific heat	C_p	1200	J/kg·K
Thermal diffusivity	κ	7.6×10^{-7}	m^2/s
Thermal expansion	α	2.5×10^{-5}	1/K
Gravitational acceleration	g	10	m/s^2
Concentration	$C_{U_{238}}$	30.8×10^{-9}	kg/kg
Concentration	$C_{U_{235}}$	0.22×10^{-9}	kg/kg
Concentration	C_{Th}	124×10^{-9}	kg/kg
Concentration	C_K	36.9×10^{-9}	kg/kg
Heating rate	$H_{U_{238}}$	9.46×10^{-5}	W/kg
Heating rate	$H_{U_{235}}$	5.69×10^{-4}	W/kg
Heating rate	H_{Th}	2.64×10^{-5}	W/kg
Heating rate	H_K	2.92×10^{-5}	W/kg
Half-life	$\tau_{U_{238}}$	4.47	Gy
Half-life	$\tau_{U_{235}}$	0.70	Gy
Half-life	τ_{Th}	14.0	Gy
Half-life	τ_K	1.25	Gy
Scale factor (W-I)	H_{sf}	1.44	
Scale factor (W-D)	H_{sf}	1.02	
Activation energy	E	300	kJ/mol
Water fugacity exponent	r	1	
Stress-strain exponent	n	1	
Ideal gas constant	R_g	8.31	J/mol·K
Planet radius	r_s	6371	km
Core radius	r_{cmb}	3491	km
Planet surface area	S	3.25×10^{21}	m^2
Mantle volume	V	9×10^{20}	m^3
Average plate length	L	6000	km
Initial mantle conc. (W-I)	$\chi_m(0)$	851	ppm
Initial mantle conc. (W-D)	$\chi_m(0)$	742	ppm
Water conc. in plate	χ_p	2600	ppm
Degassing efficiency	F_d	1	
Degassing efficiency	F_r	0.15	

Table C.1: Parameters for sample evolution calculations.

Appendix D

Additional calculations for Chapter 5

D.1 Onset of stagnant lid convection

We consider the conditions necessary for the onset of convection in a cold thermal boundary layer with temperature dependent viscosity. The cold boundary layer extends from the surface to a depth of D in the fluid. The surface temperature is T_s and the temperature at the base of the thermal boundary layer is T_m. For highly temperature dependent viscosity, the onset of convection will first begin at the base of the cold thermal boundary layer. The thickness of the sub layer that begins to convect (the lower part of the thermal boundary layer) is d (with $d < D$). Let $\Delta T = T_m - T_s$. The temperature at the top of the sub layer that becomes unstable is

$$T_{sub} = T_m - \frac{d}{D}\Delta T \tag{D.1}$$

The viscosity at the top of the sub layer is (this is the strongest part of the layer)

$$\eta(T_{sub}) = \eta_0 e^{-\beta T_{sub}} = \eta_0 e^{-\beta T_m} e^{\beta \frac{d}{D}\Delta T} = \eta_m e^{\beta \frac{d}{D}\Delta T} \tag{D.2}$$

where η_m is the viscosity at the base of the cold thermal boundary layer (and thus also the fluid beneath). The onset of convection will begin once the Rayleigh number of the sub layer exceeds the critical Rayleigh number $Ra_c \sim 10^3$. This occurs when

$$\frac{\alpha\rho g\left(\frac{d}{D}\Delta T\right)d^3}{\eta(T_{sub})\kappa} > Ra_c \tag{D.3}$$

where $\frac{d}{D}\Delta T$ is the temperature difference across the sub layer. Substituting in the viscosity $\eta(T_{sub})$ from equation (D.2) and rearranging gives

$$\frac{\alpha\rho g\Delta T d^4}{\eta_m\kappa D Ra_c} > e^{\beta\frac{d}{D}\Delta T} \tag{D.4}$$

The exponential may be expanded to give

$$\begin{aligned}\frac{\alpha\rho g\Delta T}{\eta_m\kappa D Ra_c}d^4 &> 1+\frac{\beta}{D}\Delta T d+\frac{1}{2}\left(\frac{\beta}{D}\Delta T\right)^2 d^2 \\ &+ \frac{1}{6}\left(\frac{\beta}{D}\Delta T\right)^3 d^3+\frac{1}{24}\left(\frac{\beta}{D}\Delta T\right)^4 d^4+...\end{aligned} \tag{D.5}$$

If the inequality in Eq. (D.6) is true for some d, the d^4 coefficient on the left hand side must be greater than the d^4 coefficient on the right side and we require

$$\frac{\alpha\rho g\Delta T}{\eta_m\kappa D Ra_c} > \frac{1}{24}\left(\frac{\beta}{D}\Delta T\right)^4 \tag{D.6}$$

Finally, this can be rearranged to obtain

$$Ra_m = \frac{\alpha\rho g\Delta T D^3}{\eta_m\kappa} > \frac{(\beta\Delta T)^4}{24}Ra_c \tag{D.7}$$

Eq. (D.7) provides the relationship between the local Rayleigh number of the cold thermal boundary layer (using the viscosity from base of the layer), the critical Rayleigh number and temperature dependence of the viscosity.

We have compared this to numerical results, where we estimate the local Rayleigh number for positions throughout the layer, and Eq. (D.7) works well for predicting the onset time of convection for small accretion times ($t_a < 1.5$ Ma). The result is independent

of the radius of the planet. For larger accretion times it underestimates the onset slightly. This may be due to the fact that the derivation above assumes a linear temperature gradient and the actual diffuse gradient is slightly different for long cooling times.

D.2 The effect of a low conductivity surface layer

A pervasive idea in the literature is that a surface layer of low thermal conductivity k may insulate and depress the cooling rate of the body (Haack et al., 1990; Hevey and Sanders, 2006; Sahijpal et al., 2007). Let us assume that such a layer exists at the surface with conductivity k_l and thickness d_l. The material below this layer has conductivity k. The low conductivity surface layer would be part of the surface thermal boundary layer and as such the diffusive term in the thermal energy balance would be considerably larger than the internal heating term in this region. The layer can then be replaced with an equivalent layer of conductivity k and thickness $d_l' = (k/k_l)d_l$ that gives the same conductive heat flow and boundary temperature.

Now we consider a planetesimal of radius $a = 100$ km and thermal conductivity of k. The planetesimal has a surface layer of thermal conductivity $k_l = k/10$ and thickness $d_l = 0.5$ km. With the above argument in mind, this case is thus equivalent to a planetesimal of radius $a = 100+5 = 105$ km and thermal conductivity of k. The cooling of this planetesimal is going to be very similar to that of a body with radius $a = 100$ km and thermal conductivity of k. Thus, the presence of such a low conductivity layer will have little effect.

D.3 Effect of continuous accretion

In order to explain paleomagnetic observations of magnetized CV chondrites, continuous accretion onto a planetesimal with an internal dynamo has been invoked to allow for (partially) undifferentiated material to persist at the surface of such a planetesimal (Elkins-Tanton et al., 2011; Gupta and Sahijpal, 2010). Here, we address the effect of continuous surface accretion on the dynamics of stagnant lid convection. Consider a planetesimal that has a convecting mantle with a highly temperature dependent viscosity. As a result, the

mode of convection is stagnant lid convection and a viscous thermal boundary layer (or lid) is formed at the surface of the mantle. In the absence of accretion, the lid adjusts its thickness such that the convective heat flux at the base of the lid is balanced by conduction through the lid. With accretion, an increased heat flux will be needed to not only balance the conductive heat flux through the layer, but also to warm the cold material that is added to the surface. We investigate what the effect of continuous accretion is on the lid thickness and heat flow.

We begin by solving for a steady state solution for the temperature profile at the surface of the planetesimal with continuous accretion. We assume an accretion rate of u_a m yr^{-1}. We choose a frame of reference moving at a speed of u_a, rendering the steady state profile at the surface stationary. Material is added to the surface at a temperature of T_s. At steady state, we assume that the temperature at a depth of δ, which is to be determined, is equal to the mantle temperature $T_m = \Delta T + T_s$. The heat equation to be solved is

$$-u_a \frac{dT}{dz} = \kappa \frac{d^2T}{dz^2} \tag{D.8}$$

with boundary conditions $T(z = 0) = \Delta T + T_s$ and $T(z = \delta) = T_s$. $z = 0$ is the base of the layer considered and $z = \delta$ is the surface of the growing planetesimal. This is a linear homogeneous second order ordinary differential equation and has as its solution

$$T(z) = \frac{e^{-u_a z/\kappa} - 1}{1 - e^{-u_a \delta/\kappa}} \, \Delta T + T_m \tag{D.9}$$

Taking the derivative of Eq. (D.9) gives the temperature gradient throughout the layer

$$\frac{dT}{dz} = \frac{u_a}{\kappa} \Delta T \frac{e^{-u_a z/\kappa}}{e^{-u_a \delta/\kappa} - 1} \tag{D.10}$$

Note that for very small accretion rates ($u_a << \kappa/\delta$) Eqs. (D.9) and (D.10) reduce to $T(z) = -(z/\delta)\Delta T + T_m$ and $dT/dz = -\Delta T/\delta$ which is the linear temperature gradient we expect at steady state and in the absence of accretion.

We will use the above equations to derive the steady state dynamics of stagnant lid convection with accretion. Conceptually we follow the method of Solomatov (1995) with the linear steady state temperature profile replaced with the above steady state temperature profile that accounts for accretion. We assume a viscosity of the form

$$\eta(T) = \eta_i e^{-\beta \Delta T} \tag{D.11}$$

Convection occurs beneath the thermal boundary layer and a part of the layer will participate with and be eroded by this flow. The strain rate near the base of the layer (small z) will decrease as

$$\dot{e} \propto \tau_o \eta^{-1} \propto \tau_o \eta_i^{-1} exp\left(-\beta \left|\frac{dT}{dz}\right|_{z=0} z\right) \tag{D.12}$$

where τ_o is the stress on the base of the layer exerted by the convective flow and $|dT/dz|_{z=0}$ is the absolute value of the temperature gradient evaluated at the base of the layer. From Eq. (D.10)

$$\left|\frac{dT}{dz}\right|_{z=0} = \frac{u_a \Delta T}{\kappa} \left(1 - e^{-u_a \delta / \kappa}\right)^{-1} \tag{D.13}$$

We are interested in the value of z, which we will refer to as δ_u, for which the strain rate decreases by a factor of e. From equation (D.12) we see that this happens when

$$\beta \left|\frac{dT}{dz}\right|_{z=0} \delta_u = 1 \tag{D.14}$$

Then

$$\delta_u = \left(\beta \left|\frac{dT}{dz}\right|_{z=0}\right)^{-1} \tag{D.15}$$

δ_u is the thickness of the actively convecting portion of the thermal boundary layer. The temperature drop ΔT_{rh} over $\Delta z = \delta_u$ is given by

$$\Delta T_{rh} = \left|\frac{dT}{dz}\right|_{z=0} \delta_u = \frac{1}{\beta} \tag{D.16}$$

ΔT_{rh} is the effective temperature drop that drives thermal convection beneath the lid. We

note that δ_u is different from the case considered by Solomatov (1995) when the temperature gradient across the lid is linear, since Eq. (D.13) demonstrates that the temperature gradient is not $\Delta T/\delta$ for the case of ongoing accretion. However, the obtained effective rheological temperature difference ΔT_{rh} is identical to that found by Solomatov (1995) and depends only on the temperature sensitivity of the viscosity, and thus the parameter β. Thus far we have assumed that the thermal boundary layer thickness is equal to δ. This quantity needs to be related to the dynamics and heat transport to ensure that the system is in fact at steady state. The heat transported to the base of the lid by thermal convection may be calculated using classic thermal boundary layer theory (see for example Schubert et al. (2001)) with a mantle viscosity of $\eta_m = \eta(T_m)$ and an effective temperature drop of ΔT_{rh} driving convection. This gives a heat flux at the base of the lid of

$$q_s = \frac{k\Delta T_{rh}}{d}\left(\frac{\frac{\alpha\rho g\Delta T_{rh}d^3}{\eta_m\kappa}}{Ra_c}\right)^{\frac{1}{3}} = p^{-\frac{4}{3}}\frac{k\Delta T}{d}\left(\frac{Ra}{Ra_c}\right)^{\frac{1}{3}} \tag{D.17}$$

where we have used Eq. (D.16) for ΔT_{rh}, $p = \beta\Delta T$ which can be shown to be equal to the natural logarithm of the viscosity contrast across the thermal boundary layer (Solomatov, 1995), $Ra_c \approx 10^3$ is the critical Rayleigh number, and the mantle Rayleigh number is defined as

$$Ra = \frac{\alpha\rho g\Delta T d^3}{\eta_m\kappa} \tag{D.18}$$

The conductive heat flux at the base of the layer can be calculated using equation (D.13) and is given by

$$q_s = k\left|\frac{dT}{dz}\right|_{z=0} = k\frac{u_a\Delta T}{\kappa}\left(1 - e^{-u_a\delta/\kappa}\right)^{-1} \tag{D.19}$$

At steady state, the convective heat flux to the base of the lid must match the conductive heat flux through the lid and we can therefore equate the heat flux in Eqs. (D.17) and (D.19) to obtain the relationship

$$(\kappa/u_a)\left(1 - e^{-u_a\delta/\kappa}\right) = dp^{4/3}\left(Ra_c/Ra\right)^{1/3} \tag{D.20}$$

Eq. (D.20) relates the accretion rate u_a, the lid thickness δ and the mantle Rayleigh number Ra at steady state, and shows that accretion only becomes important for accretion rates of the order of $u_a \approx \kappa/\delta$ or larger. Let us consider the limiting behaviors.

For $u_a << \kappa/\delta$, the argument $u_a\delta/\kappa$ is very small and we may expand the exponential and drop all high order terms. Then $\exp(-u_a\delta/\kappa) \approx 1 - u_a\delta/\kappa$ and $(1 - \exp(-u_a\delta/\kappa)) \approx u_a\delta/\kappa$. Eq. (D.20) then becomes

$$\delta = dp^{4/3} \left(Ra_c/Ra\right)^{1/3} \tag{D.21}$$

Thus, for small accretion rates we recover the classic stagnant lid convection scaling that relates the lid thickness to the mantle Rayleigh number and the temperature dependence of the viscosity (Schubert et al., 2001).

For $u_a >> \kappa/\delta$, $\exp(-u_a\delta/\kappa) \approx 0$ and $(1-\exp(-u_a\delta/\kappa)) \approx 1$. Eq. (D.20) then becomes

$$\kappa/u_a = dp^{4/3} \left(Ra_c/Ra\right)^{1/3} \tag{D.22}$$

This gives the relationship between Ra and u_a for large u_a. The system will warm until Ra is large enough that the balance in Eq. (D.22) is achieved.

For an accretion rate of $u_a \approx \kappa/\delta$ Eq. (D.20) may be used to solve for the boundary layer thickness δ and gives

$$\delta = -\frac{\kappa}{u_a} log\left(1 - \frac{dp^{4/3}}{\kappa/u_a}\left(\frac{Ra_c}{Ra}\right)^{\frac{1}{3}}\right) \tag{D.23}$$

The primary phase of heating occurs over a duration of the order of the half life of ^{26}Al which is $\sim$ 0.7 Myr.The onset of convection must occur during this time if it is to occur at all. The cool thermal boundary layer grows from the surface at a rate determined by diffusion and will penetrate to a depth of $\delta \sim \sqrt{\kappa\ t_{onset}}$, where t_{onset} is the onset time of convection, which we argued must be around the half life of ^{26}Al. Using $t_{onset} = 0.7$ Myr and $\kappa \sim 10^{-6}$ m^2/s gives $\delta \approx 4$ km. Then we expect accretion rates on the order

of $u_a \approx \kappa/\delta = 8$ km/Myr to begin to have an affect on the stagnant lid thickness. This estimate is independent of the radius of the planetesimal.

Let us investigate the initial thermal evolution of the planetesimal of radius a for a duration of Δt. We will consider accretion rates which increase the radius of the planetesimal by no more than 10% over the time Δt since a fundamental assumption in the present work is that the planetesimal is mostly accreted to begin with. Then the maximum allowed accretion rate is $u_{a,max} = 0.1a/\Delta t$. From above, this will only begin to have an effect on the stagnant lid thickness when $u_a \approx 8$ km/Myr. Merk et al. (2002) estimated as a first order approximation an accretion rate of 200 km/Myr which indicates that we should take continuous accretion into account. Combining the two relationships for u_a allows us to calculate the minimum radius of the planetesimal for which accretion will begin to have an affect. This is given by

$$a_{min} \approx \frac{\Delta t}{\text{Myr}} 80 \text{ km} \tag{D.24}$$

We are interested in durations of $\Delta t = 10$ Myr, as paleomagnetic considerations require an early dynamo to persist for this long in the planetesimal (Weiss et al., 2008; Weiss et al., 2010). Thus, if we allow for a 10 % increase in radius over 10 Myr, the minimum planetesimal radius for which accretion will begin to affect the stagnant lid thickness is $a_{min} = 800$ km.

Furthermore, let us consider the case where accretion does begin to affect the stagnant lid thickness. Eq. (D.22) shows that at steady state $Ra \propto u_a^3$. An accretion rate that is twice as large requires an increase in Ra of a factor of 8 to negate it. Using $\beta = E/RT_r^2$ with $E = 500$ kJ/K mol, $R = 8.31$, a reference temperature of $T_r = 1300^oC$, and Eq. (D.11) shows that a temperature difference of $\Delta T_{adj} \approx 50^oC$ is required to decrease the viscosity by a factor of 8 and therefore increase Ra accordingly. As a result, an increased accretion rate will simply result in a small adjustment in mantle temperature and the system will run slightly hotter. This will have little effect on the cooling rates involved, just as we observed for a change of the reference viscosity in section 5.2.2.

D.4 EFFECTIVE SPECIFIC HEAT AS LATENT HEAT

Here we consider the effect of adding mantle latent heat to our thermal evolution model. The total rate of heat release Q_L from decreasing the melt fraction (freezing) is equal to:

$$\begin{aligned} Q_L &= -L_m \rho_m V_m \frac{d\phi_m}{dt} = -L_m \rho_m V_m \frac{d\phi_m}{dT_m}\frac{dT_m}{dt} \\ &= -\frac{L_m \rho_m V_m}{(T_{m,l} - T_{m,s})}\frac{dT_m}{dt} \end{aligned} \tag{D.25}$$

where L_m is the latent heat of fusion of silicate and calculate $d\phi_m/dT$ with Eq. (5.23)

$$\phi_m = \frac{T_m - T_{m,s}}{T_{m,l} - T_{m,s}} \tag{D.26}$$

The thermal energy equation for the mantle Eq. 5.15, with the addition of Q_L, then becomes

$$\begin{aligned} \rho_m V_m c_p \frac{dT_m}{dt} &= -A_m F_{surf} + A_c F_c \\ &+ \rho V_m Q_r - \frac{L_m \rho_m V_m}{(T_{m,l} - T_{m,s})}\frac{dT_m}{dt} \end{aligned} \tag{D.27}$$

which can be written as

$$\rho_m V_m c_p' \frac{dT_m}{dt} = -A_m F_{surf} + A_c F_c + \rho V_m Q_r \tag{D.28}$$

with

$$c_p' = c_p \left[1 + \frac{L_m}{c_p(T_{m,l} - T_{m,s})}\right] \tag{D.29}$$

where c_p' is an effective specific heat that includes the effect of the mantle latent heat of fusion. Using $L_m \approx 4 \times 10^5$ J/kg, $c_p = 1200$ J/kg/K, and $T_{m,l} - T_{m,s} = (1850 - 1425)$ K, the correction term is $1 + L_m/[c_p(T_{m,l} - T_{m,s})] \approx 1.8$ and thus including the latent heat is equivalent to increasing the specific heat by a factor of ~ 2. However, the dynamo time is only weakly dependent on the specific heat, which explains why the results of our model

are not sensitive to including the latent heat of fusion. The correction term is well within the range of uncertainty for the mantle specific heat.

D.5 SCALING LAWS

We can equate the magnetic energy to a fraction of the thermodynamically available power in the core determined by how much is lost to ohmic dissipation (Christensen, 2010)

$$\frac{B^2}{2\mu_0} \propto f_{ohm}\frac{l_b^2}{\lambda}\frac{\alpha_c g_c F_c}{c_{p,c}} \tag{D.30}$$

where B is the magnetic field strength, μ_0 is the magnetic permeability, f_{ohm} is the fraction of the available power that is converted to magnetic energy, l_b is the length scale of the magnetic field, λ is the magnetic diffusivity, F_c is the core heat flux, α_c is thermal expansivity and g_c is the gravity in the core.

l_b^2/λ may be considered equivalent to the ohmic dissipation time $\tau_\lambda = E_m/D$ (Christensen, 2010), which should scale with the magnetic Reynolds number (Christensen and Aubert, 2006)

$$\tau_\lambda \propto \frac{L^2}{\lambda Re_m} = \frac{L}{U} \tag{D.31}$$

where L is a length scale for which the core radius r_c is often used and U is the the core convective speed. Substituted in Eq. D.30 yields

$$\frac{B^2}{2\mu_0} \propto f_{ohm}\frac{L}{U}\frac{\alpha_c g_c F_c}{c_{p,c}} \tag{D.32}$$

where $f_{ohm} \approx 1$.

We now use different scalings for the core speed u_c to evaluate the magnetic field strength B.

Mixing length theory

$$u_{ML} = \left(\frac{4\pi G\alpha_c r_c^2 F_c}{c_{p,c}}\right)^{1/3} \tag{D.33}$$

Substituting this in Eq. D.32, assuming $L \sim r_c$, and solving for B gives

$$B_{ML} = (2\mu_0\rho_c)^{1/2} \left(\frac{4\pi\alpha_c G r_c^2 F_c}{c_{p,c}} \right)^{1/3} \tag{D.34}$$

For a particular planetesimal, we are interested, as a first step, in what, at minimum, is energetically required and possible to achieve a dynamo of certain strength and duration. We determine to what temperature the core must be heated in order to guarantee enough heat flow during secular cooling of the core for it to have both a supercritical magnetic Reynolds number and deliver a magnetic field of sufficient strength. Eqs. D.33 and D.34 provide these constraints.

The definition of the magnetic Reynolds number can be rewritten as

$$u_c = \frac{Re_m \lambda}{r_c} \tag{D.35}$$

Equating this to Eq. D.33 and solving for the heat flux yields

$$F_c = \frac{(Re_{m,crit}\lambda)^3 \, c_{p,c}}{4\pi\alpha_c G r_c^5} \tag{D.36}$$

The temperature increase beyond the core melting temperature required to allow sufficient heat flow during cooling can then be determined by

$$\rho_c c_{p,c} V_c \Delta T = \Delta t A_c F_c \tag{D.37}$$

where V_c and A_c are the core volume and surface area respectively, Δt is the time over which a dynamo must be present, for example, ~ 10 Myr (Weiss et al., 2008; Weiss et al., 2010), and ΔT is the temperature increase required to accomplish this. Solving for ΔT gives

$$\Delta T_{ML} = \frac{3\Delta t}{4\pi\alpha_c G \rho_c} \left(\frac{Re_{m,crit}\lambda}{r_c^2} \right)^3 \tag{D.38}$$

A similar constraint can be found by solving D.34 for F_c for a particular B_{min} and its

associated required ΔT_{ML*}.

$$\Delta T_{ML*} = \frac{3\Delta t}{4\pi\alpha_c G\rho_c r_c^3}\left(\frac{B_{min}}{\sqrt{2\rho_c\mu_0}}\right)^3 \tag{D.39}$$

Coriolis Inertial Archimedean (CIA) balance

The same approach can be taken with the CIA scaling for the core convective speed

$$u_{CIA} = \left(\frac{2\sqrt{2}\pi G\alpha_c}{c_{p,c}}\right)^{2/5}\left(\frac{r_c^3 F_c^2}{\Omega}\right)^{1/5} \tag{D.40}$$

where Ω is the rotation rate of the body. This gives for the magnetic field strength

$$B_{CIA} = (2\mu_0\rho_c)^{1/2}\left[(2r_c)^7\left(\frac{F_c\alpha_c\pi G}{c_{p,c}}\right)^3\Omega\right]^{1/10} \tag{D.41}$$

We again use the magnetic Reynolds number to rewrite Eq. D.40 in terms of the heat flux, and with Eq. D.37 we find for the required temperature increase

$$\Delta T_{CIA} = \frac{3\Delta t\sqrt{\Omega}}{2\sqrt{2}\pi\alpha_c G\rho_c}\left(\frac{(Re_{m,crit}\lambda)^{1/2}}{r_c}\right)^5 \tag{D.42}$$

Using Eq. D.41 we apply the minimum magnetic field strength constraint to find its associated required temperature increase

$$\Delta T_{CIA*} = \frac{3\Delta t}{16\pi\alpha_c G}\left(\frac{B_{min}^{10}}{\Omega\mu_0^5\rho_c^8 r_c^{10}}\right)^{1/3} \tag{D.43}$$

Magnetic Archimedean Coriolis (MAC) balance

Here, the same approach yields for the core convective speed

$$u_{MAC} = \left(\frac{4\pi G\alpha_c r_c F_c}{3c_{p,c}\Omega}\right)^{1/2} \tag{D.44}$$

where Ω is the rotation rate of the body. This gives for the magnetic field strength

$$B_{MAC} = (2\mu_0\rho_c)^{1/2}\left[\frac{4\pi\alpha_c G\Omega r_c^3 F_c}{3c_{p,c}}\right]^{1/4} \tag{D.45}$$

We find for the required temperature increase

$$\Delta T_{MAC} = \frac{9\Delta t\Omega}{4\pi G\alpha_c\rho_c}\frac{(Re_{m,crit}\lambda)^2}{r_c^4} \tag{D.46}$$

Applying the minimum magnetic field strength constraint to find its associated required temperature increase

$$\Delta T_{MAC*} = \frac{9\Delta t}{16\mu_0^2\pi\alpha_c G\Omega\rho_c^3}\left(\frac{B_{min}}{r_c}\right)^4 \tag{D.47}$$

Bibliography

Aubert, J., Brito, D., Nataf, H.-C., Cardin, P., Masson, J.-P., 2001. A systematic experimental study of rapidly rotating spherical convection in water and liquid gallium. Physics of the Earth and Planetary Interiors 128, 51–74.

Becker, T. W., Kustowski, B., Ekström, G., 2008. Radial seismic anisotropy as a constraint for upper mantle rheology. Earth and Planetary Science Letters 267 (1-2), 213–227.

Booker, J., 1976. Thermal-convection with strongly temperature-dependent viscosity. Journal of Fluid Mechanics 76, 741–754.

Buffett, B. A., 2002. Estimates of heat flow in the deep mantle based on the power requirements for the geodynamo. Geophysical Research Letters 29 (12), 120000–1, doi:10.1029/2001GL014649.

Buffett, B. A., 2006. Plate force due to bending at subduction zones. Journal of Geophysical Research-Solid Earth 111 (B9).

Busse, F., Richards, M., Lenardic, A., 2006. A simple model of high prandtl and high rayleigh number convection bounded by thin low-viscosity layers. Geophysical Journal International 164, 160–167.

Capitanio, F. A., Morra, G., Goes, S., 2009. Dynamics of plate bending at the trench and slab-plate coupling. Geochem. Geophys. Geosys. 10.

Carslaw, H. S., Jaeger, J. C., 1986. Conduction of Heat in Solids. Oxford University Press.

Castillo-Rogez, J., Johnson, T. V., Lee, M. H., Turner, N. J., Matson, D. L., Lunine, J., 2009. ^{26}Al decay: Heat production and a revised age for Iapetus. Icarus 204, 658–662, doi:10.1016/j.icarus.2009.07.025.

Chambers, J. E., 2004. Planetary accretion in the inner Solar System. Earth and Planetary Science Letters 223, 241–252.

Christensen, U., Olson, P., Glatzmaier, G., 1999. Numerical modelling of the geodynamo: a systematic parameter study. Geophysical Journal International 138, 393 – 409.

Christensen, Ulrich R., U., 1984. Heat trasnport by variable viscosity convection and implications for the earth's thermal evolution. Physics of the Earth and Planetary Interiors 35 (4), 264–282.

Christensen, U. R., 2010. Dynamo Scaling Laws and Applications to the Planets. Space Science Reviews 152, 565–590, doi:10.1007/s11214–009–9553–2.

Christensen, U. R., Aubert, J., 2006. Scaling properties of convection-driven dynamos in rotating spherical shells and application to planetary magnetic fields. Geophysical Journal International 166, 97–114, doi:10.1111/j.1365–246X.2006.03009.x.

Conrad, C., Hager, B., 1999. Effects of plate bending and fault strength at subduction zones on plate dynamics. Journal of Geophysical Research-Solid Earth 104 (B8), 17551–17571.

Conrad, C., Hager, B., 2001. Mantle convection with strong subduction zones. Geophysical Journal International 144, 271–288.

Conrad, C., Lithgow-Bertelloni, C., 2002. How mantle slabs drive plate tectonics. Science 298 (5591), 207–209.

Conrad, C. P., Hager, B. H., 1999. The thermal evolution of an earth with strong subduction zones. Geophysical Research Letters 26, 3041–3044.

Crowley, J. W., O'Connell, R. J., 2008. Parameterized thermal convection with a multi-layered fluid and plates. Eos Trans. AGU 89, Fall Meet. Suppl., Abstract DI31A–1783.

Crowley, J. W., O'Connell, R. J., 2012. An analytic model of convection in a system with layered viscosity and plates. Geophysical Journal International 188, 61–78.

Cuzzi, J. N., Dobrovolskis, A. R., Champney, J. M., 1993. Particle-gas dynamics in the midplane of a protoplanetary nebula. Icarus 106, 102, doi:10.1006/icar.1993.1161.

Davies, G., 1980. Thermal histories of convective earth models and constraints on radiogenic heat production in the earth. Journal of Geophysical Research 85 (NB5), 2517–2530.

Davies, G., 1999. Dynamic Earth: plates, plumes and mantle convection. Cambridge University Press.

Davies, G. F., 2009. Effect of plate bending on the Urey ratio and the thermal evolution of the mantle. Earth and Planetary Science Letters 287 (3-4), 513–518.

Dixon, J. E., Leist, L., Langmuir, C., Schilling, J.-G., 2002. Recycled dehydrated lithosphere observed in plume-influenced mid-ocean-ridge basalt. Nature 420 (6914), 385–389.

Elder, J., 1976. The Bowels of the Earth. Oxford University Press.

Elkins-Tanton, L. T., Weiss, B. P., Zuber, M. T., 2011. Chondrites as samples of differentiated planetesimals. Earth and Planetary Science Letters 305, 1–10, doi:10.1016/j.epsl.2011.03.010.

Elsasser, W., 1969. Convection and stress propagation in the upper mantle. In: Runcorn, S. K. (Ed.), The Application of Modern Physics to the Earth and Planetary Interiors. Wiley-Interscience, New York, pp. 223–249.

Forsyth, D., Uyeda, S., 1975. On the relative importance of the driving forces of plate motion. Geophys. J. R. astr. Soc. 43, 163–200.

Gable, C. W., 1989. Numerical models of plate tectonics and mantle convection in three dimensions. Ph.D. thesis, Harvard University.

Gable, C. W., O'Connell, R. J., Travis, B. J., 1991. Convection in three dimensions with surface plates; generation of toroidal flow. Journal of Geophysical Research 96 (5), 8391–8405.

Gaidos, E., Conrad, C. P., Manga, M., Hernlund, J., 2010. Thermodynamic Limits on Magnetodynamos in Rocky Exoplanets. Astrophysical Journal 718, 596–609. doi:10.1088/0004–637X/718/2/596.

Ghosh, A., McSween, H. Y., 1998. A Thermal Model for the Differentiation of Asteroid 4 Vesta, Based on Radiogenic Heating. Icarus 134, 187–206.

Golabek, G. J., Schmeling, H., Tackley, P. J., 2008. Earth's core formation aided by flow channelling instabilities induced by iron diapirs. Earth and Planetary Science Letters 271, 24–33.

Golitsyn, G., 1979. Simple theoretical and experimental study of convection with some geophysical applications and analogies. Journal of Fluid Mechanics 95, 567–608.

Grigné, C., Labrosse, S., Tackley, P., 2005. Convective heat transfer as a function of wavelength: Implications for the cooling of the earth. Journal of Geophysical Research 110 (B3).

Gubbins, D., 1977. Energetics of the Earth's core. Journal of Geophysical Research 43, 453–464.

Gupta, G., Sahijpal, S., 2010. Differentiation of Vesta and the parent bodies of other achondrites. Journal of Geophysical Research (Planets) 115, 8001, doi:10.1029/2009JE003525.

Haack, H., Rasmussen, K. L., Warren, P. H., 1990. Effects of regolith/megaregolith insulation on the cooling histories of differentiated asteroids. Journal of Geophysical Research 95, 5111–5124, doi:10.1029/JB095iB04p05111.

Hacker, B. R., 2008. H2O subduction beyond arcs. Geochem. Geophys. Geosys. 9 (Q03001).

Hager, B., 1978. Oceanic plate motions driven by lithospheric thickening and subducted slabs. Nature 276, 156–159.

Hager, B., O'Connell, R., 1981. A simple global model of plate dynamics and mantle convection. Journal of Geophysical Research 86, 4843–4867.

Hevey, P. J., Sanders, I. S., 2006. A model for planetesimal meltdown by 26Al and its implications for meteorite parent bodies. Meteoritics and Planetary Science 41, 95–106.

Hirose, K., Kawamoto, T., 1995. Hydrous partial melting of lherzolite at 1 GPa: The effect of H2O on the genesis of basaltic magmas. Earth and Planetary Science Letters 133 (3-4), 463 – 473.

Hirschmann, M. M., Aubaud, C., Withers, A. C., 2005. Storage capacity of H2O in nominally anhydrous minerals in the upper mantle. Earth and Planetary Science Letters 236 (1-2), 167–181.

Hirschmann, M. M., Tenner, T., Aubaud, C., Withers, A. C., 2009. Dehydration melting of nominally anhydrous mantle: The primacy of partitioning. Physics of the Earth and Planetary Interiors 176 (1-2), 54–68.

Hirth, G., Kohlstedt, D., 1996. Water in the oceanic upper mantle: Implications for rheology, melt extraction and the evolution of the lithosphere. Earth and Planetary Science Letters 144 (1-2), 93–108.

Höink, T., Lenardic, A., 2010. Long wavelength convection, poiseuille and couette flow in the low-viscosity asthenosphere and the strength of plate margins. Geophysical Journal International 180 (1), 23–33.

Howard, L. N., 1966. Convection at high Rayleigh number. In: Gortler, H. (Ed.), Proc. 11th Int. Cong. Appl. Mech. Munich, 1964. Springer, pp. 1109–1115.

Iwamori, H., 2007. Transportation of H2O beneath the Japan arcs and its implications for global water circulation. Chemical Geology 239 (3-4), 182–198.

Kaula, W. M., 1979. Thermal evolution of earth and moon growing by planetesimal impacts. Journal of Geophysical Research 84, 999–1008.

Kleine, T., Münker, C., Mezger, K., Palme, H., 2002. Rapid accretion and early core formation on asteroids and the terrestrial planets from Hf-W chronometry. Nature 418, 952–955, doi:10.1038/nature00982.

Korenaga, J., 2003. Energetics of mantle convection and the fate of fossil heat. Geophysical Research Letters 30 (8).

Korenaga, J., 2008. Urey ratio and the structure and evolution of earth's mantle. Reviews of Geophysics 46 (2).

Korenaga, J., 2009. How does small-scale convection manifest in surface heat flux? Earth and Planetary Science Letters.

Larimer, J. W., 1995. Core Formation in Asteroid-sized Bodies. Meteoritics 30, 533.

Lenardic, A., Richards, M., Busse, F., 2006. Depth-dependent rheology and the horizontal length scale of mantle convection. Journal of Geophysical Research 111 (B7).

Li, Z.-X. A., Lee, C.-T. A., Peslier, A. H., Lenardic, A., Mackwell, S. J., 2008. Water contents in mantle xenoliths from the Colorado Plateau and vicinity: Implications for the mantle rheology and hydration-induced thinning of continental lithosphere. Journal of Geophysical Research 113 (B9).

MacPherson, G. J., Davis, A. M., Zinner, E. K., 1995. The distribution of aluminum-26 in the early Solar System - A reappraisal. Meteoritics 30, 365.

McGovern, P., Schubert, G., 1989. Thermal evolution of the Earth - effects of volatile exchange between atmosphere and interior. Earth and Planetary Science Letters 96 (1-2), 27–37.

McKenzie, D., Roberts, J., Weiss, N. O., 1974. Convection in the earth's mantle: towards a numerical simulation. Journal of Fluid Mechanics 62 (3), 465–538.

McKenzie, D., Weiss, N., 1975. Speculations on the thermal and tectonic history of the earth. Geophys. J. Roy. astr. Soc. 42, 131–174.

McKenzie, D. P., 1967. Some remarks on heat flow and gravity anomalies. Journal of Geophysical Research 72 (24), 6261–6273.

McNamara, A., Karato, S., van Keken, P., 2001. Localization of dislocation creep in the lower mantle: implications for the origin of seismic anisotropy. Earth and Planetary Science Letters 191 (1-2), 85–99.

Mei, S., Kohlstedt, D., 2000a. Influence of water on plastic deformation of olivine aggregates 1. Diffusion creep regime. Journal of Geophysical Research 105 (B9), 21457–21469.

Mei, S., Kohlstedt, D., 2000b. Influence of water on plastic deformation of olivine aggregates 2. Dislocation creep regime. Journal of Geophysical Research 105 (B9), 21471–21481.

Merk, R., Breuer, D., Spohn, T., 2002. Numerical Modeling of ^{26}Al-Induced Radioactive Melting of Asteroids Considering Accretion. Icarus 159, 183–191, doi:10.1006/icar.2002.6872.

Mitrovica, J., Forte, A., 2004. A new inference of mantle viscosity based upon joint inversion of convection and glacial isostatic adjustment data. Earth and Planetary Science Letters 225, 177–189.

Monteux, J., Jellinek, A. M., Johnson, C. L., 2011. Why might planets and moons have early dynamos? Earth and Planetary Science Letters 310, 349–359, doi:10.1016/j.epsl.2011.08.014.

Monteux, J., Ricard, Y., Coltice, N., Dubuffet, F., Ulvrova, M., 2009. A model of metal-silicate separation on growing planets. Earth and Planetary Science Letters 287, 353–362, doi:10.1016/j.epsl.2009.08.020.

Moresi, L., Gurnis, M., 1996. Constraints on the lateral strength of slabs from three-dimensional dynamic flow models. Earth and Planetary Science Letters 138, 15–28.

Moresi, L., Solomatov, V., 1998. Mantle convection with a brittle lithosphere: thoughts on the global tectonic styles of the earth and venus. Geophysical Journal International 133 (3), 669–682.

Morris, S., 2008. Viscosity stratification and the horizontal scale of end-driven cellular flow. Physics of Fluids 20, 063103.

Morris, S., Canright, D., 1984. A boundary-layer analysis of benard convection in a fluid of strongly temperature-dependent viscosity. Physics of the Earth and Planetary Interiors 36 (3-4), 355–373.

Neumann, W., Breuer, D., Spohn, T., 2012. Differentiation of H-Chondritic Planetesimals. In: Lunar and Planetary Institute Science Conference Abstracts. Vol. 43 of Lunar and Planetary Institute Science Conference Abstracts. p. 1889.

Nimmo, F., 2009. Energetics of asteroid dynamos and the role of compositional convection. Geophysical Research Letters 36, L10201, 10.1029/2009GL037997.

Nimmo, F., Stevenson, D., 2000. Influence of early plate tectonics on the thermal evolution and magnetic field of Mars. Journal of Geophysical Research 105 (E5), 11,969 – 11,979.

O'Connell, R. J., Hager, B., 1980. On the thermal state of the earth. In: Dziewonski, A. M., Boschi, E. (Eds.), Physics of the Earth's Interior. Vol. LXXVI of Proceedings of the "Enrico Fermi" International School of Physics. North Holland.

O'Neill, C., Lenardic, A., 2007. Geological consequences of super-sized earths. Geophysical Research Letters 34.

Parai, R., Mukhopadhyay, S., 2012. How large is the subducted water flux? new constraints on mantle regassing rates. Earth and Planetary Science Letters 317, 396–406.

Reese, C., Solomatov, V., 2006. Fluid dynamics of local martian magma oceans. Icarus 184 (1), 102 – 120.

Ricard, Y., Šrámek, O., Dubuffet, F., 2009. A multi-phase model of runaway core-mantle segregation in planetary embryos. Earth and Planetary Science Letters 284, 144–150.

Rüpke, L. H., Morgan, J. P., Hort, M., Connolly, J. A. D., 2004. Serpentine and the subduction zone water cycle. Earth and Planetary Science Letters 223 (1-2), 17–34.

Sahijpal, S., Gupta, G., 2011. Did the carbonaceous chondrites evolve in the crustal regions of partially differentiated asteroids? Journal of Geophysical Research (Planets) 116, 6004, doi:10.1029/2010JE003757.

Sahijpal, S., Soni, P., Gupta, G., 2007. Numerical simulations of the differentiation of accreting planetesimals with 26Al and 60Fe as the heat sources. Meteoritics and Planetary Science 42, 1529–1548, doi:10.1111/j.1945–5100.2007.tb00589.x.

Samuel, H., Tackley, P. J., Evonuk, M., 2010. Heat partitioning in terrestrial planets during core formation by negative diapirism. Earth and Planetary Science Letters 290, 13–19, doi:10.1016/j.epsl.2009.11.050.

Sandu, C., Lenardic, A., McGovern, P., 2011. The effects of deep water cycling on planetary thermal evolution. Journal of Geophysical Research-Solid Earth 116.

Schubert, G., Stevenson, D., Cassen, P., 1980. Whole planet cooling and the radiogenic heat-source contents of the earth and moon. Journal of Fluid Mechanics 85 (NB5), 2531–2538.

Schubert, G., Turcotte, D., Olson, P., 2001. Mantle convection in the Earth and planets. Cambridge University Press.

Senshu, H., Kuramoto, K., Matsui, T., 2002. Thermal evolution of a growing Mars. Journal of Geophysical Research (Planets) 107, 5118.

Sharpe, H., Peltier, W., 1979. A thermal history model for the earth with parameterized convection. Geophys. J. R. astr. Soc. 59, 171—203.

Silver, P. D., Behn, M. D., 2008. Intermittent plate tectonics? Science 319 (DOI: 10.1126/science.1148397), 85–88.

Sleep, N., 2000. Evolution of the mode of convection within terrestrial planets. Journal of Geophysical Research 105 (E7), 17,563–17,578.

Solomatov, V., 1995. Scaling of temperature-and stress-dependent viscosity convection. Physics of Fluids 7 (2), 266–274.

Sotin, C., Labrosse, S., 1999. Three-dimensional thermal convection in an iso-viscous, infinite prandtl number fluid heated from .... Physics of the Earth and Planetary Interiors 112, 171–190.

Spohn, T., Schubert, G., 1982. Modes of mantle convection and the removal of heat from the earth's interior. Journal of Geophysical Research 87, 4682–4696.

Stengel, K. C., Oliver, D. S., Booker, J. R., 1982. Onset of convection in a variable-viscosity fluid. Journal of Fluid Mechanics 120, 411–431, doi:10.1017/S0022112082002821.

Stevenson, D. J., 1990. Fluid dynamics of core formation. pp. 231–249.

Stevenson, D. J., 2003. Planetary magnetic fields. Earth and Planetary Science Letters 208, 1–11, doi:10.1016/S0012–821X(02)01126–3.

Thommes, E. W., Duncan, M. J., Levison, H. F., 2003. Oligarchic growth of giant planets. Icarus 161, 431–455, doi:10.1016/S0019–1035(02)00043–X.

Torrance, K., Turcotte, D., 1971. Thermal convection with large viscosity variations. Journal of Fluid Mechanics 47, 113–125.

Tozer, D., 1970. Factors determining the temperature evolution of thermally convecting earth models. Physics of the Earth and Planetary Interiors 2, 393–398.

Turcotte, D., 1967. A boundary-layer theory for cellular convection. International Journal of Heat and Mass Transfer 10 (8), 1065–1074.

Turcotte, D., Oxburgh, E., 1967. Finite amplitude convective cells and continental drift. Journal of Fluid Mechanics 28 (1), 29–42.

Turcotte, D., Schubert, G., 2002. Geodynamics. Cambridge University Press.

Turcotte, D. L., Schubert, G., 1982. Geodynamics. Applications of Continuum Physics to Geological Problems. John Wiley, New York.

Urey, H. C., 1955. The Cosmic Abundances of Potassium, Uranium, and Thorium and the Heat Balances of the Earth, the Moon, and Mars. Proceedings of the National Academy of Science 41, 127–144, doi:10.1073/pnas.41.3.127.

Valencia, D., O'Connell, R., Sasselov, D., 2007. Inevitability of plate tectonics on super-earths. Astrophysical Journal Letters.

Valencia, D., O'Connell, R. J., 2009. Convection scaling and subduction on earth and super-earths. Earth and Planetary Science Letters 286 (3-4), 492–502.

Weidenschilling, S. J., Cuzzi, J. N., 1993. Formation of planetesimals in the solar nebula. In: E. H. Levy & J. I. Lunine (Ed.), Protostars and Planets III. pp. 1031–1060.

Weiss, B. P., Berdahl, J. S., Elkins-Tanton, L., Stanley, S., Lima, E. A., Carporzen, L., 2008. Magnetism on the Angrite Parent Body and the Early Differentiation of Planetesimals. Science 322, 713–716.

Weiss, B. P., Gattacceca, J., Stanley, S., Rochette, P., Christensen, U. R., 2010. Paleomagnetic Records of Meteorites and Early Planetesimal Differentiation. Space Science Reviews 152 (1-4), 341–390.

Woolum, D. S., Cassen, P., 1999. Astronomical constraints on nebular temperatures: Implications for planetesimal formation. Meteoritics and Planetary Science 34, 897–907, doi:10.1111/j.1945–5100.1999.tb01408.x.

Wu, B., Conrad, C. P., Heuret, A., Lithgow-Bertelloni, C., Lallemand, S., 2008. Reconciling strong slab pull and weak plate bending: The plate motion constraint on the strength of mantle slabs. Earth and Planetary Science Letters 272 (1-2), 412–421.

Yoshino, T., Walter, M. J., Katsura, T., 2003. Core formation in planetesimals triggered by permeable flow. Nature 422, 154–157.

Youdin, A. N., Shu, F. H., 2002. Planetesimal Formation by Gravitational Instability. Astrophysical Journal 580, 494–505, doi:10.1086/34310.

Zhong, S., 2006. Constraints on thermochemical convection of the mantle from plume heat flux, plume excess temperature, and upper mantle temperature. Journal of Geophysical Research-Solid Earth 111 (B4).